

Imperial College of Science, Technology and Medicine
University of London

Travelling Wave Speed Coincidence

by

Philipp Schmiechen

schmiechen@alum.mit.edu

A thesis submitted to the University of London
for the degree of Doctor of Philosophy
and the Diploma of Imperial College

Department of Mechanical Engineering
Imperial College of Science, Technology and Medicine
London, South Kensington

May 1997

Abstract

This thesis presents an analysis of the *travelling-wave-speed instability* between a rotating bladed disc and a flexible casing. This type of interaction with structural contact can occur under certain circumstances in high-speed turbo-machinery, e.g., aircraft engines or compressors, and can amplify the vibration of the coupled rotor-stator system in an unstable manner by feeding the kinetic rotational energy of the rotor into the vibration. In order for turbo-machinery to operate safely, the travelling-wave-speed coincidences must be avoided and analysed for the possibility of the occurrence of the associated instability.

Previously, most casings of aircraft engines had additional structures such as the gear box attached to them. These attachments mistuned the casings, thereby reduced the travelling-wave components in the response and hence made the mechanism of energy transfer less efficient, which dropped below a non-critical threshold level defined by other system parameters such as damping and the gap size between rotating and stationary parts. New aircraft-engine designs tend towards axisymmetric casings for which the investigation of the travelling-wave-speed instability becomes more important.

In the literature, the few authors who treated elastic stators in contact with bladed discs did not investigate the possibility of travelling-wave-speed instability maybe due to lack of applicability to existing designs, but the majority of researchers analysed systems with rigid stators only. For systems with elastic rotors and stators, this approach is inadequate as the inclusion of the stator dynamics results in an increase in the number of critical speeds for the coupled system.

In this thesis, the rotor and the stator are modelled individually as structures with linear dynamics. In order to reduce the number of differential equations, modal models are employed to limit the computational effort to the relevant participating modes. The contact between the bladed disc and the stator is modelled by an impact friction law, including impact loss.

The effects of including the casing dynamics in the analysis of rotor-stator systems are described analytically, computed in a numerical simulation, and demonstrated in an experiment. Good qualitative agreement is achieved between the predictions and the experimental results for the investigated instability. Both numerical predictions and the experimental data show the occurrence of the travelling-wave-speed instability and validate the selected approach.

The results of the research indicate that the travelling-wave-speed instability exists and that it is a potential safety threat that must be avoided either by design or by choice of operating conditions.

Acknowledgement

I would like to express my gratitude to my supervisors, Professor D. J. Ewins and Mr. D. A. Robb, for their support and encouragement throughout the project.

Special thanks are due to Dr. I. Bucher, now at the Technion, Haifa, Israel, for his valuable advice and encouragement. He answered an infinity of questions and made this stay in London an invaluable experience.

Many thank to my colleagues and friends at Imperial College for the discussions, ideas, and help during the project.

I thank the European Union for funding this work as part of the Rostadyn-project in the Brite/Euram framework and all colleagues in the project. I would like to acknowledge especially Mr. R. Gaffney of Rolls-Royce plc. for the informative discussions.

I am grateful to my parents and my sisters, and Lindsay and Claude for all their love and support, and the joyful memories they created.

Table of Contents

Notation	1
CHAPTER 1: INTRODUCTION	3
1.1 Efficiency of Rotating Machines	3
1.2 Objectives of Research	4
1.3 Literature Survey	5
1.3.1 Rotor dynamics	5
1.3.2 Dynamics of rotating bladed discs	6
1.3.3 Models and analysis techniques	8
1.3.4 Travelling waves as principal coordinates	8
1.3.5 Vibration tests of rotating machinery	9
1.3.6 Contact models	9
1.3.7 Dynamic interaction between rotor and stator	10
1.4 Scope and Layout of the Thesis	10
1.4.1 Theoretical development	11
1.4.2 Numerical simulation	14
1.4.3 Experimental validation	14
CHAPTER 2: DYNAMICS OF STRUCTURES	16
2.1 Definition of Linearity	16
2.2 Modal Superposition	16
2.3 Eigenanalysis	17
2.3.1 Equations of motion	17
2.3.2 Modal description of the system characteristics	18
2.3.3 Mass normalisation of the modeshapes	19
2.3.4 Effect of damping	20
2.3.5 Forced response behaviour	21
2.4 Finite Element Approach	24
2.4.1 Introduction	24
2.4.2 Underlying idea	25
2.4.3 Spatial discretisation of the structure	25
2.4.4 General features of the FE solution	27
2.4.5 Solution methods	27
2.4.6 Program selection	32
2.5 Vibration Properties of Bladed Discs	32
2.5.1 Coupling approach	32

2.5.2 Disc vibrations	33
2.5.3 Blade vibrations	39
2.5.4 Assembly vibration	42
2.5.5 Experimental results	45
2.5.6 Effects of mistuning on the dynamics of rotationally periodic structures	45
2.5.7 Discussion - Stator	47
2.6 Vibration Properties of Rotating Discs	48
2.6.1 Admissible modeshapes	48
2.6.2 Computation of the natural frequencies	48
2.6.3 Discussion - Rotor	53
2.7 Conclusions	54
CHAPTER 3: DYNAMICS OF THE ROTOR-STATOR SYSTEM	56
3.1 Description of Dynamic Properties in non-body-fixed Coordinates	56
3.1.1 Stationary and rotating reference frames	56
3.1.2 Waves	57
3.1.3 Frequency-speed diagram	57
3.1.4 Wave velocity	61
3.1.5 Sense of direction in the rotating and stationary reference frame	63
3.2 Interaction Diagram	65
3.2.1 Travelling-wave-speed coincidence	65
3.2.2 Critical speeds	67
3.2.3 Energy transfer from one structure into the other	69
3.2.4 Balance of energy input and dissipation	73
3.2.5 Effect of mistuning on the energy transfer	74
3.3 Discussion	76
CHAPTER 4: NUMERICAL SIMULATION OF THE INTERACTION PROBLEM	78
4.1 Problem Description	78
4.2 Statement of Objective	78
4.3 Mathematical Model of the Rotor-Stator System	78
4.3.1 Steps in the modelling process	79
4.3.2 Models of the individual structures	80
4.3.3 Model of the contact forces	82
4.4 Formulation of the Dynamics	84
4.4.1 Equations of motion	84
4.4.2 Standard form of integration	85
4.5 Setting up the Integration	87
4.5.1 Problem size	87
4.5.2 Selection of the integration scheme	88

4.5.3 Selection of modes	90
4.5.4 Computation of the contact forces	92
4.6 Solution Procedure	96
4.6.1 Selection of the sampling frequency	96
4.6.2 Choice of initial conditions	96
4.6.3 Test cases	97
4.6.4 Program description	97
4.7 Discussion	98
CHAPTER 5: SIMULATION RESULTS	99
5.1 Test Cases	99
5.1.1 Engine-order excitation of the stator	99
5.1.2 Engine-order excitation of the rotor	101
5.2 Preliminaries for the numerical Simulation	102
5.2.1 General layout of figures	102
5.2.2 Initial conditions	103
5.3 Simulation of the 2ND Travelling-Wave-Speed Coincidence	103
5.3.1 Simulation at critical speed of rotation (Simulation 1)	103
5.3.2 Simulation at subcritical speed of rotation (Simulation 2 to 4)	105
5.3.3 Simulation at supercritical speed of rotation (Simulation 5)	107
5.3.4 Simulation of mistuned stator at critical speed of rotation (Simulation 1m)	108
5.4 Conclusions	109
CHAPTER 6: RIG DESIGN	112
6.1 Purpose of the Test Rig	112
6.2 Rig Requirements	112
6.3 Design Simplifications	112
6.3.1 Simplification of the geometry	112
6.3.2 Change of observer frame	113
6.4 Geometry Selection	115
6.4.1 Critical speed equation	115
6.4.2 Fixing the geometry	117
6.4.3 Axis direction	119
6.5 Alignment of Rotor and Stator	119
6.5.1 Problem definition	120
6.5.2 Alignment dilemma	120
6.5.3 The global error motions	120
6.5.4 Solution to the alignment problem	120
6.5.5 Results	123
6.5.6 Discussion	124

6.6 Balancing of the Rotor	124
6.6.1 Goal of balancing	124
6.6.2 Requirements	125
6.6.3 Balancing method	125
6.6.4 Results	127
6.7 Safety and Overload Protection	129
6.8 Data-Acquisition System	131
6.9 Conclusions	131
CHAPTER 7: EXPERIMENTAL RESULTS	132
7.1 Aim of the Test Program	132
7.2 Travelling-Wave-Speed Coincidence Diagram	132
7.3 Interpretation of the Signals from the Displacement Transducers	133
7.3.1 AC filtering	133
7.3.2 Low-pass filtering	134
7.3.3 Spectral analysis	136
7.4 Test of the 2ND Travelling-Wave-Speed Coincidence	137
7.4.1 Parameters	137
7.4.2 Test at critical speed of rotation (Test 1)	138
7.4.3 Test at subcritical speed of rotation (Test 2)	141
7.4.4 Test at supercritical speed of rotation (Test 3)	143
7.4.5 Test of mistuned system at critical speed of rotation (Test 1m to 3m)	145
7.5 Test of Higher ND Wave-Speed Coincidences	149
7.6 Conclusions	150
CHAPTER 8: CONCLUSIONS	151
8.1 Achievements	151
8.1.1 Theoretical background	151
8.1.2 Simulation	152
8.1.3 Experiment	153
8.1.4 Post-processing	153
8.1.5 Software	153
8.1.5.1 Analytical solution	153
8.1.5.2 FE program	154
8.1.5.3 Numerical simulation	154
8.1.5.4 Modal Analysis	154
8.1.5.5 Measurement	154
8.2 Summary of Conclusions	155
8.3 Outlook	156

CHAPTER 9: REFERENCES	158
APPENDICES	165
Appendix 1: Eigenanalysis	165
Appendix 2: Physical Data of Rotor and Stator	170
Appendix 3: Modal Tests	171
Appendix 4: Natural Frequencies of a Rotating Disc	173
Appendix 5: Data of the Test Rig	174
Appendix 6: Interaction Experiments	176
Appendix 7: Programs	177
Appendix 8: Terminology	187

Notation

Symbols

Coordinate systems, unit vectors

(x, y, z) :	Cartesian coordinate system
(r, θ, z) :	Cylindrical coordinate system: radial, tangential, and axial directions
$(n, t, b)_i$:	local Cartesian coordinate system attached to each blade tip: normal, tangential, and bi-normal directions
$\{e\}_i$:	unit vector

Scalar quantities

ω :	natural frequency [rad/s]
λ :	eigenvalue [(rad/s) ²]
ν :	wave velocity [rad/s]
Ω :	speed of rotation [rev/min]
t :	time
N_{blades} :	number of blades or sectors
N :	size of problem
n :	mode under investigation, primary mode
m :	arbitrary mode, secondary mode, possibly identical to n

Vectors and matrices

$[M], [C], [K]$:	mass, damping, and stiffness matrices
$[m_r], [c_r], [k_r]$:	modal mass, damping, and stiffness matrices (diagonal)
$[\lambda_r], [\omega_r]$:	eigenvalue and natural-frequency matrices (diagonal)
$[\zeta_r]$:	damping ratio matrix (diagonal)
$\{\psi\}_r, \{\phi\}_r$:	arbitrary and mass-normalised modeshape
$[\Psi], [\Phi]$:	arbitrary and mass-normalised modeshape matrix
$\{x\}$:	position coordinate
$\{u\}$:	response, degree of freedom, vibration around a equilibrium position
$\{y\}$:	secondary coordinates
$\{u\}_r$:	generalised coordinate, response to mode r
$\{p\}$:	principal coordinates
$\{f\}$:	force
$[I]$:	identity matrix
$[0], \{0\}$:	zero matrix and vector

Superscripts

T:	transpose
-1:	inverse; for functions: inverse functions
([^]):	(complex) magnitude
([*]):	complex conjugate
([.]):	time derivative
([']):	(locally) modified quantity
+ , -:	forward/backward travelling or co-/counter-rotating

Subscripts

R, S :	rotating, stationary reference frame
r, s :	rotor, stator; $r+s$: both structures, rs, sr : between both structures
f, b :	forward and backward in stationary reference frame co-rotating and counter-rotating in rotating reference frame
n :	nodal diameter
r, θ, z :	component in the direction of the global cylindrical coordinate system
n, t :	component in the direction of the local Cartesian coordinate system
0 or o, f :	original, undisturbed, initial and final state

Indices/Counters

r, s :	r^{th} and s^{th} mode, primary and secondary mode
i :	general counter
n, m :	nodal diameter, primary and secondary mode

Terms

Use

frequency:	for the vibration: ω [rad/s]
speed:	for the speed of rotation Ω [rev/min]
velocity:	for wave propagation. v [rad/s]

forward, backward: in the stationary reference frame

co-, counter-rotating: in the rotating reference frame

Note: the following terms are explained in the Appendix:

wave – mode, description, reference frame – coordinate system,
direction, frequency – speed – velocity

Chapter 1: Introduction

The basic objective of engineering research is to advance technology safely and make processes more efficient. Advancing a matter safely requires the researcher to understand the underlying principles but most engineering achievements were made without a complete understanding of the underlying principles. Engineers were and still are forced to develop theories of their own, which would be generalised by scientists only later, (Evans, 1989, Szabó, 1984, Wilson, 1990).

In vibration engineering in the aerospace industry, researchers have endeavoured to reduce levels of vibration, increase the life of components, and increase the efficiency of machines safely.

1.1 Efficiency of Rotating Machines

Efficiency can be defined in many ways but in the context of high-speed turbo-machinery, one usually means the overall efficiency of the energy-transformation process: the ratio of energy output to energy input.

The efficiencies of both turbo-generators and jet engines depend strongly on the clearance between the rotating and the stationary parts: the wider the clearance, the less efficient the machine. Hence it is desirable to reduce the clearance by as much as possible. It cannot be reduced below a certain minimum level due to uncertainties in the dynamic, fluid dynamic, and thermal loads, the machining tolerances and material properties. The more accurate these forces and parameters are known, the smaller the clearance can be made.

After the clearance, weight is the second quantity that governs the efficiency of an engine and a whole plane: lighter aeroplanes carry higher payloads or fly further at the same fuel consumption or, alternatively, consume less fuel for the same load and distance. Reducing the weight of an aircraft engine generally reduces its overall stiffness, which in turn causes larger deflections for a given force.

Reduced clearance and reduced stiffness together increase the possibility of violent contact between rotor and stator by enabling contact in the first place due to load-deformed shapes and smaller clearances and by maintaining contact more easily due to the reduced stiffness, in the second place. Small, possibly random, forces acting on one structure may cause deflections large enough to bridge the gap between the rotor and the stator and may cause initial contact. Under certain operating conditions, including the dynamic properties of the rotor and stator and the speed of rotation, the contacts may continue and drive the rotor-stator system unstable.

The proof of existence of the instability at a particular set of conditions, namely the coincidence of rotor and stator travelling wave velocities, or short *the travelling-wave-speed instability*, is the topic of this thesis.

In the case of a travelling-wave-speed coincidence, the rotational kinetic energy of the rotor feeds the vibration of the rotor-stator system, which responds with growing vibration amplitudes.

Most designs of power-generating machines have made provisions to reduce the chances of contact and to limit the possibly devastating effects of an eventual structural contact between the rotor and the stator. Uncertainties remain and instabilities like the travelling-wave-speed instability may cause accidents where the interaction between rotor and stator was assumed to be instrumental, (Smailes, 1993). In a particular case, a rotor-stator interaction expelled a fan blade from the engine, causing severe damage to the air frame, (NTSB, 1975)

Provisions to avoid contact between rotor and stator add both cost and weight to the structure which stands in conflict with economic goals. Detailed knowledge of the interaction between rotor and stator will help to optimise the design towards a less conservative, safe, and affordable solution.

The European Union sponsored research of the possible interactions between rotating and stationary parts in turbo-machinery to help the European turbo-machinery industry to maintain their competitiveness under the Brite/Euram framework. The work described in this thesis was carried out in the project ROSTADYN: Modelling of Rotor/Stator Interaction Dynamics, (European Union, 1992). In today's international markets, competitive products only guarantee the long-term survival of a company, and more and more it is the customer who decides what a 'competitive' product constitutes – by choosing from the variety that the global market produces. Products that once were competitive must be developed and optimised continuously so as not to lose onward-moving customers. For users of turbo-machinery the increased competition meant that they could ask not only for a lower purchasing price but also, and more importantly, a higher fuel efficiency without compromise on safety.

The necessity to direct research into the area of contacting elastic structures was highlighted recently by the following note:

The FAA has approved a [...] plan to increase the clearance between [...] fan blades and case-mounted abrasible strips to eliminate potential fan blade rubs and subsequent engine surges...

Aviation Week and Space Technology, January 1, 1996

1.2 Objectives of Research

A common interest of the rotating-machinery industry is to understand better the dynamic behaviour of rotating structures and the interaction of these with the surrounding casing and fluid in order to provide the designers with less conservative design guidelines and ways of improving their products. The possible improvements are manifold: reduction of the uncertainty in the design and operation of such machines; reduction in production and

operation cost; increase in life and maintenance cycles; and increase in safety due to more accurate predictions. The work described in this thesis forms part of the effort to increase the understanding and to explain powerful phenomena that occur in high-speed turbomachinery such as compressors and aircraft engines.

The specific objectives of the research presented in this thesis are:

- to establish the existence of the travelling-wave-speed instability;
- to derive the necessary conditions for the occurrence of the travelling-wave-speed instability;
- to develop a tool for predicting the dynamic behaviour of an elastic rotor and an elastic stator each individual with linear vibration characteristics when they come into contact with each other; and
- to demonstrate the validity of the model experimentally.

1.3 Literature Survey

A literature survey was carried out to gain insight into the analysis of rotating structures with linear dynamics and the contact between two elastic structures. Historically, the field of rotating machinery splits into two areas: rotor dynamics and dynamics of rotating discs, Figure 1-1.

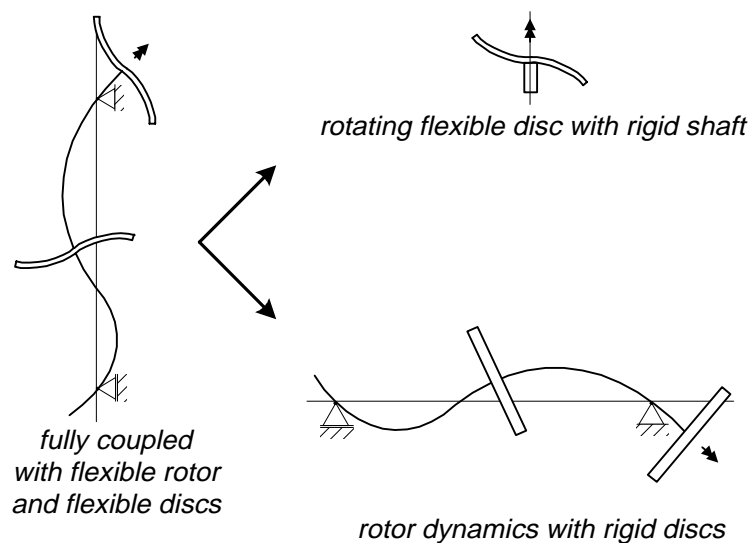


Figure 1-1: Analysis path

1.3.1 Rotor dynamics

Rotor dynamics generally considers an elastic shaft with rigid discs supported in bearings, the earliest work carried out by Föppl (1895), Jeffcott (1919), Laval, and Stodola (1910). Current textbooks include Biezeno and Grammel (1953), Ehrich (1992), Gasch and Pfützner (1975), Krämer (1993), Lee (1993), Rao (1991), and Vance (1988) to name a few. Nelson (1994) gave a general survey over modelling and analysis techniques.

There are variations to the problem, ranging from the simplest model of a massless, symmetric shaft in symmetric, undamped bearings with linear dynamics with a disc at

mid-span to complex models with asymmetric, elastic shafts with internal damping, multiple discs with different moments of inertia and eccentricities at arbitrary positions supported in anisotropic, nonlinear bearings on elastic foundations. Correspondingly, the equations of motion range from those for the simple system with constant, symmetric, mass and stiffness matrices, $[M]$ and $[K]$, respectively:

$$[M]\{\ddot{u}\} + [K]\{u\} = \{f_u\} \quad (1-1)$$

where the coordinates $\{u\}$ are either rectilinear (x,y) or polar (r,θ) , to the complex system:

$$[M]\{\ddot{u}\} + [C + G(\Omega)]\{\dot{u}\} + [K + S(\Omega)]\{u\} = \{f_u\} \quad (1-2)$$

where $[C]$ denotes the damping matrix, $[G]$ the skew-symmetric gyroscopic matrix, and $[S]$ the geometric stiffness matrix, (Ewins and Henry, 1988, Wang and Kirkhope, 1994). The latter two matrices depend explicitly on the speed of rotation, while the elements of all matrices may depend on the cosine and sine of the rotation angle Ωt . $\{f_u\}$ represents the forcing vector acting upon the system. Only recently have researchers begun to consider the effects of disc flexibility on the dynamics of a shaft, Flowers and Ryan (1991), Wang (1992).

Torsional vibrations, caused by, for example, electrical motors, gearboxes, misaligned Hooke's joints, or pulsating forces from generators, are considered separately by all researchers, assuming that the bending and axial vibrations are decoupled from the torsional vibrations, (Stelter, 1995).

1.3.2 Dynamics of rotating bladed discs

Quite apart from the general field of rotor dynamics is the field of rotating elastic discs, possibly with blades, (Crawley, 1988, Loewy and Khader, 1984).

1.3.2.1 Shaft-disc coupling

Assuming only small deflections of the shaft at the location of the elastic disc, the dynamics of discs are coupled to the shaft dynamics by the rigid-body modes of the discs only. The elastic modes of the disc do not transfer forces or moments to the shaft and thus do not influence the dynamics of the shaft. This assumption is valid for most turbo-generators, but must be checked for compliant, light-weight structures used in aircraft- and spacecraft-engineering. If the assumption of small displacements at the position of the discs is dropped, which may be the case for overhung flexible discs, the dynamics of shaft and elastic disc become coupled even for the elastic modes. This fully-coupled analysis is the most intricate problem, approached by a few researchers only: Flowers and Ryan (1991), Khader and Loewy (1984, 1990), and Wang (1992).

1.3.2.2 Bladed discs

Assuming that the shaft and disc motion decouple according to the preceding paragraph, the rotating shaft and the rotating elastic disc can be studied separately. The shaft dynamics with rigid discs is covered by the field of classical rotordynamics as outlined above.

Generally, the elastic discs of a turbo-machine carry blades to exchange impulse with the surrounding fluid. The rotating bladed disc was studied separately by, for example, Ewins (1976), Tomioka, Kobayashi and Yamada (1996). The analysis simplifies considerably, if the bladed disc is not rotating. Ewins (1980) gives an overview over analytical and experimental aspects of these structures. Many researchers have done work in the area, but major work was done by Ewins: Ewins (1973, 1988), Ewins and Imregun (1984), Sanliturk, Imregun and Ewins (1992), and Irretier: Irretier (1979), Irretier and Reuter (1995). For the stationary analysis, the effects of rotation must be estimated separately. The influence of the rotation on the bladed disc dynamics is twofold: the centrifugal force changes the natural frequencies and affects the modeshapes. While the former is a first order effect, the latter is often neglected, (Loewy and Khader, 1984).

1.3.2.3 Symmetry

For rotationally periodic structures such as bladed and unbladed discs, symmetry allows the designer to reduce the three-dimensional problem to two dimensions by using a Fourier-expansion of the modeshapes, (Elchuri, Smith and Gallo, 1984, Garvey and Penny, 1994, Mézière, 1993, Minas and Kodiyalam, 1995, Thomas, 1979 and, implicitly, Biezeno and Grammel, 1953). Most engineering structures have small imperfections due to machining tolerances or material variations. Ewins (1991) presents a comprehensive survey on the subject including current questions and an evolution of the research. Mistuning makes it necessary to describe the modeshape in all three dimensions explicitly, and complicating the analysis further by changing the natural frequencies and making predictions more difficult, (Cornwell and Bendiksen, 1992, Ewins, 1975, Irretier, 1983, Kaza and Kielb, 1985, Stange and MacBain, 1983). Mistuning affects the response level considerably, (Ewins and Han, 1984, Irretier and Schmidt, 1982, Kaneko, Mase, Fujita and Nagashima, 1994, MacBain and Whaley, 1993), which, if not considered or underestimated, can lead to unexpected fatigue failure, (Basu and Griffin, 1985). Ways to spatially ‘mistune’ the forcing to reduce the vibration levels in a rotating disc were investigated by Jones, Barton and O’Brien (1996). Recently, stochastic methods have been applied to study problems associated with mistuning, Yiu (1995).

1.3.2.4 Disc-blade coupling

Substructure coupling is an important technique to analyse complex systems. The dynamics of the whole system are obtained by coupling the dynamics of conveniently defined substructures of the system, (Craig, 1995, Hurty, 1960). For the bladed disc, the

natural substructures are the disc and the blades, (Ewins, 1973, Irretier, 1979, Imregun, 1988, Loewy and Khader, 1984). The bladed disc assembly can include further elements such as shrouds connecting the blades, (Cottney and Ewins, 1974, Ewins, 1988, Ewins and Imregun, 1984).

1.3.2.5 Discs and blades

Rotating discs and rotating blades were studied separately: discs of arbitrary shape by, for example, Biezeno and Grammel (1953), Eversman and Dodson, (1969), Mignolet, Eick and Harish (1996), Renshaw and Mote, (1995), and Yang (1993), and rotating blades by Biezeno and Grammel (1953), Chen and Chern (1993), Irretier and Mahrenholtz, (1981), Filippov, (1971), Leissa, Lee and Wang, (1984), and Bauer, (1980). Most of the analyses were performed for twisted and tapered blades with arbitrary geometry.

1.3.3 Models and analysis techniques

Different models are used to represent bladed disc assemblies: Wagner and Griffin (1992) modelled the bladed disc as a continuous, one-dimensional string, Sanliturk, Imregun and Ewins (1992) derived a lumped-parameter model, but most other researcher used a discretised, finite-element model of the continuous structure. Biezeno and Grammel (1953) and Lamb and Southwell (1921) used low-order polynomials to approximate the modeshapes in the radial direction. They and Jen and Johnson (1995) used a Rayleigh-Ritz approach to obtain approximations of the natural frequencies and modeshapes.

Analytical techniques are detailed in, for example, Gérardin and Rixen (1994), Timoshenko (1955), Szabó (1956), and Meirovitch (1970, 1980), and the details of the numerical realisation of these techniques are described in Argyris and Mlejnek (1991) and Biezeno and Grammel (1953).

For some systems, the assumption of linearity of the dynamic behaviour is valid only over a certain range of parameters, for example the bending vibration of thin discs can be described accurately by a description of the linearised system around the undeflected position. These approximations, known as Kirchhoff theory for plates and Euler-Bernoulli theory for beams, (Szabó, 1956), are sufficiently accurate for small deflections but become increasingly inaccurate for large deflections, (Swamindham, 1990).

1.3.4 Travelling waves as principal coordinates

Complex waves instead of real normal modes have been used as principal coordinates in the analysis of rotationally periodic structures for a long time (Lamb and Southwell, 1921, Macke, 1966, Srinivasan and Lauterbach, 1971, Tobias, 1957, Tobias and Arnold, 1957).

Backward travelling waves are probably the most common vibration patterns in rotors as they are easily excited by pressure fluctuations in the surrounding fluid, (Ewins, 1976, Gorman, 1979, Hardy, 1995, Jones, Barton and O'Brien, 1996, Li-Tang and Qi-Han,

1992, Owczarek, 1983, Weaver and Fleeter, 1994, Williams, 1991). The forced vibrations of bladed discs due to general spatial and temporal force patterns were investigated by, for example, Ewins (1973), Honda, Matsuhisa and Sato (1985), Mehdigohli, Robb and Ewins (1992), and Schmiechen, Ewins and Bucher (1995).

The transformation of quantities, such as displacements and forces, between the rotating and stationary reference frame is presented in detail in Bucher, Ewins, Robb, Schmiechen (1995), Irretier and Reuter (1995) and Okubo, Evensen and van Karsen, (1995). The principles of a travelling-wave ultrasonic motor were presented by Hagedorn and Wallaschek (1992) and the industrial application of the theory was shown in Gérardin and Rixen (1994).

Recently Lee started to use negative frequencies to distinguish backward travelling waves from forward travelling ones, (Lee, 1993, Lee and Kim, 1995, 1996).

1.3.5 Vibration tests of rotating machinery

The complexity of the analysis of rotating bladed discs is quite high, and for academic studies the problem of validation becomes immense, (Kaiser and Hansen, 1994, Swaminadham, 1990). The major difficulty is the measurement of the disc dynamics without changing its characteristics. As mentioned above, a loss of symmetry introduces large changes to the dynamics of any symmetric structure, and the attachment of a sensor may mistune a structure. Measuring with a non-contacting sensor in the body-fixed frame of reference will leave the structure undisturbed but adds cost to the measurements and the signals must be still transmitted to the stationary observer where they can be analysed. Measuring with non-contacting sensors in the stationary reference frame makes it necessary to relate the measured quantities to the quantities experienced by the disc, (Heath and Imregun, 1995, Irretier and Reuter, 1994, Nava, Paone, Rossi and Tomasini, 1994).

1.3.6 Contact models

Different types of contact were considered by the researchers:

- Frictionless rub: The elastically-supported stator hinders the rotor and causes it to travel further away from the geometric centre. The stator acts as a time-varying motion constraint. Without friction, which may be approximately the situation in a journal bearing, the stator exerts a radial force on the rotor only. The dynamics follow from the next type by neglecting the effects of friction.
- Rub with friction: in the presence of friction, for example if a journal bearing does not receive sufficient oil, a tangential force is caused by the friction, generating a braking torque. It also forces the stator into a different trajectory from the frictionless case, (Ehrich 1969). Most researchers assume Coulomb-type friction, relating the tangential force to the normal force by a single, possibly velocity-dependent, coefficient and the sign of the velocity.

- Impact with friction: Pfeiffer and Glocker (1994, 1995) and Schweitzer and Fumigalli (1995, 1996) investigated the high-frequency effects of rubs assuming that the contact time is small compared to the wave propagation velocity. Ostermeyer (1988) and Lesser (1995) gave details on the numerical realisation of modelling impact friction.

Friction is a non-linear phenomenon. It depends nonlinearly on the relative velocity between the contacting structures, (Glocker and Pfeiffer, 1994), and the indentation, (Schweitzer and Fumigalli, 1996).

1.3.7 Dynamic interaction between rotor and stator

The literature search on the interaction between a rotor and a stator revealed that the literature splits into two areas according to the machine component investigated. Goldman and Muszynska (1993), Choy and Padovan (1987), Ehrich (1969) consider unbladed rotors touching rigid stators supported on springs, with a geometry representative of bearings, seals, or other low-clearance sections of the shaft.

Recently, Hatman, Haque and Bagchi (1996) have reported research on the contact of a bladed rotor and a ‘stator’ to study the dynamics of machine tools like polishing brushes. Only Padovan and Choy (1987) studied the interaction between the rotor and stator of a turbo-machine but assumed the stator to be rigid, representative possibly for a compressor section of an aircraft engine.

There was no published literature found on the analysis of a fully-elastic rotor-stator structures representing systems like low-pressure fans of jet engines. Ehrich (1969), the National Transportation and Safety Board (1975) and Smailes (1993) have mentioned this case briefly as the most general one. The difference to the previously-described systems is that the natural frequencies of the nacelle are of the same order as those of the bladed rotor. Hence both stator and bladed rotor have to be modelled as elastic structures and considered simultaneously. This problem will be dealt with in this thesis.

1.4 Scope and Layout of the Thesis

The scope of the thesis is to investigate the instability caused by a travelling-wave-speed coincidence. This interaction between an elastic rotor and an elastic stator depends on the dynamic characteristics of the structures and on the running speed of the machine, it can be initiated by random disturbances as they are present in any operating machine, (Schlack and Kessel, 1969, Schmiechen, 1994). The instability can occur in aircraft engines long after the wear-in period, after many hundreds of hours in operation. For that reason, it is particularly dangerous, as the close monitoring of new engine designs has long ended. So, an engine operating normally for many months and years can suddenly cause catastrophic failure, (Smailes, 1993).

The theoretical development of the instability will be presented in Chapters 2 and 3, followed by a simulation of the problem, Chapters 4 and 5, and the development and

design of the test rig and data-acquisition system and the experiments, Chapters 6 and 7. The epilogue of Conclusions, References and Appendices closes the thesis.

1.4.1 Theoretical development

The theoretical basis for further analysis of the instability includes the dynamic behaviour of axisymmetric discs and plates and the influence of rotation on the vibration of these structures, and the dynamics of rotationally-periodic structures, such as bladed discs. Both analytical and numerical approaches are pursued using general-purpose mathematics packages available. The theoretical predictions and the numerical approximations are validated by measurements.

1.4.1.1 Speed-dependent natural frequencies

For non-rotating systems with perfectly linear time-invariant vibration characteristics, the natural frequencies are constant. Resonance occurs when the excitation has frequency components at one or more of the natural frequencies of the system. For rotating structures, the natural frequencies are functions of the rotation speed due to centrifugal forces, (Biezeno and Grammel, 1956). The transformation of the natural frequencies of a rotating structure into a frame of reference rotating relative to the structure modulates the frequencies further, (Schmiechen and Ewins, 1995).

1.4.1.2 Coupled system dynamics

The project concentrates on structures similar to those found in aircraft engines or high-speed compressors. In these systems the rotating element is disc-shaped with blades attached to it to impart an impulse on the working fluid or vice versa. This rotor is housed in a stator to maximise efficiency. For typical aircraft engines and compressors the stators can be described approximately as conical shells with opening angles between 0° and 90° , from a cylindrical shell to a flat disc.

If the natural frequencies of two structures are separated by a wide margin, the analysis can be simplified by splitting it into two independent analyses. For rotating structures, the natural frequencies depend on the rotation speed and such an approach is generally not valid. The two structures described above, rotating bladed discs and conical shells, have natural frequencies in the same frequency band and meaningful investigations of the rotor and the stator separately are impossible. The inclusion of the stator dynamics in the model makes this thesis broader in range than previously investigated and published cases.

1.4.1.3 Modal representation of vibrations

Vibrations of spatially continuous linear time-invariant systems can be represented by an infinite sum of *generalised coordinates* or *modal responses*. Modes are natural vibration

patterns of the structure. Excited close to one of its natural frequency, the structure will respond predominantly in the vibration pattern of the associated mode.

For many structures, good approximations of the responses can be achieved with a small number of modes retained in a model of their dynamics.

1.4.1.4 Vibration patterns of axisymmetric structures

The modeshapes of rotationally-periodic and axisymmetric structures can be classified by their number of *nodal diameters* and nodal circles. Along these nodal lines the vibration is zero at all times.

The symmetry of the structures gives rise to mode pairs which have identical natural frequencies and similar or congruent modeshapes. Vibration in the mode pairs can also be expressed as two travelling waves, one with a positive velocity (forward) and the other with a negative velocity (backward). For almost-periodic or mistuned periodic structures, the double modes split into two single modes with distinct natural frequencies and unique modeshapes and the travelling waves are not of equal amplitude any more.

For the data analysis, the concept of waves and their spatial interpretation has been developed further. By decomposing the available sensor information of the response in both temporal and spatial senses, one can obtain information about the wave content of arbitrary vibration patterns. In this context, negative spatial frequencies can be interpreted as backward travelling waves. This decomposition is also necessary if a coordinate transformation is to be performed, as waves of different nodal diameters transform differently.

1.4.1.5 Change of reference frame

If the response of a wave pair of the rotor is transformed into a stationary reference frame, their velocities are modulated by the speed of rotation times the number of nodal diameters. Depending on the speed of rotation, the *counter-rotating wave* can change its direction in the stationary reference frame from a *backward-travelling wave* at low rotation speeds, via a *stationary wave* at the *engine-order speed*, to a *forward-travelling wave* at rotation speeds higher than the engine-order speed, (Schmiechen, 1994). The forces that excite the stationary wave at engine-order speed in resonance are time-invariant forces spatially varying in the angular direction are called engine-order excitation. It is a common problem in most turbo-machinery, and is carefully avoided by design or setting of the operating speed.

1.4.1.6 Travelling-wave-speed coincidence

Current design rules seek to avoid the engine-order speed, where time-invariant forces drive rotors in resonance due to the frequency modulation of their natural frequencies.

The contact of a rotor vibrating in a specific wave pattern appears to the stator as a rotating, time-varying engine-order excitation. The force pattern excites the stator

predominantly in a rotating, spatial pattern similar to that in the rotor, (Schmiechen, 1995). For a certain *critical speed*, always higher than the *engine-order speed*, the counter-rotating wave of the rotor travels at the same absolute speed as the forward-travelling wave of the stator. At this speed both structures are driven in resonance by the contact forces. Resonances can cause undesired, large vibration amplitudes and hence these critical speeds should be avoided. The travelling-wave-speed coincidence implies an extension to the standard design rule that tries to avoid the rotor resonance due to static engine-order excitation, which is a special case of the travelling-wave-speed coincidence when the stator is assumed to behave like a rigid body.

By considering the dynamics of the structures in radial, tangential, and axial directions, an energy transfer mechanism between the kinetic energy of the rotor due to the rotation and vibration energy in the coupled rotor-stator system can be identified that can lead to potentially dangerous instabilities. At the critical speeds, where both structures have the same natural frequencies for particular waves, and assuming initial contact, rotational energy of the rotor is fed into the stator structure so that the stator tends to respond with ever increasing vibration amplitudes until failure occurs or non-linearities change the system behaviour and lead to a limit-cycle response.

The finding of these extra critical conditions, beyond the standard engine-order speeds, is generally quite disturbing but it gains special importance from the fact that future engine designs are moving towards symmetric designs for the casings. This will result in stronger travelling wave components in the response with an increased potential for the travelling-wave-speed instability. In this respect, the travelling wave speed coincidence with its mechanism of energy transfer between rotational energy, which is plentiful in rotating structures, and vibratory motion is becoming increasingly important.

1.4.1.7 Cause of initial contact

During normal operation of an aircraft engine, background excitation can be expected from many sources to be always present. Most importantly is the residual unbalance from the rotor. Reducing the unbalance to zero is technically impossible and the residual unbalance will excite the stator through the bearings. Flight manoeuvres introduce forces into the stator due to inertial forces and into the rotor where gyroscopic forces act. Static pressure distributions in the working fluid will force the stator into a static deformation, while the rotor will react with a standing wave. Bird strikes, where one or many objects hit the nacelle or the fan may cause initial contact. The list is certainly not complete but indicates that there will be always initial conditions present capable of starting the travelling-wave-speed instability, if the other conditions are met.

1.4.2 Numerical simulation

The difficulties of obtaining a low-order analytic description of this time-varying problem with nonlinear discontinuous contact forces led to the development of a numerical model to integrate the differential equations of motion.

The model is built from modal data of the structures computed beforehand. The speed-dependent modal data are obtained from modal tests and are used to confirm the results of FE computations.

The interface parameters are estimated as experimental data is not available. The formulation of the contact forces required assumptions on the contact type and the local material properties, (Lesser, 1995, Schweitzer and Fumigalli, 1996). Impact is a high-frequency phenomenon and it will require very small time steps to capture the high-frequency components in the numerical simulations. In order to keep the computational cost as small as possible, the integration scheme used an adaptive time step.

The responses of the structures are approximated by truncated modal summations. The output of the simulation consists of time histories of the principal coordinates which describe the state of the rotor-stator system at any time instance, capturing its dynamics completely. From the principal coordinates, responses at the physical coordinates can be computed.

1.4.3 Experimental validation

Experiments are conducted on the test rig to validate the theoretical predictions. In order to simplify the modelling and the experiments of the system, advantage is taken of the fact that the physics are independent of the frame of reference. The change of reference frame affects the description only. The system is modelled in the rotating frame of reference: the rotor of the turbo-machine, represented by a bladed disc, is stationary in this study, while the casing of the turbo-machine, modelled as a disc, rotates here. Thus, instead of having to analyse a rotating bladed disc and a stationary disc, the tasks balanced more evenly to the analysis of a stationary bladed disc and a rotating plain disc. The change greatly simplified the test rig and measurement system. Measurements of the blade dynamics could be conducted in the stationary reference frame; the measurements of the continuous surface of the rotating disc are much less difficult than measurements on rotating blades, (Heath, 1995). By simplifying the geometry of the blades compared with the geometry of blades in turbo-machinery, the complexity of the vibration of the blade tips is reduced to two-dimensions.

Based on the ideas developed above, a test rig is designed and built, (Schmiechen, 1996). The main purpose of the rig is to demonstrate the travelling-wave-speed instability. This broke down to a short list of major requirements that in turn necessitated the fulfilment of further constraints. The first requirement is to support the stator at its interface. For the disc geometry chosen, this meant that the stator is to be supported at its centre. The second requirement is to support and to drive the rotor. In order to concentrate

on the travelling-wave-speed instability, the support is designed rigidly so to exclude shaft dynamics. The third requirement is to enable controlled contact to take place between the individual structures and to take measurements of all relevant quantities.

The dynamics of rotor and stator dictated the design in many ways, and after initial considerations, a vertical-axis configuration is chosen. This made the influence of gravity symmetric on the discs, simplified access to the rig, and made it more convenient for testing. Further, the decision to put the blades on the stator component, rather than on the rotor had the advantage of reducing the power requirements for the motor as aerodynamic drag is minimised and of making measurements of the blades' motion much easier. The parts at the interface are designed so that they could be changed easily in order to accommodate necessary changes in the design and wear and plastic deformation on the parts in contact. The stator support provided accurate control in the translational degrees of freedom and is massive enough to support the stator during heavy rubs.

The design analysis performed included stress and deflection calculations for stationary and spinning discs and the estimation of the natural frequencies of a spinning disc and a stationary bladed disc.

A data acquisition system is developed to capture data for analysis. The system with its functions: data acquisition, waveform generation, signal conditioning and motor control, is controlled from a PC. The analysis programs are developed in high-level languages for flexibility.

Chapter 2: Dynamics of Structures

In the course of this study the dynamic behaviour of discs, stationary bladed discs and rotating unbladed discs, is investigated. The underlying assumption is that the dynamics of each structure is linear. Emphasis is put on the features particular to the dynamics of rotationally periodic structures. Different approaches are presented that can be used to obtain the desired modal data consisting of the natural frequencies and the modeshapes.

2.1 Definition of Linearity

A major assumption made in this chapter and the whole study is that of linearity of the component structures. Linearity in the mathematical context requires that the following equation holds for all functions:

$$\{f(\alpha\{u\}_1 + \beta\{u\}_2)\} = \alpha\{f(\{u\}_1)\} + \beta\{f(\{u\}_2)\} \quad (2-1)$$

which states that the value of a function, $\{f\}$, which can be a scalar-, vector- or matrix-valued function, applied to a sum of (scalar-, vector- or matrix-) arguments $\{u\}_1, \{u\}_2$, scaled by arbitrary scalar factors α, β , equals the sum of the scaled function values applied to the individual arguments.

2.2 Modal Superposition

Based on the linear assumption, Equation (2-1), the dynamic response of a structure can be expressed as sum of modal components or generalised coordinates, (Ewins, 1984):

$$\{u(t, \{x\})\} = \sum_{r=1}^{N_{modes}} \{u(t, \{x\})\}_r \quad (2-2)$$

In the case of continuous structures, the sum has an infinite number of terms, for discrete, lumped-parameter structures the number is finite. Continuous structures can be approximated as discrete structures and are called, in this description, discretised structures. The response and the generalised coordinates are functions of position, $\{x\}$, and time, t . The next step is to express the generalised coordinates, $\{u\}_r$, as products of position-dependent modeshapes, $\{\psi(x)\}_r$, and time-varying principal coordinates $p_r(t)$:

$$\{u(t, \{x\})\}_r = \{\psi(\{x\})\}_r p_r(t) \quad (2-3)$$

This Bernoulli-separation has the advantage that the properties of the structure, the modeshapes, $\{\psi\}_r$ need to be computed for the structure only once.

Continuous structures have an infinite number of modes, $N_{modes} = \infty$, but for the subsequent analysis, a truncated modal summation is assumed to be sufficiently accurate to compute the response, (Gasch and Knothe, 1989) and, in addition, the most efficient way to express the dynamic behaviour of linear structures in a finite frequency range:

$$\{u(t, \{x\})\} = \sum_{r=1}^{\infty} \{\psi(\{x\})\}_r p_r(t) \approx \sum_{r=1}^{N_{modes}} \{\psi(\{x\})\}_r p_r(t), \quad N_{modes} \neq \infty \quad (2-4)$$

For continuous structures, the modeshapes, $\{\psi(x)\}_r$, are continuous functions over the whole structure; for discrete structures and discretised structures, the modeshapes describe the vibration at discrete points only, $\{\psi(\{x\})\}_r$.

2.3 Eigenanalysis

The aim of structural dynamics analysis is to gain insight into the dynamic behaviour of structures: their free vibration behaviour and their responses to time-varying forces. For ease of analysis, Equation (2-3), the modeshapes, $\{\psi(\{x\})\}_r$, need to be determined.

The procedure to obtain the modal properties or eigenproperties is called modal analysis or eigenanalysis. Because of the intricacies of the analysis of continuous structures, these are generally approximated by discretised or lumped-parameter models. For this reason, the eigenanalysis will be presented for discretised and discrete structures, the continuous case is presented in the Appendix for completeness.

2.3.1 Equations of motion

At some stage, most dynamic analyses, independent of their final output (say, displacements or stresses), arrive at a force balance in the form of the equations of motion. For continuous systems, the force balances are partial differential equations in time and the spatial coordinates; for discretised, linear, time-invariant, undamped systems they are sets of ordinary differential equations with constant coefficients which can be presented compactly in vector notation, dropping the arguments, (Meirovitch, 1986):

$$[M]\{\ddot{u}\} + [K]\{u\} = \{f_u\} \quad (2-5)$$

where $[M]$ is the mass matrix or, in more general terms, the inertia matrix, $[K]$ is the stiffness matrix, and $\{u\}$ is the vector of the *degrees of freedom* (translations and rotations) that describe the configuration of the system:

$$\begin{aligned} \{u(t)\} &= \{x(t)\} - \{x_0\} \\ \{\dot{u}(t)\} &= \{\dot{x}(t)\} \end{aligned} \quad (2-6)$$

with $\{x(t)\}$ denoting the instantaneous position, $\{x_0\}$ the static translational and rotational position, and dots denoting derivatives with respect to time. The right-hand side, $\{f_u\}$, is the vector of external dynamic forces acting upon the system. As the matrices $[M]$ and $[K]$ and the force vector, $\{f_u\}$, change with the coordinate basis, $\{u\}$, the resulting equations of motion are referred to as EOM(u). Nonlinear systems can often be approximated sufficiently accurately by Equation (2-5) for small displacements around an operating point for which the mass and stiffness matrices are computed.

If no kinematic constraints exist, one equation can be derived per degree of freedom. As the consecutive analyses depend on the form of the equations, it is desirable to obtain the equations in their simplest and most compact form.

2.3.2 Modal description of the system characteristics

For structures with linear dynamic behaviour, the coordinate basis in which the problem is expressed influences the shape of the solution. In particular, there exists one set of coordinates, the *principal coordinates*, for which the equations of motion become uncoupled from each other, i.e., the describing matrices of the discretised problem are diagonal, (Ewins, 1984, Gasch and Knothe, 1989). Using this particular set of coordinates has the advantages of efficiency and clarity when further analysing the solution.

In most cases, the principal coordinates cannot be found directly, but are obtained via the modal matrix: the modal matrix which contains the eigenvectors and is the solution of the eigenproblem, which can be stated mathematically as:

Eigenproblem:

Given the homogeneous EOM(u):

$$[M]\{\ddot{u}\} + [K]\{u\} = \{0\}$$

Find the modal matrix, $[\Psi]$, such that

$$[\Psi]^T[M][\Psi] = [m_r]$$

$$[\Psi]^T[K][\Psi] = [k_r]$$

(2-7)

where $[m_r]$ and $[k_r]$ are the diagonal matrices of the modal masses and modal stiffnesses, respectively. Examples illustrating the eigensolution of continuous, discrete and discretised systems are given in the Appendix. The orthogonality relation between the eigenvectors can be written as a scalar equation:

$$\{\psi\}_r^T[M]\{\psi\}_s = \begin{cases} 0 & r \neq s \\ m_r & r = s \end{cases} \quad (2-8)$$

The eigenvalue matrix, $[\lambda_r]$, can be computed from:

$$[\lambda_r] = [\omega_r^2] = [m_r]^{-1}[k_r] \quad (2-9)$$

Each eigenvector and its associated eigenvalue describe a ‘natural’ vibration pattern or *mode* of the structure. Each such mode can be excited independently from the others, which follows from the orthogonality of the modes, Equation (2-8). This feature is used commonly in modal analysis to extract the system parameters sequentially, (Ewins, 1984).

The eigenproblem in Equation (2-7) is stated for discretised continuous structures or lumped parameter models with a finite number of coordinates and hence the degrees of freedom. The modal information is only available at these coordinates and the eigensolution consists of an equal number eigenvalues and eigenvectors, presented in the

diagonal eigenvalue matrix, $[\lambda_r]$, and the fully populated eigenvector or modal matrix, $[\Psi]$. The vibration characteristics at other coordinates are estimated by interpolation from neighbouring points.

Only the mode-‘shapes’ are defined, their magnitudes can be scaled arbitrarily. If $[\Psi]$ is a modal matrix, so also is

$$[\Psi'] = [\Psi][\alpha_r] \quad (2-10)$$

as

$$\begin{aligned} ([\Psi][\alpha_r])^T [M] ([\Psi][\alpha_r]) &= [m_r][\alpha_r]^2 = [m'_r] \\ ([\Psi][\alpha_r])^T [K] ([\Psi][\alpha_r]) &= [k_r][\alpha_r]^2 = [k'_r] \end{aligned} \quad (2-11)$$

which satisfies Equation (2-7) as it does not destroy the diagonality of the matrices $[m_r]$ and $[k_r]$, and

$$[\lambda'_r] = [m'_r]^{-1}[k'_r] = [m_r]^{-1}[k_r] = [\lambda_r] \quad (2-12)$$

showing the invariance of the eigenvalues with respect to scaling of the eigenvectors.

Following the ideas leading to Equation (2-3), a new set of coordinate $\{p\}$ can be introduced:

$$\{u\} = [\Psi]\{p\} \quad (2-13)$$

Substitution of the new coordinates into Equation (2-5) and premultiplying by $[\Psi]^T$ changes EOM(u) to EOM(p)

$$\begin{aligned} [\Psi]^T [M] [\Psi] \{\ddot{p}\} + [\Psi]^T [K] [\Psi] \{p\} &= [\Psi]^T \{f_u\} \\ [m_r] \{\ddot{p}\} + [k_r] \{p\} &= \{f_p\} \end{aligned} \quad (2-14)$$

This similarity transformation does not change the eigenvalues of the problem, (Maciejowski, 1989). EOM(p) are decoupled and, by definition, $\{p\}$ represents the principal coordinates. The set of principal coordinates are not unique for the modal matrix not being unique:

$$\{u\} = [\Psi][\alpha_r][\alpha_r]^{-1}\{p\} = [\Psi']\{p'\} \quad (2-15)$$

The key feature of the principal coordinates is, that they allow the multi-degree-of-freedom system to be described as many single-degree-of-freedom systems, which is mathematically much easier.

2.3.3 Mass normalisation of the modeshapes

One particular set of scaling factors leading to the mass-normalised modal matrix, $[\Phi]$, in Equation (2-15) is the Cholesky decomposition $[Q]$ of the modal mass matrix $[m_r]$:

$$[m_r] = [Q]^T [Q] \quad (2-16)$$

and

$$[\Phi] = [\Psi][Q]^{-1} \quad , \quad [\alpha_r] = [Q] \quad (2-17)$$

In the present case of a diagonal mass matrix, the elements of the Cholesky decomposition are simply $q_r = m_r^{1/2}$. $[\Phi]$ is called the mass-normalised modal matrix as it scales the modal masses to unity. The following orthogonality relations hold (from Equations (2-7) and (2-17)):

$$\begin{aligned} [\Phi]^T[M][\Phi] &= [I] \\ [\Phi]^T[K][\Phi] &= [\lambda_r] \end{aligned} \quad (2-18)$$

where $[I]$ is the identity matrix. This mass normalisation simplifies the equations of motion to:

$$\{\ddot{p}'\} + [\lambda_r]\{p'\} = [\Phi]^T\{f_u\} = \{f_{p'}\} \quad \text{or} \quad \{\ddot{p}'\} + [\omega_r^2]\{p'\} = \{f_{p'}\} \quad (2-19)$$

and:

$$\{p\} = [Q]\{p'\} \quad (2-20)$$

which can be transformed into the generalised coordinates by Equation (2-13).

2.3.4 Effect of damping

Velocity-proportional damping is reflected in the equations of motion of a linear time-invariant discretised system by the viscous damping matrix $[C]$:

$$[M]\{\ddot{u}\} + [C]\{\dot{u}\} + [K]\{u\} = \{f_u\} \quad (2-21)$$

Modal decoupling as described in the previous sections can still be applied and can still diagonalise the mass and stiffness matrices, but will do so only under certain assumptions on the structure of the damping matrix. If the damping matrix can be represented as a linear combination of the mass and stiffness matrices then it will, by application of Equation (2-7) and the overall assumption of linearity, also be diagonalised by the change to the undamped system's principal coordinates:

$$\begin{aligned} [C] &= \alpha[M] + \beta[K] \\ [c_r] &= [\Phi]^T[C][\Phi] = \alpha[I] + \beta[\lambda_r] \end{aligned} \quad (2-22)$$

where α and β are arbitrary, positive, scalar values. More generally, the damping matrix can be of the form:

$$\begin{aligned} [C] &= \alpha[M] + \beta[K] + [\Phi]^{-T}[\gamma_r][\Phi]^{-1} \\ [c_r] &= [\Phi]^T[C][\Phi] = \alpha[I] + \beta[\lambda_r] + [\gamma_r] \end{aligned} \quad (2-23)$$

where $[\gamma_r]$ is a diagonal matrix of arbitrary scalars, and still bring about the same result. The assumption of *proportional damping* has been used successfully in many engineering applications and hence can be used as good working assumption. Under certain circum-

stances though, especially in structures where the damping is very localised, the validity of this assumption breaks down, (Ewins, 1984), as it causes non-proportional damping.

For the general case of $\beta > 0$, the damping increases with the eigenvalue. So modes with high natural frequencies are more highly damped than modes with low natural frequencies. This can be modified by the choice of $[\gamma_r]$.

Another advantage of proportional damping is that it does not affect the modeshapes, (Ewins, 1984). The modeshapes can still be computed from the eigenproblem of the undamped model, Equation (2-7), which reduces the size of the eigenproblem by a factor of two compared with the general formulation of the eigenproblem for a damped system, Equation (2-24):

Eigenproblem (damped):

Given the homogeneous EOM(u):

$$[M]\{\ddot{u}\} + [C]\{\dot{u}\} + [K]\{u\} = \{0\}$$

or expanded to state – space form:

$$\begin{bmatrix} M & 0 \\ 0 & M \end{bmatrix} \begin{Bmatrix} \dot{u} \\ \ddot{u} \end{Bmatrix} + \begin{bmatrix} 0 & -M \\ K & C \end{bmatrix} \begin{Bmatrix} u \\ \dot{u} \end{Bmatrix} = \begin{Bmatrix} 0 \\ 0 \end{Bmatrix} \quad (2-24)$$

$$[A]\{\dot{y}\} + [B]\{y\} = \{0\}$$

Find the modal matrix, $[\Psi]$, such that

$$[\Psi]^T[A][\Psi] = [a_r]$$

$$[\Psi]^T[B][\Psi] = [b_r]$$

The present analysis is limited to proportional damping for the above mentioned advantage of decoupling the damped equations of motion. The equations of motion for the proportionally-damped systems in the principal coordinates are:

$$\{\ddot{p}\} + 2[\zeta_r][\omega_r]\{\dot{p}\} + [\omega_r^2]\{p\} = \{0\} \quad (2-25)$$

where $[\zeta_r]$ is the damping ratio:

$$[\zeta_r] = \frac{1}{2}[m_r]^{-1}[c_r][\omega_r]^{-1} \quad (2-26)$$

As a result of the assumption of proportional damping, Equation (2-23), the equations of motion of the damped system, Equation (2-25), are decoupled by the undamped system's principal coordinates.

2.3.5 Forced response behaviour

Up to now, only the free vibration of structures has been studied. For the subsequent analysis, the response of structures with linear dynamics to external forces will be investigated.

2.3.5.1 Equation of motion

The forced response of a real (or complex) mode is computed from the non-homogeneous force balance, Equation (2-25) extended to the external forces:

$$\{\ddot{p}\} + 2[\zeta_r][\omega_r]\{\dot{p}\} + [\omega_r^2]\{p\} = \{f_p\} \quad (2-27)$$

where $\omega_r^2 = \lambda_r$ and $\{f_p\}$ is the modal projection of the external forces, for the discrete and discretised continuous structure given by

$$\{f_p\} = [\Phi]^T \{f_u\} \quad (2-28)$$

where $[\Phi]$ is the mass-normalised modal matrix and $\{f_u\}$ is the force in the physical coordinates u .

2.3.5.2 Spectral distribution: frequency response

Studying the response to a harmonic force of frequency ω , the assumption of a harmonic response at the same frequency leads to the forced response equation:

$$\{\hat{p}\} = [-\omega^2[\mathbf{I}] + i2[\zeta_r][\omega_r]\omega + [\omega_r^2]]^{-1}\{\hat{f}_p\} = [H_p(\omega)]\{\hat{f}_p\} \quad (2-29)$$

where the hat denotes the generally complex amplitude and $[\mathbf{I}]$ is the r -by- r unit matrix. $[H_p(\omega)]$ is the frequency-response-function (FRF) matrix for the coordinates p . Only for the principal coordinates it is a diagonal matrix: for the physical coordinates, $\{u\}=[\Phi]\{p\}$ and the forces related by Equation (2-28), the FRF matrix is given by

$$[H_u(\omega)] = [\Phi][H_p(\omega)][\Phi]^T \quad (2-30)$$

which is not diagonal any more, (Ewins, 1984). For a single mode r , the vector-equation, Equation (2-29), reduces to the familiar scalar equation, for example Timoshenko, (1986):

$$\hat{p}_r(\omega) = \frac{1}{-\omega^2 + i2\zeta_r\omega_r\omega + \omega_r^2} \hat{f}_{p,r}(\omega) = H_{pr}(\omega)\hat{f}_{p,r}(\omega) \quad (2-31)$$

where the argument shall indicate that the response amplitude is a function of the excitation frequency. For a single mode and a small value of damping, $\zeta_r < 1$, the scalar frequency response function has the following shape:

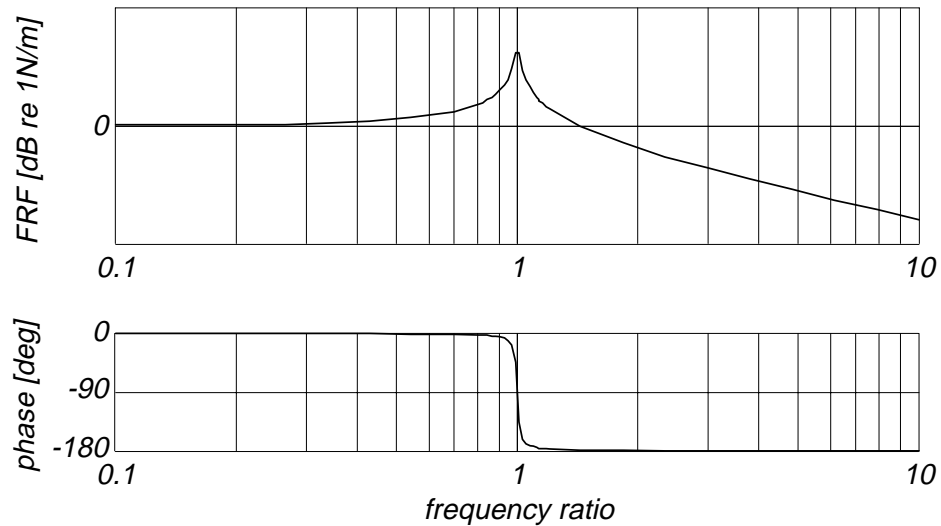


Figure 2-1: Normalised frequency response function of a mode

The frequency ratio of the abscissa in Figure 2-1 is the ratio of excitation frequency ω to natural frequency ω_p : at low values, the magnification factor is almost constant 0 dB = 1 and rises to a peak at the natural frequency ω_p . At this resonance peak, the phase between excitation and response equals 90°. The higher the value of damping, the lower the peak and the wider the frequency smear-out of the peak and the phase change-over. For a frequency ratio larger than 1, the magnification asymptotically decays with $1/\omega^2$ or -20dB/decade.

From Equation (2-31) and Figure 2-1 one can conclude that the magnification factor drops rapidly away from resonance.

2.3.5.3 Spatial distribution

The presence of a physical force does not necessarily mean that it will excite a mode. A second requirement is a similar spatial distribution of the force and the modeshape. The spatial information will determine to what extent a force will excite a particular mode, which follows from Equation (2-28). Assume the following modal matrix, as it may be the result of an analysis of a pinned-pinned beam, and two representative forcing functions: a spatially constant and a spatially-varying force pattern:

$$[\Phi] = \begin{bmatrix} 0 & 0 & 0 \\ 0.71 & 1 & 0.71 \\ 1 & 0 & -1 \\ 0.71 & -1 & 0.71 \\ 0 & 0 & 0 \end{bmatrix}, \quad \{f_x\}_1 = \begin{Bmatrix} 1 \\ 1 \\ 1 \\ 1 \\ 1 \end{Bmatrix} \cos \omega t, \quad \{f_x\}_2 = \begin{Bmatrix} 0 \\ 1 \\ 0 \\ -1 \\ 0 \end{Bmatrix} \cos \omega t \quad (2-32)$$

The products $\{f_p\}_i = [\Phi]^T \{f_x\}_i$, Equation (2-28) can be computed to:

$$\{f_p\}_1 = \begin{bmatrix} 2.42 \\ 0 \\ 0.42 \end{bmatrix} \cos \omega t, \quad \{f_p\}_2 = \begin{bmatrix} 0 \\ 2 \\ 0 \end{bmatrix} \cos \omega t \quad (2-33)$$

Every zero entry in the force vector $\{f_p\}$ implies that the corresponding mode is not affected by the particular force. The smaller the values, the less efficient is the energy transfer into the structure. The force must be spatially similar to a mode to excite it, even at resonance. The second force pattern is proportional to the second mode and, by virtue of orthogonality of the modes, the force does excite this mode only.

2.4 Finite Element Approach

As mentioned before, the analysis of the dynamics of continuous structures leads to partial differential equations. Much insight can be gained from a closed form, analytical eigensolution, but for structures other than the very simplest, solving for the eigen-properties analytically soon becomes an intractable task. In the light of the need to analyse a more complex structure, such as a bladed disc, the method of finite elements (FE) is pursued. This more numerical approach provides a solution for an approximated, discretised structure, and the difficulty changes from obtaining a solution at all to assessing the quality of the solution obtained.

2.4.1 Introduction

The advantage of the FE-based analysis is that the solution method is well established for structures of arbitrary geometry and thus no advanced analytical analysis is necessary: after specification of the geometry and the material properties, the algorithm will produce an eigensolution consisting of the complete modal properties: natural frequencies, modeshapes and modal masses.

The FE analysis consists of the following steps: discretisation of the structure by approximating it using the available building blocks (element types); assembly of the element mass and stiffness matrices into the global system matrices; introduction of the connections between the elements and the boundary conditions; and solution of the global eigenproblem.

The data have to be viewed critically as their basis is the discretised structure, not the continuous structure. The discretisation of the structure and the necessary approximation of the boundary conditions will have a generally detrimental effect on the accuracy of the solution.

The following paragraphs are not intended to explain the method (Bathe, 1983, Gasch and Knothe, 1989, Zienkiewicz, 1982) but only to give a short introduction and then to identify in detail difficulties encountered in the analysis. An example of the application of the method of finite elements to a simple beam structure is given in the Appendix.

2.4.2 Underlying idea

The idea behind the finite element method is to use small building blocks, the finite elements, to describe structures of any shape. The dynamics of the elements, expressed in the element mass and stiffness matrices, are computed prior to the analysis of the structure.

The element matrices are derived for certain element types: beam, plate, shell, 3D-brick, and certain element shapes: triangular plate, quadrilateral shell, etc. The geometric dimensions and the material properties are left variable in the element matrices. This way, versatile building blocks are available that can be combined almost arbitrarily, as long as certain conditions are fulfilled, (Bathe, 1983, Zienkiewicz, 1982).

2.4.3 Spatial discretisation of the structure

The finite elements are defined geometrically by points and their connections. The set of points is commonly referred to as a mesh. This mesh must be chosen with as much physical insight as available at any time. Refinements of the mesh are common after weaknesses of an initial mesh are identified.

2.4.3.1 Guidelines

As a general rule, meshes with compact elements and smooth transitions between elements are desired as they promise to produce more accurate results compared to rough, erratic meshes of similar detail. A second rule is that in order to capture accurately rapid changes of the displacement, the element sizes in these regions must be small; in areas with little or no change, the element sizes can be larger without losing accuracy of the overall solution.

A more analytical guideline to selecting the right mesh detail is the characteristic lengths of the desired modes. The characteristic lengths or wavelengths are related to Shannon's sampling theorem, originally devised for temporal data sampling but valid for all types of sampled data. The theorem states the dependency between the frequency content of a signal and the minimum sampling frequency:

Shannon's Sampling Theorem:

In order to extract the frequency components of a sampled, time- (or space-) discrete signal correctly, the sampling frequency must be at least twice the frequency of the highest component in the unsampled signal.

In the spatial domain, the theorem implies that two nodes must be spaced less than half the characteristic length of a mode apart. For example, for modes along the perimeter of a disc which are described by harmonic functions, the number of nodes must be at least twice the number of nodal diameters or half a period of the cosine function. A factor of two is strictly sufficient, but will still not lead to accurate modeshapes in the eigen-

solution. A factor of 3 to 5 is often advisable. For the modes in the radial direction of a disc the characteristic length is not so easily defined, but the distance between nodal circles can be used as an indicator.

Another guideline is concerned with the shape of the resulting elements: distortion of the elements, manifesting itself by very different dimensions in different directions or very acute angles, should be kept as small as possible: a quadrangular element must not collapse to a triangle; if a triangular shape is required, triangular elements should be used instead.

2.4.3.2 Example: Stator mesh

As an example of a mesh, that developed for the stator is presented. The highest number of nodal diameters for a bladed disc with 20 blades is $20/2=10$, and the characteristic length guideline leads to a mesh of 40 nodes in the tangential direction. In order to capture up to one nodal circle and not to distort the elements too much, 8 nodes in the radial direction are chosen. To describe the blade dynamics accurately up to and including the third flapping mode, 9 nodes in the axial direction are chosen by the characteristic length guideline. Two elements in the direction of the width of the blades, the global radial direction, lead to a reasonable distortion of the blade elements.

The resulting mesh has 600 elements giving approximately 4500 degrees of freedom. Figure 2-2 shows the discretised stator structure in the deformed state of a computed low-frequency mode.

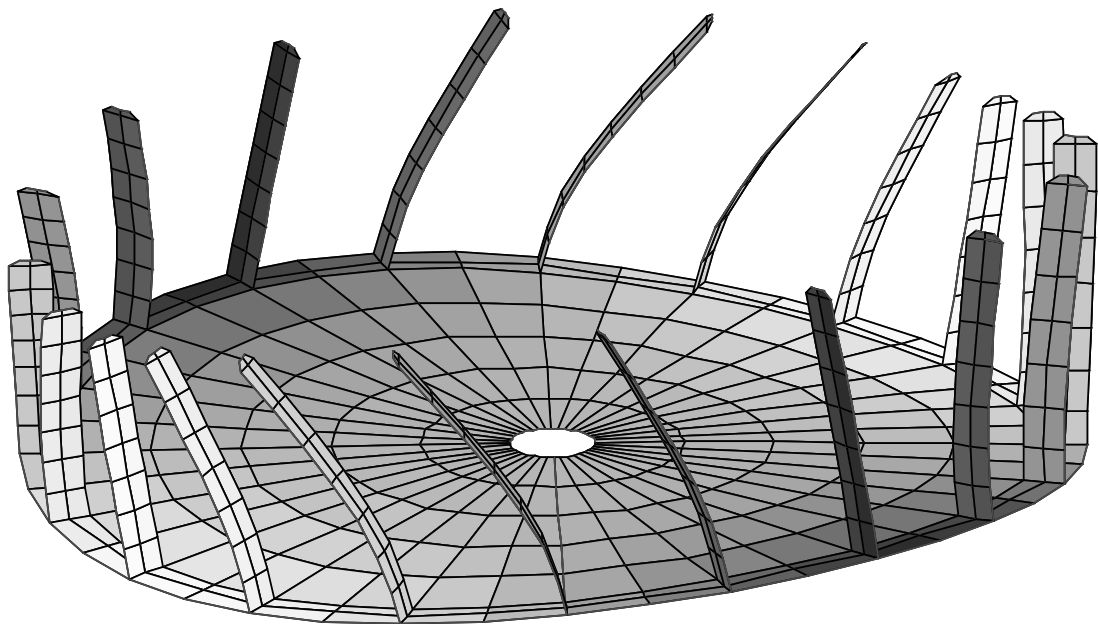


Figure 2-2: Mesh and 2ND mode

Shades of grey indicate the axial deflection of the disc in Figure 2-2 ranging from white to dark grey for the smallest to largest deflections. Thus a single blade is painted in uniform colour because the axial deflection of the disc is almost constant over the blade attachment area. Finding a scheme which can simultaneously colour the disc and blade deflection is difficult and so a compromise is chosen to use colour to emphasise the disc pattern and rely on the spatial deflection to identify the blade shapes.

2.4.4 General features of the FE solution

It is a general feature of the finite element analysis that the modes with higher spatial and temporal frequencies are poorly predicted, both in frequency and modeshape. Refining the mesh shifts the problem to higher frequencies but inevitably increases the problem size. This is demonstrated in the Appendix. Therefore, the option for solving only for modes with low natural frequencies for a mesh of any detail is an economic imperative.

Another general observation is that the eigenvalues are always over-estimated. This is due to the fact that the computed modeshapes are only approximations to the true modeshapes and thus the Rayleigh-Ritz quotient over-estimates the eigenvalue, (Bathe, 1983).

2.4.5 Solution methods

The equations of motion of the discretised bladed-disc structure of the stator are solved for the modal properties, eigenvalues and eigenvectors or modeshapes. The eigenproblem is computationally very demanding and scales with the cube of the problem size or number of degrees of freedom. The following paragraphs detail other approaches and methods to obtain a solution. These steps were initially investigated to understand how they function but are only partially used to obtain the eigensolution as it was anticipated that the full solution would not introduce any further approximation or modelling constraint and thus could be relied on in subsequent analysis. In particular, the coupling approach is discarded after initial trials.

2.4.5.1 Real modeshapes

Real eigenvectors are expected for structures with homogeneous equations of motion of the form of Equation (2-5):

$$[M]\{\ddot{u}\} + [K]\{u\} = \{0\} \quad (2-34)$$

and the eigensolver should return real modal matrices. Due to numerical inaccuracies some solvers return ‘complex’ modal matrices, with whole eigenvectors rotated by an arbitrary angle, β_r . The modal matrix can be forced to be a matrix with real entries only by multiplying each modeshape by $e^{-i\beta_r}$, Equation (2-10):

$$[\Psi_{real}] = [\Psi_{complex}][e^{-i\beta_r}] = [\Psi_{complex}][\alpha_r] \quad (2-35)$$

Specialised solvers will do this automatically.

2.4.5.2 Preservation of symmetry

Some eigensolvers expect the mass matrix to be the unit matrix. Multiplication of the eigenproblem with the inverse of the mass matrix should be avoided in this case as it results generally in a non-symmetric system matrix whose eigensolution can be expected to be less accurate than the solution of a symmetric matrix. An approach that retains the symmetry of the stiffness matrix, uses the Cholesky-decomposition of the mass matrix, Equation (2-16), (Bathe, 1983). Changing the coordinates to:

$$\{u\} = [Q]^{-1}\{y\} \quad (2-36)$$

where $[Q]$ is the Cholesky-decomposition of the mass matrix:

$$[M] = [Q]^T[Q] \quad (2-37)$$

results in the equations of motion in the new coordinates

$$\begin{aligned} [Q]^{-T}[M][Q]^{-1}\{\ddot{y}\} + [Q]^{-T}[K][Q]^{-1}\{y\} &= \{0\} \\ \{\ddot{y}\} + [K_y]\{y\} &= \{0\} \end{aligned} \quad (2-38)$$

where the system matrix $[K_y] = [Q]^{-T}[K][Q]^{-1}$ is symmetric. After this transformation, a standard eigensolver can be applied to solve the problem:

$$(\lambda[I] + [K_y])\{\psi_r\} = \{0\} \quad (2-39)$$

2.4.5.3 Treatment of rigid-body modes in the FE solution

Rigid-body modes are inelastic modes with natural frequencies of 0 Hz. They are caused by an underdetermined configuration with too few constraints. The lack of constraints makes the system matrix rank-deficient. This can cause problems for the numerical algorithm and can affect the accuracy of all modes: rigid-body and elastic. The proper treatment of rigid-body modes will help to improve the quality of the elastic modes as it conditions the problem. The approach is to reduce the system matrices to the elastic system by means of the range space of the stiffness matrix prior to the eigensolution. Starting from the homogeneous equations of motion in $\{u\}$, EOM(u), Equation (2-34):

$$[M]\{\ddot{u}\} + [K]\{u\} = \{0\}$$

the range space of the stiffness matrix has to be found. The range space $[Q]$ is the orthogonal basis of the space spanned by the columns of $[K]$. The number of columns of the range space is equal to the rank of $[K]$. Any range space can be normalised so that the following relation holds:

$$[Q]^T[Q] = [I] \quad (2-40)$$

A new set of coordinates is introduced:

$$\{u\} = [Q]\{y\} \quad (2-41)$$

thereby transforming EOM(u) into EOM(y)

$$\begin{aligned} [Q]^T[M][Q]\{\ddot{y}\} + [Q]^T[K][Q]\{y\} &= \{0\} \\ [M_y]\{\ddot{y}\} + [K_y]\{y\} &= \{0\} \end{aligned} \quad (2-42)$$

The eigenproblem is solved for the elastic modes, non-zero natural frequencies and modeshapes $[\Phi_{el}]$ of the structure. The transformations of the previous paragraphs can be applied subsequently. The modeshapes obtained are back-transformed into the u -coordinates by Equation (2-41).

The rigid-body modes can be found by realising that they span the null-space of the stiffness matrix:

$$[\Phi_{rb}] = nullspace([K]) \quad (2-43)$$

where the null space is the complement of the range space in the N -dimensional space spanned by the coordinates and the following relation holds for any matrix:

$$rank(rangespace([K])) + rank(nullspace([K])) = N \quad (2-44)$$

where N is the size of the matrix.

Thus the complete set of modeshapes is obtained:

$$[\Phi] = [\Phi_{rb} \ \Phi_{el}] \quad (2-45)$$

If the stiffness matrix, $[K]$, is not known exactly, say, due to numerical inaccuracies, a singular value approach should be used to obtain the range space. It should also be mentioned that finding the range space of a matrix is a very expensive operation on computer memory, (Golub and van Loan, 1983, IMSL, 1980).

2.4.5.4 Subspace iteration

As mentioned above, the inaccuracies of the higher modes of an FE solution and the cost of obtaining a modeshape make it imperative to be able to solve for the modes with lower spatial and temporal eigenvalues only. Iterative methods satisfy this requirement and solve the eigenproblem for the lower modes accurately, (Zienkiewicz, 1982). A subspace solver will only solve for a user-specified number of lower modes. This feature is the single most important one in saving computation time. A full solution of a problem of even a few thousand degrees of freedom would require great computational resources, and still, the higher modes would be estimated inaccurately due to the discretisation of the structure.

2.4.5.5 Fourier expansion

If rotationally-periodic or axisymmetric structures are analysed, the problem can be reduced by one dimension by taking advantage of the fact that the modeshapes must be

periodic or even harmonic functions in the tangential direction, (Thomas, 1979, Wildheim, 1979, 1981). For rotationally periodic structures only one sector need to be computed; for axisymmetric structures, one cross-section, (Mézière, 1993).

Harmonic boundary conditions are introduced such that the displacement and slope remain continuous in the tangential direction. A major disadvantage for the present analysis is that deviations from the symmetry (or mistuning) cannot be modelled using this technique. Commercial FE programs generally offer axisymmetric analysis. In order to compute a symmetric structure with asymmetric forcing by this method, the forcing must be Fourier-decomposed, which may require many terms for an accurate representation, (Bathe, 1983).

2.4.5.6 Sub-structure coupling

The coupling approach comes quite naturally for a bladed disc as it splits clearly into sub-structures disc and blades, Gasch and Knothe (1989). The separate sub-structures can be modelled easily, either analytically or by finite elements. For a large number of blades the coupling approach carries a big computational advantage.

If only the low-frequency dynamics of the bladed disc are of interest, both structures can be approximated by a few low-frequency modes. For the blades, these are the first few flap modes, bending modes around the axis with the smallest moment of inertia, and for the disc the low-frequency modes are those with a small number of nodal diameters and few, maybe zero or one, nodal circles.

Hurty (1960) proposed and Gasch and Knothe (1989) presented the standard component mode synthesis algorithm. It is modified in the following paragraphs to make it more amenable for use with the structure at hand and to avoid some of the algorithmic difficulties encountered in the approach as presented by the above authors. The steps of the proposed algorithm are:

- a) to obtain the modal properties of the separate structures by solving the individual eigenvalue problems: $[M_i]\{\ddot{u}_i\} + [K_i]\{u_i\} = \{0\} \Rightarrow [\Phi_i], [\lambda_i]$,
(the blade matrices can differ from blade to blade to model mistuning),
- b) to retain a small number of low-frequency modes only: $[\Phi_i] \Rightarrow [\Phi'_i]$,
(ideally, the eigensolver obtains the modes in $[\Phi'_i]$ only),
- c) to reduce the model to the degrees of freedom necessary: $[\Phi'_i] \Rightarrow [\Phi_{i,red}]$,
- d) to couple the reduced systems, and
- e) to compute the eigenproblem of the assembly.

Compared with the order of the direct solution the orders of the eigenproblems to be solved in a) and e) are much smaller. Considering that the cost of the eigensolution rises with N^3 (Press, Flannery, Teukolsky and Vetterling, 1989), the algorithm still is more efficient computationally, even though $(N_{blades}+2)$ eigenproblems must be solved, where N_{blades} is the number of blades.

The proposed algorithm couples the sub-structures in the spatial domain, as the constraints are usually more easily expressed in the physical coordinates. The mode-truncated modal data are transformed back into the spatial domain and reduced to a mesh of relevant nodes – nodes where the structures are coupled, or nodes where forces are introduced or responses are to be computed.

For each sub-structure a different number of modes can be retained, in general, but for a bladed disc, the same number of modes must be retained for each blade, otherwise the model cannot be expected to be consistent in the frequency band. The reduced sub-structure matrices are placed in the matrix of the assembled structure:

$$\begin{aligned}
 & \begin{bmatrix} [M'_{disc}] & & & \\ & [M'_{blade}]_1 & & \\ & & \ddots & \\ & & & [M'_{blade}]_{N_{blades}} \end{bmatrix} \frac{d^2}{dt^2} \begin{pmatrix} \{u_{disc}\} \\ \{u_{blade}\}_1 \\ \vdots \\ \{u_{blade}\}_{N_{blades}} \end{pmatrix} \\
 & + \begin{bmatrix} [K'_{disc}] & & & \\ & [K'_{blade}]_1 & & \\ & & \ddots & \\ & & & [K'_{blade}]_{N_{blades}} \end{bmatrix} \begin{pmatrix} \{u_{disc}\} \\ \{u_{blade}\}_1 \\ \vdots \\ \{u_{blade}\}_{N_{blades}} \end{pmatrix} = \begin{pmatrix} 0 \\ 0 \\ 0 \\ 0 \end{pmatrix} \quad (2-46)
 \end{aligned}$$

$$[M]\{\ddot{u}\} + [K]\{u\} = \{0\} \quad (2-47)$$

Vectors $\{u\}_i$ contain the retained degrees of freedom of the disc and the blades. The prime denotes the reduced matrices of the system matrices obtained from an FE computation:

$$[M'_i] = \left([\Phi'_i][\Phi'_i]^T \right)^{-1} \quad (2-48)$$

Up to now, the equations of the sub-structures are still uncoupled as can be deduced from the block-diagonal form of the matrices. In order to couple the sub-structures, the coupling conditions must be established. Usually, they relate displacements and/or slopes of points on two structures, like the blade root and the attachment location on the disc. The resulting equations form the coupling matrix $[B]$ for which holds:

$$[B]\{u\} = 0 \quad (2-49)$$

Each row of $[B]$ describes one coupling condition. For rigid coupling conditions, the non-zero entries of $[B]$ are ± 1 . The eigenproblem, Equation (2-7), has to be solved with the vector constraint of Equation (2-49). The solution to this constrained eigenproblem involves a coordinate transformation using the null space of the coupling matrix, $[B]$. Equation (2-49) is the standard null space problem of a rectangular matrix. If a matrix, $[Q]$, can be found for which the product with the coupling matrix, $[B]$, is identically zero, then any vector fulfils Equation (2-49).

$$[B][Q] = [0] \Rightarrow [B][Q]\{y\} = \{0\}, \quad \{y\} \text{ arbitrary} \quad (2-50)$$

Together with Equation (2-49), the relation between the two sets of coordinates follows:

$$\{u\} = [Q]\{y\} \quad (2-51)$$

Introducing the new coordinates, and noting that the null space is a constant matrix, changes EOM(u) to EOM(y):

$$\begin{aligned} [Q]^T[M][Q]\{\ddot{y}\} + [Q]^T[K][Q]\{y\} &= \{0\} \\ [M_y]\{\ddot{y}\} + [K_y]\{y\} &= \{0\} \end{aligned} \quad (2-52)$$

The coupling matrix, $[B]$, is usually not square as there generally exist fewer coupling equations than degrees of freedom and so the system order is reduced to the number of unconstrained degrees of freedom. The resulting matrices do not generally possess diagonal form any more but are fully populated, expressing the coupling between the degrees of freedom. An eigensolver is then applied to solve the matrix equation for the modal data.

2.4.6 Program selection

Although commercial FE packages are available and tested, the MATLAB-based code MATFEM (Link, 1994) is used in the analysis of the rotor and the stator. Among the advantages are the full access to all variables, in particular mass and stiffness matrices of each element and the whole structure, and to the algorithms. This made it possible to add a further eigensolver that handles repeated natural frequencies, as they occur in the analysis of axisymmetric structures correctly, and to modify the post-processor to display output in the cylindrical coordinate system.

This concludes the description of some of the details particular to the eigensolution of rotationally-periodic and axisymmetric structures.

2.5 Vibration Properties of Bladed Discs

The goal of this section is to provide an understanding of the dynamics of a bladed disc such as the stator structure used in this investigation. The dynamics of the coupled system will be governed by the dynamics of its components: the disc and the blades. Throughout this thesis only the bending vibrations are considered.

2.5.1 Coupling approach

A coupling approach attempts to describe the dynamics of a complex structure in terms of the dynamics of simpler sub-structures, the solution to which is known or can be obtained from recursively sub-structuring, (Cottney and Ewins, 1974, Ewins, 1973). This approach has the advantage that known solutions for simple shapes can be used as building blocks to arrive at the solution for a complex structure, thus avoiding going back to first

principles, (Loewy and Khader, 1984). The stator in this analysis breaks naturally into the disc and the blades.

The approach considers each sub-structure on its own and includes the remaining sub-structures in the description as frequency-dependent boundary conditions: for the blades, the disc provides the boundary condition at one end.

This substructuring can be repeated to any desired level and often allows the analyst to maintain the insight gained from the analysis of the dynamics of individual structures. The next paragraphs demonstrate this approach for the stator.

2.5.2 Disc vibrations

The equation of motion of a circular disc of uniform thickness can be derived from a force or energy balance and solved by different methods.

2.5.2.1 Thin plates

The investigated structures of this thesis are modelled as ‘thin plates’. For these, the Kirchhoff theory is applicable which describes the bending vibration and arrives at solutions by neglecting the effects of the rotary inertia and – more importantly – the shear deformation.

2.5.2.2 Equation of motion

The equation of motion and the boundary conditions for the bending vibration of an axisymmetric disc can be obtained explicitly. It is a partial differential equation of fourth order in space and second order in time. The derivation is quite complex but can be found in many textbooks on dynamics of continua, (Géradin and Rixen, 1994, Meirovitch, 1986). According to Szabó (1953), the equation of motion of a thin disc can be written as:

$$(\Delta^4 - \beta^4)\psi(x)p(t) = 0 \quad (2-53)$$

where ψ is an unknown, non-zero, modeshape to be determined in the analysis and p is the time-dependent component. Only the shape is determined as arbitrary scaling can be introduced into Equation (2-53). The general differential Laplace-operator is defined in cylindrical coordinates (r, θ, z) by

$$\Delta^2 = \left(\frac{\partial^2}{\partial r^2} + \frac{1}{r} \frac{\partial}{\partial r} + \frac{1}{r^2} \frac{\partial^2}{\partial \theta^2} \right) \quad (2-54)$$

For axisymmetric modes, the derivatives with respect to the tangential coordinate vanish. β is the spatial eigenvalue:

$$\beta^4 = \omega^2 \frac{\rho h}{D} \quad (2-55)$$

which has to be determined in the analysis, and depends on the radii, the thickness and the Poisson ratio of the disc, the boundary conditions and the modeshape. The symbols

denote the unknown natural frequency, $\pm \omega$, the density, ρ , the thickness of the disc, h , and the stiffness of the disc, D , given in terms of the modulus of elasticity, E , and the Poisson's ratio ν :

$$D = \frac{Eh^3}{12(1 - \nu^2)} \quad (2-56)$$

The spatial eigenvalue scales directly with the mass measure, ρh , and inversely with the stiffness of the disc. This type of scaling holds for other structures, too, such as the beam described later in this chapter.

Applying a Bernoulli separation in the spatial variables of the modeshape, $\psi = R(r)\Theta(\theta)$, reduces the problem to two independent problems of finding the amplitude functions in radial and tangential directions separately. The tangential amplitude function is found by solving:

$$\frac{d^2}{d\theta^2} \Theta + n^2 \Theta = 0 \quad (2-57)$$

For $n > 0$ the solution is a harmonic function, $\Theta = a_1 \cos n\theta + a_2 \sin n\theta$, giving a modeshape with n nodal diameters. As the two coefficients, a_i , are arbitrary, two solutions exist, labelled the *cosine* and *sine mode* respectively. These mode pairs are commonly called *double modes* or twin modes. This is a feature common to all axisymmetric structures: rotating a modeshape by $\pi/2n$ around the axis of symmetry results in that modeshape to coincide with its twin modeshape. For $n=0$, the equation collapses and only one solution exists: $\Theta = a_1$.

To solve for the radial amplitude function, Equation (2-53) can be rewritten as:

$$(\Delta^2 + \beta^2)(\Delta^2 + (i\beta)^2)\psi = 0 \quad \text{or} \quad (\Delta^2 + (i\beta)^2)(\Delta^2 + \beta^2)\psi = 0 \quad (2-58)$$

reducing the order of the problem by a factor of two. The resulting equations are equations of the Bessel-type, (Beitz and Küttner, 1985, Rothe, 1952):

$$\begin{aligned} \frac{d^2}{dr^2} R + \frac{1}{r} \frac{d}{dr} R - \frac{n^2}{r^2} R &= 0 \\ \frac{d^2}{dr^2} R + \frac{1}{r} \frac{d}{dr} R + \frac{n^2}{r^2} R &= 0 \end{aligned} \quad (2-59)$$

with solutions of the form:

$$\begin{aligned} R_1 &= b_1 J_n(\beta r) + b_3 Y_n(\beta r) \\ R_2 &= b_2 I_n(\beta r) + b_4 K_n(\beta r) \end{aligned} \quad (2-60)$$

where I_n, Y_n, J_n, K_n are Bessel functions of order n of first and second kind and the modified functions of first and second kind, respectively.

The solution simplifies for circular discs, where for a finite solution, the coefficients b_3, b_4 must be set equal to zero, leading to:

$$R(r) = b_1 J_n(\beta r) + b_2 I_n(\beta r) \quad (2-61)$$

The zeros of the radial amplitude function are the nodal circles, concentric circles where the displacement from this mode is zero. The coefficients, b_1 and b_2 , are determined from two further boundary conditions, Table 2-1.

Deflection	$\psi = 0$	
Slope	$\frac{\partial \psi}{\partial r} = 0$	
Shear force	$\frac{\partial}{\partial r} \left(\frac{\partial^2 \psi}{\partial r^2} + \frac{1}{r} \frac{\partial \psi}{\partial r} + \frac{1}{r^2} \frac{\partial^2 \psi}{\partial \theta^2} \right) = 0$	<i>(The in-plane twisting moment $m_{r\theta}$ must also vanish.)</i>
Moment	$\frac{\partial^2 \psi}{\partial r^2} + \nu \left(\frac{1}{r} \frac{\partial \psi}{\partial r} + \frac{1}{r^2} \frac{\partial^2 \psi}{\partial \theta^2} \right) = 0$	

Table 2-1: Boundary conditions for an annular disc

The conditions for the shear-force and moment are intricate functions of r due to the two-dimensional stress field. Two boundary conditions each must be specified at the inner and outer boundary. The boundary conditions at the centre, finite displacement and slope, are used already by consideration of the values of the Bessel-functions at zero argument and resulting in setting b_3 and b_4 to zero.

Using the boundary conditions for zero force and moment at the outer diameter, two equations for the two unknowns are obtained. These have non-trivial solutions only for zero determinant, which leads to the following characteristic polynomial, CP , presented compactly in vector notation to show the various factors clearly.

$$\begin{aligned}
 CP = & I_{n+1} \begin{pmatrix} J_n & J_{n+1} \end{pmatrix} \begin{pmatrix} (\beta r_o)^4 + 2(\beta r_o)^2(n^2 - n)(1 - \nu) + (n^4 - n^2)(1 - \nu)^2 \\ -2(\beta r_o)^3(1 - \nu) \end{pmatrix} \\
 & + I_n \begin{pmatrix} J_n & J_{n+1} \end{pmatrix} \begin{pmatrix} -4(\beta r_o)(n^3 - n^2)(1 - \nu) \\ (\beta r_o)^4 - 2(\beta r_o)^2(n^2 - n)(1 - \nu) + (n^4 - n^2)(1 - \nu)^2 \end{pmatrix} \quad (2-62)
 \end{aligned}$$

The common argument of the Bessel-functions, βr_o , is dropped for brevity. The characteristic polynomial is a function of the number of nodal diameter n , Poisson's ratio, ν , the boundary conditions, and, of course, the spatial eigenvalue, β . Solving the characteristic polynomial determines β and the coefficients b_1 and b_2 to within a scaling constant. A solution can be found graphically or numerically, as shown in Figure 2-3 for the two-nodal-diameter mode, $n=2$.

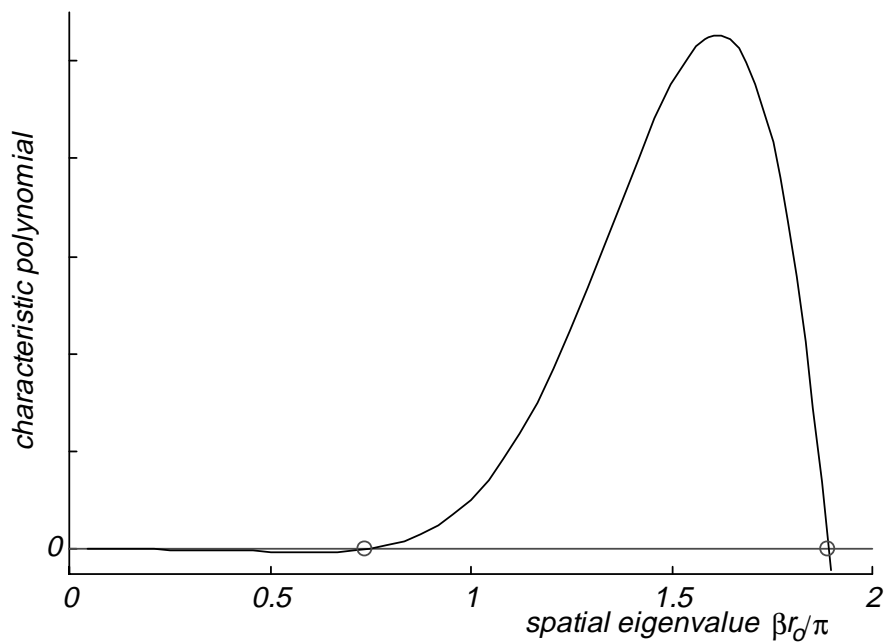


Figure 2-3: Zeros of the characteristic polynomial

The lower zero-crossing corresponds to the fundamental mode with zero nodal circles and the second crossing corresponds to the mode with one nodal circle, (Biezeno and Grammel, 1953). The separation between the higher spatial eigenvalues of the modes with more nodal circles approaches π , (Blevins, 1984).

With the spatial eigenvalue, the radial amplitude function is determined and it only remains to determine the natural frequency to specify the mode completely.

2.5.2.3 Natural frequencies

The natural frequency of each mode is obtained from Equation (2-55):

$$\omega^2 = \beta^4 \frac{D}{\rho h} \quad (2-63)$$

The natural frequencies for the two modes in a mode pair are identical as they share the same spatial eigenvalue. For the disc used in the experiments in Chapter 7 with the following geometry:

$$\begin{aligned} r_i &= 20 \text{ mm} && \textit{clamped} \\ r_o &= 250 \text{ mm} && \textit{free} \\ h &= 1 \text{ mm} \end{aligned} \quad (2-64)$$

the natural frequencies are computed and plotted in ascending magnitude showing the single and double modes, Figure 2-4.

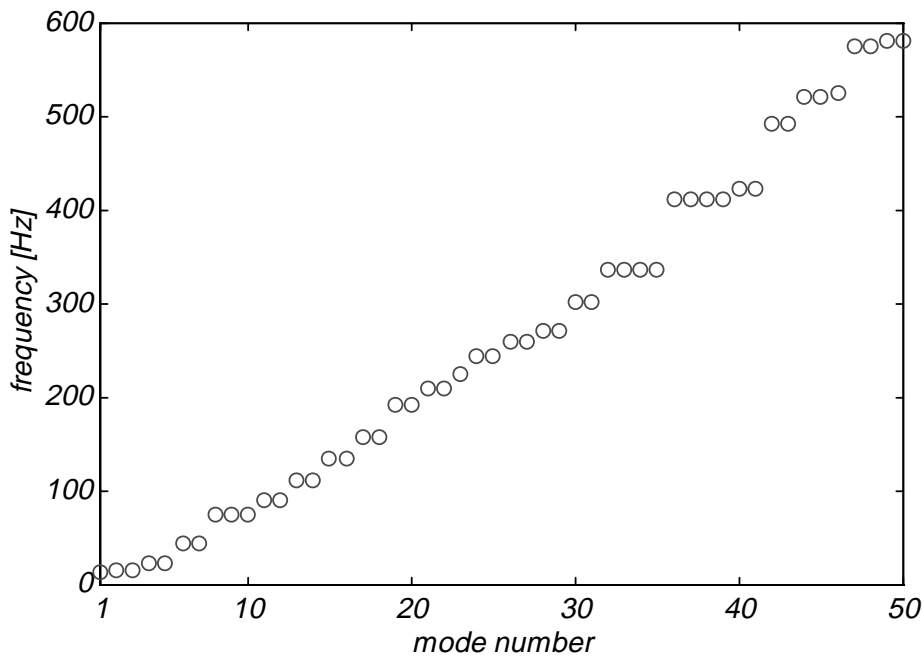


Figure 2-4: Natural frequencies versus mode number for the plain disc

The groups with more than two modes, like modes 8–10, have close natural frequencies, but there are never more than two modes with identical natural frequencies. Using the spatial features of the modeshapes in the natural-frequency plot, much more information can be conveyed to the reader and the groups with more than two modes are separated logically, Figure 2-5, (Ewins, 1980).

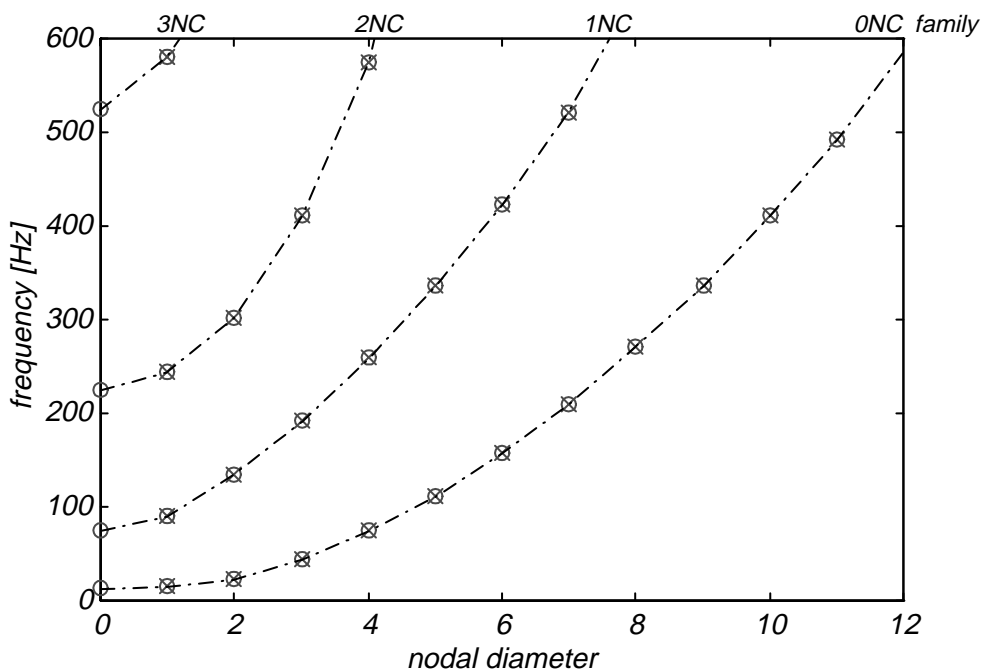


Figure 2-5: Natural frequencies versus nodal diameters, plain disc

In Figure 2-5, crossed circles indicate double modes while empty circles denote single modes. The natural frequencies group into families of modes, dashed lines in Figure 2-5, in which all modes have the same number of *nodal circles*, concentric circles where the

modeshapes are zero. The families correspond to the zero-crossings of the characteristic polynomial, Equation (2-62) and Figure 2-3: the 0NC family to the first crossing, the 1NC family to the second crossing etc. Except for the zero-nodal-diameter modes, the modes are double modes for the above-mentioned reasons, stemming from the axisymmetry of the structure. The natural frequency rises with the number of nodal diameters, as the disc becomes increasingly stiff in the tangential direction.

The group of three modes in Figure 2-4 can now be resolved as the 0ND single mode of the 1NC family and the 4ND double mode of the 0NC family, etc.

2.5.2.4 Influence of the blades

The blades will influence the disc dynamics depending of the relation of disc frequency to cantilever blade frequency. Away from the natural frequencies of the blade, the blades can be approximated as rigid bodies, (Loewy and Khader, 1984), adding only mass to the disc and so one can write symbolically

$$\omega_r^2 = k_r / (m_r + m_{blades,r}) \quad (2-65)$$

where k_r and m_r are the modal stiffness and modal mass of the disc and $m_{blades,r}$ is the participating mass of all blades for mode r , in effect a modal mass of the blades. These modes are called *disc modes* because the elastic deformations are mainly in the disc. Computation of the effective blade masses, $m_{blades,r}$, from Equation (2-65) is not possible as the addition of discrete masses changes the modeshapes. In general, a nodal circle will lie at or close to the attachment circle of the blades due to the inertia of the blades.

Close to the natural frequencies of the blades, their dynamics cannot be neglected any more. The natural frequencies of the bladed disc will asymptotically approach the cantilever frequency of the blades. In effect, the blades will act as tuned-mass absorbers, where the disc deflections become small compared with those of the blades. These modes are called *blade modes*.

For all these difficulties, the natural frequencies of the bladed disc are computed numerically and are discussed in Paragraph 2.5.4 below.

2.5.2.5 Modeshape notation

As has been shown above, the modeshapes of discs can be characterised by their numbers of nodal diameters and nodal circles. Conventionally, the modes are referred to by a pair of indices: (2,1) or 2ND1 indicate the mode with 2 nodal diameters and 1 nodal circle. Quite often, if it is clear from the context or when only one family of modes is considered, the index specifying number of the nodal circles is dropped, so that 2ND specifies the two nodal diameter mode of the current family.

To distinguish the modes of a mode pair, indices a and b or c and s are commonly used, (Irretier, 1994). This classification allows the designer to sort the modes intelligently by modeshape rather than just by magnitude.

2.5.3 Blade vibrations

The blades are analysed in a similar way to the discs in the previous paragraphs.

2.5.3.1 Thin beams

It is assumed that the blades can be described accurately by Euler-Bernoulli beams. The assumption behind these is that the effects of rotary inertia and shear deformation on the bending dynamics can be neglected. For many slender structures this has been found to be a valid assumption, (Timoshenko, 1986).

2.5.3.2 Equation of motion

From a force and moment balance of a beam element of constant geometric and material properties the partial differential equation governing the bending dynamics of an Euler-beam can be derived, (Gasch and Knothe, 1989)

$$EI \frac{\partial^4 u(x,t)}{\partial x^4} + \rho A \frac{\partial^2 u(x,t)}{\partial t^2} = 0 \quad (2-66)$$

subject to four spatial boundary conditions and two temporal ones. Constants E , I , A , ρ are the beam's modulus of elasticity, its moment of inertia perpendicular to the coordinate w , its cross-section area, and its density, respectively. Using a Bernoulli-separation:

$$u(x,t) = \psi(x)p(t) \quad (2-67)$$

this equation separates into two ordinary differential equations:

$$\begin{aligned} \frac{d^4 \psi}{dx^4} - \beta^4 \psi &= 0 \\ \frac{d^2 p}{dt^2} + \omega^2 p &= 0, \quad \beta^4 = \omega^2 \frac{\rho A}{EI} \end{aligned} \quad (2-68)$$

with spatial eigenvalue, β , and the natural frequencies, $\pm \omega$. As for the disc, the spatial eigenvalues scale directly with the mass measure, ρA , and inversely with the stiffness measure, EI . The general solution for the spatial fourth-order differential equation can be written as

$$\psi(x) = A_1 \cosh(\beta x) + A_2 \cos(\beta x) + A_3 \sinh(\beta x) + A_4 \sin(\beta x) \quad (2-69)$$

where the four coefficients, A_i , are determined by four spatial boundary conditions. For a beam clamped rigidly at one end and force- and moment-free at the other, these are the cantilever boundary conditions, given by:

$$\begin{aligned} \psi(x_c) &= 0 & \text{and} & & \frac{d^2}{dx^2}\psi(x_f) &= 0 \\ \frac{d}{dx}\psi(x_c) &= 0 & & & \frac{d^3}{dx^3}\psi(x_f) &= 0 \end{aligned} \quad (2-70)$$

These four equations can be solved for non-trivial coefficients only if the determinant of the coefficient matrix is zero, which leads to the characteristic polynomial, CP , which is a transcendental equation in the spatial eigenvalue with an infinite number of solutions:

$$CP = \begin{vmatrix} 1 & 1 & 0 & 0 \\ 0 & 0 & 1 & 1 \\ C & -c & S & -s \\ S & s & C & -c \end{vmatrix} \propto (1 + \cosh \beta l \cos \beta l) \quad (2-71)$$

c and s stand short for cosine and sine function and C and S for the hyperbolic cosine and sine functions respective, all with argument βl . The zeros of the characteristic polynomial are the sought spatial eigenvalues. The polynomial cannot be solved analytically, in general, but is easily solved numerically or graphically using suitable scaling to avoid infinite function values, Figure 2-6.

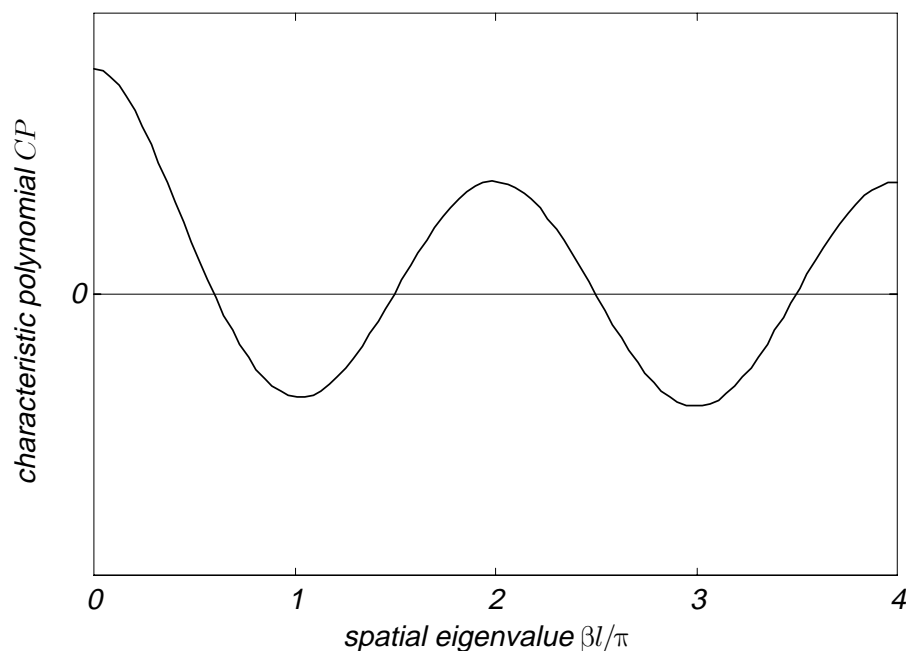


Figure 2-6: Spatial eigenvalue of the cantilever beam

The crossings at higher values of the characteristic polynomial, CP , in Figure 2-6, correspond to the higher order flap modes with one and more nodal lines. The modes are commonly called flap modes and denoted 1F for the first flap mode with 1 nodal line at the clamped root, etc.

2.5.3.3 Natural frequencies

After the spatial eigenvalues are obtained either graphically or numerically, the temporal eigenvalues follow from Equation (2-68):

$$\omega^2 = \beta^4 \frac{EI}{\rho Al} \quad (2-72)$$

The computations are based on a model of the blades with the geometry used later in the experiment: 175x1x20 mm³, length by thickness by width. The frequencies of the lowest flap modes estimated by the method of finite elements are given in Table 2-2.

modeshape	1F	2F	3F
frequency [Hz]	27.3	171	479

Table 2-2: Predicted blade natural frequencies

Further modes, like the bending modes about the axis with the larger moment of inertia (Y: yaw) and torsional modes (T), exist, but cannot be predicted with the bending theory used. A finite-element computation with plate elements revealed the following additional modes, Table 2-3.

modeshape	1T	1Y
frequency [Hz]	486	589

Table 2-3: FE-predicted torsion and yawing modes

2.5.3.4 Influence of the disc

The dynamics of the structure at the attachment location define the boundary conditions of the blade. Obvious this is a feedback, bi-directional, relation: the disc influences the blade dynamics, but, at the same time, the blades affect the dynamics of the disc, as described in Paragraph 2.5.2.4. If the dominant influence of the disc on the dynamics of the blade is modelled by a torsional spring due to the disc's finite angular stiffness, then the boundary conditions change to:

$$\begin{aligned} \psi(x_c) &= 0 & \frac{d^2}{dx^2} \psi(x_f) &= 0 \\ & & \text{and} & \\ \frac{d^2}{dx^2} EI \psi(x_c) &= -k_{yy} \frac{d}{dx} \psi(x_c) & \frac{d^3}{dx^3} \psi(x_f) &= 0 \end{aligned} \quad (2-73)$$

and the characteristic polynomial changes accordingly:

$$CP = \begin{vmatrix} 1 & 1 & 0 & 0 \\ C & -c & S & -s \\ EI\beta & -EI\beta & k_{yy} & k_{yy} \\ S & s & C & -c \end{vmatrix} \propto k_{yy} / EI(1 + \cosh \beta l \cos \beta l) + \beta(\cosh \beta l \sin \beta l - \sinh \beta l \cos \beta l) \quad (2-74)$$

where again c and s stand short for cosine and sine and C and S for the respective hyperbolic functions, all with argument βl . For zero stiffness, $k_{yy}=0$, the characteristic polynomial is that of the simply-supported-free beam, (Gasch and Knothe, 1989):

$$\beta(\cosh \beta l \sin \beta l - \sinh \beta l \cos \beta l) = 0 \quad (2-75)$$

If the stiffness becomes very large, the polynomial approaches that of the rigidly-clamped-free, or cantilever beam, Equation (2-71), in accordance with physical intuition:

$$(1 - \cosh \beta l \cos \beta l) = 0 \quad (2-76)$$

Again, the zeros of the characteristic polynomial are found numerically or graphically, Figure 2-7.

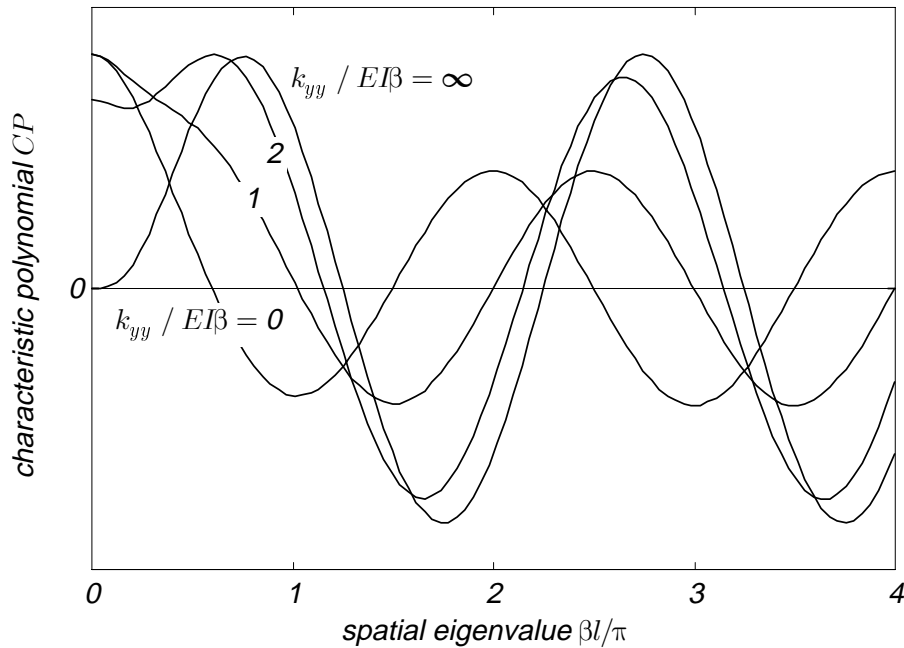


Figure 2-7: Spatial eigenvalue sensitivity to boundary condition

The different lines are labelled with their values of $k_{yy} / EI\beta$. The shift in eigenvalues is clearly noticeable, the eigenvalues vary between the two limits of the pinned beam with zero torsional stiffness at the boundary and the clamped beam with an infinite stiffness.

The situation becomes more intricate as the angular stiffness of the disc, seen as torsional spring by the blade is frequency-dependent itself. If the natural frequencies of the blade are to be determined in the described way, the solution would be found by an iterative method.

2.5.4 Assembly vibration

With a knowledge of the dynamics of the individual sub-structures, the coupled structure can be investigated. From the analysis of the disc and the blade separately, one can anticipate that the assembly modes can be described by three spatial parameters: the numbers of nodal diameters and circles from the disc modes and the number of nodal lines from the blade modes, (ND/NC/F). If nodal circles are defined as nodal lines of constant radius, then the blade-‘nodes’ (F) count towards the number of nodal circles (NC), and the modeshape of the assembly can be described by only two numbers, (ND, NC).

Rather than pursuing the described coupling approach, the assembly natural frequencies are calculated directly using the finite element model of the bladed disc described in Section 2.4, Figure 2-2. The eigenproblem is solved for the lowest 150 modes using an iterative subspace solver. The natural frequencies are plotted against the number of nodal diameters in Figure 2-8, where the abscissa is limited to ten nodal diameters which is the spatial Nyquist frequency for the bladed disc, $N_{blades} / 2$. Higher spatial orders or nodal diameters are folded back, or *aliased*, and appear as lower nodal diameter modes.

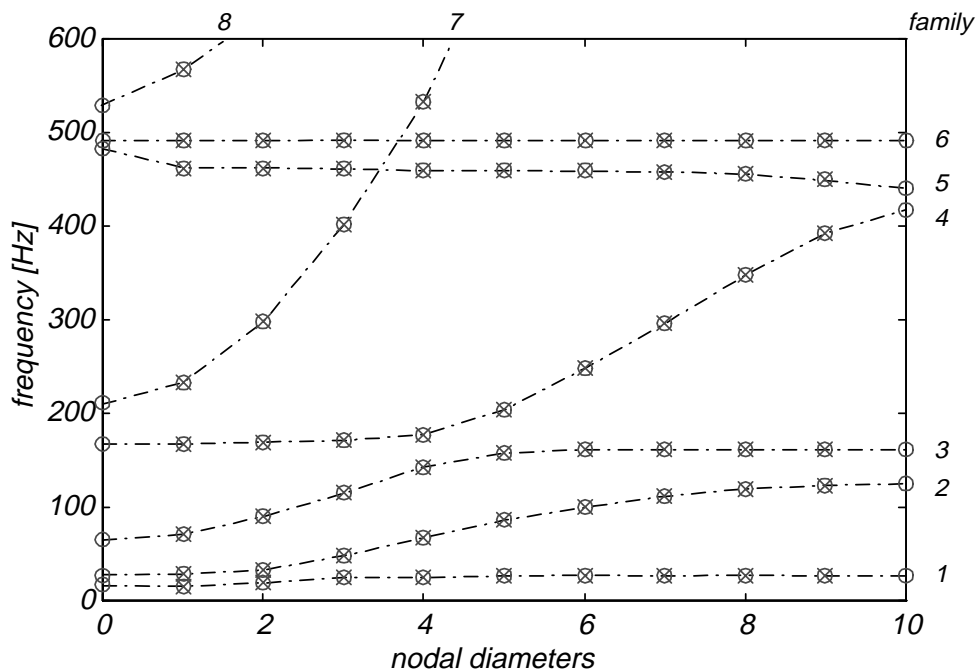


Figure 2-8: Bladed disc: predicted natural frequencies versus nodal diameters

The modes can be grouped by inspection of the modeshapes in families, indicated by the dashed lines in Figure 2-8. Modes within one family have common features and can be considered together. Inspection of the modeshapes of the 6th family identifies the group as family of 1T-blade modes with mostly in-plane bending in the disc. This family cannot be predicted by a out-of-plane-bending theory and shows the need to use always a model that includes the complete dynamics in the frequency range of interest. As the in-plane vibration of discs is decoupled from the out-of-plane vibration, the 6th family is neglected

in the further analysis. Below 400 Hz, the simple theory is sufficiently accurate and predicts all modes. The 5th family in Figure 2-8, the only family decreasing in frequency with nodal diameters, is actually a case of spatial aliasing: by inspection, it is found that the modes of the 5th family are the modes with higher nodal diameters, 11 through 20, of the 4th family.

Figure 2-9 shows the natural-frequency nodal-diameter plot with the 5th and 6th families of modes removed. This also removes the frequency crossing of the families. Rather than by number, the mode families are labelled by shape: number of nodal circles and the flapping mode of the blades. Figure 2-9 reveals several features familiar from the analyses of the sub-structures: double modes, mode families and constant blade cantilever modes. Most modes appear as double modes, except for the 0ND modes, as before, but now also the 10ND modes are single modes because of the spatial Nyquist frequency at $N_{blades} / 2$.

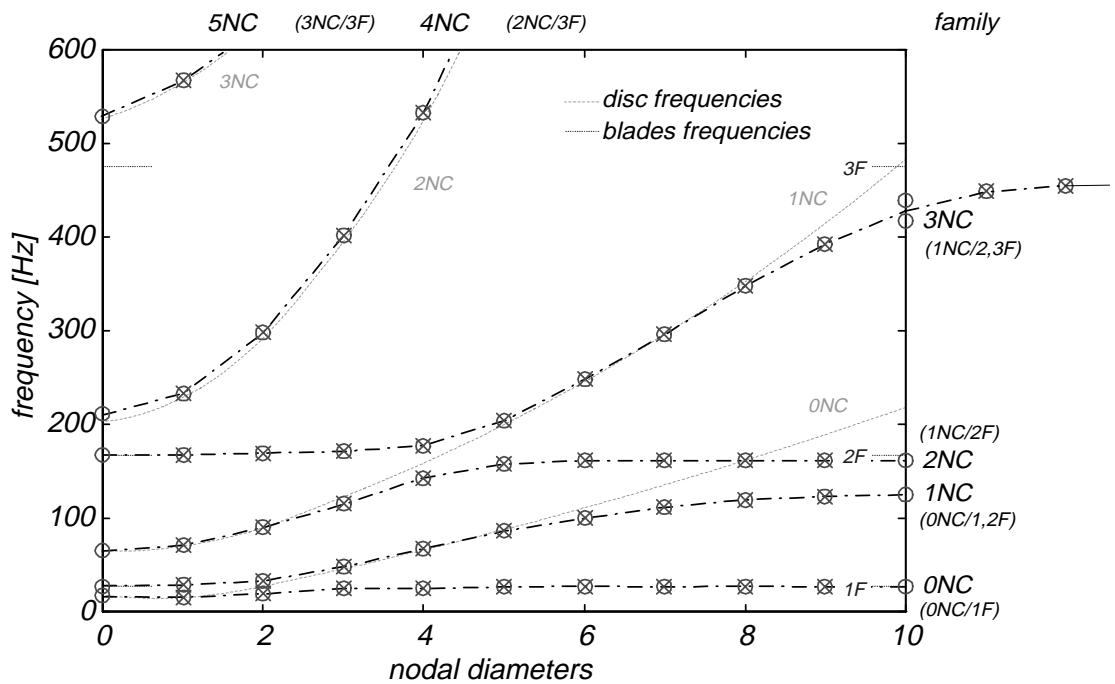


Figure 2-9: Component frequencies vs. assembly frequencies, predictions

For each mode family, the number of nodal circles is constant, but now, different from the plain disc, Figure 2-4, more than one family share each nodal circle in the disc, for example the 3rd and 4th family are both 1NC families, indicated by the rising dotted lines in Figure 2-9. These families differ in the slope at the outer diameter, the family with the higher natural frequencies having an almost horizontal slope at the outer radius.

While the number of nodal circles does not change within a family, the modeshape of the blade can change between the bracketing blade cantilever modeshapes listed in Table 2-2, indicated by the horizontal dotted lines in Figure 2-9. The 2nd family, for example, is a 0NC mode which vibrates with the 1F blade modeshape for low nodal diameters but changes to the 2F modeshape with increasing nodal diameters. Thus the family is labelled

(0NC/1,2F), Figure 2-9. If the nodal lines of the blades are counted towards the number of nodal circles as explained in Paragraph 2.5.4, the number of nodal circles is unique for each family, the (0NC/1,2F)-family is labelled 1NC-family.

In the regions where the natural frequencies remain fairly constant, for example between 0 and 2, and 8 and 10 nodal diameters for the 1NC-family, the modes are predominantly *blade modes* with the strain energy concentrated in the blades, whereas in the region where the frequencies change with nodal diameters, 3 to 7 nodal diameters for the same family, the modes can be categorised as *disc modes* with most of the strain energy in the disc, (Loewy and Khader, 1984). The disc modes lie close to the rising dotted lines in Figure 2-9. For the modes with higher numbers of nodal circles, 2 and 3, these lines coincide with the natural frequencies of the plain disc, Figure 2-5, which indicates that the influence of the blades on the natural frequencies of these modes is very small. For modes with lower numbers of nodal circles in the disc, 0 and 1, the influence of the blades is very noticeable and reduces the frequencies considerably, (Loewy and Khader, 1984).

The blade cantilever frequencies are approached asymptotically by the mode families. The faster the disc frequency rises, the quicker the assembly frequency will reach the asymptotic value of the blade frequency, both for low and high numbers of nodal diameters. This can be used during the design stage to obtain rough estimates of the natural frequencies of the bladed disc: the disc-alone natural frequencies, possibly corrected for the influence of the blades, and the blade cantilever frequencies are drawn against the nodal diameters and the assembly natural frequencies are then estimated by connecting the lines by smooth curves. Additionally, a torsional disc mode is expected at the cantilever frequency of the blades when the motion of the blades is counteracted by in-plane tangential motion of the disc. These modes are not shown in the figure but are computed to lie exactly at the blade cantilever frequencies.

2.5.5 Experimental results

As the low-frequency modes are the most important ones in the subsequent analysis, and these modes are dominated by the first cantilever frequencies of the blades, this parameter is determined experimentally and the FE-input data are adjusted to that effective blade length. After that, results of a calculation based on the FE model of the bladed disc are compared with the results of a modal test carried out on the bladed disc representing the stator in this study, Figure 2-10.

The differences are mostly in the natural frequencies of the disc modes and may be due to modelling errors of the disc thickness and the boundary conditions.

2.5.6 Effects of mistuning on the dynamics of rotationally periodic structures

Mistuning, i.e., the asymmetric distribution of system parameters, is a very complex phenomenon. Yiu (1995) gives a detailed overview over the whole area. Only the most

fundamental aspects of mistuning were relevant to this research, namely the separation of the mode pairs.

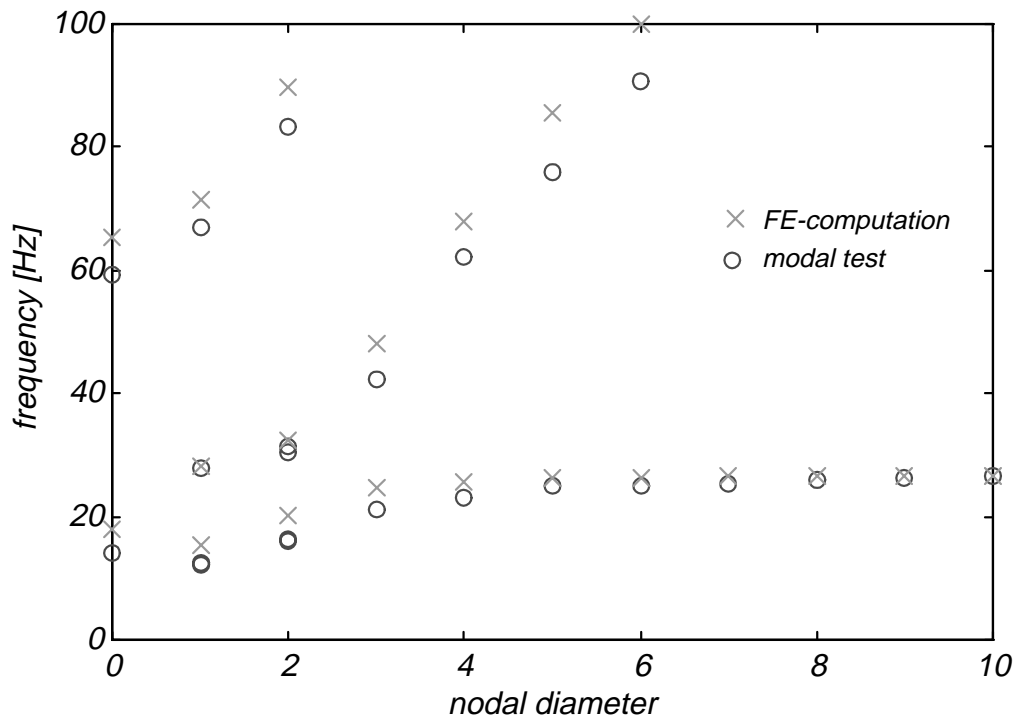


Figure 2-10: Comparison between measured and predicted natural frequencies

Even though the first cantilever frequency of each blade was adjusted to within 0.3% of the mean value of all blade frequencies, the natural frequencies of the bladed disc showed a split in natural frequencies of the double modes, (Arnold and Tobias, 1957). This effect of mistuning was noticeable in the low-nodal-diameter modes of the first and second family, Figure 2-10. As the frequency split was also detected in the spectrum of the unbladed rotor, presented later in this chapter, the mistuning is assumed not be caused by the blades but by initial, static, deformation of the disc. This initial deformation changed the stiffness of the disc to bending due to the geometric deformation of the bending axis, and affected the modes of a mode pair differently and thus split their natural frequencies.

Mistuning by either mechanism – initial deformation or asymmetric system property distribution – fixes the modes uniquely in the structure. In mistuned structures, preferential orientations exist and the modes are defined completely, whereas in the axisymmetric case no preferential directions exist and the mode pairs are defined up to an arbitrary angle only, and are free to rotate around the axis of symmetry.

Any spatially distributed system quantity, such as mass or stiffness, can be decomposed into a spatial Fourier series with each element of the series corresponding to a different number of nodal diameters. Each non-zero element of the series fixes the orientation of the mode pairs of that nodal diameter and splits their natural frequencies.

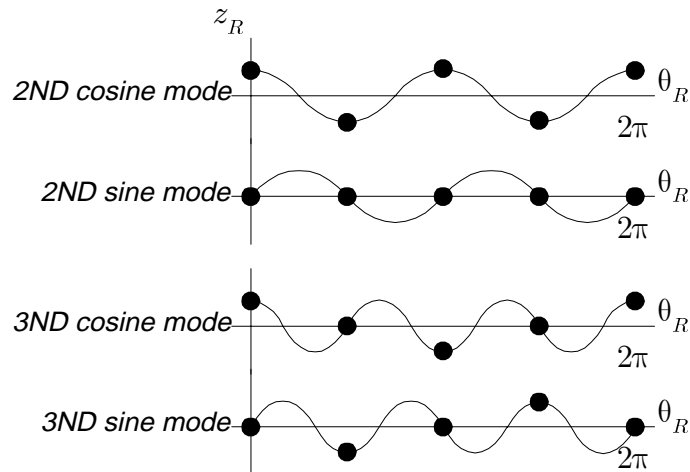


Figure 2-11: Effect of four-mass mistuning

Figure 2-11 shows a deliberate 2ND-mass mistuning, or detuning. The corresponding 2ND modes are fixed in their orientation: the masses lie on anti-nodal points for the cosine mode and on the nodal points for the sine mode. The effect on each of the two 3ND modes is similar, and hence, the mode pair does not split. A mass or stiffness distribution exactly proportional to a modeshape would affect that modeshape only. In addition to the change of frequency, the modeshapes themselves will be affected and will not be pure harmonic functions any more, (Ewins, 1975).

The discussion above holds for well-separated modes only, where the effects of mistuning remain local to a mode pair. If the mistuning causes the modes of two mode pairs to get intermingled, the effects cannot be described as perturbation of the axisymmetric case any more.

2.5.7 Discussion - Stator

In the above paragraphs of Section 2.5 the dynamics of the stator are presented. The bladed disc dynamic characteristics are deduced from those of the blades and the disc separately. The coupling effect is described for the individual structures: the blades lower the natural frequencies of the modes with small numbers of nodal circles, and the natural frequencies of the blades change according to the boundary stiffness presented by the disc. Especially for the low-frequency modes, the dynamics of the blades and the disc predict those of the bladed disc quite well. The relative difference of disc and blade frequencies determine whether the assembly mode is a disc mode or a blade mode.

The effects of mistuning or asymmetric mass or stiffness properties on the dynamics of rotationally periodic structures have been explained. The frequency split of mode pairs is observed in experimental data and the formation of preferential directions is discussed.

The finite-element method has proven capable of predicting the dynamic behaviour of the bladed disc accurately.

As mentioned in the introduction, the change from a rotating bladed disc of turbomachinery to a stationary bladed disc in the analysis and the test rig, is possible only

because the test rig's sole task is to be dynamically similar to typically turbo-machinery and to enable measurements of the dynamic responses but not to exchange energy between the rotor and the surrounding working fluid.

2.6 Vibration Properties of Rotating Discs

The natural frequencies of a plain disc at rest can be found analytically. For rotating discs or discs with non-uniform thickness, introduced by, for example, a centre hole, closed-form solutions generally do not exist and approximate methods must be employed, (Eversman, 1969, Harris, 1967, Mansfield, 1961, Irretier, 1979). This section describes the bending vibrations of the rotor in the body-fixed reference frame.

2.6.1 Admissible modeshapes

The admissible modeshapes for axisymmetric discs, i. e., functions of the position that fulfil the equation of motion of the disc for all times and positions, are simple harmonic functions in the tangential direction, (Biezeno and Grammel, 1953). Therefore, a Bernoulli separation of variables can be used to simplify the equations of motion as presented previously:

$$\psi(r, \theta) = R(r) \cos(n\theta) \quad (2-77)$$

where (r, θ) are the body-fixed coordinates of the disc. The number of periods of the modeshape along the perimeter, n , is called the number of *nodal diameters*. The term 'node' (not used in the FE sense here) becomes obvious if it is noted that for $\cos(n\theta) = 0$, the generalised coordinates is zero for all times and all radii at the nodal lines. For $n > 0$, twin modes exist with cosine and sine shapes in the tangential function with identical eigenvalues. The analytic shapes of the modeshapes in the tangential direction simplify considerably the integral expression for the energies, reducing them to integrals in just one variable. Thus, standard, uni-variate methods can be used.

2.6.2 Computation of the natural frequencies

The natural frequencies of the rotor as a function of the speed of rotation are determined from an energy balance. The rotor is modelled as a thin disc.

2.6.2.1 Rayleigh-Ritz method

Using Hamilton's Principle, the variational problem solves for both eigenfrequency and modeshape, (Szabó, 1956):

$$\delta \int_{t_0}^{t_1} (U(t) - T(t)) dt = 0 \quad (2-78)$$

$T(t)$ and $U(t)$ are the kinetic and potential energy, respectively. Maybe the most straightforward approach to estimating the natural frequency of conservative systems is the

Rayleigh-Ritz method, which requires the maxima of the kinetic and potential energies to be identical:

$$\lambda K = U \quad (2-79)$$

where λ is the eigenvalue, the square of the natural frequency, ω , K is the maximum specific kinetic energy, respectively, and U denotes of the maximum potential energy. The energy terms are functions of the modeshape and the closer the assumed shape is to the modeshape, the better the approximation of the associated eigenvalue, (Biezeno and Grammel, 1953). This translates the problem of finding the eigenvalue into a standard minimisation: in order to obtain a good estimate for the eigenvalue, the assumed shape is described in terms of parameters ε_i and the expression for the eigenvalue is then minimised with respect to these parameters:

$$\omega^2 = \lambda \leq \min_{\varepsilon_i} U(\varepsilon_i) / K(\varepsilon_i) \quad (2-80)$$

The equality holds for modeshape but for discretised continuous structures the modeshape is only an approximation to the continuous eigenfunction, and the eigenvalue is always over-estimated, (Bathe, 1983). The natural frequency of the mode follows from $\lambda = \omega^2$.

2.6.2.2 Determination of the kinetic and potential energies

The potential energy of the rotating disc splits into two parts, (Biezeno and Grammel, 1953, Lamb and Southwell, 1921): a first component due to the bending stiffness of the disc and a second due to the centrifugal potential:

$$U = U_b + U_\Omega \quad (2-81)$$

The eigenvalue equation, Equation (2-80), changes accordingly:

$$\omega^2 = \lambda \leq \min_{\varepsilon_i} \frac{U_b(\varepsilon_i) + U_\Omega(\varepsilon_i)}{K(\varepsilon_i)} = \lambda_b + \lambda_\Omega \quad (2-82)$$

where λ_b is the eigenvalue of the disc at rest and λ_Ω is the eigenvalue of a rotating membrane without bending stiffness, (Lamb and Southwell, 1921). The rotation increases the natural frequency of a rotating structure, this effect is called *centrifugal stiffening*.

The maximum specific kinetic energy can be expressed as:

$$K = \frac{\pi}{2} \rho \int_{r_i}^{r_o} h R^2 r dr \quad (2-83)$$

where r is the radial coordinate, $R = R(r)$ is the radial amplitude function of the assumed shape, $\{\psi\}$, Equation (2-77), $h = h(r)$ is the thickness of the disc, and ρ is the mass density, the latter assumed to be constant over the disc. r_i and r_o are the inner and outer radii, respectively. The bending energy is given by:

$$\begin{aligned}
U_b = \frac{\pi}{2} \frac{E}{12(1-\nu^2)} \int_{r_i}^{r_o} h^3 \left(\left(\frac{d^2 R}{dr^2} + \frac{1}{r} \frac{dR}{dr} - n^2 \frac{R}{r^2} \right)^2 \right. \\
\left. - 2(1-\nu) \left(\frac{1}{r} \frac{d^2 R}{dr^2} \left(\frac{dR}{dr} - n^2 \frac{R}{r} \right) - \frac{n^2}{r^2} \left(\frac{dR}{dr} - \frac{R}{r} \right)^2 \right) \right) r dr
\end{aligned} \tag{2-84}$$

where E denotes the modulus of elasticity, ν is the Poisson ratio, and n is the number of nodal diameters. The centrifugal potential is given by:

$$U_\Omega = \frac{\pi}{2} \Omega^2 \int_{r_i}^{r_o} h \left(\frac{\sigma_r}{\Omega^2} \left(\frac{dR}{dr} \right)^2 - n^2 \frac{\sigma_\theta}{\Omega^2} \frac{R^2}{r^2} \right) r dr \tag{2-85}$$

where Ω is the speed of rotation, and the radial and tangential stresses are denoted by σ_r and σ_θ , respectively. For a rotating disc of uniform thickness, the stresses are given by (Biezeno and Grammel, 1953):

$$\begin{aligned}
\sigma_r &= \frac{3+\nu}{8} \rho \Omega^2 \left(-\frac{r_i^2 r_o^2}{r^2} + (r_i^2 + r_o^2) - r^2 \right) \\
\sigma_\theta &= \frac{3+\nu}{8} \rho \Omega^2 \left(\frac{r_i^2 r_o^2}{r^2} + (r_i^2 + r_o^2) - \frac{1+3\nu}{3+\nu} r^2 \right)
\end{aligned} \tag{2-86}$$

If the centrifugal loading from the blades is to be considered, corrections need to be applied to the formulae. Without initial stresses on the inner or outer radii, the eigenvalue equation, Equation (2-82), takes the following form

$$\omega^2 = \lambda \leq \frac{\beta^2 J_b + \Omega^2 J_\Omega}{J_k} \tag{2-87}$$

where $\beta = \sqrt{E/\rho}$ is the speed of transverse waves in solids and the J_i contain the terms that depend on the modeshape and the properties of the disc.

2.6.2.3 Choice of radial amplitude function

A trial solution for the radial amplitude function should satisfy all boundary conditions of the differential equation, for the Rayleigh approximation only the geometric ones, (Meirovitch, 1980). For a disc clamped at the inner diameter and free at the perimeter, the boundary conditions split into geometric conditions at the inner radius – zero deflection and zero slope, (Mignolet, Eick and Harish, 1996):

$$\begin{aligned}
R(r_i) &= 0 \\
\frac{dR}{dr}(r_i) &= 0
\end{aligned} \tag{2-88}$$

and the dynamic boundary conditions at the outer radius – moment- and force-free:

$$\frac{d^2 R}{dr^2}(r_o) + \nu \left(\frac{1}{r_o} \frac{dR}{dr}(r_o) - n^2 \frac{R(r_o)}{r_o^2} \right) = 0 \quad (2-89)$$

$$\frac{d^3 R}{dr^3}(r_o) - \left((1 + \nu) + n^2(2 - \nu) \right) \frac{1}{r_o^2} \frac{dR}{dr}(r_o) + 3n^2 \frac{R(r_o)}{r_o^3} = 0$$

A low-order polynomial in r that satisfies the boundary conditions at the inner radius exactly and approximates the conditions at the outer radius is, for example:

$$R(r) = \frac{(r - r_i)^2}{r_o} \left(1 + \varepsilon \frac{r - r_i}{r_o} \right) \quad (2-90)$$

where ε is the variational parameter used to minimise the eigenvalue estimate, Equation (2-80). The boundary conditions can be fulfilled exactly by higher-order polynomials, (Weber, 1996), but the increase in computational effort is large for little gain in accuracy. So the third-order polynomial, Equation (2-90), is used to compute the natural frequencies of the rotor used in the experiment, Chapter 7.

2.6.2.4 Influence of boundary conditions

Applying St. Venant's Principle to slender discs with small inner-to-outer radius ratios, one can appreciate that the boundary conditions at the inner diameter do not influence the natural frequencies of slender discs greatly. According to Blevins (1984), the difference in the natural frequencies for slender discs between a clamped and simply-supported inner diameter for the 2ND mode is less than 4% and for the 3ND mode it is smaller than the recorded precision.

2.6.2.5 Experimental Validation

Programs are written to evaluate Equation (2-82) numerically. The geometric data chosen for the computation are those of the disc eventually used in the experiments: 0.8 mm thick, 500 mm outer diameter, and 40 mm inner diameter. The disc is clamped at the inner diameter and free at the outer diameter.

Figure 2-12 shows the computed natural frequencies of the rotor as functions of the speed of rotation.

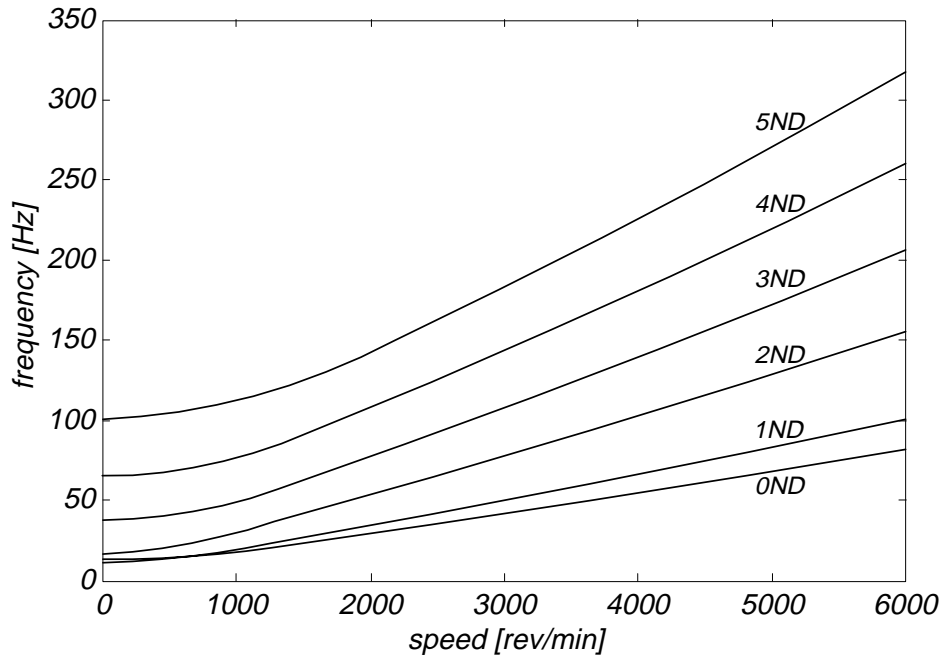


Figure 2-12: Predicted natural frequencies of a plain disc as a function of speed

As expected, modes with low natural frequencies at zero speed approach their high-speed asymptotes more quickly than modes with high natural frequencies, which follows from the dominance of the speed-dependent term in Equation (2-87), Figure 2-13:

$$\lim_{\Omega \rightarrow \infty} \omega = \sqrt{J_{\Omega}/J_k} \Omega \tag{2-91}$$

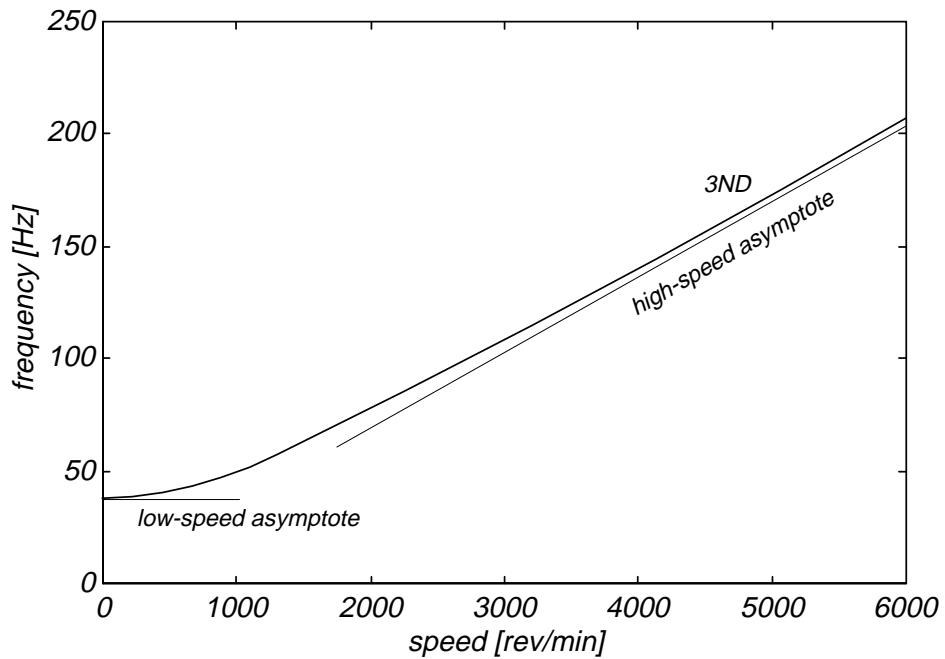


Figure 2-13: Eigenvalue asymptotes for the 3ND mode

Limit values for the expressions J_b/J_k and J_{Ω}/J_k are tabulated in the Appendix for the disc used in the experiment. From the different slopes of the curves in Figure 2-12, it can

be seen that the speed influence rises with the number of nodal diameters. The measured natural frequencies agree well with the computed ones, validating the numerical method, Figure 2-14, where the circles denote the measured natural frequencies.

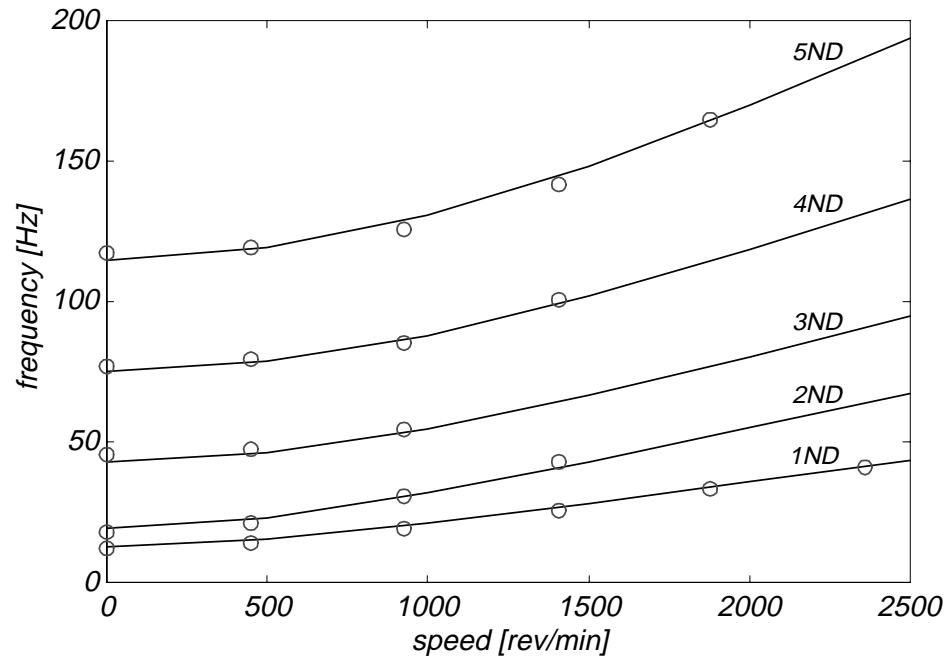


Figure 2-14: Measured and computed natural frequencies of a plain disc against speed

2.6.2.6 Parameter Sensitivities

As expected, the bending potential governs the magnitudes of the eigenvalues at low speeds, Equation (2-80), and the speed-dependent components become dominant at high speeds, Figure 2-13. A more thorough analysis reveals:

$$\lambda = \lambda_b + \lambda_\Omega \propto \frac{E}{\rho} \frac{h^2}{r_o^4} n^4 + \Omega^2 \frac{1}{r_o} n^2 \quad (2-92)$$

The first term represents the dependencies for the eigenvalues of the disc at rest, λ_b , and are the ones given in Blevins (1984), quoted there for the natural frequencies:

$$\omega_b \propto \sqrt{\frac{E}{\rho} \frac{h}{r_o^2}} n^2 \quad (2-93)$$

The second term in Equation (2-92) shows the proportionality factors of the eigenvalues of the rotating floppy membrane without bending stiffness, λ_Ω : this component grows linearly with speed, as shown in Figure 2-13, and with the number of nodal diameters squared, and inversely with the outer radius.

2.6.3 Discussion - Rotor

The method presented above assumes that the motion is mostly governed by the elastic potential. The modes with one nodal diameter store elastic energy almost entirely in the

vicinity of the inner clamped radius, while closer to the outer rim they behave very much like rigid-body modes. For a thin disc of uniform thickness it is found that the approximations for the 1ND mode have much larger relative errors than the estimates of the ‘truly’ elastic modes with higher numbers of nodal diameters, (Weber, 1996).

The method presented above estimates the modeshapes as functions of the speed of rotation. From a preliminary study it became evident that the rotation does not distort the modeshapes greatly but only scales them. The scaling of the modeshapes is arbitrary and for constant running speed as applies to most of the simulations, Chapter 7, the scaling does not change. Mignolet, Eick and Harish (1996) investigate singular and regular perturbation approaches to obtain the modeshapes of a rotating disc as functions of speed, but limit the investigation to modes with 0, 1, and 2 nodal diameters only.

The presented method allows the designer to understand the influence of the physical parameters and to carry out parameter studies with relative ease and computational efficiency.

2.7 Conclusions

In this chapter the analysis of the dynamics of linear structures is presented. This leads to the eigenanalysis of linear structures. The eigenproperties of a structure are required for an efficient forced response analysis using modal superposition. This approach relies on the assumption of linearity and violation of this basic assumption invalidates subsequent analysis.

The analytic approach operating on continuous structures has the advantage of providing exact results within the limits of the theory, but can be applied to structures with simple geometry only, due to the difficulty of having to find the eigenvectors explicitly. The method of finite elements is presented as a way to obtain the modal properties of complex, arbitrarily shaped structures. The necessary discretisation of the structures introduces further errors in the results which show usually in the high-frequency modes. Only general rules exist to judge the quality of the modal matrix obtained for discretised structures.

Another disadvantage of the method of finite elements is the potentially high computational cost. In order to alleviate this, special algorithms exist. Also, the capability of the solver to solve for a few low-frequency modes only is essential once the model size reaches a few hundred degrees of freedom. Iterative subspace solvers provide for this requirement efficiently. The computational saving of a partial low-frequency solution can be of the order of a hundred. If parameter influences are required, they need to be determined numerically, which becomes prohibitively expensive.

Any eigensolver for rotationally periodic structures must be able to handle repeated eigenvalues, where, quite often, numerical inaccuracies help the solver as they change the eigenvalues slightly, making all the roots of the characteristic polynomial distinct.

More complex structures can be split into sub-structures which are analysed separately. The results of the individual analyses can be combined to give results for the whole structure. This coupling approach is shown to reduce the computational effort of the analysis considerably, (Gasch and Knothe, 1989).

On today's computers, the computation of eigensolutions of the order of 5000 degrees of freedom takes a reasonable time. And as the solution is computed only once, some of the methods described in this chapter may not justify the effort it takes to implement them. Nevertheless, a good understanding of the underlying principles helps to guide in the interpretation of the results of any finite element analysis.

The eigenproperties of the stator and rotor are obtained using an FE analysis. An analytic solution of the stator's components – disc and blades – provided qualitative insight into the dynamic behaviour of the assembly. For the rotor, an energy-based approach provided the speed dependent natural frequencies while the modeshapes are computed analytically and by the FE method.

Chapter 3: Dynamics of the Rotor-Stator System

Having modelled the stator and the rotor individually, both systems must be considered together. To do so, the dynamics of both structures must be expressed in the same frame of reference. Once the dynamics of both systems are described in one reference frame, the dynamics of the coupled system can be analysed.

3.1 Description of Dynamic Properties in non-body-fixed Coordinates

The choice of the frame of reference in which the dynamics of both structures are described is entirely arbitrary. From an experimentalist's point of view, the stationary frame of reference is favoured as it simplifies conducting the experiments. In order to express the dynamics of the rotor in the stationary reference frame, a coordinate transformation must be carried out.

3.1.1 Stationary and rotating reference frames

The two reference frames that need to be related to one another are the body-fixed reference frames of the stator and the rotor, for brevity labelled the stationary and rotating frame of reference, Figure 3-1.

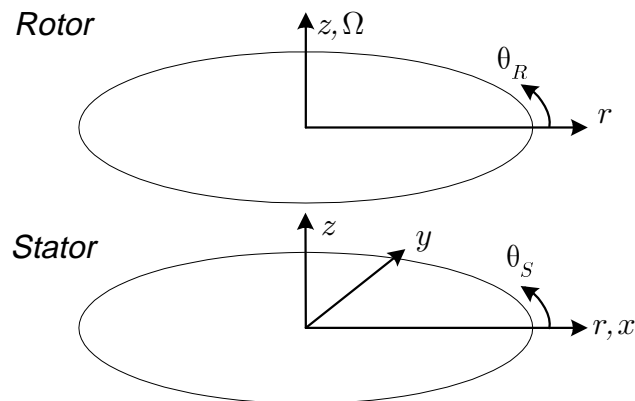


Figure 3-1: Coordinate systems

(r, θ, z) are the cylindrical coordinate systems, indices R and S denote quantities expressed in the rotating or stationary reference frame respectively. Both cylindrical coordinate systems are defined as right-hand, orthogonal coordinate systems for which the cross product gives:

$$\{e_r\} \times \{e_\theta\} = \{e_z\} \quad (3-1)$$

and all permutations thereof.

All quantities of either structure, such as displacements and velocities, can be expressed in either frame. The analysis of the coupled system will be performed in the stationary reference frame to ease the experimental validation described in Chapter 7, and so the quantities expressed in the rotating reference frame need to be translated. The

necessary transformation will be developed in the following paragraphs.

For a constant speed of rotation, the tangential coordinates of the two reference frames are related to each other by a Galilean transformation:

$$\theta_R = \theta_S - \Omega t \quad (3-2)$$

where Ω denotes the rotational speed. The axial z -axes of the two reference frames are assumed to coincide at all times.

3.1.2 Waves

During the analysis of the individual structures, the modeshapes are assumed to be real. Especially for periodic and in the limit axisymmetric structures, it is often convenient to rewrite the double modes as pairs of complex *waves*.

The double modes with equal natural frequency and similar modeshape are combined into two waves, a *co-rotating wave* and a *counter-rotating wave*:

$$\begin{aligned} \cos(n\theta) + i \sin(n\theta) &= e^{in\theta} \\ \cos(n\theta) - i \sin(n\theta) &= e^{-in\theta} \end{aligned} \quad (3-3)$$

As waves are linear combinations of modeshapes, they are solutions to the eigenproblem and thus are valid modeshapes as well.

In addition to the complex modeshape the natural frequencies are interpreted slightly differently: instead of taking the positive root of the eigenvalue λ as natural frequency, the natural frequency of the co-rotating wave is taken as the positive root, as is done traditionally for all modes, but the natural frequency of the counter-rotating wave is taken as the negative root of the eigenvalue:

$$\begin{aligned} \omega_{nf} &= +\sqrt{\lambda_n} \\ \omega_{nb} &= -\sqrt{\lambda_n} \end{aligned} \quad (3-4)$$

This distinction may seem academic at first but will become useful in the analysis later.

3.1.3 Frequency-speed diagram

For sake of simplicity, assume a displacement of a rotating structure described in the body-fixed, rotating reference frame from a single n nodal diameter wave pair: a co-rotating wave and counter-rotating wave with equal natural frequencies, ω_{nR} , excited in resonance by a harmonic force:

$$\begin{aligned} u_{rnR} &= \frac{1}{2}(e^{in\theta_R} + e^{-in\theta_R}) \cos \omega_{rnR} t \\ &= \cos(\omega_{rnR} t - n\theta_R) + \cos(-\omega_{rnR} t - n\theta_R) \end{aligned} \quad (3-5)$$

or, using positive and negative frequencies:

$$u_{rnR} = \cos(\omega_{rnRf} t - n\theta_R) + \cos(\omega_{rnRb} t - n\theta_R) \quad (3-6)$$

where the indices identify the rotating structure, the number of nodal diameters, the reference frame, and the direction, where consistently f and b are used rather than the lengthy *co-rotating* and *counter-rotating*. Describing the deflection in the stationary frame of reference by substitution of the angle, Equation (3-2), leads to:

$$\begin{aligned} u_{rnS} &= \cos(\omega_{rnRf}t - n(\theta_S - \Omega t)) + \cos(\omega_{rnRb}t - n(\theta_S - \Omega t)) \\ &= \cos((\omega_{rnRf} + n\Omega)t - n\theta_S) + \cos((\omega_{rnRb} + n\Omega)t - n\theta_S) \end{aligned} \quad (3-7)$$

or:

$$u_{rnS} = \cos(\omega_{rnSf}t - n\theta_S) + \cos(\omega_{rnSb}t - n\theta_S) \quad (3-8)$$

It must be stressed that this is only a change in the *description* of the quantity, not in the quantity itself. Changing the reference frame changed the *apparent frequencies* of the response. The term shall indicate descriptions of quantities in a non-body-fixed frame. Looking at the indices, it occurs for index combinations rS and sR . Frequencies of both co-rotating and counter-rotating wave increase by $n\Omega$ and it is said they are modulated by the speed of rotation, Figure 3-2:

$$\begin{aligned} \omega_{nSf} &= \omega_{nRf} + n\Omega \\ \omega_{nSb} &= \omega_{nRb} + n\Omega \end{aligned} \quad (3-9)$$

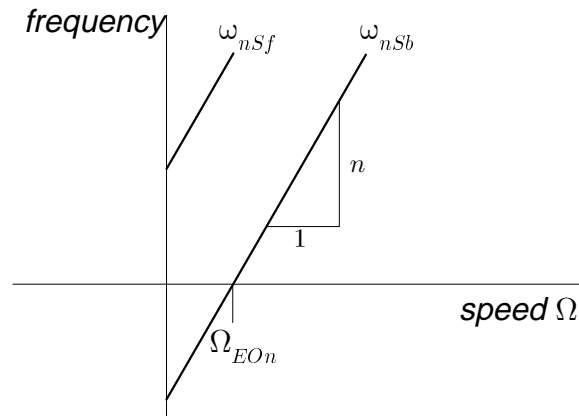


Figure 3-2: Frequency transformation

Each natural frequency transforms according to its number of nodal diameters. This makes the transformation from one reference frame into the other an expensive operation from an experimental point of view, as not only the frequency but also the spatial distribution is required to transform quantities between reference frames, (Bucher, Ewins, Robb and Schmiechen, 1995). This transformation holds for all frequencies, not just the natural frequencies of the structures.

A single transducer cannot detect the direction of the wave and thus cannot distinguish between co- and counter-rotating waves and positive and negative frequencies. Due to this aliasing of negative and positive frequencies, the sign of the counter-rotating waves is often ignored and their frequencies are given by the absolute value:

$$\omega_{nSb} = |\omega_{nRb} + n\Omega| \quad (3-10)$$

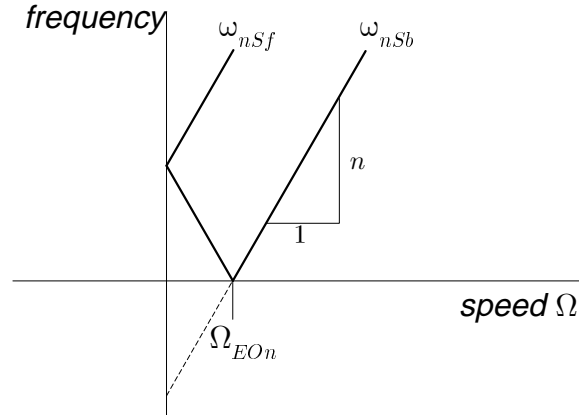


Figure 3-3: Aliasing at the 0 Hz line

In both the preceding figures, the frequency of the counter-rotating wave crosses or touches the abscissa at a certain speed, Ω_{EO_n} :

$$0 = \omega_{nRb} + n\Omega_{EO_n} \quad (3-11)$$

This speed is called the *engine-order speed* of the n nodal diameter mode or n th engine-order speed:

$$\Omega_{EO_n} = -\omega_{nRb} / n \quad (3-12)$$

ω_{nRb} is speed-dependent due to the centrifugal forces as shown in Section 2.6 and hence the engine-order speeds cannot be determined from the natural frequencies of the structure at rest:

$$\Omega_{EO_n} = -\omega_{nRb}(\Omega_{EO_n}) / n \quad (3-13)$$

As n is arbitrary, this result holds for all nodal diameters.

The natural frequencies are actually functions of the speed of rotation and the straight lines in Figure 3-2 and Figure 3-3 are bent, (Tobias and Arnold, 1957). Figure 3-4 shows the computed natural frequencies of the thin rotating disc used to model the rotor in the experiment, whose properties are given in the Appendix.

The number of nodal diameters of the associated modeshape is indicated for each natural frequency line in Figure 3-4. The directions are labelled with '+' and '-' for the co-rotating and counter-rotating waves, respectively. Notice also the reflection of the frequencies at the 0 Hz line due to aliasing and the bend of the curves due to centrifugal stiffening.

The number of nodal diameters can be computed from the angle of the departing frequency lines at low speeds, Equation (3-9): the higher the number of nodal diameters, the larger the angle at low speeds of rotation:

$$\tan \alpha = \frac{\Delta \omega_{nSf}}{\Delta \Omega} = \frac{n\Omega}{\Omega} = n \quad (3-14)$$

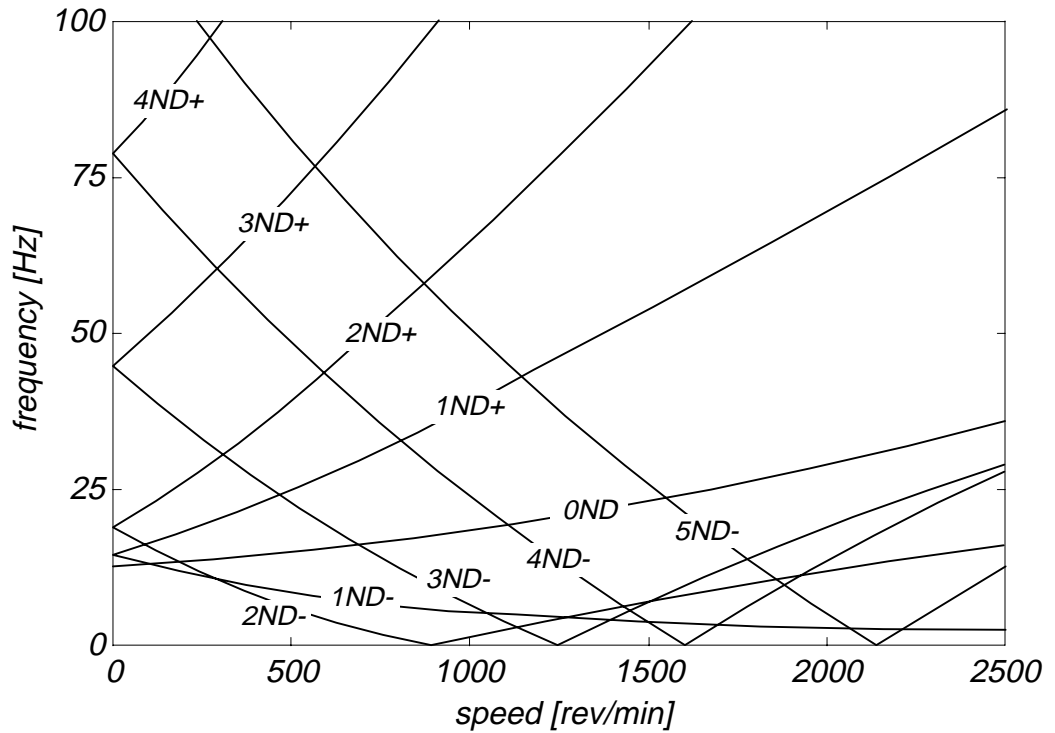


Figure 3-4: Computed natural frequencies of the travelling waves in the stationary frame of reference

The analytic predictions, Figure 3-4, compare favourably with the experimental results, Figure 3-5, where dark shades of grey indicate strong vibration signals.

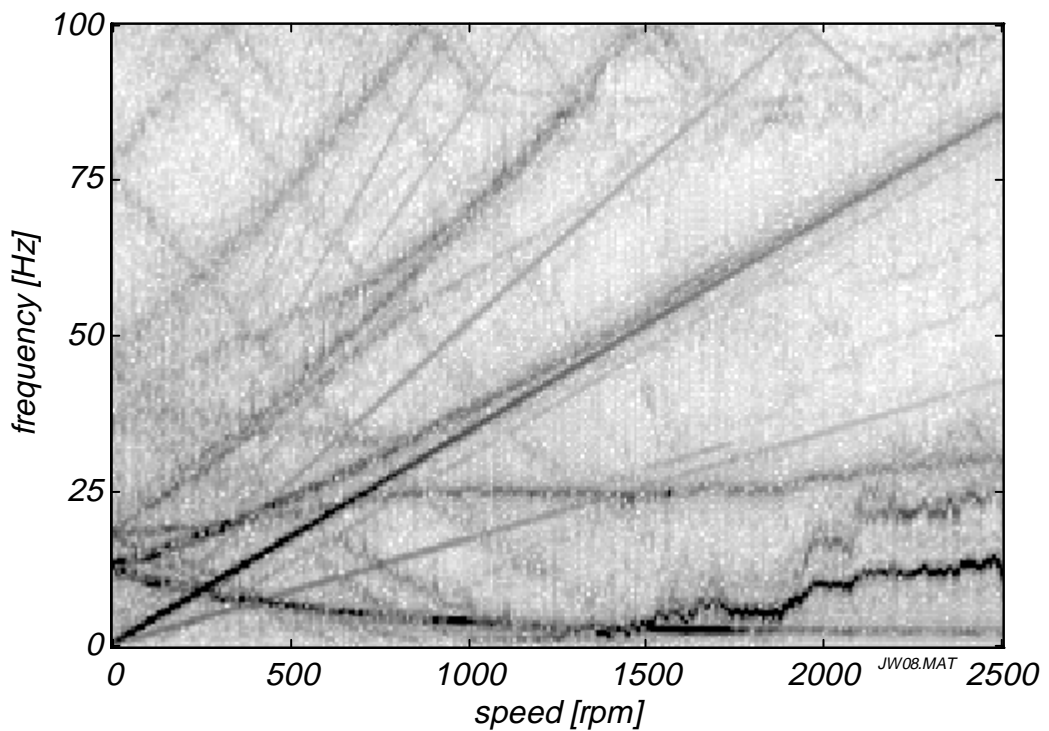


Figure 3-5: Measured natural frequencies of the travelling waves in the stationary frame of reference

The figure shows a spectrogram of the time record of a sensor facing the test disc. Each vertical line represents the magnitude of the Fourier transform of a short period of the time record.

In addition to the computed features shown in Figure 3-4, Figure 3-5 contains straight lines that all start at the origin but have different slopes. These are caused by the initial deformation or wobble of the rotor. In the body-fixed reference frame, this wobble is time-invariant, or one could say, it vibrates with 0 Hz. Due to the transformation of the frame of reference, these ‘vibrations’ change their frequency according to Equation (3-9):

$$\omega_{nSf} = 0 + n\Omega \quad (3-15)$$

where n is the number of nodal diameters. The initial deformation can be spatially Fourier-decomposed, and each component with different number of nodal diameters will show in the figure as a different line proportional to the speed of rotation, the engine-order lines.

The same mechanism makes time-invariant forces time-variant in the body-fixed frame of reference of the rotor.

3.1.4 Wave velocity

The slopes of the curves in Figure 3-2 and Figure 3-3 (and also Figure 3-4 and Figure 3-5) depend on the number of nodal diameters, n . Introducing the wave velocity, ν_n :

$$\nu_n \stackrel{def}{=} \omega_n / n \quad (3-16)$$

the relation between the wave velocities measured in the stationary and rotating reference frame is given by, Equation (3-9):

$$\begin{aligned} \nu_{nSf} &= \nu_{nRf} + \Omega \\ \nu_{nSb} &= \nu_{nRb} + \Omega \end{aligned} \quad (3-17)$$

and the engine-order speeds, Equation (3-13) just equal the wave velocities of the counter-rotating waves:

$$\Omega_{EO_n} = \nu_n \quad (3-18)$$

Figure 3-2, changes accordingly:

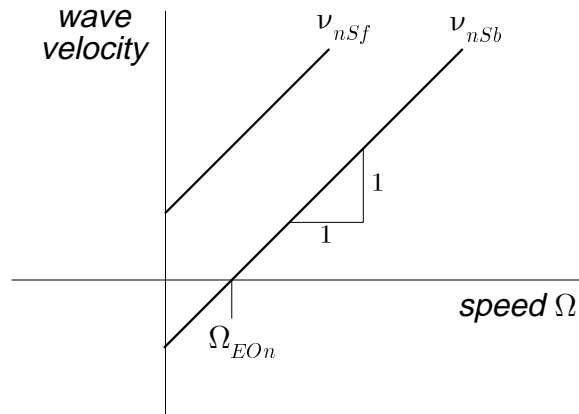


Figure 3-6: Wave-velocity diagram

In this representation all waves have a slope of 1:

$$\tan \alpha = \frac{\Delta v_{nSf}}{\Delta \Omega} = 1 \tag{3-19}$$

The predicted wave velocities of the rotating disc are shown in Figure 3-7, where once more the effect of the centrifugal forces bends the curves, changing the slope at higher speeds of rotation.

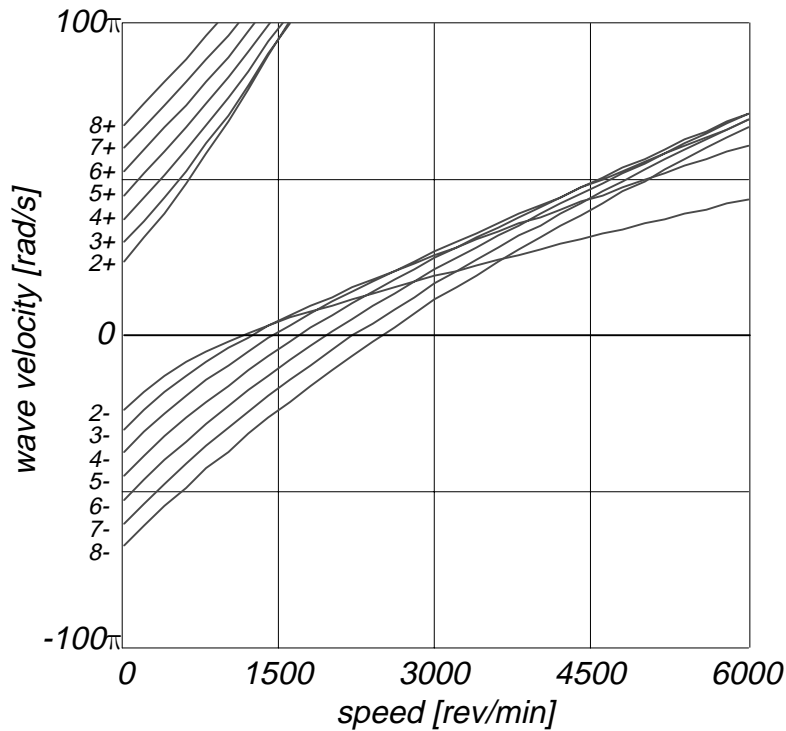


Figure 3-7: Wave-velocity diagram for the rotating disc

The figure is drawn to equal scale, so that the slopes at low speeds are drawn correctly. Centrifugal stiffening affects very quickly the two nodal diameter mode and changes the slope of the curve.

3.1.5 Sense of direction in the rotating and stationary reference frame

In the present analysis the axis of rotation is assumed to be the z -axis of the global coordinate system, Figure 3-1. In rotordynamics, as opposed to bladed disc analysis, the axis of rotation is usually assigned the x -axis.

Directions are defined in terms of the coordinate directions. A positive rotation will cause an increase in the tangential direction. This can be determined conveniently by the cross product of the right-hand cylindrical (r, θ, z) coordinate system, Equation (3-1):

$$\begin{Bmatrix} 0 \\ 0 \\ \Omega \end{Bmatrix} \times \begin{Bmatrix} r \\ 0 \\ 0 \end{Bmatrix} = + \begin{Bmatrix} 0 \\ r\Omega \\ 0 \end{Bmatrix} \quad (3-20)$$

When an elastic wave propagates through a body, its direction of travel is an important element in the description of the motion. In rotationally periodic structures the terms ‘forward’ and ‘backward’ are common but other combinations are used too, like ‘progressive’ and ‘retrogressive’ by Loewy and Khader, (1984). In this thesis, the terms *forward* and *backward* are used in the stationary frame of reference and *co-rotating* and *counter-rotating* are used in the rotating frame of reference. In the rotating frame of reference, a wave may propagate a finite angle during a period t , indicated in Figure 3-8 for the two nodal-diameter mode:

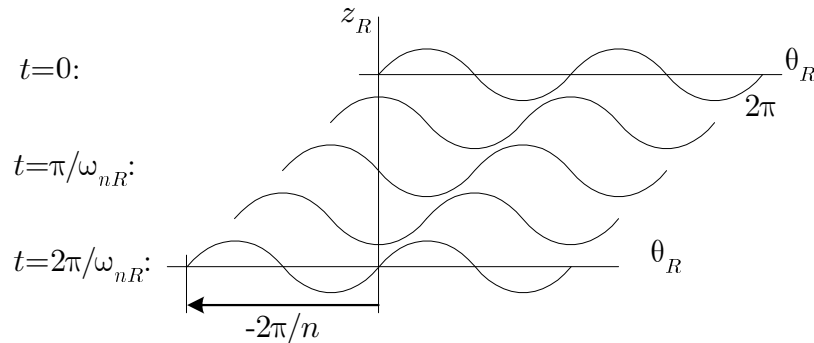


Figure 3-8: Determination of the wave velocity

The wave velocity can be computed from the indicated angle and time:

$$v_{nRb} = \frac{\Delta\theta_R}{\Delta t} = \frac{-2\pi/n}{2\pi/\omega_{nR}} = -\omega_{nR}/n \quad (3-21)$$

which, by its sign, indicates that the wave is a counter-rotating wave. The indices identify the wave velocity as the velocity of the n nodal-diameter, counter-rotating wave, that is the backward travelling wave in the rotating reference frame.

If the velocity of the wave in the stationary reference frame is to be determined, the speed of rotation has to be added to the wave velocity, Equation (3-17):

$$v_{nSb} = v_{nRb} + \Omega = -\omega_{nR}/n + \Omega \quad (3-22)$$

Index b in the rotating frame of reference denotes the counter-rotating wave, and does not necessarily indicate a backward travelling wave, Figure 3-9:

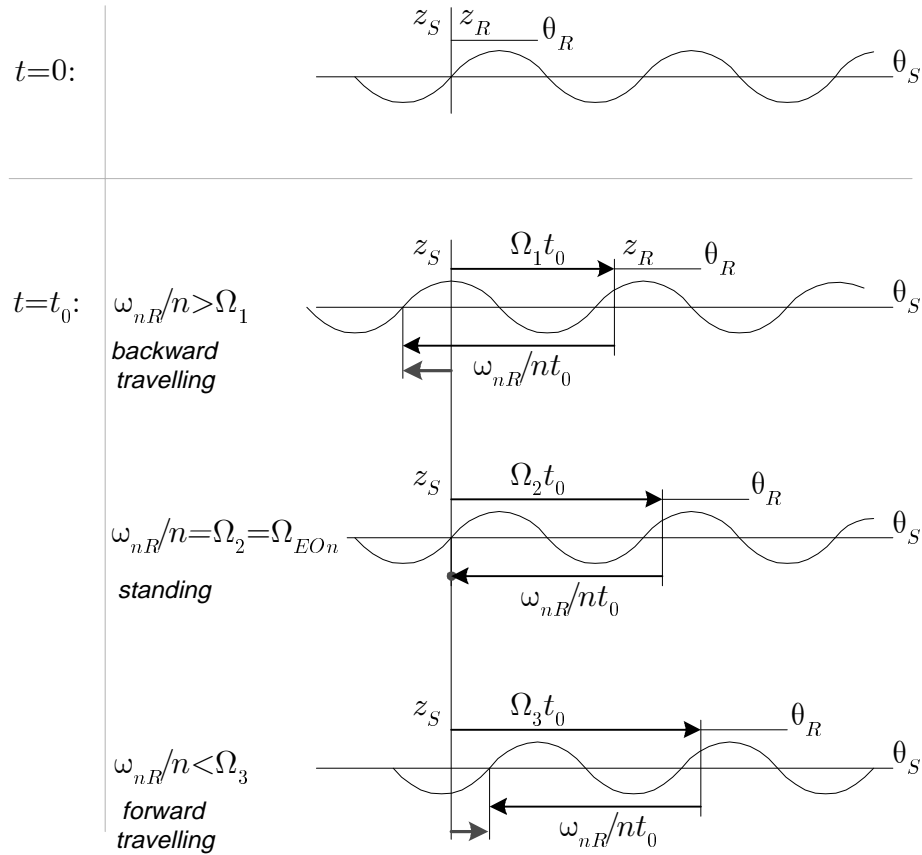


Figure 3-9: Direction of the counter-rotating wave in the stationary frame of reference

For some low speeds, $\Omega_1 < \Omega_2$, the counter-rotating wave is indeed a backward travelling wave in the stationary frame of reference, not changing its sign:

$$v_{nS} = v_{nRb} + \Omega_1 = -\omega_{nR} / n + \Omega_1 < 0 \tag{3-23}$$

At Ω_2 , the wave velocity is zero and the wave appears to stand still in space, hence the term *standing wave*:

$$v_{nS} = v_{nRb} + \Omega_2 = -\omega_{nR} / n + \Omega_{EOn} = 0 \tag{3-24}$$

The term ‘standing wave’ is used differently in the mathematical literature, where it describes the time-varying response of a real mode, (Bronstein and Semendjajew, 1981). Tobias and Arnold (1957) use the more accurate term *stationary wave*. Even though the wave is stationary in appearance, every particle of the rotor vibrates with the appropriate natural frequency. Ω_2 is the engine-order speed of the n nodal diameter mode, Equation (3-13).

For higher speeds, $\Omega_3 > \Omega_2$, the counter-rotating wave is actually progressing forward for a stationary observer and is a forward travelling wave:

$$v_{nS} = v_{nRb} + \Omega_3 = -\omega_{nR} / n + \Omega_3 > 0 \tag{3-25}$$

This can be depicted in a diagram of natural frequency against rotation speed, Figure 3-10.

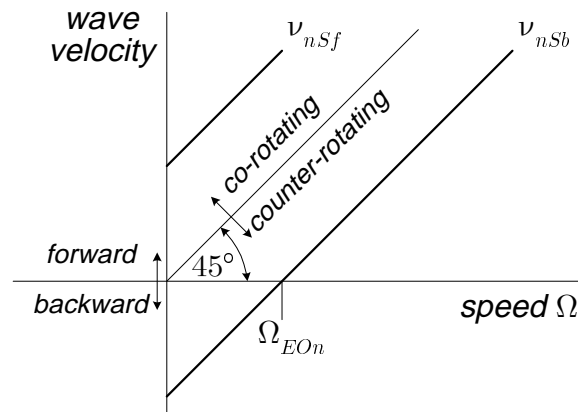


Figure 3-10: Wave velocity versus rotation speed explaining directional terms

Directly on the lines between the terms, the 45°-line and the speed axis, the waves are stationary or standing in the respective frame of reference: in the rotating reference frame, the standing wave is the static deformation of the disc and in the stationary reference frame, it is the counter-rotating wave in the rotor rotating at that particular engine-order speed. The co-rotating waves in the rotor are always travelling forward.

In the context of travelling waves and rotating machinery, the notion of negative frequencies and velocities is very useful and so the conventional simplification of neglecting the negative roots of the eigenvalues and taking the positive roots only as the natural frequencies, is actually not simplifying the description, but makes it, at times, less clear.

3.2 Interaction Diagram

In the diagrams in the previous section, the crossings of the speed axis at the engine-order speeds are pointed out to be of special significance. At those speeds, the apparent natural frequencies of the backward travelling waves in the stationary reference frame are zero and the structure is in resonance with time-invariant forces. The term ‘time-invariant’ is used instead of ‘stationary’ to avoid confusion with the use for the reference frames. At speeds different from the engine-order speeds the backward travelling waves can be excited by time-invariant forces, too, but, as they are not in resonance, the vibration level is much smaller, which will be explained in the following paragraph.

3.2.1 Travelling-wave-speed coincidence

The wave-velocity diagram, Figure 3-7, is drawn for the rotor alone, not showing the dynamics of the stator. The only line shown that does not belong to the rotor is the 0Hz line. Its crossings with the velocities of the counter-rotating waves determine the engine-order speeds, where the structure is excited into resonance by a time-invariant force in the

stationary frame of reference. The wave-velocity diagram, Figure 3-7, is now extended to include the wave velocities of the stator.

The stator is not experiencing the centrifugal forces and thus its dynamics are not speed dependent. In the wave-velocity-versus-speed diagram, they are shown as horizontal lines, Figure 3-11.

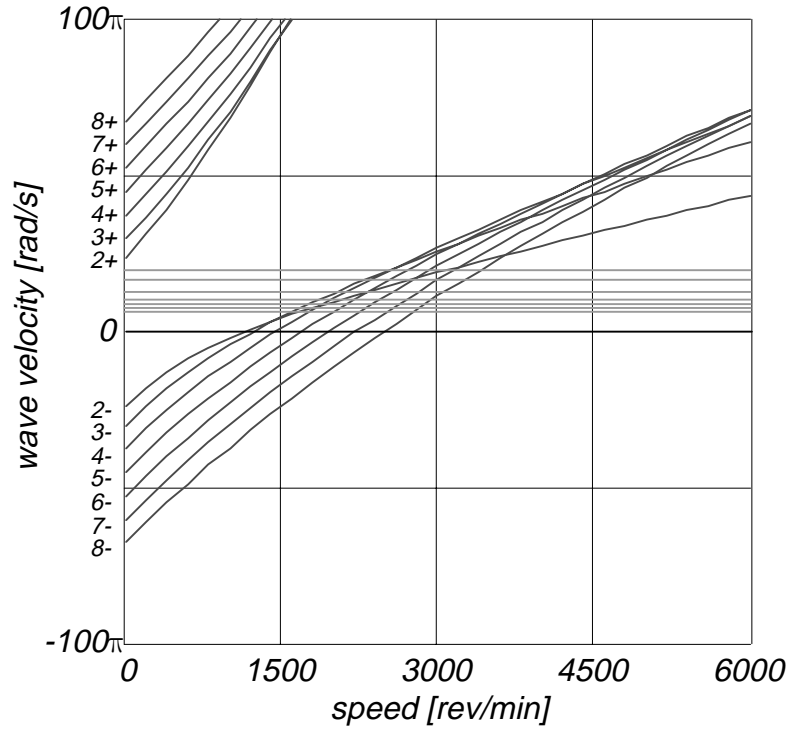


Figure 3-11: Wave velocity over speed for rotor and stator

In order to clarify some important aspects and increase the area of interest, only the waves

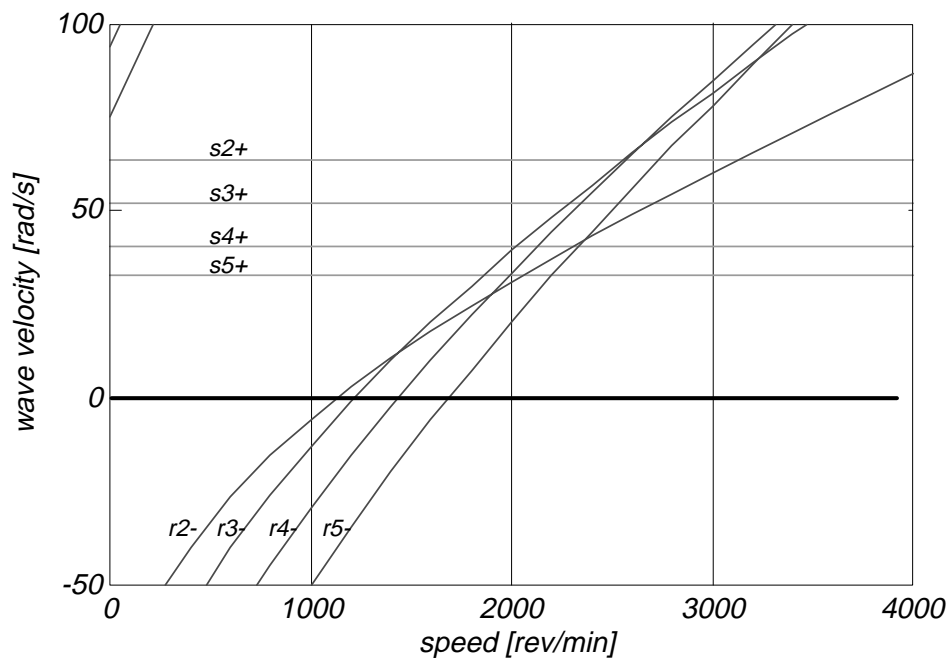


Figure 3-12: Detail of wave velocity over speed diagram

with 2 to 5 nodal diameters will be shown in the following plots and the equal axes constraint will be dropped, Figure 3-12.

r and s denote the rotor and stator quantities and ‘+’ and ‘-’ the direction of the waves. All crossings of rotor and stator natural frequency lines indicate speed-frequency combinations where both rotor and stator have the same natural frequency in the same frame of reference, Figure 3-12 in the stationary reference frame:

$$\omega_{rS} = \omega_{sS} \tag{3-26}$$

If the structures are excited at one of these frequencies, they are susceptible to large vibrations.

3.2.2 Critical Speeds

If the two structures are to contact each other, the vibration of the one would force the other structure. Assume that the rotor is vibrating predominantly in a counter-rotating wave, and is rotating at a speed where this wave’s natural frequency crosses a stator natural frequency. If the rotor is touching the stator under these circumstances, the stator experiences a force at one of its natural frequencies. The rotor will contact the stator initially at the crests of the waves and so the forcing pattern will repeat itself n times in the tangential direction. If the spatial patterns of force and stator wave are similar, the stator will respond strongly to this excitation. The following relations hold for waves:

$$\frac{1}{2\pi} \int_0^{2\pi} e^{in\theta} (e^{im\theta})^* d\theta = \begin{cases} 1 & n = m \\ 0 & n \neq m \end{cases} \tag{3-27}$$

which is a mathematical way of judging similarity between waves. In effect, it directly

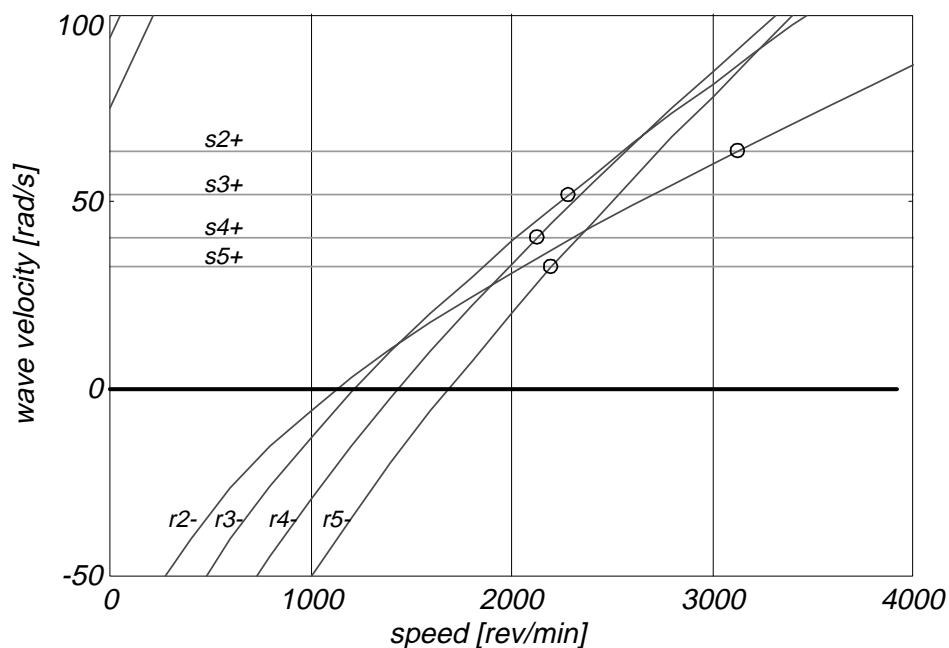


Figure 3-13: Critical travelling-wave-speed coincidences

shows the energy transfer between the forward travelling wave in the stator and the counter-rotating wave (the conjugate complex) in the rotor. If the units of the rotor wave are those of force and the stator wave has units of displacement, then the integrals in Equation (3-27) have the units of energy.

So, only the frequency-crossings of waves with the same number of nodal diameters have the potential of driving the coupled system into instability and are indicated by circles in Figure 3-13.

The crossings are called *critical points* in this thesis and occur at critical speeds, $\Omega_{crit,n}$, critical as they have the potential of driving the rotor-stator system unstable. The *critical speeds* are given by, (Schmiechen, 1994):

$$v_{rnSb} = v_{snSf} \quad (3-28)$$

or, remembering that v_{rnRb} is negative:

$$v_{rnRb} + \Omega_{crit,n} = v_{snSf} \quad (3-29)$$

This form of the derivation of these critical speeds is new in this thesis.

A critical speed diagram for an actual aircraft engine exhibits qualitatively the same features, Figure 3-14:

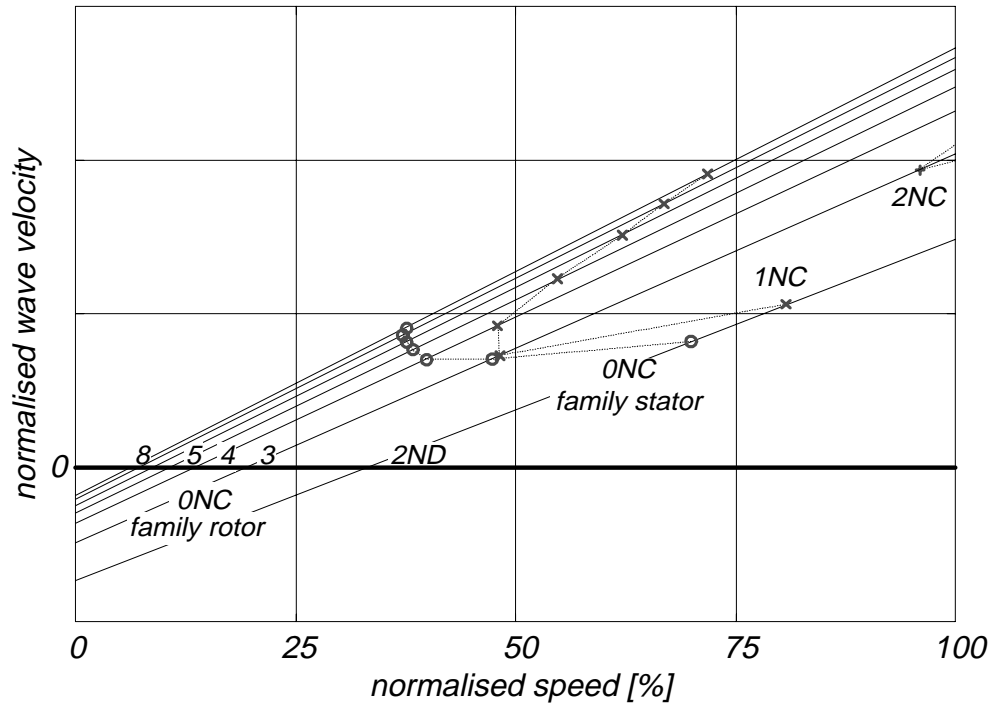


Figure 3-14: Wave-speed coincidence diagram of an aircraft engine

More critical speeds exist for all nodal-circle families of the rotor natural frequencies.

The equations of motion of the rotor and stator at these critical points are given by:

$$\begin{aligned} \ddot{p}_r + 2\zeta_r \omega_s \dot{p}_r + \omega_s^2 p_r &= f_{rs}(\omega_s, p_r, p_s) \\ \ddot{p}_s + 2\zeta_s \omega_s \dot{p}_s + \omega_s^2 p_s &= f_{sr}(\omega_s, p_r, p_s) \end{aligned} \quad (3-30)$$

where the principal coordinates in resonance are the complex counter-rotating wave in the rotor and the forward travelling wave in the stator. The frequency of the forcing functions is the natural frequency of these waves of the rotor and stator, and the shape of the forces will be related to the travelling waves in resonance. By Newton's Third Law:

$$f_{rs}(\omega_s) = -f_{sr}(\omega_s) \quad (3-31)$$

3.2.3 Energy transfer from one structure into the other

The coupling as described in the previous section by itself does not constitute a critical situation. Only if the energy of the coupled rotor-stator system increases with time, does the vibration become unstable.

3.2.3.1 Source of energy

An energy source in rotating machinery is the rotational energy of the rotor, and it will be shown in the subsequent paragraphs that at the identified critical speeds there exists a mechanism that feeds this rotational energy into the vibration energy of the coupled dynamics, Equation (3-30).

3.2.3.2 Coupling of the tangential and axial direction of a modeshape

The modeshapes of the bladed disc, Figure 2-2, are coupled, predominantly two-dimensional vibration patterns, if for simplicity, the radial components are neglected: the blade tip performs an elliptical motion during one vibration cycle, depicted in Figure 3-15 without showing the blade bending:

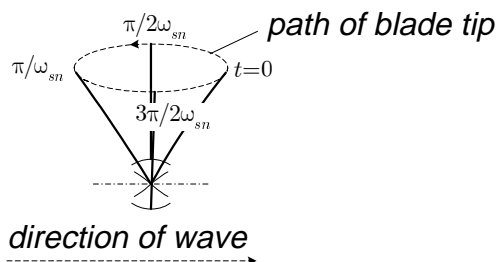


Figure 3-15: Motion of the blade tip

The blade tip is moving in the opposite direction to the forward travelling wave for the upper part of its cycle and in the same direction for the lower half.

The elliptical path of the blade tips changes with the modeshape. For the stator used in the experiments whose geometry is given in the Appendix, the two paths are shown in Figure 3-16, for different nodal diameters: the tangential semi-axis decreases with increasing number of nodal diameters. The axes in both plots are drawn to the same scale and are normalised to the two-nodal-diameter tangential deflection. The arrows indicate the direction of motion for a forward, to the right-hand side travelling wave in the structure.

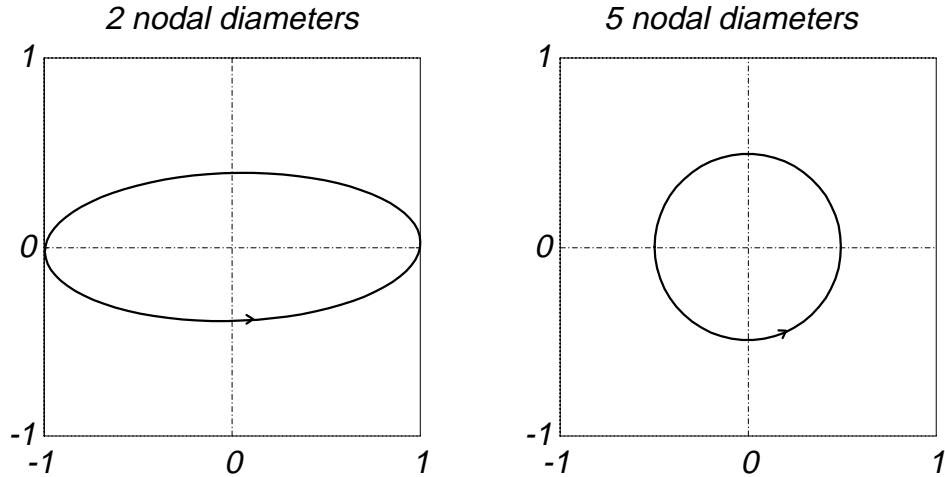


Figure 3-16: Path of the blade tip of the test stator for different nodal diameter waves

Figure 3-16 shows that the tangential and the axial vibrations are coupled and hence the ellipses grow in both axial and tangential directions simultaneously if energy is fed into the vibration of this mode.

3.2.3.3 Model of the contact force

A contact between rotor and stator at some speed of rotation causes a tangential force opposing the motion of the rotor: for a positive speed of rotation in the negative tangential direction. The friction force is modelled according to Coulomb's friction law:

$$F_t = -\text{sgn}(v)\mu F_n \quad (3-32)$$

where sgn is the signum-function, returning one for positive argument, minus one for negative arguments, and zero for an argument of zero. v is the relative velocity between the bodies in contact, μ is the dynamic coefficient of friction, which is generally speed dependent, and F_n and F_t are the normal and tangential force, respectively. During contact, the normal force must be always positive, and the surface velocity can be assumed to be positive, too, due to the large speed of rotation; in detail, the contact velocity depends on the speed of rotation, the contact radius and the vibration velocities of the two structures.

The stator experiences the reaction force in the positive tangential direction and one in the negative axial direction.

3.2.3.4 Integral of the energy input

Energy or work can be expressed as integral of force times displacement:

$$E_{cycle} = \int_{cycle} \{F\} \cdot \{dr\} = \int_{t_{cycle}} \{F\} \cdot \{v\} dt \quad (3-33)$$

where the dot denotes the scalar product between the force and the displacement/velocity vectors, basically saying that only the projection of the velocity vector onto the force vector contributes to the energy integral. Assuming a two-dimensional model with normal

and tangential directions and that energy is to be fed into the stator wave motion at the blade tips, the integral takes the specific form

$$E_{rs} = \int_0^{2\pi/\omega_r} (F_n v_n + F_t v_t) dt > 0 \tag{3-34}$$

The force-velocity products can be analysed separately.

From Figure 3-15, the following qualitative sketch of the normal components of the tip displacement, velocity and force can be drawn, Figure 3-17:

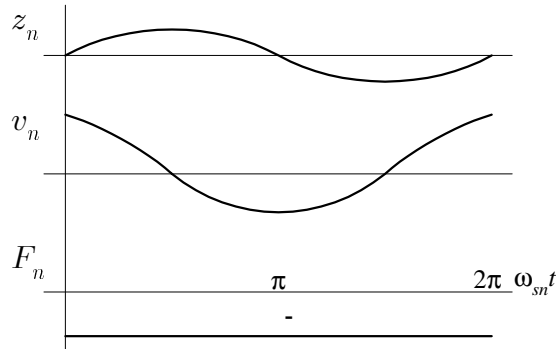


Figure 3-17: Normal velocity and force components

The integral of velocity times force over the intervals 0 to π and π to 2π is very small as the normal velocity changes sign half way through the interval, even if the actual magnitude is not constant.

The sketch of the velocity and force in the tangential direction is shown in Figure 3-18:

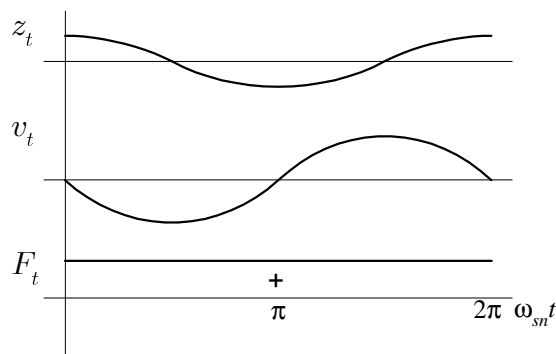


Figure 3-18: Tangential velocity and force components

For the tangential components, the integral of velocity times force does not vanish. For the top half cycle of the elliptical path of the tip, corresponding to the interval 0 to π , the energy is negative and for the bottom half, the interval from π to 2π , the energy is positive, velocity and force are acting in the same direction.

So, in order to feed energy into the stator, the contact between rotor and stator must occur during the bottom half cycle of the blade-tip motion.

3.2.3.5 Possible vibration pattern

A wave form in the rotor that provides contact between the rotor and the stator during the bottom half of the cycle according to Figure 3-15, is a travelling wave with the same number of nodal diameters as the stator, Figure 3-19. The small arrows denote the tangential velocity of the rotor disc and the blade tips, and the axial velocity of the stator disc.

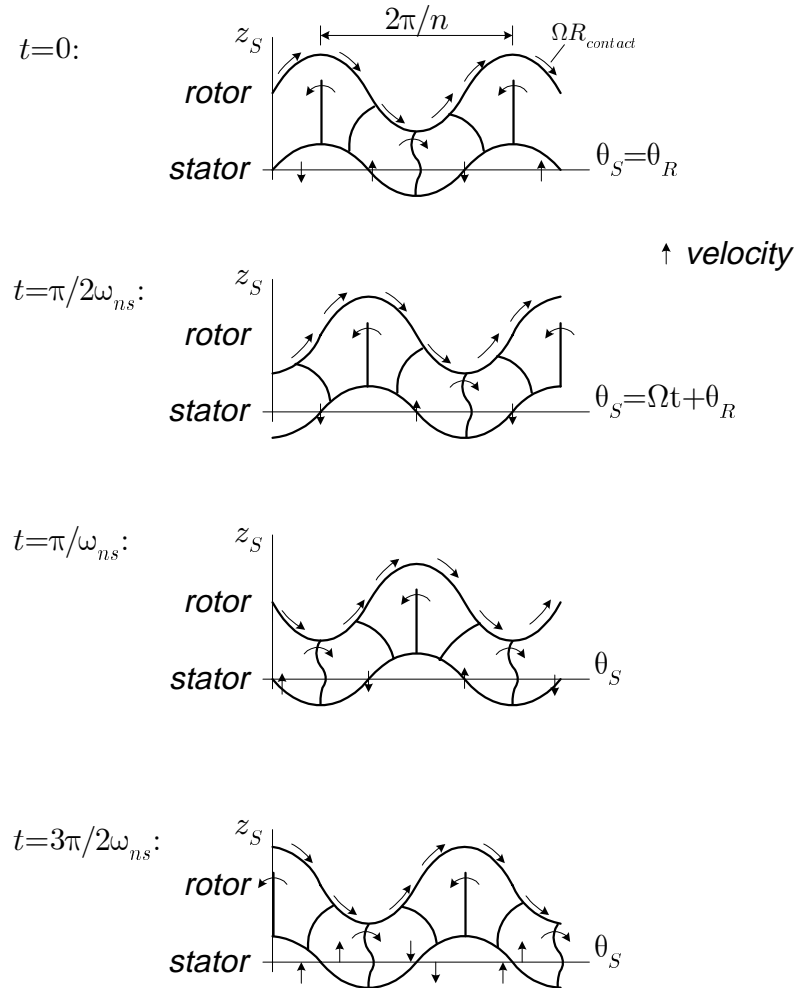


Figure 3-19: Contact cycle

To understand the cycle that drives the system unstable, follow the left blade in Figure 3-19: the blade swings freely back and hits the rotor that is vibrating in a counter-rotating wave progressing with the same absolute velocity as the forward travelling wave in the stator. The material points of the rotor progress with the speed of rotation which is higher than the wave velocity and drag the blade forward. For the next half cycle the blade and the rotor stay in contact. During this period, the tangential force and the tangential displacement are parallel and energy is fed into the stator, according to Equation (3-34). In the last picture, blade and rotor loose contact, just to start the cycle anew with a larger amplitude. At the same time n other blades go through the identical cycle, while the remaining blades adhere to a similar cycle but are phased differently.

In the schematic, Figure 3-19, the amplitude growth during the cycle is not shown and also, the exact contact times are possibly different from the ones given, but small deviations from the indicated times will affect the magnitude of the energy integral marginally.

The normal force does not contribute to the energy integral as explained before, Figure 3-18, but it is instrumental to the occurrence of the instability, as it is a prerequisite for the existence of the tangential force that feeds rotational energy into the system's vibration.

3.2.4 Balance of energy input and dissipation

In the absence of any energy dissipation, the energy input would drive the stator and hence the system unstable. Assuming that dissipation exists the vibration of a mode becomes unstable only, if the energy input is larger than the dissipation:

$$E_{rs} > E_{dissipation} \quad (3-35)$$

Energy dissipated by proportional damping, described by coefficients c_s or ζ_s , in one mode of the stator driven at its natural frequency can be computed to, e.g., Meirovitch, (1986):

$$E_{dissipation} = c_s \pi \omega_s (\phi_s \hat{p}_s)^2 = 2\omega_s^2 \zeta_s \pi (\phi_s \hat{p}_s)^2 > 0 \quad (3-36)$$

where \hat{p}_s is the amplitude of the principal coordinate and ϕ_s is the blade-tip component of the modeshape that is in resonance. Both the energy dissipation, $E_{dissipation}$, and the energy input, E_{rs} , grow with the amplitude of vibration as the vibration velocity and the contact force are both functions of the displacement. On a very simple, one-dimensional, linear calculation, the interaction energy can be roughly estimated to:

$$E_{rs} \approx \int_{0+t_0}^{\pi/\omega_s-t_0} \mu k_{rs} (\phi_{r,z} \hat{p}_r \sin \omega_s t - \phi_{s,z} \hat{p}_s \sin \omega_s t - z_0) \cdot (\omega_s \phi_{s,\theta} \hat{p}_s \sin \omega_s t) dt \quad (3-37)$$

where μ is the kinematic coefficient of friction, k_{rs} is the contact stiffness between the rotor and the blade tip, \hat{p}_i are the magnitudes of the principal coordinates, and $[t_0, \pi/\omega_s t_0]$ is the interval of contact, Figure 3-20.

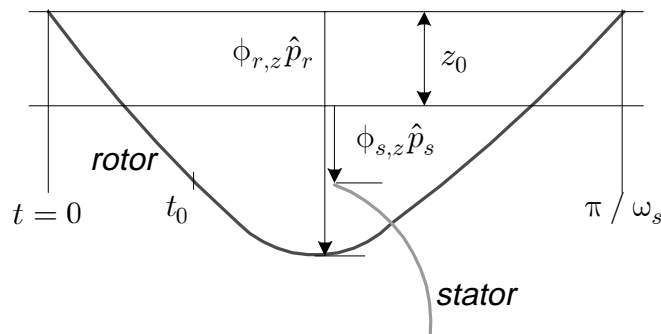


Figure 3-20: Approximation of geometry during interaction

t_0 can be computed to:

$$t_0 = \frac{1}{\omega_s} \sin^{-1} \left(\frac{z_0}{\phi_{r,z} \hat{p}_r - \phi_{s,z} \hat{p}_s} \right) \quad (3-38)$$

Assuming that $\phi_{s,\theta} \approx \phi_{s,z}$, Figure 3-15, and introducing the stator-to-rotor-amplitude ratio $\alpha = \phi_{s,z} \hat{p}_s / \phi_{r,z} \hat{p}_r$, one can find the following series approximation:

$$E_{rs} \approx \mu k_{rs} (\phi_{r,z} \hat{p}_r)^2 \alpha (1 - \alpha) \left(\pi - \frac{2}{3} \left(\frac{z_0}{\phi_{r,z} \hat{p}_r (1 - \alpha)} \right)^3 \right) + O \left(\left(\frac{z_0}{\phi_{r,z} \hat{p}_r (1 - \alpha)} \right)^5 \right) \quad (3-39)$$

where the fraction is always much smaller than 1 and already its third power can be neglected. Comparing $E_{dissipation}$, and E_{rs} , one can see that both are functions of the square of the amplitude. Whether the coupled system goes unstable or not depends on the coefficient of the amplitude:

$$\mu k_{rs} \alpha (1 - \alpha) > 2\omega_s^2 \zeta_s \quad (3-40)$$

Due to the simplicity of the assumptions, it is not sensible to derive exact conditions from this equation. Qualitatively, one can conclude that the low-frequency modes will go unstable more easily than the high-frequency modes but one has to keep in mind that the interface stiffness is a function of the frequency as well.

The origin of the energy flowing into the stator from the rotor is the rotational energy and hence the vibration energy of the system increases if Equation (3-40) holds.

3.2.5 Effect of mistuning on the energy transfer

The above discussion of the interaction and in particular the analysis of the contact geometry assumed that the responses in both structures are travelling waves. This happens to be possible for rotationally periodic structures but is not the case for mistuned structures. For the understanding of the effect that mistuning has on the energy transfer, it is sufficient to assume that one structure, either rotor or stator, is mistuned. The responses of two modes of a mistuned structure do not add up to a purely travelling wave any more, but there will always remain a standing, body-fixed wave component. In the case of a excitation of the rotor by a stationary force, the response sums as follows:

$$\begin{aligned} u &= u_1 + u_2 \propto H_1(\omega) \cos \omega t \cos n\theta + H_2(\omega) \sin \omega t \sin n\theta \\ &= H_1 \cos(n\theta - \omega t) + (H_2(\omega) - H_1(\omega)) \sin n\theta \sin \omega t \end{aligned} \quad (3-41)$$

The first part is the travelling wave component and the second part is the standing wave component, Figure 3-21, drawn for 1% damping.

The frequency ratio of the abscissa is the ratio between the excitation frequency and the mean of the two natural frequencies of the mode pair. Mistuning is defined in this thesis as

$$\text{mistuning} = \frac{\omega_2 - \omega_1}{\frac{1}{2}(\omega_2 + \omega_1)} \quad (3-42)$$

where the natural frequencies are those of the two modes of the mistuned structure. If the mistuning is introduced deliberately by adding mass to the structure, the mean frequency in the denominator will be lower than the natural frequency of the original, tuned, system.

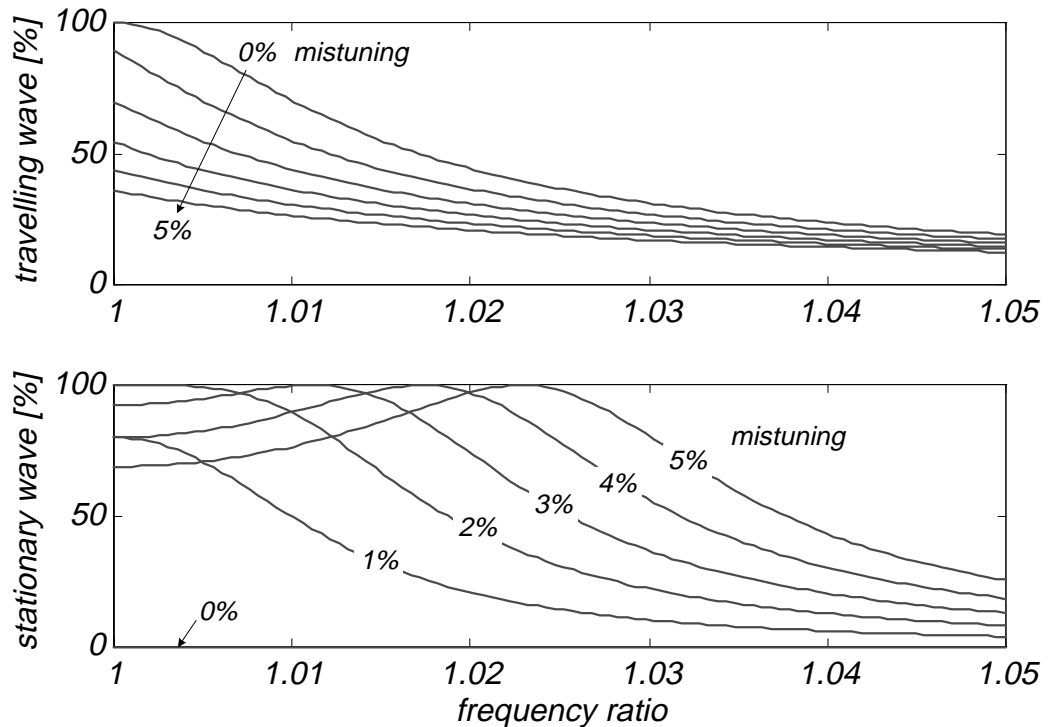


Figure 3-21: The effect of mistuning on the wave components, 1% damping

The travelling wave component of the mistuned structure reduces sharply with increasing levels of mistuning and thus the amount of energy transferred in one cycle is reduced. More significantly, the standing wave component, which is zero for tuned structures only and increases rapidly with the degree of mistuning, Figure 3-21, is body-fixed and hence disturbs the sequence of events depicted in Figure 3-19, by modulating the zero line of the mistuned structure. This reduces further the energy-transfer, possibly to levels controlled by damping. Hence mistuning is the prime and most effective way of reducing the energy transfer and avoiding the travelling-wave-speed instability.

Reducing damping reduces the energy dissipation which is, in the light of instability not desirable. Interestingly, low damping reduces the chance of the occurrence of the travelling-wave-speed instability by reducing the possibility of forming a travelling wave: at low levels of damping the frequency response function peaks very sharply at the modes and decays very quickly for frequencies away from the natural frequencies. Hence the travelling wave which is a combination of the responses of the two modes diminishes for all frequencies for the mistuned, low-damped, system, Figure 3-22.

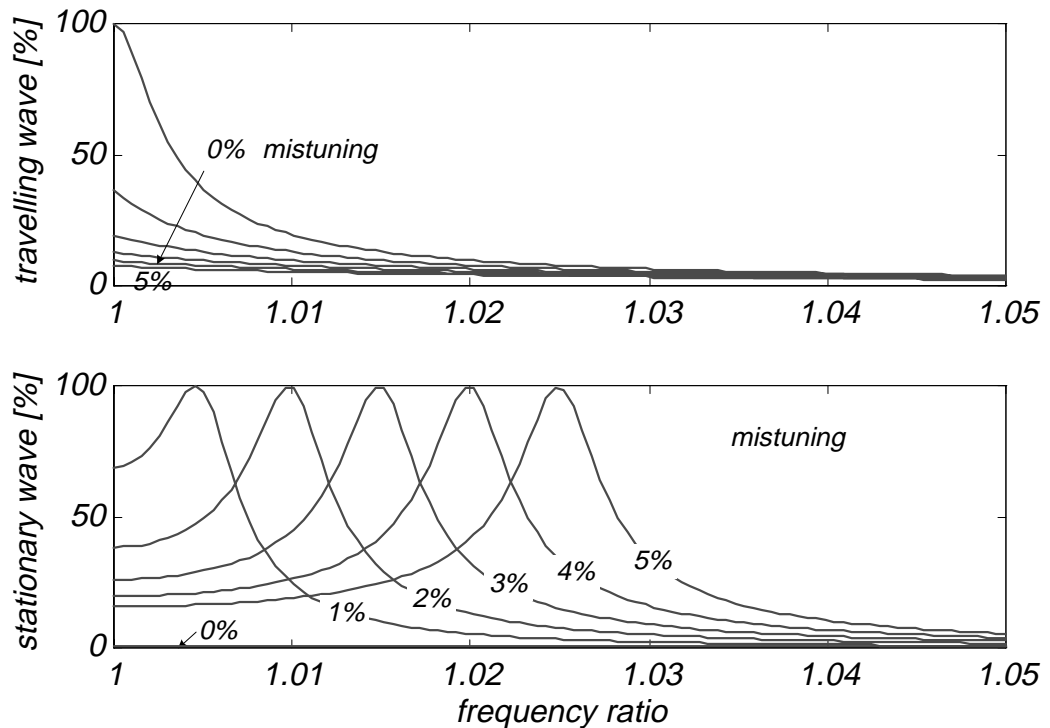


Figure 3-22: The effect of mistuning on the wave components, 0.2% damping

Tobias and Arnold (1957) noted that the aerodynamic forces damp the forward travelling wave. This is caused, it can be argued by the relative velocity between the rotating structure and the surrounding fluid. A stationary wave in space has no surface velocity and thus cannot be damped by aerodynamic effects. Similarly, acoustic radiation, related to the normal surface velocity, is a minimum for a stationary wave, which is noticed during the experiments presented in Chapter 7. Tobias and Arnold were confronted with the paradox of having the forward travelling wave affected by aerodynamic damping only, as they assumed real principal coordinates. If complex principal coordinates – waves – are used in the analysis, the paradox does not exist.

3.3 Discussion

In this chapter the interaction of the two structures, rotor and stator, has been investigated. New critical speeds are discovered at which both structures are in resonance. At those speeds, a counter-rotating wave of the rotor and a forward travelling wave of the stator of the same number of nodal diameters can interact and drive the coupled system unstable.

This is a new feature, not explored in this way before and, together with the experimental proof in Chapter 7, forms the main result of this thesis.

The existence of these critical points and the explanation of the energy transfer has been motivated from basic vibrations theory. An energy balance between energy input and dissipation is devised, but has to remain of questionable practical application due to the extreme simplifications. The interaction must be assumed to go unstable for typical damping levels present in turbo-machines.

The existence of the identified critical points in the normal range of operation should cause some concern among the designers of turbo-machinery.

The following chapters will investigate this instability both numerically and experimentally. The concepts developed in this chapter influenced the design of the numerical integrator but also the experimental set-up, and vice versa.

Chapter 4: Numerical Simulation of the Interaction

In the course of the study it became evident that a closed-form solution to the coupled interaction problem could not be achieved and so a numerical approach was pursued.

4.1 Problem Description

The difficulty of finding a closed-form solution lay to some extent in the complexity of the structures but mostly in the intermittent and nonlinear nature of the contact forces. During contact, these forces couple the structures and change their dynamic behaviour to that of the coupled system. The contact locations change with time, making the problem analytically intractable.

Thus, efforts were concentrated on developing a numerical simulation of the problem. Advantages of a numerical simulation are: (*i*) that no physical structure needs to be available, so the simulation can be carried out at the design stage, and (*ii*) the relative ease with which parameter studies can be conducted. Changing a structural parameter like the damping in an experimental set-up can be very tedious whereas in a simulation it requires a change of value of a (matrix-) variable only. The simulation can be supplied with data from an experiment (but see (*i*)) or from a preceding analysis, or from both. Another advantage is the output possible from a simulation: time traces of the deflection at any point of the structures in any reference frame, velocities and accelerations, contact times and forces, to name but a few. To gather the same information in an experiment would require a much greater effort, especially if it involved measurements in the rotating frame of reference.

In order to fulfil its purpose, a mathematical model must be able to reproduce measured data from a test rig. After the model has been validated in such a way, it can be used to conduct parameter studies with confidence for a certain range of the parameters. Beyond these ranges, the model may yield inaccurate results as the modelling errors increase.

4.2 Statement of Objective

The mathematical model to be developed shall be able to predict accurately the dynamic behaviour of the coupled rotor-stator system. By that it is understood that the model shall be able to predict the positions and velocities of arbitrary points of both structures as functions of time.

4.3 Mathematical Model of the Rotor-Stator System

In order to describe the travelling wave speed coincidence mathematically, the model must include the dynamics of the individual structures and the contact dynamics.

4.3.1 Steps in the modelling process

The necessary steps to obtain a mathematical model include: the determination of the system boundaries; the abstraction of the physical model; the introduction of simplifications to keep the model manageable; and, for continuous systems, discretisation in the spatial domain. Each of these steps will be detailed in the following paragraphs.

4.3.1.1 System boundaries

Introducing system boundaries separates the problem from its environment that it is embedded in: the original problem of describing a structure and its environment is changed to the description of the dynamics of the structure and the description of the boundaries.

These fictitious system boundaries can be drawn everywhere, but physical insight into the problem will help to solve the subsequent problems more easily. If the system boundaries cut through areas with complex coupling, the description of the boundaries, possibly functions of time themselves, may become very complex and may reduce the benefits gained from introducing the boundaries in the first place.

4.3.1.2 Abstraction

After the system's boundaries have been defined, the system dynamics must be derived. For a complex system this is usually done by breaking down the system into smaller sub-systems with known solutions. This process continues until the solutions to all (sub-) sub-systems are known. These solutions are then combined to yield a solution of the assembly.

Many different elements in physics and engineering exhibit the capability to store, transfer, or transform a quantity such as energy. The model of a system can be moved from its original domain into an abstract domain to clarify the task of each of its elements. The domain in which the abstraction is made, for example mechanical or electrical, is arbitrary and will strongly depend on various considerations, including past experience and the tools available, (Karnopp and Rosenberg, 1968).

4.3.1.3 Simplification

The general goal of the process of simplification is to reduce the order and complexity of the problem without changing its essential physics: in our case, its dynamics.

In the case of engineering structures, manufacturing tolerances will result in small deviations of the geometry and hence the dynamics of each part of a series built to the same, nominal, specifications will vary. For example, the dynamic properties of joints such as screws and rivets are highly affected by differences in geometry, and, as joints are the major source of damping in engineering steel structures, these structures' characteristics can change dramatically due to subtle geometric changes. One simplification is to start from the design data, ignoring the manufacturing differences.

Assumptions regarding the type of damping or the magnitudes of any other unknown factors will lead to further simplifications. Modelling a structure by using idealised simple shapes, such as beams of uniform cross section (which make the problem amenable to analytical solutions), is another case of simplification.

It is important to validate and to justify any of these simplifications. The objective of simplification is to obtain a manageable model that represents the system under investigation. If the model is neither manageable nor representing the system properly, then the effort was spent in vain.

4.3.1.4 Discretisation

Closed-form solutions exist only for the simplest of continuous structures. More complex structures are discretised spatially and the solution is computed at a finite number of points only. The set of points is commonly called the mesh and the considered displacements of these mesh points are the *degrees of freedom*. The solution at other points of the structure must be obtained by interpolating the results of neighbouring points.

Generally, the results of calculations based on the discretised structure depend on the mesh, its detail and topology. The problem of mesh generation cannot be solved deterministically and the mesh will need to be refined continuously with as much physical insight into the problem as is available at any time.

4.3.2 Models of the individual structures

Following the analytical models of Chapter 2, the individual components are modelled as structures with *linear, time-invariant dynamics*. The rotor is modelled as a rotating disc of uniform thickness with a central hole, and the stator is modelled as a stationary bladed disc of uniform thickness with identical blades around the perimeter.

The idealised models will be presented first, followed by a description of the difficulties arising from physical imperfections.

4.3.2.1 Rotor

The rotor is modelled as a thin disc using Kirchhoff theory for thin plates (e. g. Szabó 1956). Due to *centrifugal stiffening* caused by the additional in-plane, membrane stresses causing, the natural frequencies of rotating structures increase with speed of rotation, (Lamb and Southwell, 1921). The effect of the rotation on the modeshapes is neglected in the simulation.

For an axisymmetric disc of uniform thickness there exists a closed-form solution, (Szabó, 1956). Already, a central hole makes the problem intractable analytically, and approximate or tabulated values must be used, (Blevins, 1984). Following St. Venant's Principle, by neglecting the effects of the hole, the solutions of slender discs with small

thickness-to-diameter ratios and inner radii much smaller than the outer radii will approximate those of discs without a hole.

Due to the continuity of physical structures, the modeshapes of axisymmetric structures must be harmonic functions in the tangential direction, characterised by the number of periods or *nodal diameters*, n , (Tobias and Arnold, 1957).

Most modes of the disc occur in pairs due to the axisymmetry. Both modes of such a pair have the same eigenvalue and the modeshapes are similar but rotated around the axis of symmetry by $\pi/2n$. Modes with zero nodal diameters do not occur in pairs but are single modes.

For the simple structure used as rotor in the study, the modeshapes are known analytically, but for more complex structures they will be obtained from a finite element computation.

4.3.2.2 Stator

The stator is modelled as a thin disc, just like the rotor. The blades which are modelled as beams or, more accurately, as two-dimensional shells, are equally spaced around the perimeter of the disc, making the overall structure rotationally-periodic rather than axi- or cyclic symmetric.

Again, the modeshapes must be continuous and the modes can be characterised by the dominant number of nodal diameters, n , while smaller components with other numbers of nodal diameters will always be present. By design, the coupling in the investigated bladed disc is dominant between the axial motion of the disc and the bending or flap vibration of the blades. In the vicinity of the bending modes of the blades, the blades act like tuned-mass absorbers and the deflections in the disc diminish and the eigenvalues of the coupled structure approach the cantilever bending frequencies in these cases.

4.3.2.3 Modelling of Mistuning

The above comments on the dynamics of the rotor and the stator hold for perfectly periodic or *tuned structures* only. If the blades have slightly different dynamics due to manufacturing or material tolerances, or if the discs are not of uniform thickness, the structures are said to be mistuned. The modeshapes cannot be separated in tangential and radial directions any longer and the description of their dynamics generally becomes more complex. For small amounts of mistuning only, the structures can still be approximated as tuned structures: the natural frequencies of the mode pairs split and the modeshapes can be approximated by their dominant spatial Fourier components.

Tuned structures can be modelled analytically, but if mistuning is to be included in the model, the dynamic characteristics will be obtained generally by the method of finite elements. The solution of an FE model provides the modal matrix $[\Phi]$ and eigenvalues $[\lambda_r]$ of that model. Most FE programs will not treat damping and so the diagonal non-zero elements of the assumed modal damping matrix $[\zeta_r]$ must be either identified from

measured data or, more likely, set to a nominal value. If extensive measured data are available, the experimental modal matrix could be used in preference to one obtained from an FE analysis. Obviously, measured data will only be available for structures which already exist and thus cannot be used in the design stage.

4.3.3 Model of the contact forces

The forces of particular interest in this study are the contact forces acting between the blade tips and the rotor. These forces are intermittent and nonlinear in nature, making the whole problem nonlinear. In the force computation the following assumptions are made, and their validity explored in detail:

- the contact is assumed to occur at the blade tips only;
- the axial force is described as a function of both interference and its time-derivative;
- Coulomb's friction law defines the tangential force; and that
- the high-frequency impact dynamics are captured by the integration scheme.

4.3.3.1 Points of contact

From the geometry of the problem it is safe to say that the contact would occur only at the blade tips. One or more blades may be in contact at any time.

4.3.3.2 Determination of the axial force

A complex model of the axial force is developed to include advanced features. In a very simple, preliminary model, the axial force is assumed to be proportional to the axial interference at the contact points:

$$\begin{aligned} \{\Delta z\} &= \{z_r\} - \{z_s\} + z_0 \\ \{f_z\}_i &= \begin{cases} k_{rs} \{\Delta z\}_i & \{\Delta z\}_i > 0 \\ 0 & \{\Delta z\}_i \leq 0 \end{cases} \end{aligned} \quad (4-1)$$

where an initial gap, z_0 , is taken into account. A contact force exists only for positive interference. The interference is calculated from the displacements in the z -direction only. Other approaches to calculate the contact force are possible, such as taking the normal distance or any other measure involving the deflections of rotor and stator, but these necessitate the introduction of further assumptions. The accuracy of the presented approach should be sufficiently accurate for small interferences.

The simple force expression is not differentiable at zero interference, a feature that can cause problems for the numerical integration routine. In order to avoid problems of that type, a stiffness force proportional to the square of the interference is introduced around the zero point which continues linearly after some transition value Δz_{lin} :

$$\{f_z\}_i = \begin{cases} k_{rs} (\{\Delta z\}_i - \Delta z_{lin}/2) & \{\Delta z\}_i > \Delta z_{lin} \\ \frac{k_{rs}}{2} \frac{\{\Delta z\}_i^2}{\Delta z_{lin}} & \{\Delta z\}_i \in [0, \Delta z_{lin}] \\ 0 & \{\Delta z\}_i \leq 0 \end{cases} \quad (4-2)$$

The model is further refined by the inclusion of a loss factor for the impact. This is accomplished by extending the contact force to be a function of the interference and the relative velocity, generally $F = f(\Delta z, \Delta \dot{z})$. Effectively, this replaces the constant stiffness in Equation (4-2) by a velocity-dependent one:

$$k'_{rs} := k_{rs} e^{-d\Delta \dot{z}} \quad (4-3)$$

where d is a parameter defining the loss factor of the impact.

The development of the contact force from a linear function of the interference over a smooth function in the derivative to a smooth, dissipative force function is shown for a sinusoidal interference in Figure 4-1.

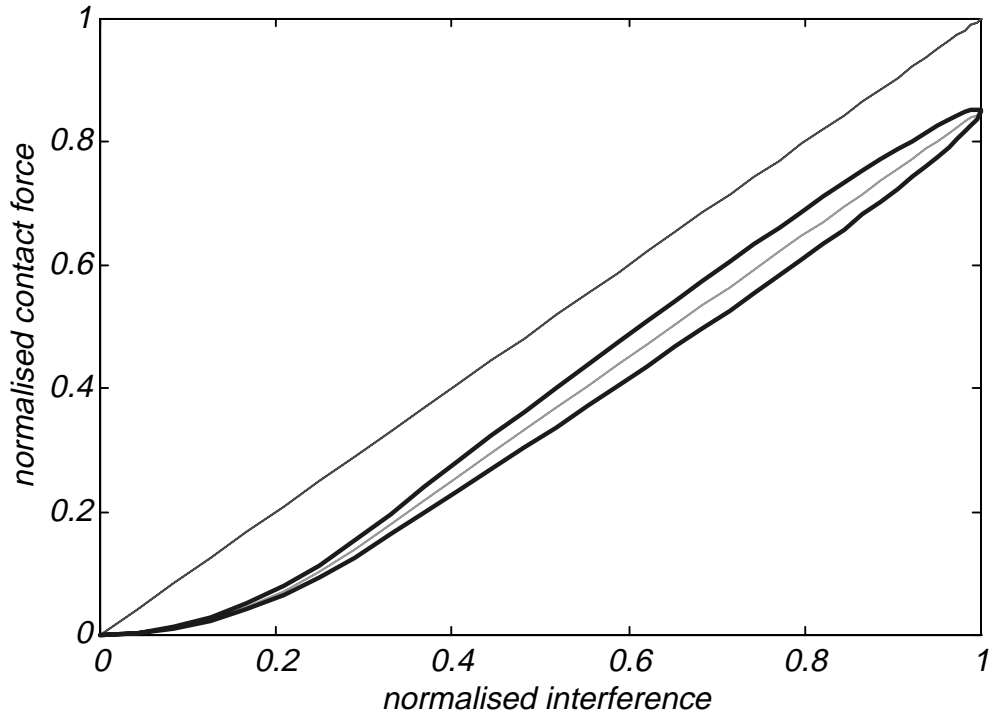


Figure 4-1: Displacement- and speed-dependent contact force

Fumigalli and Schweitzer (1996) pointed out that only a nonlinear interference-force relation would guarantee physically valid models. Both their model and the model presented here ensure that the impact force remains always positive. The area encircled by the thicker line in Figure 4-1 is proportional to the energy dissipated during one impact for the nonlinear model.

The contact force expression could be modified further to give a non-zero force for 'negative' interferences. Physically, this could be justified by the assumption that the airflow around the rotor excites the stator before actual contact.

4.3.3.3 Tangential force model

The difficulty in determining the correct friction law lies in the difficulty of understanding the contact dynamics. Even after the mechanism is understood, it remains to identify the parameters of the model. Especially for the simulation of a non-existing structure, such as one that is currently in its design stage, it will require a great deal of expertise to choose the right parameter set. For these reasons, Coulomb's law of friction is used frequently in engineering analysis. It relies on a single coefficient, the kinematic coefficient of friction, relating the friction force to the relative velocity at the interface:

$$F_t = -\text{sgn}(v)\mu F_n \quad (4-4)$$

where sgn is the signum-function returning one for positive arguments, zero for an argument of zero, and minus one for negative arguments. Although originally only intended for a small class of rigid body contacts, the Coulomb friction model has been found to represent a wide range of contact problems quite well.

In the literature, a speed dependency of the friction coefficient is cited, (Stelter, 1996), but for the current problem it was decided that the coefficient of friction can be taken to be constant as the contact velocity was assumed to vary only slightly around 80m/s.

4.4 Formulation of the Dynamics

The abstract model of the structures and their interaction was presented in the preceding section. The remaining task is to solve the coupled problem by combining the solutions of the sub-problems. To do this, a mathematical formulation of the problem is derived and manipulated to render it amenable to numerical solution methods.

4.4.1 Equations of motion

The problem formulation for the dynamics of a continuous system leads to one or more partial differential equations. The spatial discretisation transforms these equations into a system of ordinary differential equations, presented compactly as a vector equation, where the size of the vectors depends on the detail of the discretisation, and can rise to the tens of thousands in today's modelling practises. The form of the equations of motion for a discretised system is:

$$\begin{aligned} [M_r]\{\ddot{u}_r\} + [C_r]\{\dot{u}_r\} + [K_r]\{u_r\} &= \{f_{rs}\} \\ [M_s]\{\ddot{u}_s\} + [C_s]\{\dot{u}_s\} + [K_s]\{u_s\} &= \{f_{sr}\} \end{aligned} \quad (4-5)$$

or more compactly:

$$\begin{bmatrix} M_r & 0 \\ 0 & M_s \end{bmatrix} \begin{Bmatrix} \ddot{u}_r \\ \ddot{u}_s \end{Bmatrix} + \begin{bmatrix} C_r & 0 \\ 0 & C_s \end{bmatrix} \begin{Bmatrix} \dot{u}_r \\ \dot{u}_s \end{Bmatrix} + \begin{bmatrix} K_r & 0 \\ 0 & K_s \end{bmatrix} \begin{Bmatrix} u_r \\ u_s \end{Bmatrix} = \begin{Bmatrix} f_{rs} \\ f_{sr} \end{Bmatrix} \quad (4-6)$$

$$[M]\{\ddot{u}_{r+s}\} + [C]\{\dot{u}_{r+s}\} + [K]\{u_{r+s}\} = \{f_u\} \quad (4-7)$$

where $[0]$ is the zero matrix, dots indicate differentiation with respect to time t , $\{u_i\}$ is the vector of the degrees of freedom, and the indices r , s , and $r+s$ denote quantities of the rotor, stator, and both structures, respectively. Thus, $\{u_{r+s}\}$ and its derivatives describe the dynamic motion of the system completely. The mass, damping, and stiffness matrices of each structure, $[M_i]$, $[C_i]$, and $[K_i]$, are generally fully populated and the quantities without subscripts are easily recognised as combinations of the properties of both structures.

The task now is to solve Equation (4-7) for the unknown vector $\{u_{r+s}\}$ for arbitrary initial conditions. The right-hand side, $\{f_u\}$, introduces the coupling between the two structures: $\{f_{rs}\}$ is the force exerted on the rotor by the stator, and $\{f_{sr}\}$ is that exerted on the stator by the rotor. If there is no external forcing, then, by Newton's Third Law:

$$\{f_{rs}\} = -\{f_{sr}\} \quad (4-8)$$

Generally, the forces can be functions of the degrees of freedom, their time-derivatives, and time itself explicitly:

$$\{f_u\} = f(u_{r+s}, \dot{u}_{r+s}, t) \quad (4-9)$$

In the simulation the forces will be assumed not to depend on time explicitly, making the set of equations autonomous. This difference is important for closed-form solutions of differential equations, (Jordan and Smith, 1992), but it sometimes influences the strategy of the numerical solver as well.

4.4.2 Standard form of integration

The problem as formulated is not in a standard form for autonomous systems as required by most solvers:

$$\{\dot{u}\} = f(\{u\}) \quad (4-10)$$

where f is an arbitrary vector-valued function, not to be confused with the force-vector, $\{f_u\}$, and $\{u\}$ is the state vector. Problems in structural dynamics, after spatial discretisation, lead usually to second-order ordinary differential equations in time, Equation (4-7):

$$\{\ddot{u}\} = f(\{u\}, \{\dot{u}\}) \quad (4-11)$$

4.4.2.1 Transformation of the equations of motion to standard form

To cast the differential equations, Equation (4-7), into standard form requires the formation of a state vector that includes the degrees of freedom and their time derivatives:

$$\{u\} = \begin{Bmatrix} \{u_{r+s}\} \\ \{\dot{u}_{r+s}\} \end{Bmatrix} \quad (4-12)$$

With this state vector, Equation (4-7) can be rewritten into the standard form:

$$\{\dot{u}\} = \begin{bmatrix} \mathbf{I} & 0 \\ 0 & \mathbf{M} \end{bmatrix}^{-1} \left(\begin{bmatrix} 0 & \mathbf{I} \\ -\mathbf{K} & -\mathbf{C} \end{bmatrix} \{u\} + \begin{Bmatrix} 0 \\ f_u \end{Bmatrix} \right) \quad (4-13)$$

where $[\mathbf{I}]$ is the identity matrix. Translating the problem into state space increases its order by a factor of two.

4.4.2.2 Transformation to principal coordinates

Equation (4-13) can be supplied to the solver, which, starting from initial conditions would integrate the equations and output the state vector at discrete times. This proves to be very expensive computationally and a further transformation is introduced. For the integration of the equations of motion, the direct formulation, Equation (4-13) is not very well suited. The computationally-expensive full matrix inversion and multiplications can be avoided if modal decompositions of the individual structures are available. The following paragraphs describe the application of the theory of modal decoupling as detailed in Chapter 2 to the problem of integrating the equations of motion. For better readability, some equations from the earlier chapter are repeated here.

Under the assumption of proportional damping, changing the basis of Equation (4-13) to principal coordinates, Equation (2-12):

$$\{u\} = [\Phi]\{p\} \quad (4-14)$$

will uncouple the equations of motion, i.e., the coordinate transformation will diagonalise the matrices $[\mathbf{M}]$, $[\mathbf{C}]$, and $[\mathbf{K}]$. This is advantageous, as operations on diagonal matrices are computationally very inexpensive.

The required modal matrix can be obtained either by numerical analysis techniques like the finite element method or by experiment. The matrix is composed of the modal matrices of the rotor and stator.

For the mass-normalised modal matrix $[\Phi]$ the following relations hold:

$$\begin{aligned} [\Phi]^T[\mathbf{M}][\Phi] &= [\mathbf{I}] \\ [\Phi]^T[\mathbf{K}][\Phi] &= [\lambda_r] = [\omega_r^2] \\ [\Phi]^T[\mathbf{C}][\Phi] &= 2[\zeta_r][\omega_r] \end{aligned} \quad (4-15)$$

$[\omega_r]$ is the diagonal matrix with the natural frequencies on the diagonal, $[\lambda_r]$ is the square of $[\omega_r]$ with the eigenvalues on the diagonal, and $[\zeta_r]$ is the diagonal modal damping matrix. With these relations, Equation (4-13) changes to:

$$\{\dot{p}\} = \begin{bmatrix} \mathbf{I} & 0 \\ 0 & \mathbf{I} \end{bmatrix}^{-1} \left(\begin{bmatrix} 0 & \mathbf{I} \\ -[\lambda_r] & -2[\zeta_r][\omega_r] \end{bmatrix} \{p\} + \begin{Bmatrix} 0 \\ [\Phi]^T\{f_u\} \end{Bmatrix} \right)$$

or:

$$\{\dot{p}\} = \begin{bmatrix} 0 & \mathbf{I} \\ -[\lambda_r] & -2[\zeta_r][\omega_r] \end{bmatrix} \{p\} + \begin{Bmatrix} 0 \\ \{f_p\} \end{Bmatrix} \quad (4-16)$$

From Equation (4-16) the advantage of changing to principal coordinates is obvious: a computationally-expensive matrix inversion is avoided and the blocks of the system matrix are all diagonal, reducing the matrix-vector multiplication to a summation of two element-by-element multiplications. The only remaining full matrix-vector operation is the computation of the force projection into the modal space: $[\Phi]^T \{f_u\} = \{f_p\}$.

As the modal matrix $[\Phi]$ is time-invariant for the systems investigated in the study, the time derivatives of $\{p\}$ obey the same transformation:

$$\{\dot{u}\} = [\Phi]\{\dot{p}\} \quad \{\ddot{u}\} = [\Phi]\{\ddot{p}\} \quad (4-17)$$

The modal matrix and eigenvalue matrix of the state vector $\{u\}$, introduced in Equation (4-12), are related to those of the physical coordinates $\{u_{r+s}\}$ by:

$$[\Phi_u] = \begin{bmatrix} [\Phi_{u_{r+s}}] & [\Phi_{u_{r+s}}]^* \\ i[\omega_{u_{r+s}}][\Phi_{u_{r+s}}] & i[\omega_{u_{r+s}}][\Phi_{u_{r+s}}]^* \end{bmatrix} \quad [\omega_u] = \begin{bmatrix} [\omega_{u_{r+s}}] & 0 \\ 0 & [\omega_{u_{r+s}}] \end{bmatrix} \quad (4-18)$$

where the star denotes the complex conjugate. So, neither the modeshapes of the state vector nor its natural frequencies contain more information than was available from the initial coordinate set.

4.5 Setting up the Integration

For ease of parameter changes and display of results, the simulation is carried out on a digital computer. Analogue computers would have been faster but changing system parameters would have been more difficult to model and the intermittent nature of the contact was not very well suited for this type of computer. With digital computers, for all purposes sequential automata, two variables are of crucial importance: the problem size and the numerical integration scheme. Misjudging either of these will lead to meaningless results – and it may be very difficult to identify these as such.

4.5.1 Problem size

The consideration for the choice of the right problem size are twofold: on the lower side, the simulation needs to include only the ‘relevant’ dynamics and on the upper side, it will not finish in reasonable time if the problem is too big. The right reduction will result in a compact model that predicts the physical events faithfully in reasonable time. The ‘reasonable time’ cannot be defined in absolute terms. For a real engine, a simulation will take longer than for a simplified model. If many parameter studies are to be performed, the time constraint becomes even more important.

As with any computation, there exists the trade-off between effort and accuracy. The smaller the problem size, the more economical it is to solve the problem. Assuming that

the storage requirements can be fulfilled, the effort translates into speed: the smaller the number of modes included, the faster the simulation will run.

The danger of reducing the model too far is the suppression of relevant dynamics of the structure. By removing physical modes from the simulation, the system is hindered in its ability to move naturally. So, even if modes are not under direct scrutiny, they may be instrumental to the initiation of the phenomenon. For undamped systems, Yoram (1995) found the natural frequency to be the most useful selection criteria. The methods of model reduction are detailed in, for example, Samar, Postlethwaite, Gu, (1995), and Yae and Inman, (1992).

Therefore it is safer to approach the minimum problem size from above and to reduce the size after investigating the effects of the other modes. Approaching the smallest size viable ensures that all relevant modes are included in the simulation. It makes initially the computation of more modes necessary, but the excess cannot be avoided as it cannot be determined beforehand.

4.5.2 Selection of the integration scheme

The second important choice in the simulation is the choice of the integration scheme. The algorithm must be capable of integrating the differential equations accurately. For the problem at hand there are many difficulties for a numerical solver or algorithm: the time-step, short-time events like impacts, changing system parameters, and intermittent forces. These difficulties require the algorithm to take extra care when progressing in time. This translates into a high computational effort or integration time.

The general program flow of the simulation is summarised in Figure 4-2:

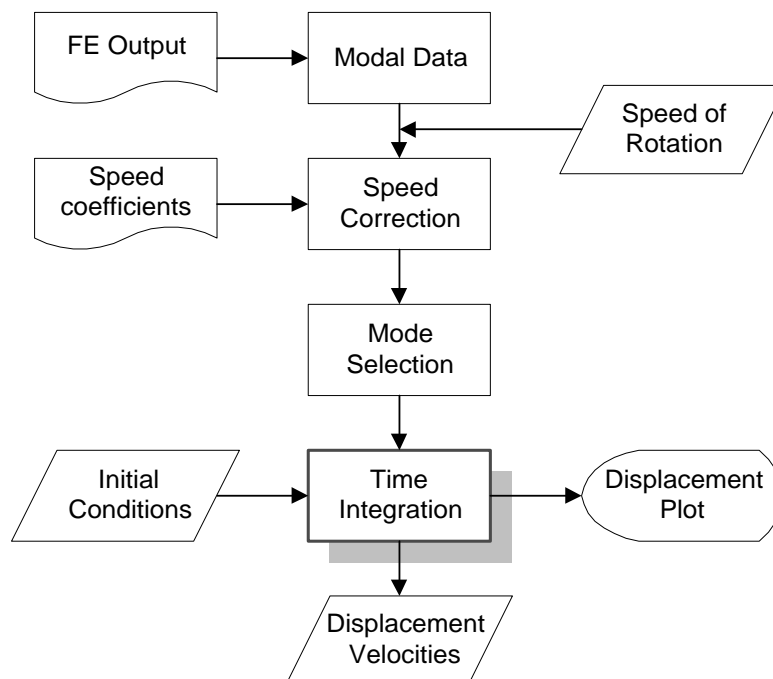


Figure 4-2: Integration Scheme

The initial set-up takes the modal data of the rotor and stator and corrects the natural frequencies of the rotor for the selected running speed. It then selects the modes that are going to be considered in the integration, and reads the initial conditions in both deflections and velocities. The time integration provides as output the displacements and velocities as functions of time at the computed time-steps. Immediate display allows the user to observe the evolution of any computed quantity. The next paragraphs explain some steps in more detail, concentrating on the numerical and physical aspects of the problem.

4.5.2.1 Changing system parameters and step size

The function $f(\{u_i\})$ in Equation (4-10) describes the dynamic of the states. Any numerical solver will have difficulties with changing system parameters because all integration schemes have to extrapolate in time at some stage. At times where the system parameters are constant, the solver can predict the response at the next time step easily from the recent history and will use large time steps to increase overall efficiency. When the blades impact the rotor and the two separate structures change to a coupled system, the system parameters change and the time extrapolation mispredicts grossly.

After such an ‘error’ the procedure restarts from the last predicted point with a smaller time step and repeats this until it predicts the next point with sufficient accuracy or exits with an error. The smaller the time step, the longer the simulation will run. In order not to be restricted to the smallest necessary time step, a scheme with an adaptive step size is an absolute necessity for the solution of differential equations describing systems with changing parameters.

The determination of the step size depends on an error criterion, based on relative and absolute error bounds. The step size will decrease when the system parameters are changing and it will increase when the system parameters are constant or change only slowly, for example, when the structures are vibrating freely without contact. Some of the discussion is sketched in Figure 4-3, further control parameters are used in actual algorithms.

4.5.2.2 Determination of the sampling time

Different from the step size and completely independent of it is the sampling frequency, or the time interval at which the solution is provided.

The minimum sampling time is determined by the highest frequency present in the simulation. For the present simulation, the frequencies are known and the minimum sampling rate can be determined exactly. Due to the choice of principal coordinates in two reference frames, and the speed modulation, the sampling rate must be much higher than in would be in an experiment, this will be detailed below.

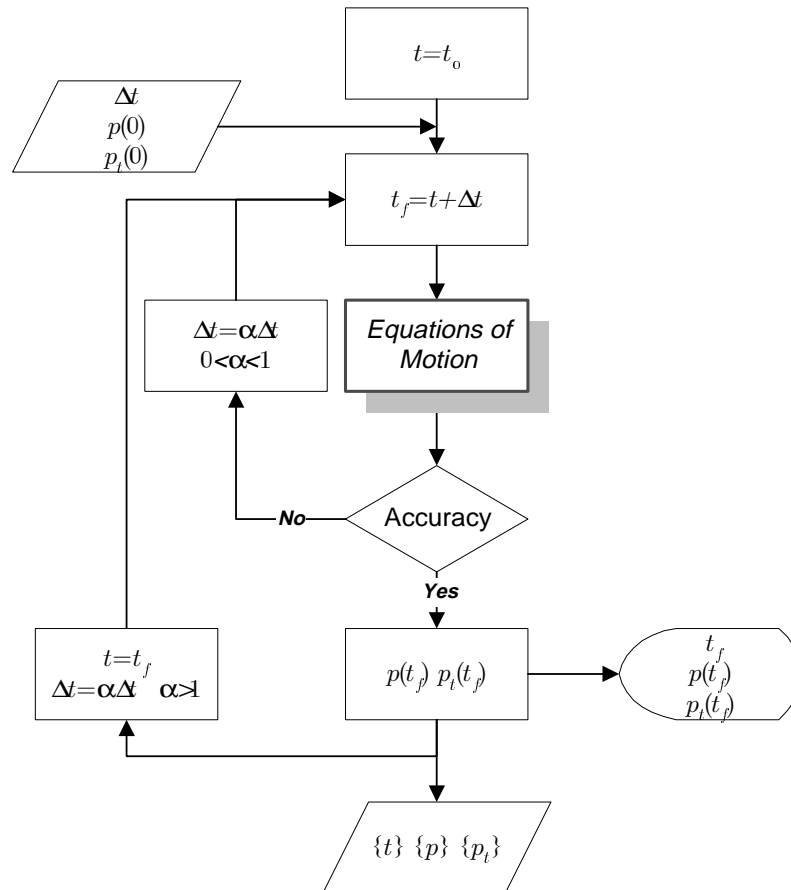


Figure 4-3: Integration algorithm with adaptive step-size

4.5.3 Selection of modes

Different approaches to select the modes can be used. One possible approach would be to include only modes with certain spatial patterns, say, only 2ND and 4ND modes, another approach is to select the modes by frequency.

4.5.3.1 Selection by spatial pattern

This sort of selection implies that the other modes are irrelevant to the simulation by consideration that their average contribution tends to zero. In the limit this leads to the minimum configuration of 2 double modes (one from each structure): the simulation includes only those modes whose nodal diameter pattern is under investigation.

The danger of this approach is that short-time interactions may be lost. Another difficulty is to obtain the proper initial conditions. Especially random initial conditions cannot be simulated. For the latter reason, this minimum approach with only 4 modes is too unrealistic to be pursued further in the current study.

4.5.3.2 Selection by frequency range

Another way of selecting the modes for the simulation is to select them by frequency. Usually, a frequency range is chosen and all modes within are included in the simulation. This approach guarantees that all dynamics in that range are accounted for. Effects

outside the chosen frequency band, such as short impacts and other high-frequency phenomena, will not be covered, so care must be taken in the selection of the range. Where to set the frequency limit is a matter of engineering judgement and careful analysis of preliminary modelling and simulations.

In selecting the frequency range one has to remember the twofold speed-dependency of the rotor natural frequencies due to centrifugal stiffening and due to the transformation into the stationary reference frame. In order to ensure that both points are addressed properly, the rotor frequencies for a particular set speed of rotation must be calculated before the selection can be made. Figure 4-4 exemplifies this for one mode: in a simulation there would be many of them to be considered.

Even if the rotor natural frequencies at zero speed are outside the band, the frequencies of the counter-rotating waves (the lower of the two rising curves in Figure 4-4) might rise into the band, so that the modes must be included in the simulation.

Once the mode is included in the simulation, its co-rotating wave (the higher of the two rising curves in Figure 4-4) defines the highest frequency due to this particular mode. The maximum of all selected rotor modes defines the upper bound of the frequency band from which the stator modes are selected. The upper frequency of the frequency band also determines the sampling frequency. In order to satisfy the Nyquist Criterion, the sampling frequency must be larger than ω_{min} :

$$\omega_{min} = 2 \max(\omega_{rn}(\Omega) + n\Omega) \quad (4-19)$$

half of which is indicated in Figure 4-4 by $\omega_{min}/2$.

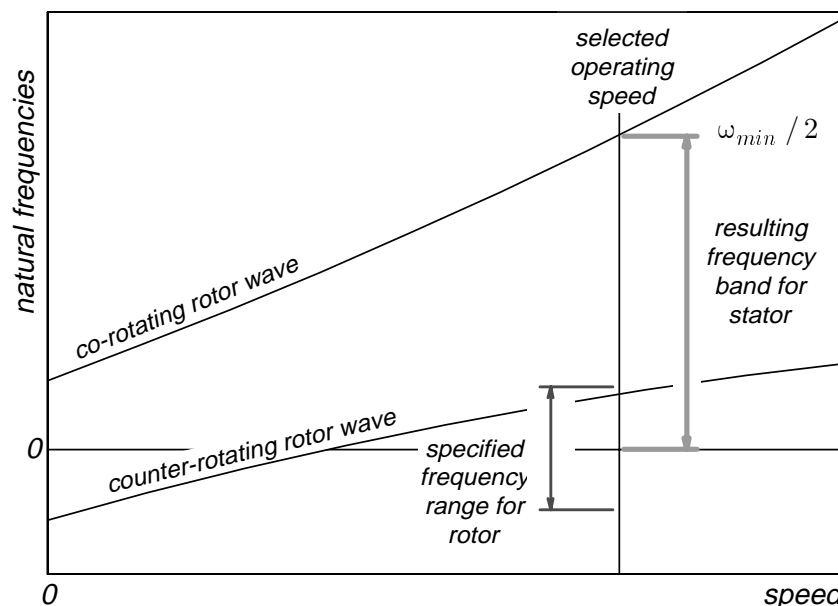


Figure 4-4: Selection of Modes

Selecting the modes according to the outlined scheme may result in a very high upper frequency, Figure 4-4, which in turn will lead to many stator modes falling into the frequency band. Analysis of the principal coordinates of the data from an initial simula-

tion with all selected modes included serves as an indication of which modes need not be carried through in further simulation runs.

4.5.4 Computation of the contact forces

The computation of the contact forces starts from the computation of possible interferences and the resulting axial forces, sketched in Figure 4-5. The axial force and the state vector determine the tangential force. The individual steps of the computation of the contact force are detailed below.

4.5.4.1 Contact points

It is reasonable to assume the contact to be limited to the blade tips. Depending on the geometry, one or more nodes will define the tip. In order to find the contact points the responses of both structures need to be expressed in the same reference frame. In the following, the contact points and forces will be computed in the stationary frame of reference, indicated by the shaded area in Figure 4-5; any other frame of reference is equally valid and possible.

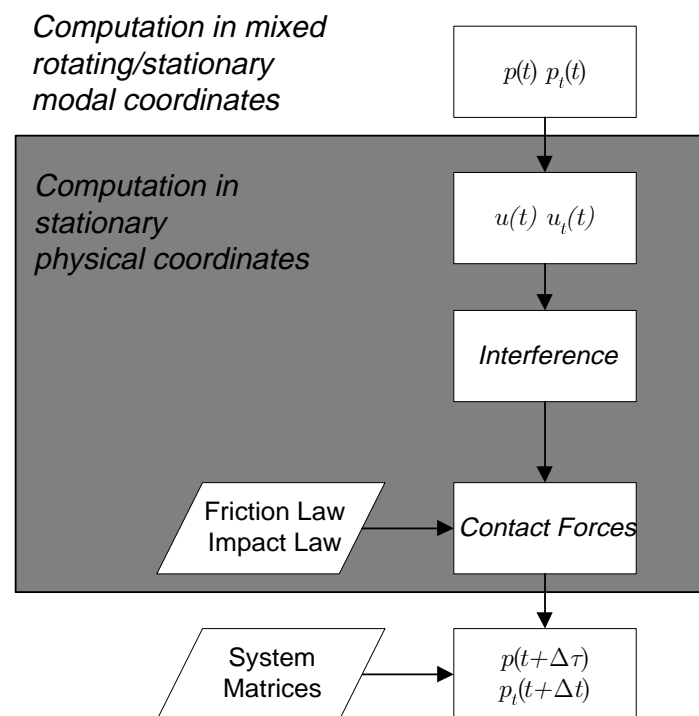


Figure 4-5: Contact force computation

4.5.4.2 Response Computation

The responses u are computed by modal superposition from the principal coordinates and the modeshapes:

$$\{u_i\} = [\Phi_i]\{p_i\} \quad (4-20)$$

where $i = r, s$ for rotor and stator, respectively. As the principal coordinates of the rotor are integrated in the rotating frame of reference they must be transformed into the stationary reference frame by:

$$\theta_S = \theta_R - \int_0^t \Omega(\tau) d\tau \quad (4-21)$$

assuming that the coordinates system originally coincided. For constant speed of rotation this simplifies to:

$$\theta_S = \theta_R - \Omega t \quad (4-22)$$

4.5.4.3 Tangential Contact Coordinates

The tangential coordinate is computed from the position of the blade tips around the perimeter and the angle due to their tangential deflection.

As the rotor node positions will not coincide with the computed contact positions, the rotor responses, both displacements and velocities, are interpolated to the computed blade tip positions. The rotations are interpolated linearly and the deflections, quadratically. The contact is supposed to occur on a constant radius, $R_{contact}$, which implies a reduction of the problem to two dimensions; the extension to three dimensions, making the contact radius a variable, is straightforward but is deemed unnecessary for the model used due to its particular geometry.

4.5.4.4 Interferences

From the displacements of rotor and stator the interferences, Δx , are computed. The relevant measure is assumed to be the interference in axial direction for the reason given in Paragraph 4.3.3.2. The interference is kept small by the adaptive step-size algorithm of the integration routine and a large contact stiffness, effectively simulating an impenetrable rotor and stator.

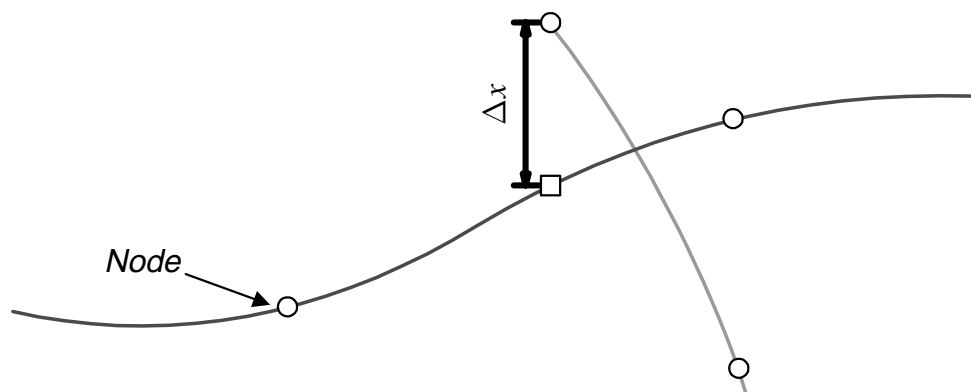


Figure 4-6: Determination of the interference

4.5.4.5 Axial force

The axial force can then be computed from the contact stiffness, the interference, the loss factor, and the time-derivative of the interference. The force model can accommodate different impact velocities by weighting the velocity more or less strongly, parameter d in Equation (4-3):

$$k_{rs}^l := k_{rs} e^{-d\Delta\dot{x}}$$

The axial force follows from Equation (4-2).

4.5.4.6 Tangential force

The tangential force follows from the contact geometry and the axial force, Figure 4-7.

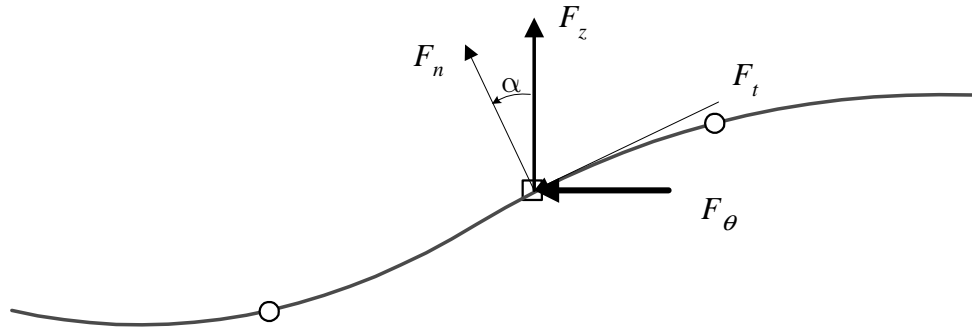


Figure 4-7: Determination of the global tangential force

The normal and tangential forces in the local contact coordinate system are not derived explicitly, but could be computed if required. The chosen approach combines the coordinate transform, Figure 4-7, with the kinematic condition on the forces:

$$\begin{Bmatrix} F_z \\ F_\theta \end{Bmatrix} = \begin{bmatrix} \cos \alpha & \sin \alpha \\ -\sin \alpha & \cos \alpha \end{bmatrix} \begin{Bmatrix} F_n \\ F_t \end{Bmatrix} \quad (4-23)$$

$$F_t = \text{sgn}(v)\mu F_n$$

where α is the angle between the global axial direction and the local normal direction.

The sign of the velocity will always be positive because of the high surface velocity due to the rotational speed and so the normal and tangential forces are related by the coefficient of kinematic friction. Combining the equations yields:

$$F_\theta = F_z \frac{\mu - \tan \alpha}{1 + \mu \tan \alpha} \quad (4-24)$$

which is a highly nonlinear relation between the two forces in the global coordinate system, Figure 4-8.

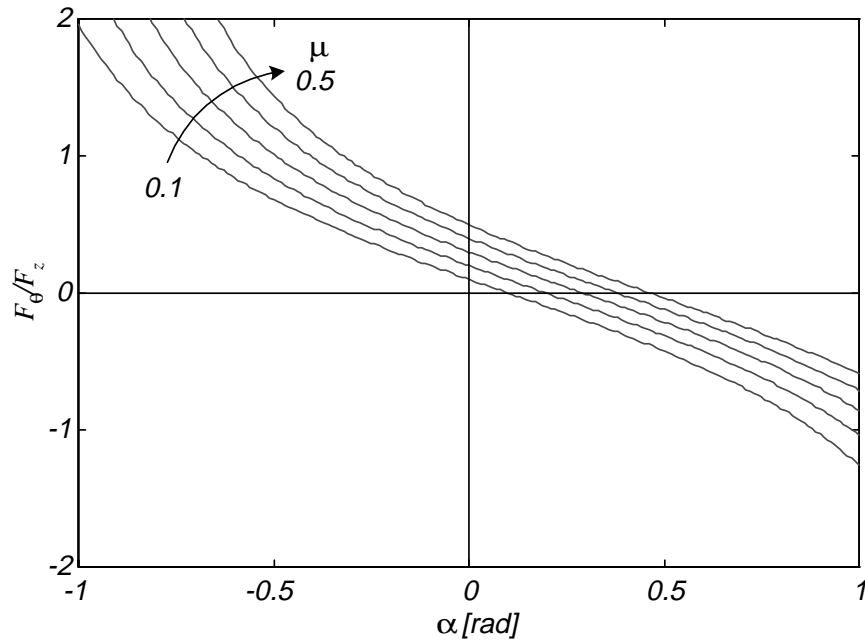


Figure 4-8: Ratio between tangential and axial force

4.5.4.7 Transformation into physical and modal space

The forces for the stator are easily put into the equations of motion as the computed contact forces act at the blade tips where there is always a node. For the rotor, the contact positions generally do not coincide with the positions of the nodes and the computed contact forces must be split between the neighbouring nodes. Different approaches are possible, but a simple first-order force and moment balance between the adjacent nodes seems most appropriate.

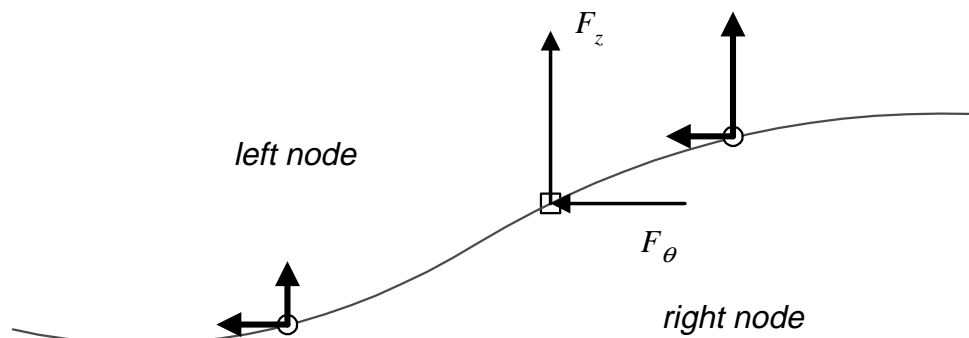


Figure 4-9: Computation of nodal forces

The forces are only split between the two neighbouring nodes to introduce the forces into the system. The response of the structures to these forces then travels from the ‘entry points’ through the whole structure over time. If the forces were decomposed modally and applied to all nodes simultaneously, this temporal delay would not be captured. The underlying assumption is that the wave-propagation speed is not negligible compared with the system dynamics, (Schweitzer and Fumigalli, 1996).

Once the nodal forces are obtained, the force vector in the degrees of freedom is defined and can be transformed into the modal space by left-multiplication with the transpose of the modal matrix, Equation (4-16).

4.6 Solution Procedure

The integration is performed in the MATLAB environment, (Mathworks, 1994). The advantages in using this software for solving the differential equations are the full control over the algorithm with access to the source code. This way, for example, all variables are accessible and can be saved for later use. Also, a powerful graphics engine is available at any time to present computed results immediately.

In the computing environment are many different integration algorithms available, standard Runge-Kutta algorithms and Rosenbrock methods for stiff systems of different orders, Shampine and Reichelt (1995).

Algorithmic stability, as opposed to structural stability, is an important part of any integration scheme. Two types of algorithmic stability exist: unconditional stability is independent of the step size while conditional stability depends on the step size and becomes unstable beyond a certain step size, Δt_{\max} . As Argyris and Mlejnek (1991) pointed out, most of the time stability is a necessary, but not sufficient, feature of an algorithm: naturally, an accurate solution is sought and so accuracy is the second key part of any solver. How the accuracy can be controlled, and which steps of caution are to be taken, is detailed in the above references. They also address the phenomenon of numerical damping. This occurs because of the finite word lengths of digital automata. and is sometimes useful (Wilson's θ -method) to suppress spurious modes at the Nyquist frequency introduced by the integration scheme, (Xie, 1996). The danger of numerical damping is that it also suppresses physical modes and the way to overcome this problem by reducing the step size is very costly.

4.6.1 Selection of the sampling frequency

The sampling frequency, ω_{\min} , is chosen according to Equation (4-19), and is rounded, so that, instead of, say, 1858 Hz, a sampling rate of 2000 Hz is used.

4.6.2 Choice of initial conditions

Little has been said about the initial conditions. The theory as outlined above requires that the initial conditions should not be critical for the occurrence of the phenomenon as the required modes are in resonance.

For the simulation, it turns out to be difficult to select initial conditions that start the contact without causing the simulation to exit due to numerical problems caused by excessively high contact velocities. Implemented choices for the initial conditions are:

- random: assuming nothing about the conditions that caused these initial conditions.

- velocity impact at a point: simulating an impact of some sort. This should be promising as the experiment conducted in this way established the travelling-wave-speed coincidence, Chapter 7.
- modal: asserting that some resonance condition prevailed that amplified the response of these modes or waves.

4.6.3 Test cases

In order to ensure the proper functioning of the code as it is developed, test cases are developed, one of them being the engine-order test, where the rotor, spinning at an engine-order speed, is excited by a spatially-varying, time-invariant force to vibrate in a standing wave. The speed of a counter-rotating wave, $-\nu_r$, equals the speed of rotation Ω_{EO_n} and so it appears to the stationary observer as if the disc is deflected statically in space, deformed in an wavy, n -nodal-diameter pattern. As a side effect, the sound emission from the rotor tends to zero as there is no normal direction to the vibration. The stator exposed to the same excitation force experiences a static force and deforms into a force-proportional deflection pattern, after the initial disturbances have decayed.

A general check for the simulation results is to ensure that the frequencies of the response signals are the correct ones: starting from non-zero initial conditions without contact throughout the simulation, the stator frequencies are expected to be the natural frequencies only, and those of the rotor measured in the stationary reference frame should be modulated by the speed of rotation times the number of nodal diameters, n :

$$\omega_{rnS} = \omega_{rnR} \pm n\Omega \quad (4-25)$$

4.6.4 Program description

The programs for the simulation are developed under the MATLAB environment. The programs are fully portable between IBM PCs and IBM RS/6000 workstations.

In order to keep the programs modular and easy to maintain, the code is broken into functions residing in separate files. The driver program and the important functions are given in the Appendix and will be explained below to clarify the program flow:

The simulation is started by calling `STARTINT`, which sets up all relevant parameters and global declarations.

The input data from the FE program are computed in `MODPARMS`, which returns the modal properties of both structures at interface nodes, selected in `PATHR` and `PATHS`. The modeshapes are returned in cylindrical coordinate system of (r, θ, z) .

`MODPARMS` also determines the number of nodal diameters of the modes. The modes are selected according to the methods detailed above to keep the size of the problem manageable.

The running speed is set, either arbitrarily or as a function of the natural frequencies of rotor and stator in OMEGACRT. This function enables one to set the speed of rotation to, for example, the engine order speed Ω_{EO_n} .

Correcting the natural frequencies of the rotor is carried out in CfOMEGA. Due to the centrifugal forces acting on the rotor, the natural frequencies increase. The correction factors necessary were calculated in advance.

The initial conditions are set and the integration is started by calling any of the solver provided in the Matlab ODE-Suite: ODE45 or ODE23S. The solvers are provided with a function that computes the derivative of the state vector with respect to time, function DERIV.

Function DERIV computes the deflections of rotor and stator at the position of the blade tips in DISPCONT. From the displacements, the possible interferences are computed in INTERFER and the contact forces are calculated in FORCEC. The axial force is computed in RSF from the interference and the normal velocity of the impact. The tangential force is computed using Coulomb's friction in FORCEC.

Again in DERIV, the contact forces are transformed into the body-fixed coordinate systems, rotating for the rotor and non-rotating for the stator, and finally into the modal space spanned by the principal coordinates.

When the integration proceeds in time, RSODEPLT is called to plot the responses at one blade.

After the integration finishes, the responses are computed from the modeshapes and the principal coordinates in POSTPROC. The response of the rotor is transformed into the stationary reference frame in WRAPRESP and both responses are low-pass filtered and resampled using the Matlab routine DECIMATE. Eventually the evolution of responses with time can be presented with PRINCPLT, PARTPLT, and Matlab's own SURF function.

4.7 Discussion

The mathematical model developed above describes the dynamics of the individual structures and the dynamics of the contact between the structures. Initial tests, presented in the next chapter, show the validity of the approach and indicate that the program as developed can predict the behaviour of the structures within the limits of the assumptions and approximations made, namely:

- linear, time-invariant dynamics of the structures
- complex impact stiffness for the normal contact force
- Coulomb-friction for the tangential contact force

Chapter 5: Simulation Results

The numerical model developed in the previous chapter has all the necessary elements to simulate the dynamical behaviour of the fully-elastic rotor-stator system. The first step of using the simulator is to make sure that it is working correctly by running test cases with known results. Once the simulator produces the expected results, it is assumed that all programming errors are corrected, and the simulation of the travelling-wave-speed coincidence instability can be started.

In order to distinguish between temporal stationarity and spatial stationarity, the term time-invariant is used for the temporal stationarity.

5.1 Test Cases

The test cases used are the responses to engine-order excitation of both structures separately. Engine-order excitation is typical for rotating machinery where it can be caused, for example, by pressure fluctuations in the upstream working fluid. At engine-order speed a counter-rotating wave of the rotor has a natural frequency of 0 Hz in the stationary frame of reference, its velocity, v_r , being equal and opposite to the speed of rotation, Ω . Hence any time-invariant force with a non-zero spatial Fourier component with the same number of nodal diameters as the wave excites the rotor in resonance. The number of nodal diameters, n , of the wave crossing the 0 Hz line gives the engine order its name: EO_n or nEO .

In the following simulations, the structures are excited by a force with a spatial $\cos 2\theta$ pattern and the rotor is assumed to spin at its second engine-order speed, Ω_{EO2} , so that its two-nodal-diameter, counter-rotating wave is in resonance with the force.

5.1.1 Engine-order excitation of the stator

The response of the stator to a stationary, time-invariant force is a temporally-constant deflection. The deflection is expected to be relatively small because the stator has no elastic natural frequency of 0 Hz and is not in resonance with the engine-order excitation.

In the test cases, the amplitude of the force is increased slowly to avoid transient responses and hence the response of the stator grow with time, see Figure 5-1, where dark shades of grey indicate large positive deflections and light shades large negative deflections. The axes are time, the angular coordinate around the structure (labelled θ), and the axial coordinate (labelled u). The first suffix indicates the structure: s stands for stator and r for rotor, and the second suffix identifies the reference frame: S for stationary and R for the reference frame co-rotating with the rotor.

Stator response in stationary observer frame

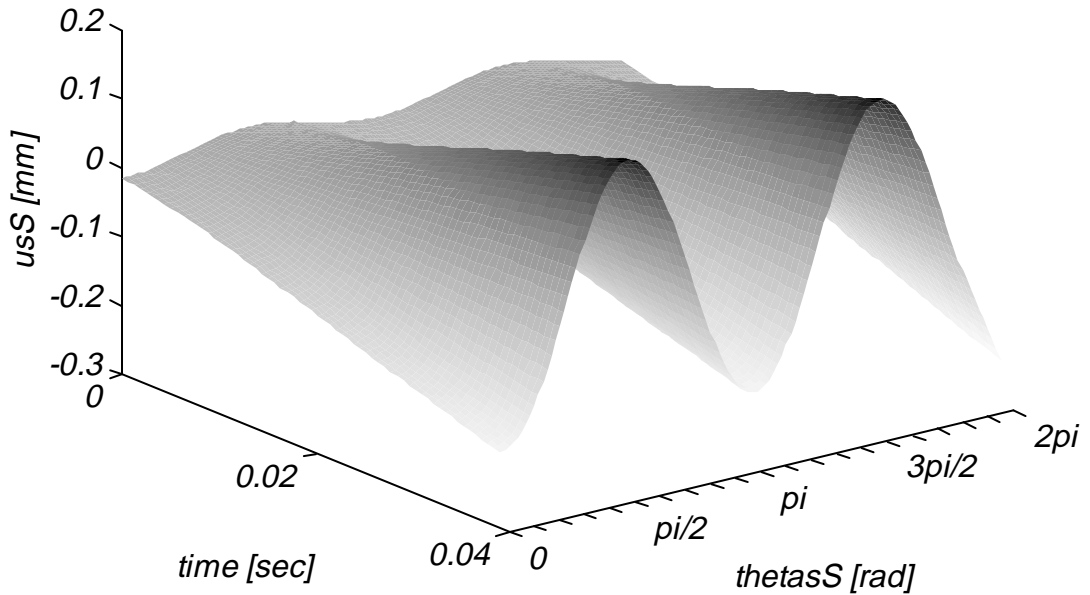


Figure 5-1: Stator response in the stationary reference frame

The stator does not vibrate but grows in amplitude with the force, it deforms statically. If the forces were constant in magnitude, the deflection of the stator would not change with time at all. This test validates the stator part of the model.

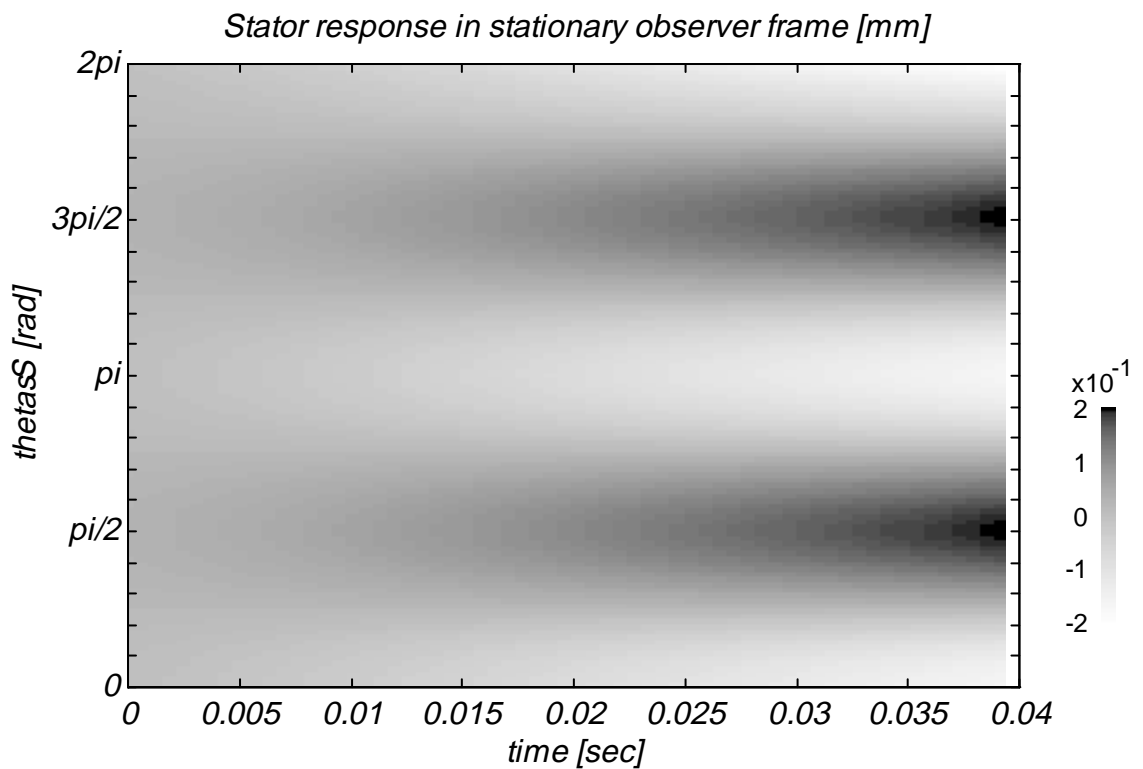


Figure 5-2: Two-dimensional view of Figure 5-1 (top view)

The display of the vibration in three dimensions, Figure 5-1, is visually attractive but carries no advantage in information density, (Tuft, 1990). Indeed, the perspective view obscures the direction of travel of the vibration pattern. Also, the third dimension and the colour are used redundantly, both visualise the magnitude of the displacement. The plot can be reduced by the third spatial dimension without losing any information, Figure 5-2. Alternatively, the colour could be disregarded.

The resulting plot is even clearer than the more complex three-dimensional figure, as it shows immediately that the deflection pattern does not move in the tangential direction, which runs from bottom to top. The colour coding is explained concisely by a small patch on the side of the plot. This two-dimensional format will be used throughout the thesis.

5.1.2 Engine-order excitation of the rotor

The response of the rotor to a 2ND-engine-order excitation is shown in Figure 5-3 in the stationary frame of reference (thetarS).

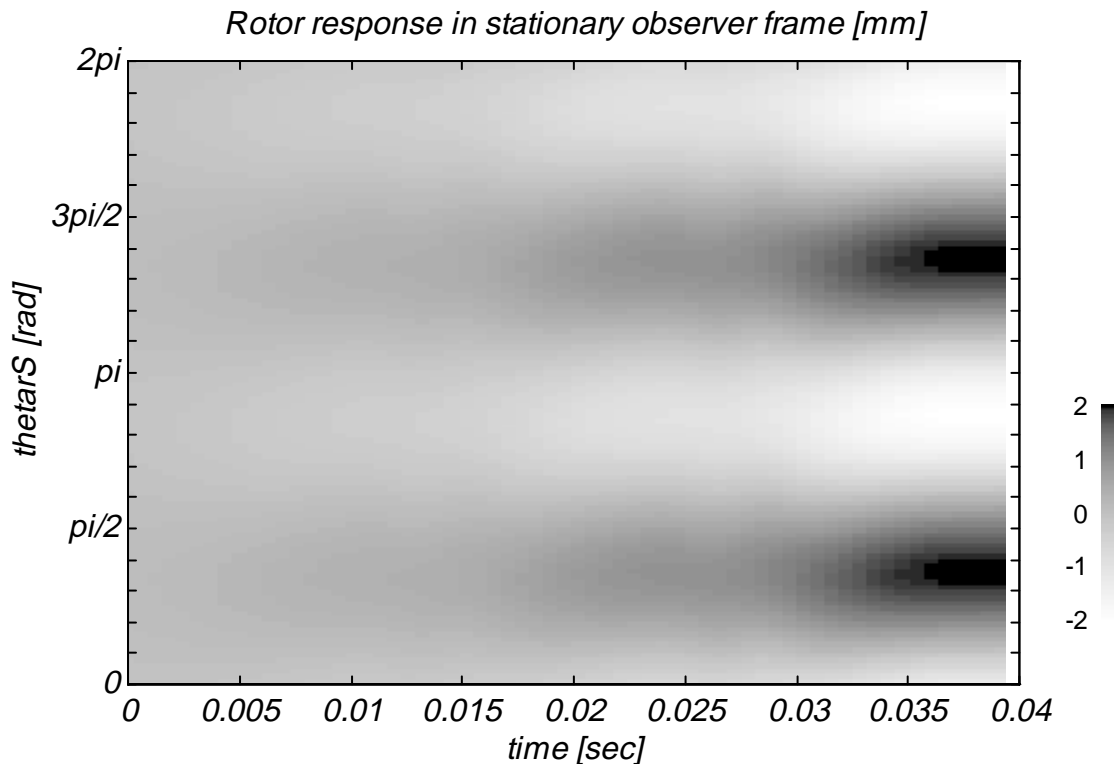


Figure 5-3: Rotor response in the stationary reference frame

The displacement is growing in the same pattern as the stator in Figure 5-2, but the displacements increase to much higher levels. This is because the rotor is excited in resonance by the engine-order force pattern. As expected, the response pattern is stationary in space, a stationary wave, similar to the force pattern. This may lead to the conclusion that the rotor does not vibrate. That this is not the case can be seen if the displacement is presented in the body-fixed, rotating frame of reference, as shown in Figure 5-4.

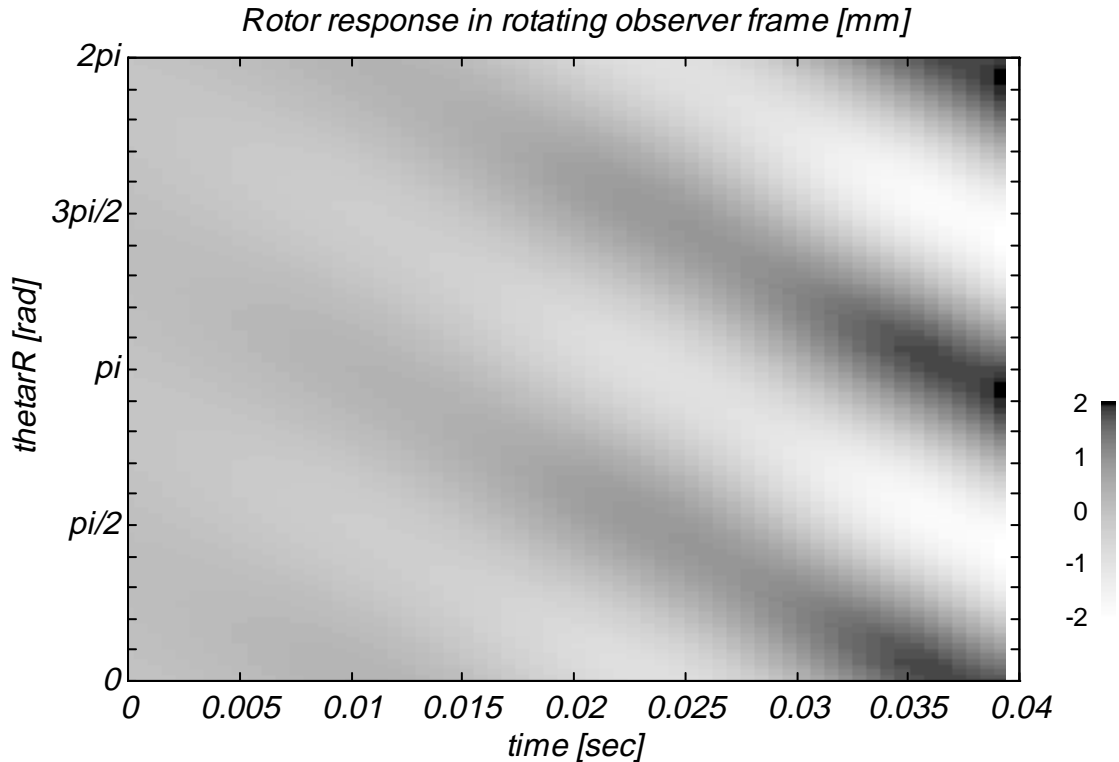


Figure 5-4: Rotor response, second engine-order excitation, stationary reference frame

The material points of the rotor vibrate at the natural frequency and from Figure 5-4 it can be concluded immediately that the rotor is vibrating in a 2ND counter-rotating wave, with velocity, ν_2 , given by:

$$\nu_2 \approx \frac{-3\pi / 2 \text{ rad}}{0.04 \text{ sec}} = -117.8 \text{ rad/sec} \approx -118.4 \text{ rad/sec} = -\Omega_{EO2} \quad (5-1)$$

5.2 Preliminaries for the numerical Simulation

5.2.1 General layout of figures

The format of the results as presented above is suited for slowly-varying responses only. In the subsequent plots, the displayed data are further reduced to one tangential position along the perimeter, corresponding to a single horizontal line in Figure 5-4, to make a visual interpretation possible. The rotor and stator responses are plotted to resemble as closely as possible the vertical configuration of the test rig where the rotor is mounted above the stator, see Chapter 6. In the following figures, the trace in dark grey is the rotor response and the lighter grey indicates the stator response. Also marked by faint dash-dotted lines are the static positions of the rotor and stator. Initial tests showed that changing the initial gap between the two structures only changes the required initial conditions to make contact and thus the parameter is fixed at 2 mm for all simulations.

5.2.2 Initial conditions

Except where noted, only the rotor has non-zero initial conditions: a counter-rotating wave of the nodal diameter under investigation with a magnitude 1.5 mm, three quarters of the initial gap of 2 mm, and a random excitation with an amplitude of one half of the initial gap, 1 mm. In this way, contact occurs with a strong initial counter-rotating wave component. In order to have contact only after the first time step, the random excitation was in specified for the velocities only.

These initial conditions may be considered to be representative of real aircraft engines where it can be assumed that some engine-order excitation is present and causes a permanent counter-rotating wave in the rotor, whereas the random vibration can be attributed to various sources such as flight manoeuvre or a bird strike.

5.3 Simulation of the 2ND Travelling-Wave-Speed Coincidence

The next figures show the results of the simulation of the dynamic behaviour of the rotor-stator system investigating the two-nodal-diameter waves. The following Figure 5-5 shows the speeds of the following simulations.

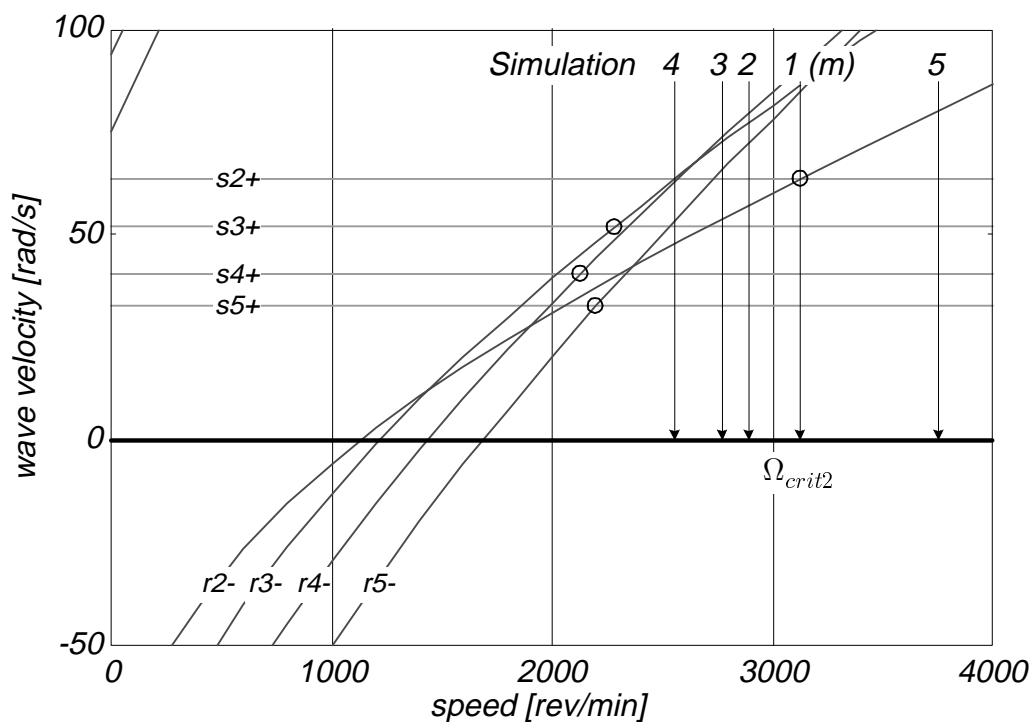


Figure 5-5: Critical travelling-wave-speed coincidences

5.3.1 Simulation at critical speed of rotation (Simulation 1)

Figure 5-6 shows the response of the two structures at the critical speed marked Simulation 1 in Figure 5-5. The critical speed of the two-nodal-diameter waves in the simulation can be computed to be:

$$\Omega_{crit2} = 3130 \text{ rev/min} \quad (5-2)$$

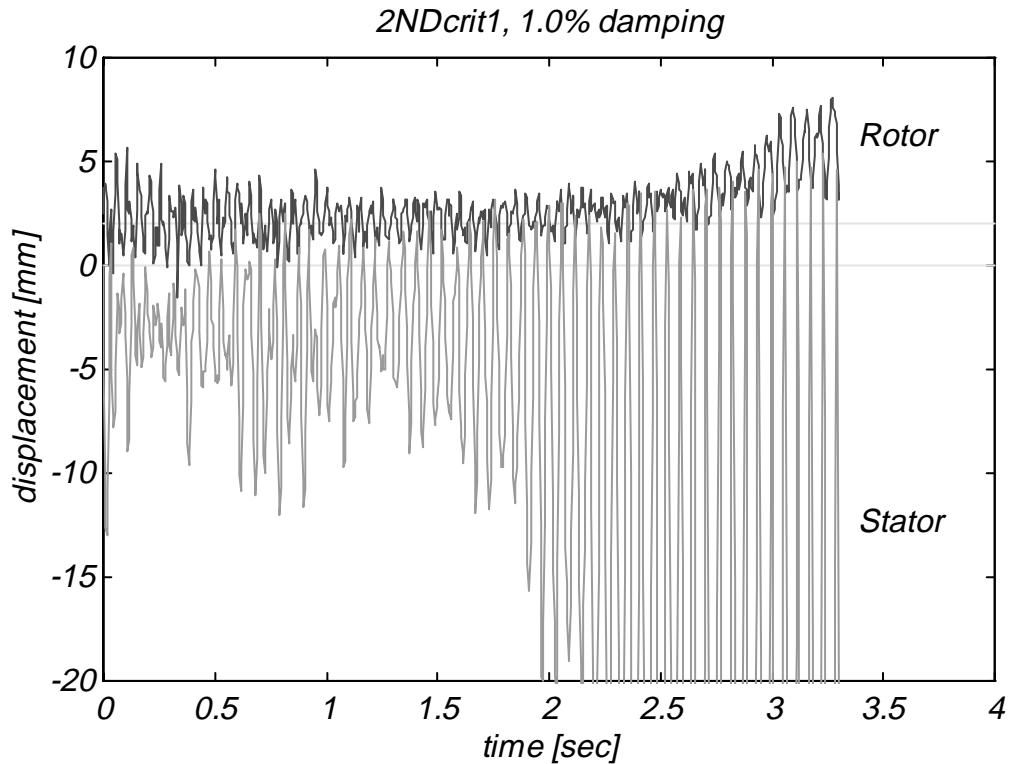


Figure 5-6: Response at critical speed, 1.0% damping

with an identical wave velocity of rotor and stator of:

$$\nu_{2S} = \nu_{r2S} = \nu_{s2S} = 63.5 \text{ rad/s} \quad (5-3)$$

The rotor starts with an almost periodic response due to the initial conditions. The response decays at first and becomes more random in nature, until it grows again after about 2.5 s. The decay can be explained by the decay of the random component in the signal. From about 2 s onwards, the rotor bends upward away from the static position indicated by the upper faint line in Figure 5-6. The dominant frequency of the vibration is that of the 2ND-counter-rotating wave for which the speed was set to be the critical speed, Ω_{crit2} .

The stator response starts randomly with no clear envelope shape but becomes periodic after about 1.5 s, and grows exponentially thereafter. The stator bends downward from the static position, indicated by the lower faint line. Again, the response is dominated by the frequency of the resonant, 2 ND-forward-travelling wave.

The simulation aborts after about 3.3 s due to numerical problems, but the simulation can be stopped long before as in real structures, such as the test rig or jet engines, the amplitudes would be limited by nonlinearities, such as contact with the sensors or nonlinear large-amplitude dynamics of the discs, (Swaminadham, 1990).

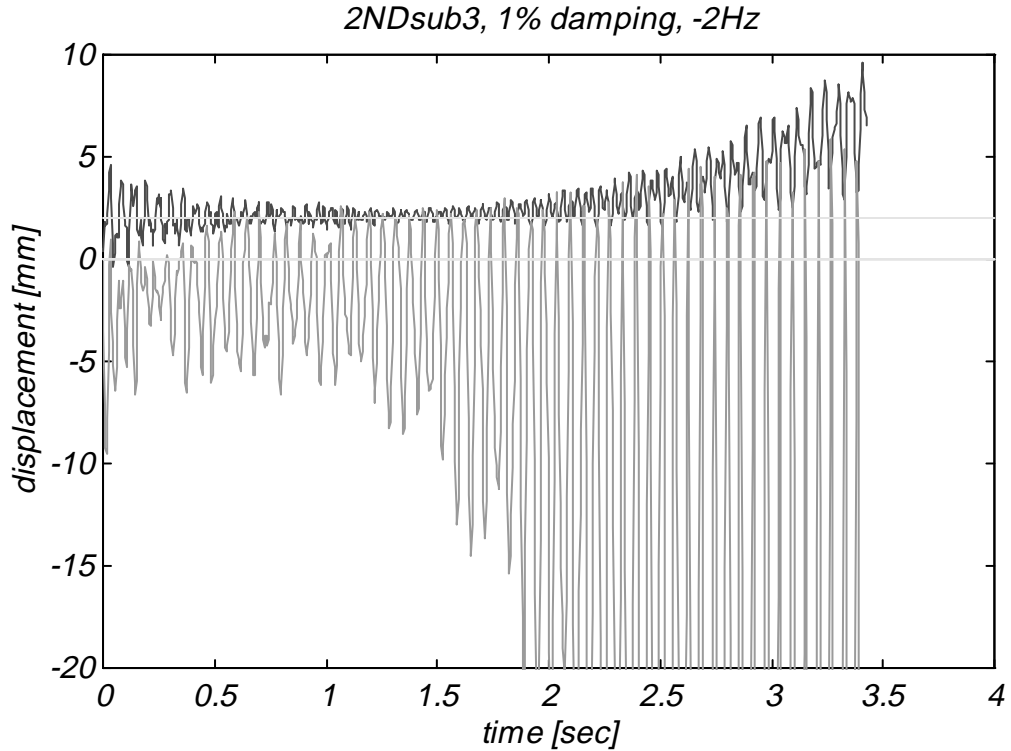


Figure 5-7: Response close to, below critical speed, 1% damping

5.3.2 Simulation at subcritical speed of rotation (Simulation 2 to 4)

The next simulations, Figure 5-8 and Figure 5-9, show the responses of rotor and stator when the speed of rotation is set below the critical speed. The speed of rotation is computed from the following relation:

$$\omega_{rR}(\Omega) + (\omega_{sS} + \Delta\omega) = n\Omega \quad (5-4)$$

where the argument of the rotor natural frequency shall serve as a reminder of the speed dependency of the natural frequency of the rotor due to the centrifugal stiffening. $\Delta\omega$ is the desired difference of the natural frequencies.

Two parameters are varied: the distance from the critical point, Figure 5-5, measured as a difference of either speed or wave velocity, and the amount of damping in the mode.

5.3.2.1 Effect of distance to critical speed (Simulation 2 and 3)

The distance of the set-point to the critical point in the following figures is given as difference of the natural frequencies of the structures. If the wave velocities differ by $\Delta\nu$, then the natural frequencies differ by $\Delta\omega = n\Delta\nu$. The difference in Hertz is noted in the title of the figures.

Very close to the critical speed, $\Delta\nu_2 = -2\pi$ rad/s, ($\Delta\omega = -2$ Hz), Simulation 2 in Figure 5-5, corresponding to a speed difference of about $\Delta\Omega = -230$ rev/min, the responses are still unstable, Figure 5-9, and the system behaviour is qualitatively similar to that at critical speed, Figure 5-6.

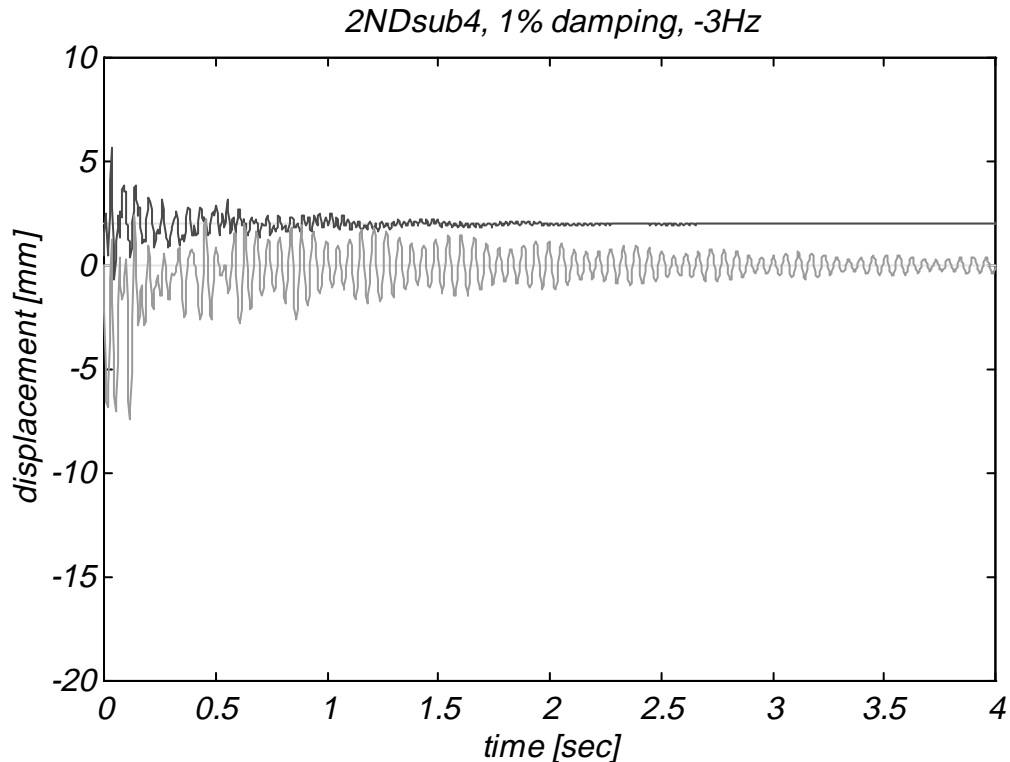


Figure 5-8: Response further below critical speed, 1% damping

Increasing the difference in wave velocities from $\Delta v_2 = -2\pi$ rad/s in Figure 5-7 to $\Delta v_2 = -3\pi$ rad/s, Simulation 3 in Figure 5-5, corresponding to a speed difference of $\Delta\Omega = -350$ rev/min below the critical speed, results in a stable response that decays to zero, Figure 5-8.

The very small increase of difference in wave velocities of 1π rad/s changes the system behaviour from going unstable to remaining stable. This shows the importance of the distance of the speed of rotation from the critical speed for the establishment of the travelling-wave-speed instability. Only if the waves of both structures have the same spatial pattern and progress with the same speed can sufficient energy be transferred into the structures to overcome the dissipation by damping.

5.3.2.2 Effect of damping (Simulation 4)

The stabilising effect of the distance to the critical speed is offset by reducing the amount of damping.

Figure 5-9 shows the system response for a difference of $\Delta v_2 = -5\pi$ rad/s in wave velocity (Simulation 4 in Figure 5-5) instead of $\Delta v_2 = -3\pi$ rad/s, but 0.2% damping only, 1/5th of the damping present in Simulation 3 shown in Figure 5-8. The larger distance to the critical speed cannot offset the destabilising effect of the reduction in damping and the response remains marginally stable. For the low level of damping of 0.2%, the response does not decay to zero but becomes almost periodic at a constant level, Figure 5-9. This response can be viewed as marginally stable, as any change in parameters will cause the amplitude of the vibration to either increase, potentially exponentially or decay to zero.

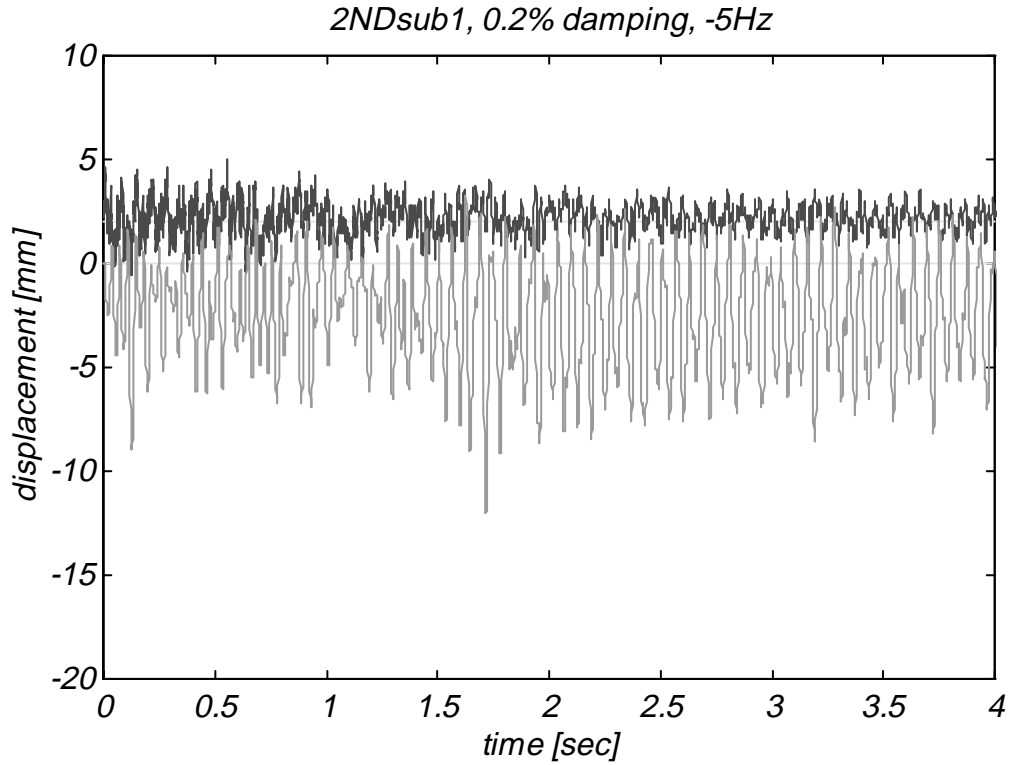


Figure 5-9: Response below critical speed, 0.2% damping

The running speed was set for a $\Delta\nu_2 = -5\pi$ rad/s difference in the wave velocities, or $\Delta\omega_2 = -5$ Hz difference in the natural frequencies:

$$\begin{aligned}\Omega_{sub} &= 2560 \text{ rev/min} \approx 0.82\Omega_{crit2} \\ \nu_{r,sub} &= 17.7 \text{ Hz} \approx 0.75\nu_{s2}\end{aligned}\tag{5-5}$$

Due to the centrifugal stiffening, 18% speed reduction causes 25% reduction of wave velocity.

5.3.3 Simulation at supercritical speed of rotation (Simulation 5)

The next simulation, Simulation 5 in Figure 5-5, shows the system behaviour for a supercritical speed, Figure 5-10.

For a difference in the wave velocities of $\Delta\nu_2 = 5\pi$ rad/s or $\Delta\omega_2 = 5$ Hz difference in the natural frequencies, roughly 25% of the natural frequencies, the running speed is computed to:

$$\Omega_{super} = 3720 \text{ rev/min} \approx 1.19\Omega_{crit2}\tag{5-6}$$

The damping level is set to 1%, the same value as in Simulations 1 to 3.

At this supercritical speed, the structures separate after about 1.2 s and the responses decay to zero.

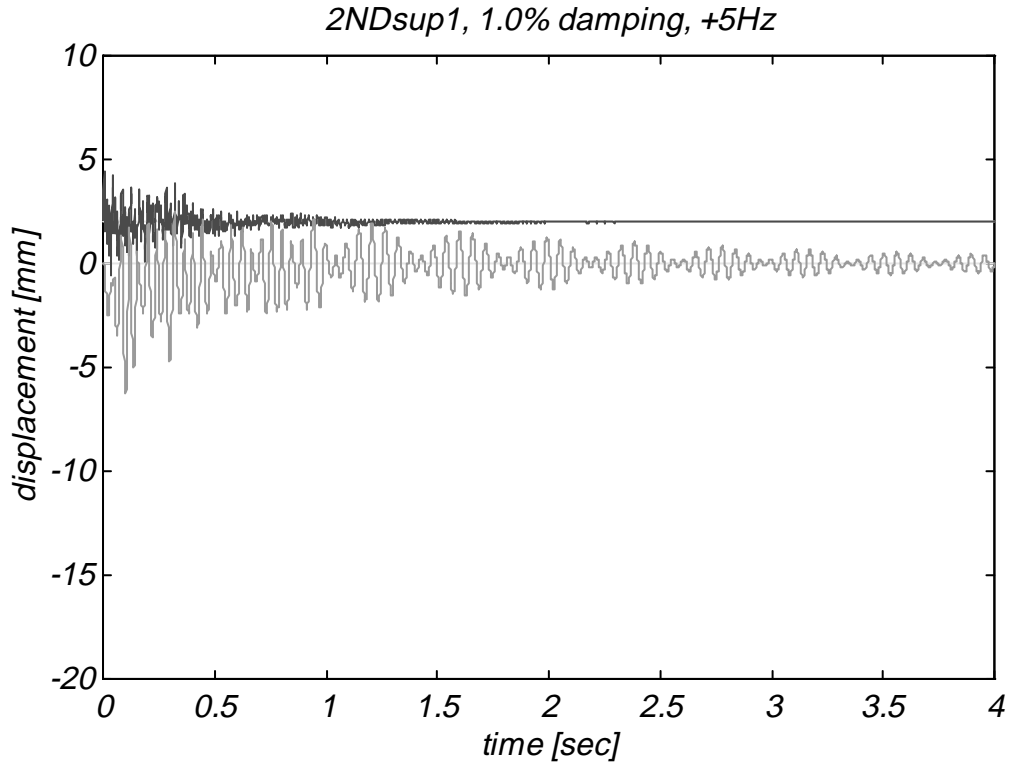


Figure 5-10: Response above critical speed, 1.0% damping.

Below $\Delta v_2 = 5\pi$ rad/s separation in wave velocities, the system response remains unstable. For the subcritical speed, the system response becomes stable at a separation of $|\Delta v_2| = 3\pi$ rad/s. The difference between subcritical and supercritical behaviour can be explained by the higher contact velocity causing more energy to be exchanged during impact.

Due to the centrifugal stiffening, the wave velocities change slower than the speed of rotation: for the same difference in wave velocity, the supercritical speed difference is larger than the subcritical one:

$$\Omega_{super} - \Omega_{crit2} > \Omega_{crit2} - \Omega_{sub} \quad (5-7)$$

5.3.4 Simulation of mistuned stator at critical speed of rotation (Simulation 1m)

The final figure in this series, Figure 5-11, shows the effect of mistuning on the response of the structures. The mistuning is modelled by changing, or detuning, the natural frequencies of the wave pair under investigation, here the 2ND wave pair. The split is introduced as fraction of the nominal natural frequency, ω_n , of the original, tuned system. In the simulation, the relative split of the natural frequencies, ε_n , is set to 5%:

$$\begin{aligned} \omega_{n1} &= (1 - \frac{1}{2}\varepsilon_n)\omega_n \\ \omega_{n2} &= (1 + \frac{1}{2}\varepsilon_n)\omega_n \end{aligned} \quad (5-8)$$

As has been explained in Chapter 3, mistuning has the effect of reducing the travelling-wave component and of bringing into existence a stationary wave component, and

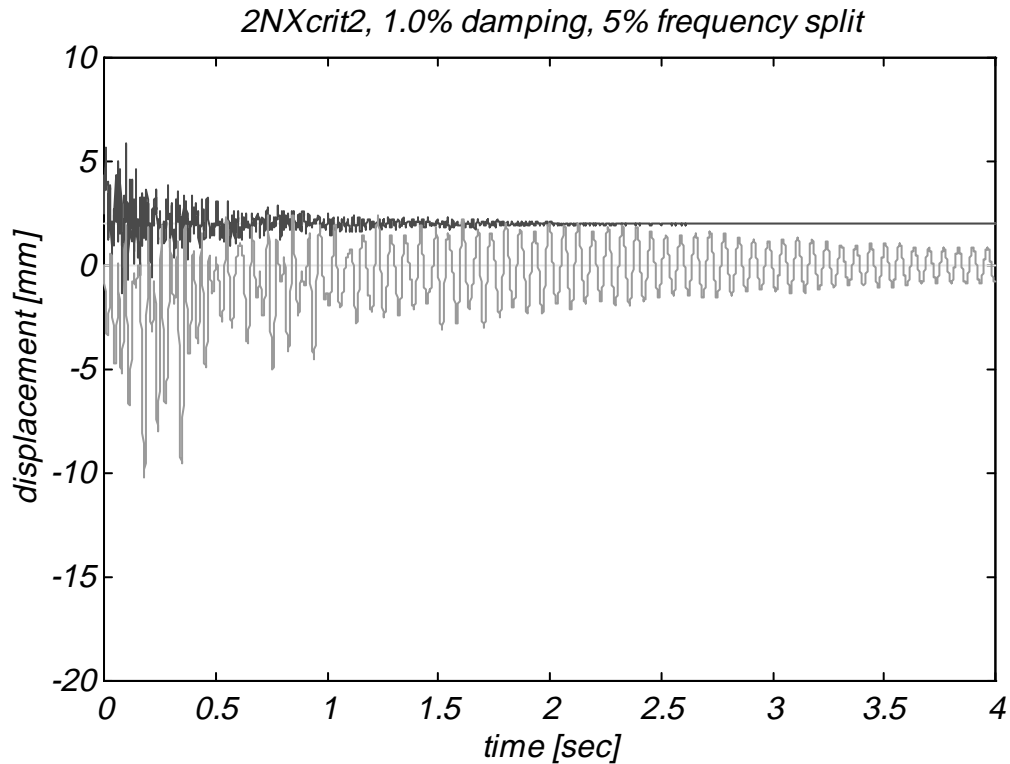


Figure 5-11: Response at critical speed, 1.0% damping, stator 5% mistuned

reducing the efficiency of the energy transfer consequently, bringing the responses to zero.

At the critical speed, Simulation 1, the responses of the tuned system with identical natural frequencies of the mode pair, become unstable, Figure 5-6. For the simulated mistuned system where the natural frequencies of the mode pair are split according to Equation (5-8), the responses remain stable and decay to zero within a few seconds, Figure 5-11. From the behaviour of the system at the critical speed, it is concluded that the structures' responses remain also stable at speeds other than the critical speed, a trend shown for the tuned system in the preceding paragraphs.

The degree of mistuning introduced to the stator is set to a realistic value for an aircraft-engine casing where gearboxes and other support structures may well introduce even larger mistuning, (Smailes, 1993).

5.4 Conclusions

The presented figures of the simulation results demonstrate the validity of the modelling method. The developed simulation tool is sufficiently flexible to investigate turbomachinery of arbitrary geometry. The geometry chosen for the presented simulation is that of the test rig in order to ease the comparison between the results of the simulation and the experiment. Once the eigensolutions of the structures, including the speed dependency of the modal properties of the rotating, part are available, the damping level and a small number of contact parameters must be chosen to set up the simulation. From there on the integration of the equations of motion is a standard procedure.

For the initial tests of engine-order excitation, the outputs from the designed numerical simulation, Chapter 4, are the expected results: both rotor and stator respond in a displacement similar to the applied, time-invariant force. For the stator this implies a time-invariant deflection, while for the rotor it implies a stationary wave, i.e., a counter-rotating wave progressing with a velocity equal and opposite to the speed of rotation.

The unstable area of the behaviour of the tuned system derived from the various simulations is sketched in Figure 5-12.

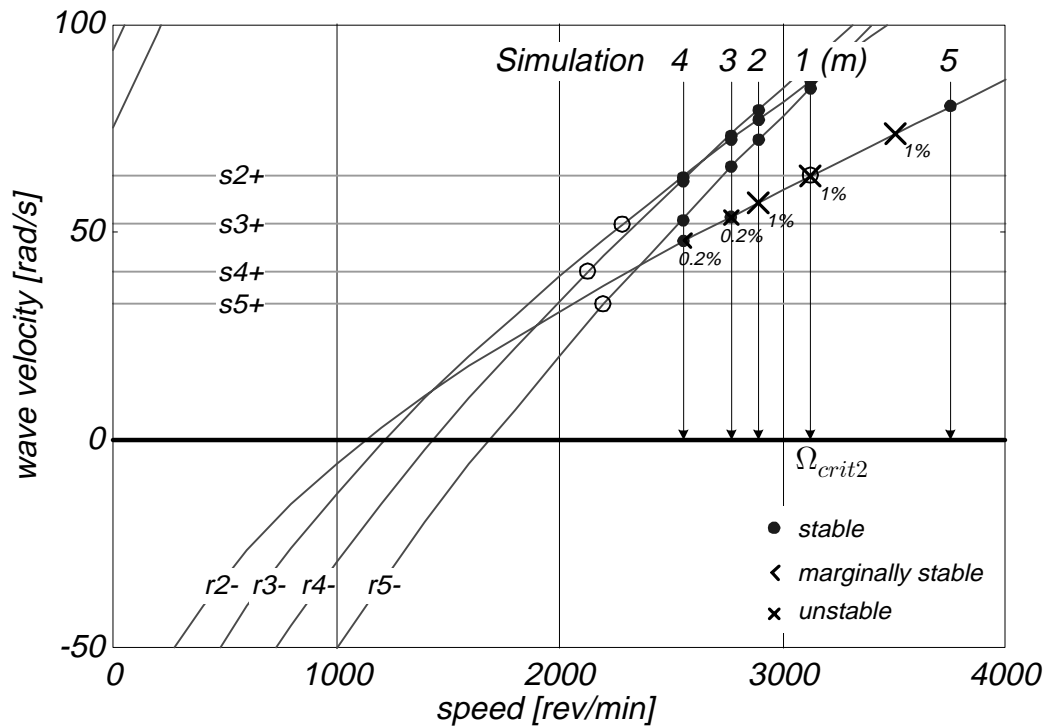


Figure 5-12: Stable and unstable areas of the system behaviour

The system response for the modes with other number of nodal diameters is stable for both levels of damping and in the speed range of the simulations (2560–3720 rev/min), hence it can be argued that the minimum differences of wave velocities ($\Delta\nu_3 = 3.7\pi$ rad/s, $\Delta\nu_4 = 7.0\pi$ rad/s, $\Delta\nu_5 = 6.4\pi$ rad/s) are sufficient to avoid the travelling-wave-speed instability.

For the mistuned system with 5% split in the natural frequencies, the system showed no unstable behaviour.

For the simulations of the travelling-wave-speed instability, the results exhibit the expected parameter dependencies:

- the initial gap controls the onset of the interaction, it governs the level of the initial disturbance that is required to bring the structures into contact;
- the required distance from the critical speed for stable behaviour is inversely proportional to the level of damping in the structures, the lower the damping the larger the unstable speed range around the critical speed; and
- at the critical speeds, where both structures are in resonance, only mistuning can avoid the establishment of the instability. Any realistic level of damping, up to 5%, did not change the quality of the behaviour at the critical speed.

With the results from the analysis and the simulation, the design of the test rig can be continued as it was shown that the two structures of this particular geometry have, at least theoretically, the potential to exhibit the travelling-wave-speed instability. In view of the later verification of the results obtained so far, emphasis was put on test cases that could be conducted experimentally.

The geometry of the structures used in the simulation was influenced by practical requirements of the experimental set up, the design of which is described in the following chapter.

Chapter 6: Design of the Test Rig

The validity of the analytical and numerical predictions of the previous chapters have to be proven experimentally. This chapter describes the design of the test rig, while the next chapter presents the measurements taken.

6.1 Purpose of the Test Rig

The purpose of the test rig is to conduct measurements of the travelling wave speed coincidence. In order to perform this task the rig has to support the rotor and the stator in a defined position; to drive the rotor at arbitrary speeds, including the critical speeds; to change the clearance between the two elements; to enable vibration measurements at different locations of the components; and to permit a controlled interaction between the rotor and the stator.

6.2 Rig Requirements

In addition to fulfilling the main tasks outlined above, the test rig should be as simple as possible so to facilitate modelling of and measurements on the rotor and the stator as far as possible. These simplifications must not affect the validity of the measurements or the relevance of the test results to engineering structures.

Necessary, identified, features of the travelling wave speed coincidence for the design are: *(i)* the existence of travelling waves in both structures, *(ii)* a relative speed between the two structures, and *(iii)* a coupling between tangential motion, collinear with the surface speed vector, and a second direction, such as axial vibration.

The first feature makes it mandatory to have symmetric structures. The second feature is achieved most easily by having relative rotation between the two structures. The third feature makes it necessary to have a two-dimensional vibratory motion, coupling two degrees of freedom.

These are the necessary features that must be present in the test rig, tests will show whether they are sufficient.

6.3 Design Simplifications

As turbo-machines are generally complex systems, major simplifications have to be made to make tests feasible.

6.3.1 Simplification of the geometry

A necessary feature mentioned above is the coupling of vibration in two dimensions. In most turbo-machinery, the vibration patterns are three dimensional, and the geometry is very complex in order to maximise the efficiency of the energy transfer. To reduce the complexity of the test rig, a design is developed that reduces the investigated vibration

patterns to two dimensions. A small coupling to the third spatial direction remains but can be neglected in the current analysis as it is small compared with the vibration in the two main directions.

The resulting design can be described concisely as a facing-discs design, and is shown in Figure 6-1.

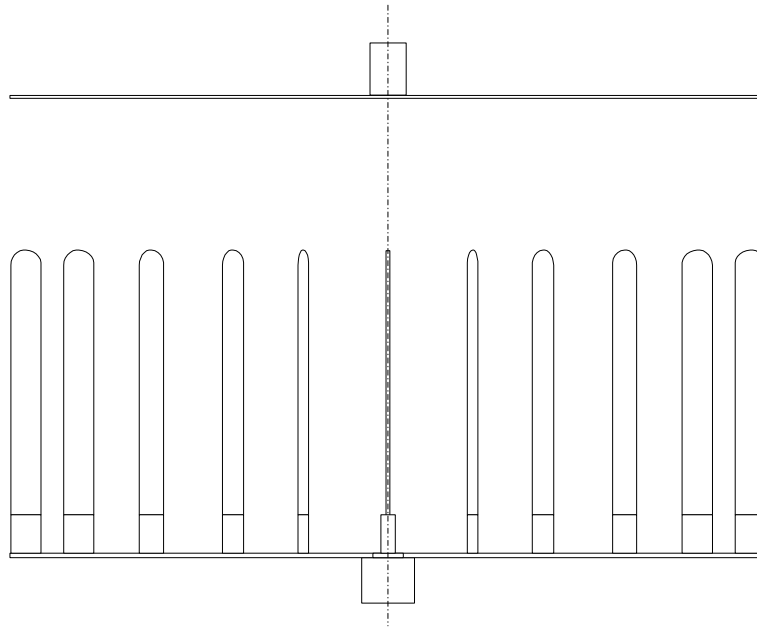


Figure 6-1: Facing-disc test rig design

One structure is represented by a plain disc and the other one by a disc to which blades of simplified geometry are attached by clamps. The blades are equally-spaced around the perimeter of the stator disc with their longitudinal axes parallel to the axis of symmetry. The structures rotate relative to each other, so that there is a tangential velocity at the location of the blade tips, where the structures are supposed to touch.

With this design, the complexity of the geometry is kept to the absolute minimum to fulfil the three requirements mentioned above. The motion of the structures will be predominantly axial vibration in the discs and axial and tangential vibration in the blades. By rotating each blade around the global axial direction, a radial component can be added to the predominantly tangential-axial motions of the blade tips as it is typical aero-engines.

6.3.2 Change of observer frame

One of the major changes compared with turbo-machinery is to change the speed of the parts around relative to a stationary observer: what is usually the bladed rotor is standing still in the test rig, and hence called the *stator* in this thesis, and the component which represents the housing rotates past it, hence called the *rotor* herein, Figure 6-2.

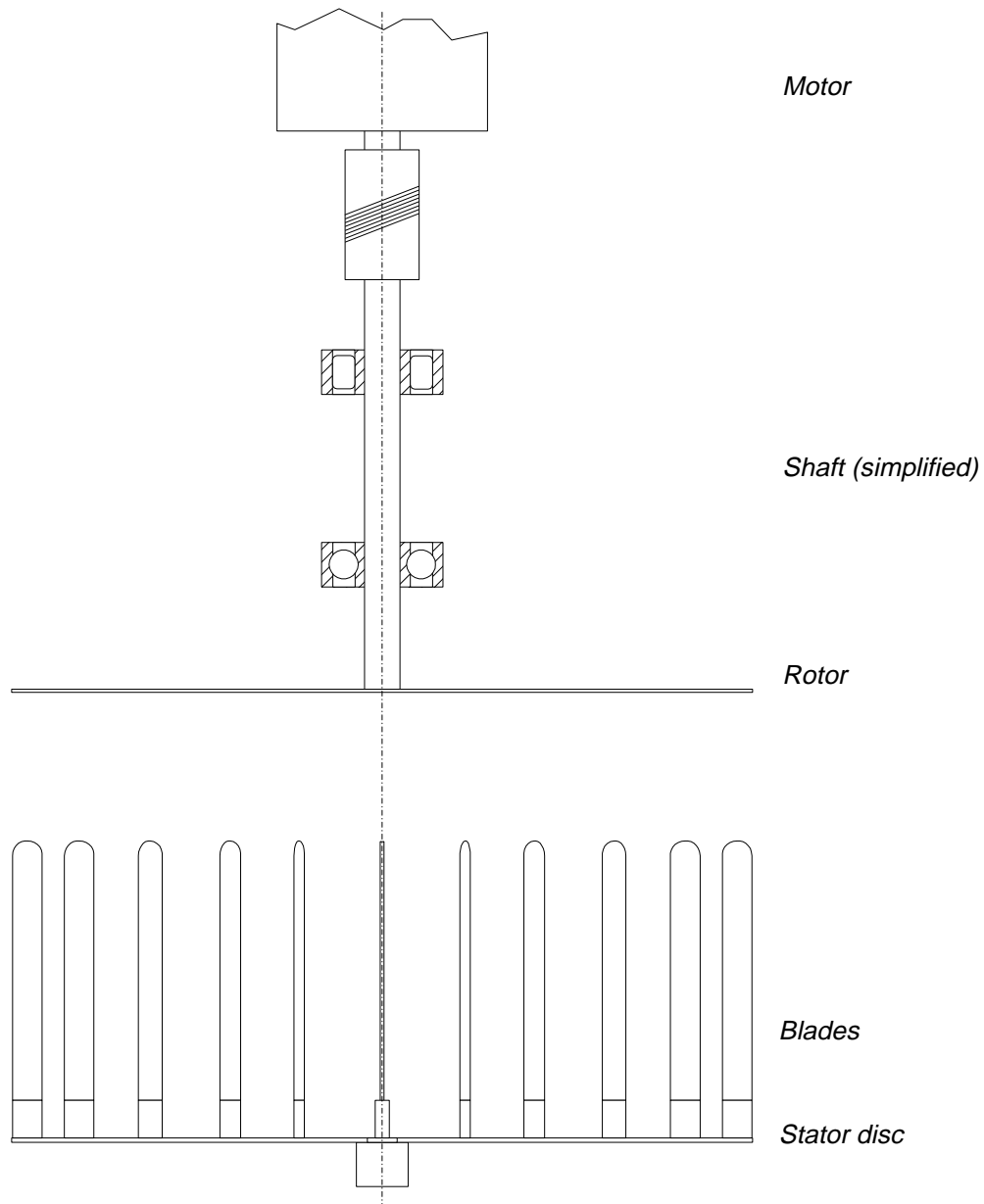


Figure 6-2: Notion of rotor and stator

Mathematically, the swap between rotor and stator is a change in the observer frame and the relation to express quantities in either reference frame, the body-fixed rotating or the stationary one, is a simple Galilean transformation. This change of rotor and stator leads to many simplifications:

- It makes the analysis simpler by splitting the tasks more evenly, as described in Chapter 3. Instead of a rotating bladed disc and a stationary unbladed structure, a non-rotating bladed structure and a rotating structure without blades must be analysed.
- It simplifies the experiment as the windage is reduced. Windage occurs now around the unbladed rotor only, and is much reduced as the rotor possesses only continuous surfaces. The aerodynamic forces are much smaller and can be considered small compared with the structural forces in the analysis. They will

enter the simulation as initial conditions and may modify the contact forces slightly. In addition, the reduced windage requires less power to drive the rotor and hence the available motor power can be used to maintain constant speed during the experiment.

- The design change simplifies measurements on the bladed structure.

Measurements of the blade dynamics are always of special interest to turbomachine engineers. Usually, this requires measurements in the rotating frame of reference which is always a demanding task. With the current design of the rig, taking measurement on the blades is considerably simpler as the blades do not rotate.

The change of reference frame is possible only because the test rig is designed to demonstrate the travelling-wave-speed instability and not to produce thrust by imparting impulse onto the working fluid.

6.4 Geometry Selection

The properties of the rotor and the stator determine the critical speed for the travelling wave speed coincidence.

6.4.1 Critical speed equation

The starting point of the design of the rig is Equation (3-29), relating the critical speed to the sum of the natural frequencies of the rotor and the stator, (Schmiechen, 1994):

$$n\Omega_{max} > \omega_{rn} + \omega_{sn} \quad \text{or} \quad \Omega_{max} > \nu_{rn} + \nu_{sn} \quad (6-1)$$

In order to investigate the travelling-wave-speed coincidence with the test rig, the maximum running speed, Ω_{max} , times the number of nodal diameters, n , must be larger than the sum of the natural frequencies of the rotor and stator, ω_{rn} and ω_{sn} , respectively. Or, using wave velocities, the speed of rotation must be larger than the combined wave speeds of rotor and stator, $\nu_{rn} + \nu_{sn}$.

Equation (6-1) governs the design of the rotor and the stator, whose interaction are to be studied on this rig.

6.4.1.1 Number of nodal diameters and number of blades

Because of the size of the displacement probes selected to take measurements on the rotor, the number of nodal diameters that can be investigated is limited. Due to the initially unknown behaviour at the travelling-wave-speed coincidence, non-contacting eddy-current sensors with a wide linear measurement range are selected. As the field disperses with distance, the displacement measurement is an average measurement over the target area, which is a circle of 25 mm radius for the selected sensors. Also, the probes cannot be placed closer than 125 mm to each other, and this limits the possible spatial resolution further. Both constraints make measurement of modes with higher

numbers of nodal diameters infeasible and thus limit the number of nodal diameters, the first quantity in the design equation, Equation (6-1).

Modes with 2 to 5 nodal diameters are selected for investigation. It is decided to make the number of blades a multiple of 2, 4 and 5 but not of 3, so that it is possible to check whether the travelling wave speed coincidence can be more easily excited by a number of blades that is an integer multiple of the number of nodal diameters under consideration. The lowest common multiple of 2, 4 and 5 defines the number of blades: $N_{blades} = 20$.

6.4.1.2 Speed of rotation

The speed of rotation is the second quantity in Equation (6-1) to be fixed. For safety reasons, it is desired to limit the running speed to about 3000 rev/min. This puts it at half the maximum speed of the motor and leaves some flexibility.

6.4.1.3 Natural frequencies of rotor and stator

It turns out that the speed constraint together with the design equation, Equation (6-1), is quite restrictive for the design of the laboratory rig, especially for modes with only a few nodal diameters.

Various alternatives to bring the sum of the rotor and stator wave velocities within this tight band of 3000 rev/min = 100π rad/s are checked. The influence of the main design parameters is as follows:

- Blade geometry: $\omega_{cantilever} \propto h/l^2$

The stator natural frequencies are governed mostly by the cantilever frequency of the blades and thus can be decreased by increasing the length of the blades. Reducing the thickness will reduce rapidly the out-of-plane load for plastic deformation as the critical load is proportional to $P_{crit} \propto h^3/l^2$, (Szabó, 1984).

- Disc geometry: $\omega_{disc} \propto h/r_o^2$

Increasing the outer diameter of the disc reduces the natural frequencies, but leads to a slender structure that is not easily handled. The design of the rig set the limit to about 550 mm. A larger disc makes measurements easier as the deflections can be expected to be larger and there is more space for the sensors.

Both rotor and stator natural frequencies are influenced by the thickness of their discs, so reducing the thickness lowers both natural frequencies. For the rotor, the reduction of natural frequency by a reduction in thickness vanishes at higher speeds. The membrane frequency, proportional to the speed of rotation, $\omega_{membrane} \propto \Omega/r_o$, and independent of the thickness of the disc, becomes more prominent at higher speeds and the reduction in frequency introduced by the change in thickness diminishes quickly at higher speeds. Reducing the thickness for the discs has the same constraints as for blades: the discs become floppy and deform plastically easily.

- Material: $\omega_{bending} \propto \sqrt{E/\rho}$

It would be possible to choose a material with a lower E/ρ -ratio than steel. This was not pursued further as the effect is only small and light high-strength material was not available. Reducing the modulus of elasticity by itself leads to soft materials which often have a smaller resistance to wear, (Rabinowicz, 1969).

From all the possibilities increasing the blade length has the most noticeable effect without having the large negative effects associated with the other options.

6.4.2 Fixing the geometry

In order to achieve the desired speed range the discs are made as thin and as large as reasonably possible and the blade length is adjusted to move the natural frequencies of the stator into the desired frequency band.

6.4.2.1 Rotor

From the maximum space of the motion-stage and the available material stock the geometry of the rotor is set to:

$$\begin{aligned} r_i &= 20 \text{ mm} && \textit{clamped} \\ r_o &= 250 \text{ mm} && \textit{free} \\ h &= 0.8 \text{ mm} \end{aligned} \tag{6-2}$$

From Equation (6-1) follows that the higher the number of nodal diameters, the larger the frequency band. For the elastic modes with more than one nodal diameter, the ratio of natural frequency over nodal diameter, the wave velocity, increases linearly with the number of nodal diameters for a circular disc, Equation (2-92). For higher speeds, the wave velocity increases more slowly with the number of nodal diameters, Figure 6-3, for a disc with the geometry of the rotor, given in Equation (6-2).

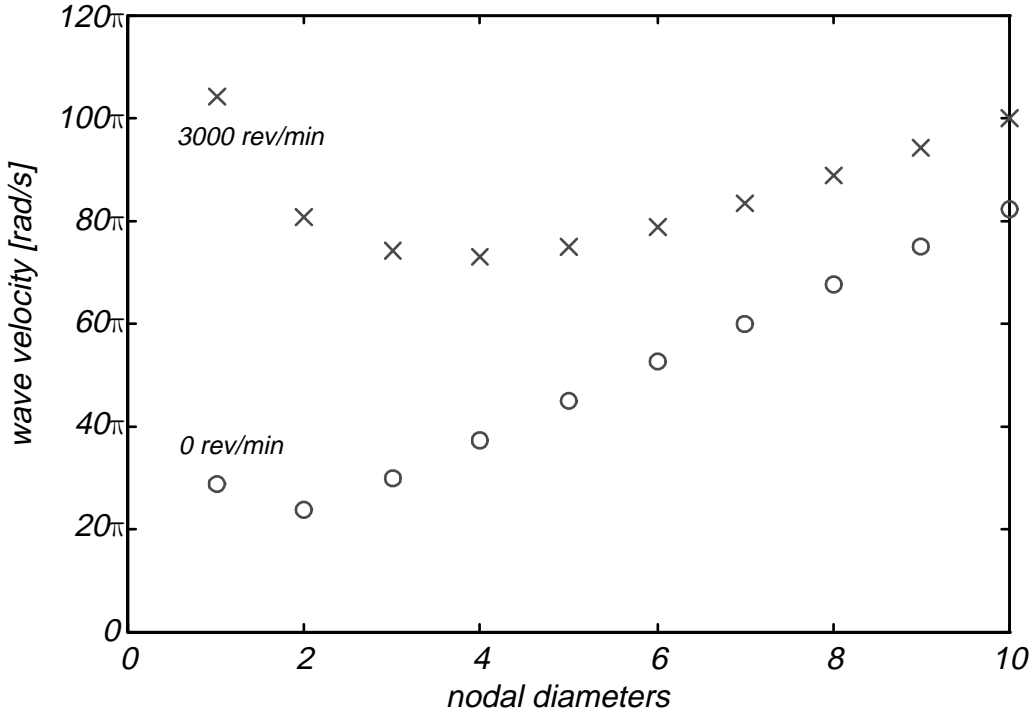


Figure 6-3: Rotor wave velocity as a function of nodal diameter and speed of rotation

6.4.2.2 Stator

After the rotor geometry is fixed, Equation (6-2), the required wave velocities of the stator are fixed, too. Equation (6-1), with the desired maximum speed of rotation of 3000 rev/min and the data from Figure 6-3, confines the wave velocities of the stator to about 20–30π rad/s. By varying the blade length, the wave velocities of the stator waves can be moved into the required band determined by Equation (6-1).

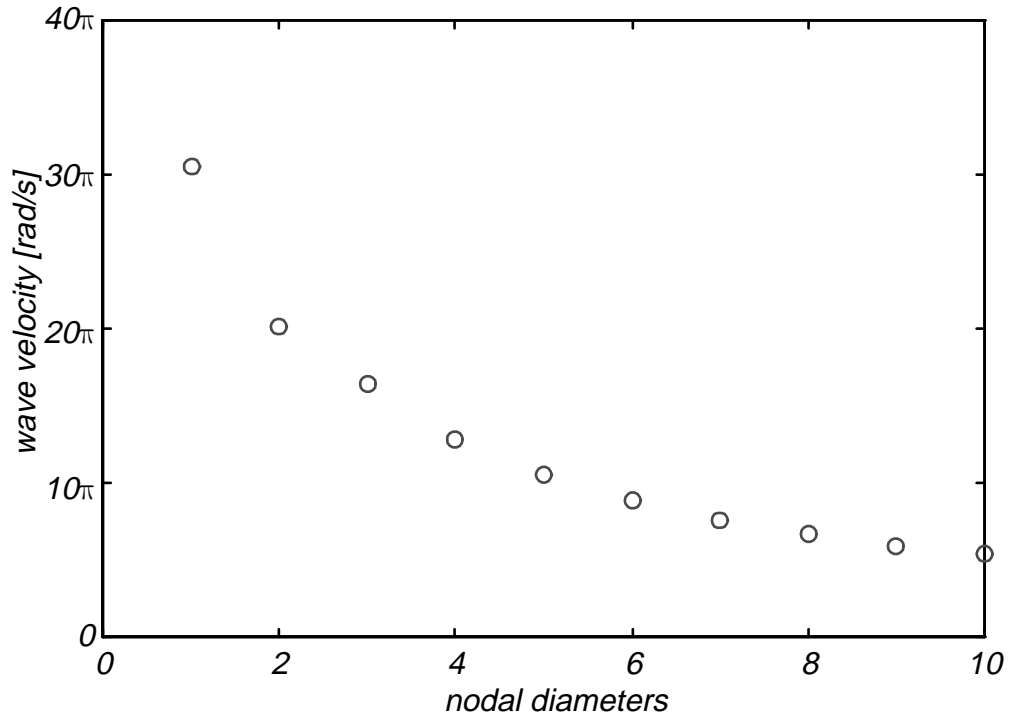


Figure 6-4: Stator wave velocity as a function of nodal diameter

The disc and blade geometry of the stator is fixed at:

$$\begin{aligned}
 r_i &= 20\text{ mm} && \textit{clamped} \\
 r_o &= 250\text{ mm} && \textit{free} \\
 h &= 1.0\text{ mm}
 \end{aligned} \tag{6-3}$$

to which N_{blades} (=20) blades with the following geometric data:

$$\begin{aligned}
 l &= 175\text{ mm} && 10\text{ mm radius at free end} \\
 w &= 20\text{ mm} \\
 h &= 1.0\text{ mm}
 \end{aligned} \tag{6-4}$$

are attached by means of rigid clamps:

$$\begin{aligned}
 l &= 25.4\text{ mm} \\
 w &= 20\text{ mm} \\
 h &= 9.5\text{ mm}
 \end{aligned} \tag{6-5}$$

With this geometry of the rotor and stator, the critical speeds of the selected 2-, 3-, 4-, and 5-nodal-diameter, 0-nodal-circle modes are located in a speed range from 2000 to 3500 rev/min, Table 6-1, Figure 3-13:

n	2	3	4	5	6	7	8
Ω_{crit} [rev/min]	3126	2281	2129	2206	2366	2563	2779

Table 6-1: Predicted critical speeds for 0NC family

6.4.3 Axis direction

With the geometry of the individual structures fixed, the ensemble can be rotated freely in space. Early in the design stage it is decided to build the rig with a vertical axis. This makes the influence of gravity on the deflections more deterministic: the resulting bending moment acts over the whole vibration cycle in the same direction, Figure 6-5.

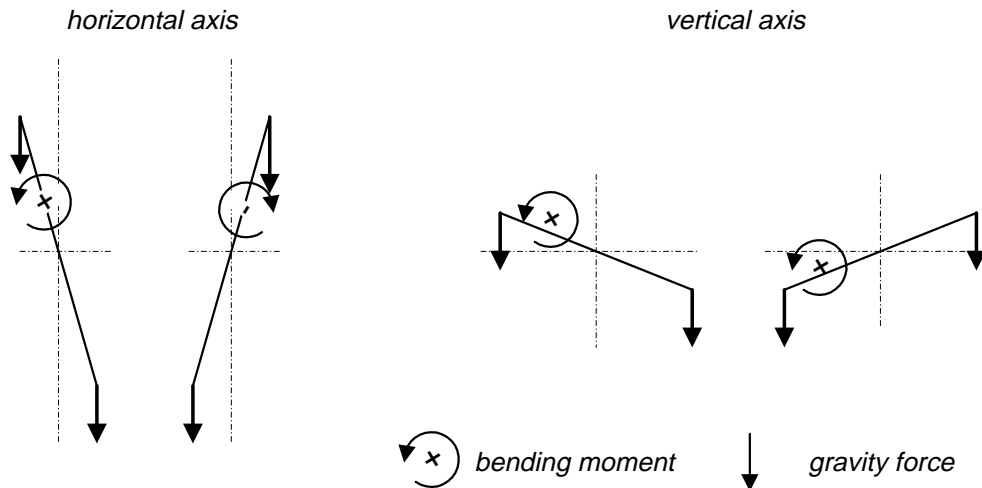


Figure 6-5: Influence of gravity in different axis orientations

At high speeds, the centrifugal forces are much stronger than the gravity force and the decision to design for a vertical axis might seem overcautious, but conducting tests and making measurements are simplified in the vertical axis arrangement as sensors can be moved around with relative ease in this layout.

6.5 Alignment of Rotor and Stator

In the analysis of the interaction phenomenon, it is assumed that contact occurs symmetrically around the axis of rotation at as many positions as nodal diameters under investigation. In order to produce this condition in the experiment, the two structures need to be aligned with respect to each other, as otherwise, further dynamic components show in the measured response.

6.5.1 Problem definition

The axes of the rotor and stator are to be made coincident. This shall be called aligning the rotor and stator.

6.5.2 Alignment dilemma

The rig is designed to have both structures isolated from each other, so that the only available interface are the blade tips contacting the rotor. For that reason the rotor is mounted to the wall and the stator rests on the floor that is vibration-isolated from the wall.

This compliance, desired for the vibration isolation, makes the task of alignment very difficult. For the slightest change of the centre of gravity the position of the stator support may have changed due to the high floor compliance. Given the weight of the support and the rough handling capabilities, a change of position is almost unavoidable.

So, even when the floor compliance does not change with time, its very existence increases the difficulty considerably.

One first step to reduce the position uncertainty introduced by the compliant floor is to confine the position of the feet to a small area by resting the support on rigid blocks.

6.5.3 The global error motions

The position of one frame of reference with respect to another frame is defined by six independent quantities: three translations and three rotations. In the present case the quantities describe the position of one axis of symmetry with respect to the other axis, and are, as the axes are supposed to coincide, called the global error motions.

Local error motions are the possible motion of adjustment elements between the two reference frames. In the rotor-stator problem, the change of position in the z -direction of the four feet are such local error motions.

6.5.4 Solution to the alignment problem

6.5.4.1 Alignment algorithm

Making rotor and stator axes coincide, requires correction of translational and rotational error motions, (Schmiechen and Slocum, 1996). The current set-up demanded a three-step procedure: (i) reducing the translational error motions for one point on the axis, (ii) cancelling the rotational error motions, and (iii) correcting translational error motions re-introduced by step (ii). The proposed method converges to an accuracy of order two for both translations and rotations.

To carry out the alignment requires the ability to measure the error motions and to relate the measured global error motions to corrections to be applied to the constraints determining the relative position of rotor and stator.

6.5.4.2 Measurement of the error motions

Two cases need to be considered: measurement of translational and rotational error motions. The measurement of translations is accomplished relatively easily by means of a x - y - z -motion stage. For the proposed method, the translational error motions are never quantified, but corrected only. In contrast, the rotational error motions must be measured. Measuring angular quantities is difficult and most measurement principles deduce these quantities from measurement of linear quantities, in the present case from the facing side and the hypotenuse of a right-angled triangle.

6.5.4.3 Algorithm to determine local error motions

The local error motions, i.e., the changes of elevation of the positions where the support structure rests on the floor, its feet, are linked to the global translational and rotational error motions by the system matrix, (Schmiechen and Slocum, 1996):

$$\{\delta_{local}\} = [S]^T \{\delta_{global}\} \quad (6-1)$$

where $\{\delta_{global}\} = \{\delta_x \ \delta_y \ \delta_z \ \varepsilon_x \ \varepsilon_y \ \varepsilon_z\}^T$ are the magnitudes of the global error motions (in the direction of the coordinates) and $\{\delta_{local}\} = \{\delta_i\}^T$ are magnitudes of the local error motions (in the directions of the contact-normals of the feet), i is the number of feet. If the local error motions are applied to the system, the global error motion will be reduced to zero.

The system matrix, $[S]$, is composed of the geometry of the problem: the position of the constraints of the support in a coordinate system located in the tip of the stator, $\{r\}_i$, and the direction of contact by $\{n\}_i$, defined by the columns of $[S]$:

$$\{S\}_i = \begin{Bmatrix} n_i \\ r_i \times n_i \end{Bmatrix} \quad (6-2)$$

With the translational error motions being zeroed in the first step, and corrected again in the last step, and the third rotational degree of freedom not to be corrected, as it coincides ideally with the axis of rotation, only two rotational error motions, ε_x and ε_y , must be corrected in the present problem. Thus only the two corresponding rows from the system matrix need to be retained:

$$\{\delta_{local}\} = [S_{red}]^T \begin{Bmatrix} \varepsilon_x \\ \varepsilon_y \end{Bmatrix} \quad (6-3)$$

Ideally, a structure should be designed deterministically as only then can the local error motions be identified uniquely from the global ones without making any assumptions on the deformation state of the structure. In the case at hand, three feet or constraints would restrict the position of the stator support uniquely, (Slocum, 1992). The stator support used has four feet or constraints, and so it is over-determined which can cause problems in the correction of the error motions as one of the feet may lose contact.

6.5.4.4 Practical procedure

After inspecting the support, the coordinate system is selected so that the normal vectors are all given by $\{n\}_i = \{0 \ 0 \ 1\}^T$ and the position vectors are determined from relative measurements between the feet and the origin of the coordinate system fixed in the centre of the stator disc. This way, only distances need to be measured, not their projections onto the coordinate axes. The stator is mounted on an x - y - z -motion stage which rests with four feet on the vibration-isolated floor of the laboratory, so $3 \times 4 = 12$ quantities are to be determined. Due to symmetry of the support and the assumption that all four feet lie in

one plane, only 7 quantities have to be determined requiring at least as many measurements. More measurements can be used to obtain a least-squares solution. With the positions of the constraints determined the actual alignment can commence:

The first step is to reduce the translational error motions of the stator tip to zero. This can be done easily with the linear adjustments of the motion stage. To increase the accuracy, pointed tips are mounted on each axis.

The second step is to determine the angular error motions. As mentioned before, they are commonly deduced from measurements of distances. So, too, in the current set-up where a gauge is fixed the rotor, measuring the change of distance to a disc fixed to the stator. First, the gauge is rotated one full revolution. This record contains the sought information from which the error motions can be computed but also the distortion of the disc, as no engineering structure can be made perfectly flat. The shape of disc is measured in a second step by rotating the disc while keeping the gauge in a fixed position. Under the assumption that the axis of rotation does not change during the rotation, this second trace records the shape of the disc only. The difference of the two records is then proportional to the deflection caused by misalignment between the two axes. This can be converted into an angle knowing the radius of the circle prescribed by the gauge.

The correctable error motion is the rigid-body tilting. This component is obtained by either curve-fitting or by Fourier decomposition. The value will generally be complex: $\varepsilon_y + i\varepsilon_x$ where the subscripts indicate the axis of rotation, and the order and sign of the terms depends on the starting point of the measurement, which is chosen to be $(0, -r_{gauge})$.

After applying the corrections to the four feet, any introduced translational error motion is minimised in the same way as described in the first step. A final check on the correction is then carried out: in the current problem, the angular error motions are reduced by a factor of more than 20, reducing the resulting deflection at the rim of a 500 mm disc from about 2.5 mm to less than 0.1 mm.

This complex procedure is developed for this specific case; with a six-degree-of-freedom motion stage, the solution of the problem is considerably simpler.

6.5.5 Results

Figure 6-6 shows the measurements from the disc. The trace labelled 'measurement' is taken with the gauge rotating, the trace labelled 'disc shape' with the disc rotating and the gauge standing still. The first measurement contains both disc shape and readings due to the misalignment, but the datum contains only the disc shape, which explains the necessity to subtract the disc shape in order to extract the correctable error motions properly.

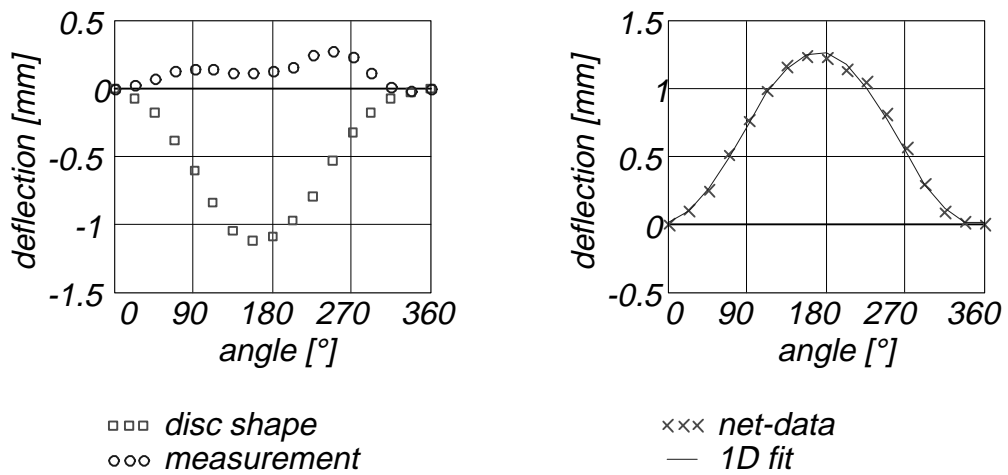


Figure 6-6: Initial error-measurements

The global error motions are determined from a curve-fit or the Fourier series:

$$\varepsilon_y + i\varepsilon_x = -4.16 + i0.70 \text{ mrad} \tag{6-4}$$

which results in local error motions of (4.2, 4.0, 0.3, 0) mm. Applying these to the four feet reduced the global error motions to:

$$\varepsilon_y + i\varepsilon_x = -0.13 + i0.16 \text{ mrad} \tag{6-5}$$

Figure 6-7 shows the final error motion on a different scale.

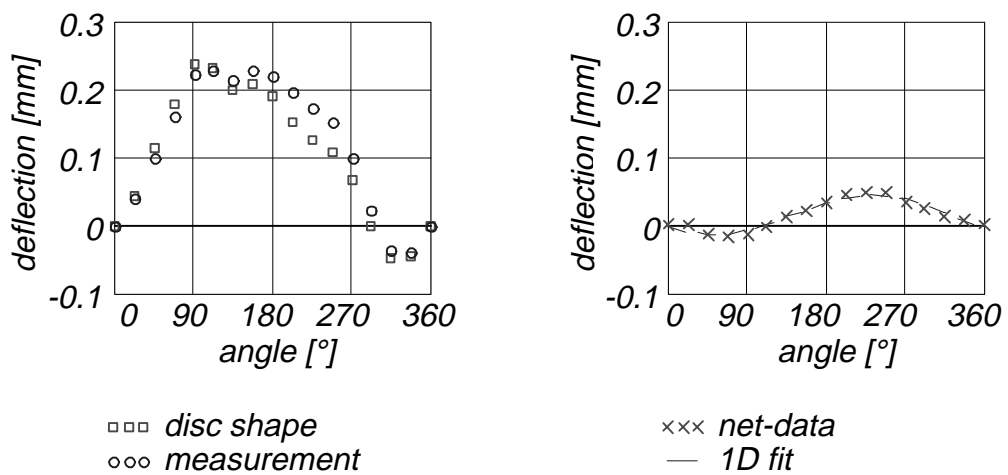


Figure 6-7: Final error-measurements

The residual local error motions are less than 0.2 mm which is considered not correctable, due to the problems that the compliant floor causes. The final error compares very favourably with the initial error, Figure 6-8

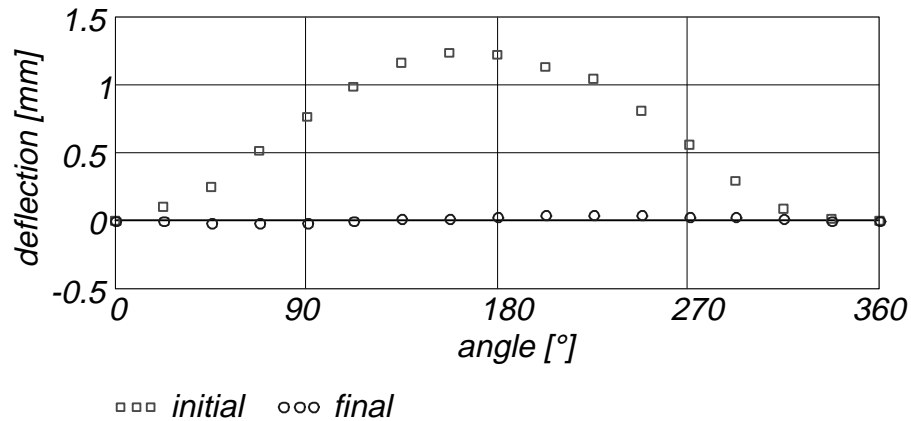


Figure 6-8: Comparison between initial and final error

6.5.6 Discussion

In the process of applying the computed corrections it is found difficult to maintain the absolute position of the base. This is due to the weight of the stator support and the difficulty of finding appropriate attachment points for the lifting gear. Also the location of the feet is not very well defined, even after small metal plates are used to ensure that the support rests only at the four corners. The exact knowledge of the position of the four feet enters the system matrix and affects the accuracy of the computation directly.

The alignment process turns out to be more intricate than initially assumed mostly due to the compliant floor. It causes a residual global error motion after the computed corrections are applied. As described above, the compliant floor is necessary to isolate rotor and stator from each other so that no energy can pass through the structural supports. Some time dependency of the floor compliance is noted and so some settling time has to be allowed to ensure that the steady-state condition is reached after the corrections are applied. Not waiting long enough for this settling to finish can cause ‘mis’-readings in the process of aligning the rotor and the stator.

6.6 Balancing of the Rotor

6.6.1 Goal of balancing

The aim of balancing is to reduce the reaction forces transmitted from the rotor into its support and, subsequently, the vibration caused by unbalance forces. These forces stem from asymmetric mass-distributions, or unbalances, caused by manufacturing tolerances present in all engineering structures. The unbalance force is synchronous with the speed of rotation and increases with its square:

$$F_{\Omega} = me\Omega^2 \quad (6-6)$$

The product unbalance mass, m , and the distance of the centre of gravity from the axis of rotation, e , is called the unbalance, (Krämer, 1993):

$$U = me \quad (6-7)$$

Balancing seeks to reduce this unbalance as much as possible, ideally to zero.

At low speeds the response due to the unbalance force may be negligible, but at higher speeds the unbalance response can become very large, a situation which is undesirable from a point of view of fatigue-life and acoustics.

6.6.2 Requirements

In order to balance a rotor successfully, its design must accommodate the needs of balancing. The design must include ‘balancing planes’ to which masses can be attached to or removed at angular locations. From Equation (6-7) it can be deduced that the larger the radius to which the masses are applied, the smaller the balancing masses can be. By design, measurements of either force or response of the rotor should be possible close to the points where the responses are to be minimised. More balancing planes will allow for more accurate balancing.

In addition, the absolute angular position of the rotor must be available to change the mass-distribution of the rotor correctly.

6.6.3 Balancing method

There exist many methods to balance a rotor, (Darlow, 1990, Ehrich, 1992), increasing the sophistication to accommodate for multiple planes, higher speeds, flexible rotors, modular design, to name but a few.

6.6.3.1 Principle

The underlying idea of all these methods is to counteract the unbalance $U=me$, Equation (6-7), by introducing balancing masses:

$$\{U_b\} = -\{U\} \quad (6-8)$$

where the unbalance is assumed to be a vector with N elements, N being the number of balancing planes.

6.6.3.2 Method of influence coefficients

In the present case, the method of influence coefficients is chosen for its ease of application. Depending on the measurement, this method can minimise response or reaction force, and response measurements are chosen in this case. The method is simple in that it only tries to minimise the response at one selected speed of rotation. It can be extended to more speeds by maintaining orthogonality between the balancing masses, but

this is not pursued further, because the next critical speed is well beyond the intended speed range.

For the considered linear time-invariant systems, the speed-synchronous Fourier-components of the displacements, $\{x(t)\}$, are related to the unbalance, $\{U\}$, by the constant square matrix of the influence coefficients, $[\alpha]$:

$$\{x\} = [\alpha]\{U\} \quad (6-9)$$

where the arguments are dropped for brevity. The phase of the signals is identified uniquely through the absolute position mark from the rotor encoder.

The goal is to determine $[\alpha]$ which is required to compute the ‘counter-balance’, Equation (6-8):

$$\{U_b\} = -[\alpha]^{-1}\{x\} \quad (6-10)$$

The initial unbalance, $\{U\}$, is unknown (otherwise the exercise was unnecessary) and the system response to known perturbations will be used to obtain the necessary information. This is done by attaching a trial mass of known mass to the rotor, causing an additional unbalance $\{U_1\}$:

$$\{x_1\} = [\alpha]\{U_1 + U\} \quad (6-11)$$

or, using Equation (6-9):

$$\{x_1 - x\} = [\alpha]\{U_1\} \quad (6-12)$$

As $[\alpha]$ has N^2 elements, this equation does not suffice to determine all influence coefficients. In order to do so, at least N independent tests have to be conducted. Then, assuming that $[\alpha]$ is time-variant:

$$[\{x_1 - x\} \dots \{x_N - x\}] = [\alpha][\{U\}_1 \dots \{U\}_N] \quad (6-13)$$

and given the independence of the measurements, $[\alpha]$ can be determined from:

$$[\alpha] = [X][U]^{-1} \quad (6-14)$$

and the balance mass can be determined from Equation (6-10).

6.6.3.3 Practical limitations

The method as presented assumes total linearity of the rotor in its support. Due to bearing clearances and other effects, the axes of typical rotors will move slightly when rotated through 360° . This static run-out cannot be corrected by balancing as it is not caused by the unbalance. It is recorded at low speed, where the unbalance response is assumed to be negligible, and subtracted from the signals at higher speed.

Most measurements during balancing are differential measurements to start with, so only Equation (6-10) changes to:

$$\{U_b\} = -[\alpha]^{-1}\{x - x_s\} \quad (6-15)$$

If a rigid rotor is balanced in more than one plane, the measurements may not be independent and the inverse may produce undesirable results. In this case the inverse should be formed by singular value decomposition. More measurements can be taken to obtain the least-squares inverse with the advantage to reduce the effects of measurement error.

Also, the influence balancing minimises the responses for the speed at which the balancing is carried out. If it is impossible to drive the rotor at the desired speed due to the large initial unbalance response, a preliminary balancing must be carried out at a lower speed to reduce the level of vibration at the desired speed.

6.6.4 Results

The outlined procedure will be demonstrated on the two-plane balancing of the rotor of the test rig. The initial step is to record the static run-out from the upper and lower plane:

$$\{x_s\} = \begin{pmatrix} 0.134 \angle -17.3^\circ \\ 0.066 \angle -47.0^\circ \end{pmatrix} \quad (6-16)$$

This is done at 500 rev/min, well below any resonance and at a speed where the unbalance response is still negligible. The second step is to record the unbalance response at the desired speed, chosen to 3500 rev/min:

$$\{x\} = \begin{pmatrix} 0.165 \angle 9.7^\circ \\ 0.162 \angle 57.5^\circ \end{pmatrix} \quad (6-17)$$

Now two experiments are conducted: in the first the balancing mass is attached to the upper plane and in the second the same mass is attached to the lower plane:

$$\{x_1\} = \begin{pmatrix} 0.176 \angle 5.0^\circ \\ 0.162 \angle 50.7^\circ \end{pmatrix} \text{ and } \{x_2\} = \begin{pmatrix} 0.175 \angle 5.3^\circ \\ 0.162 \angle 51.1^\circ \end{pmatrix} \quad (6-18)$$

Looking at these vectors in detail one can see that their difference is very small, that is to say, they are almost linearly dependent. The balance masses computed by direct inversion are:

$$\{m\} = \begin{pmatrix} 33.3 \text{ g } \angle -3.8^\circ \\ 34.4 \text{ g } \angle -177.6^\circ \end{pmatrix} \quad (6-19)$$

These are very large and, according to the computation, must be attached almost opposite to each other. If, instead, the singular value composition is used in the inversion of the influence coefficient matrix, the following balancing masses for the upper and lower plane are obtained:

$$\{m\} = \begin{pmatrix} 2.4 \text{ g } \angle -76.5^\circ \\ 2.2 \text{ g } \angle -77.8^\circ \end{pmatrix} \quad (6-20)$$

The masses are much smaller now and effectively put a combined mass of 4.6 g at about 77° , to balance an unbalance of 4.6 g at about 103° . Returning to the masses obtained by direct inversion, one notices that the phase was computed very poorly, too.

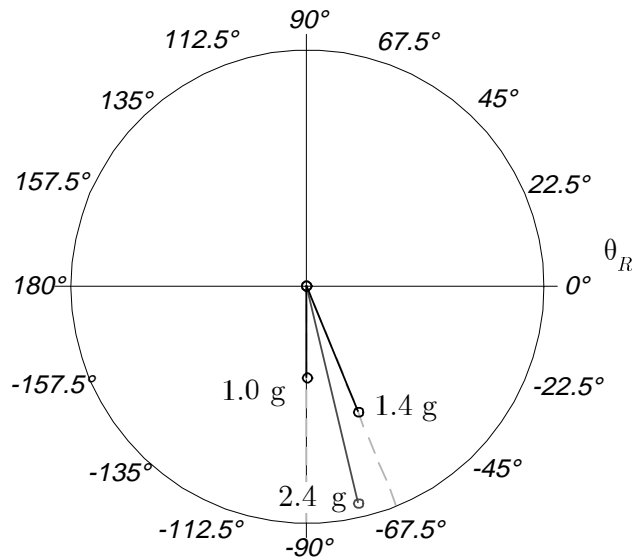


Figure 6-9: Vectorial split of upper balance mass

The balancing masses cannot be attached at arbitrary locations for the given rotor design, but are to be attached at tapped holes placed 15° apart, and so the resulting balancing masses have to be split vectorially, see Figure 6-9 for the mass of the upper balancing plane.

The effect of the balancing on the vibration level at the balancing speed is shown in Figure 6-10. It can be seen that the balancing is carried out successfully as the residual response is almost identical to the uncorrectable static run-out.

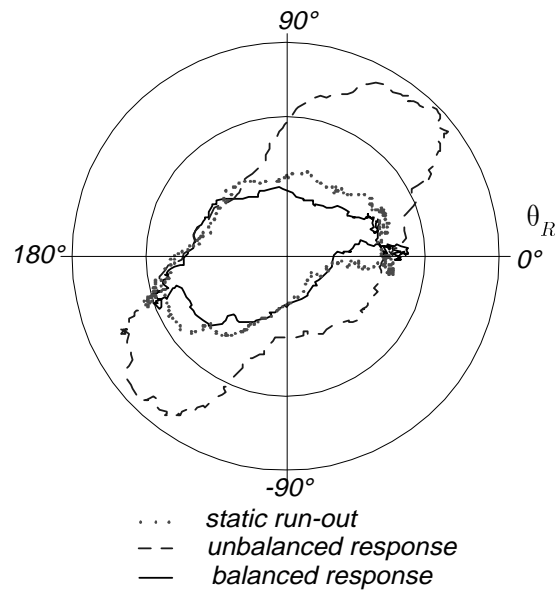


Figure 6-10: Radial response of upper balancing plane before and after balancing

Any further improvement requires the change of other parameters, like correcting the clearance in the bearings, or, generally, making the support more deterministic.

6.7 Safety and Overload Protection

As the design of the rotor allows for rotation speeds of up to 6000 rev/min, appropriate safety precautions must be taken. The kinetic energy contained in the rotor at maximum design speed can be computed with the actual geometry, given in the Appendix, to

$$K = \frac{1}{2} \int v^2 dm = \frac{1}{2} \int_{r_i}^{r_o} (r\Omega)^2 (\rho A dr) \approx 25 \text{ kJ} \quad (6-6)$$

To dissipate this energy in the case of an accident, a cage of 25 mm steel bars encloses the rotor at all times. In addition, 10 mm-thick polycarbonate sheets ensure that any smaller parts are contained. Emergency buttons and overload circuits triggered by the displacement sensors cut the electric power to the motor immediately. The non-contacting proximity probes are protected by their long range, protective covers, and the overload circuit.

The motor shaft is protected from excessive structural loads by a helical coupling which limits the transmitted torque and the residual radial and axial forces from the rotor shaft, Figure 6-11. The locating and non-locating bearings of the rotor shaft take the radial and axial loads, both static and dynamic. The rotor disc is connected to the lower end of the shaft by preloaded conical Belleville springs. This attachment acts as an overload protection for the bending moments or the torque.

During the travelling-wave interaction, the forces are predicted to be symmetric so that no bending moments should exist in either structure. In cases where they do exist, the

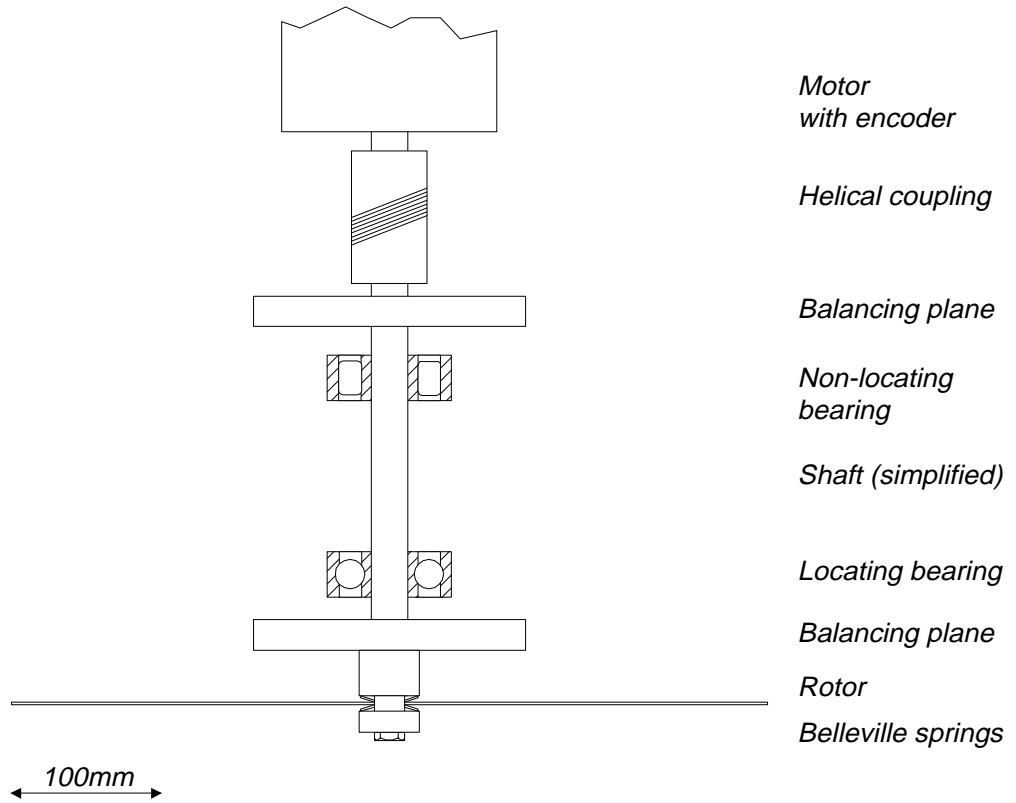


Figure 6-11: Rotor arrangement

stator rests above the motion-stage on a rigid support that provides, for the assumed load levels, rigidity against moments and forces. The stator is not mounted directly on the rigid motion stage so as to allow easy access to the stator from below for measurement equipment, Figure 6-12.

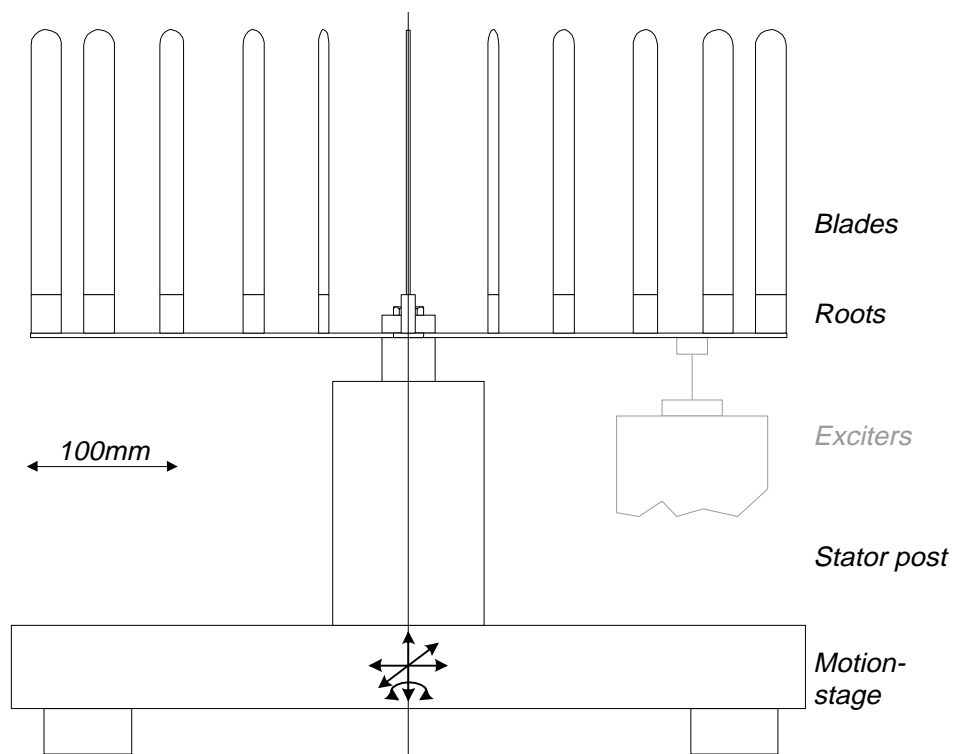


Figure 6-12: Stator arrangement

6.8 Data-Acquisition System

The subroutines necessary data-acquisition system are written as an extension to MATLAB. They control the two- and four-channel wave-form generation and the data-capturing of up to 16 channels at up to 72 kHz (single-channel) continuously to the hard disc. Thus, long time records can be stored to analyse slow transient phenomena at high temporal resolution. The response channels can be low-pass filtered by a programmable, 8-pole, 16-channel filter with variable cut-off frequencies.

In addition to the vibration response, the absolute shaft angular position is available as an analogue signal output from an encoder, from which the instantaneous speed of rotation can be derived. In a preliminary analysis it turned out that knowledge of the absolute phase angle is very important and its availability in this test rig increases the quality of the post-processing considerably.

The advantage of using a personal computer with software instead of a dedicated analyser is the significant gain in flexibility of employed analysis routines. In particular, frequency shifts as they occur in rotating machinery may render standard procedures less useful or meaningless. An open software solution can accommodate all these effects and will simplify development of further analysis routines.

6.9 Conclusions

A vertical rig has been designed with the potential to demonstrate the travelling-wave-speed coincidence between a rotor and a stator. The rig's purpose is to demonstrate the travelling-wave-speed coincidence for modes with different nodal diameters at rotation speeds below 3000 rev/min.

The change of observer frame from the stationary reference frame with a non-rotating plain stator and a rotating bladed disc to a rotating reference frame with a bladed stator and a rotating plain disc has many advantages: it reduces the complexity of the analysis of the structures, it simplifies the measurements on the bladed structure, and it makes the experimental set-up safer. Analysis shows that the results from this test rig are applicable to turbo-machinery with standard geometry of rotating bladed discs.

The test rig is fully instrumented and controlled via a PC. 16 input channels record time histories of non-contacting displacement sensors. Additionally, the absolute angular position of the rotor is recorded synchronously with the displacement data. High sampling rates and long record lengths are both possible at the same time.

The data can be manipulated subsequently. For the most frequent analysis tasks, MATLAB programs are written.

Chapter 7: Experimental Results

Once the test rig described in Chapter 6, was designed, and its dynamic properties were confirmed by modal tests, presented in Chapter 2, experiments were conducted to prove the existence of the travelling-wave-speed instability.

7.1 Aim of the Test Program

The main purpose of the experiments described in this chapter was to demonstrate the existence of the travelling-wave-speed instability. In addition, experiments were carried out to prove the validity of the model developed in Chapter 4 of this thesis and to demonstrate some of the predicted parameter sensitivities.

7.2 Travelling-Wave-Speed Coincidence Diagram

The speed-dependent modal properties of the rotor and the modal properties of the stator were obtained from the preliminary tests and the parameters of the prediction tools were corrected accordingly.

The validated travelling-wave-speed coincidence diagram is plotted in Figure 7-1.

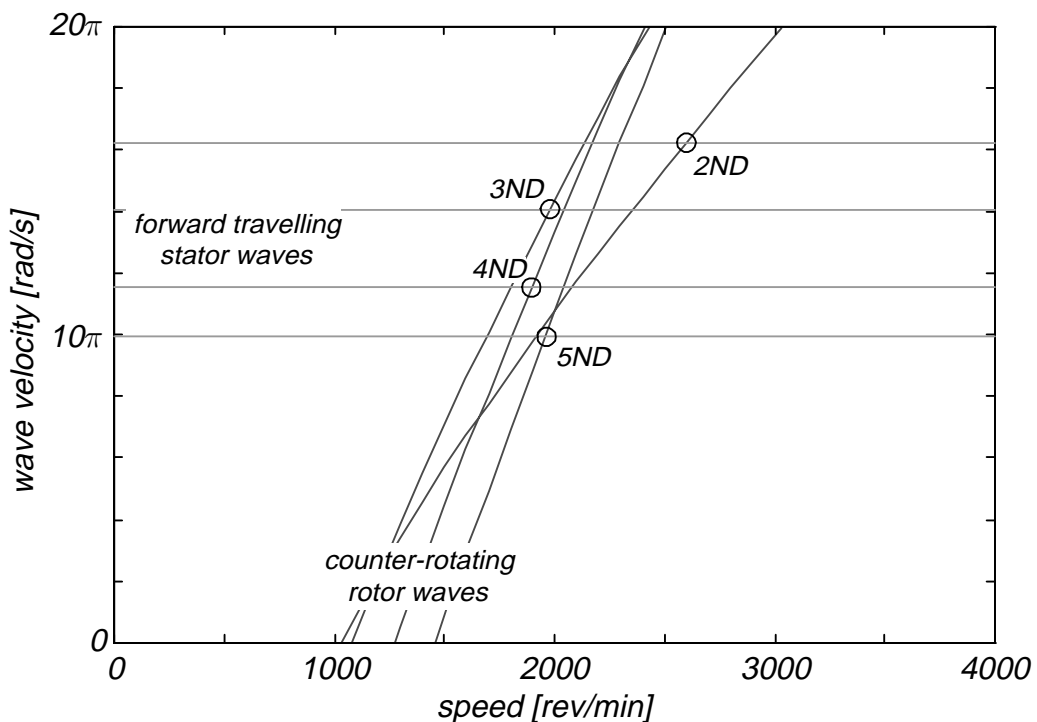


Figure 7-1: Interaction diagram, wave velocities, tuned condition

Figure 7-1 displays the same quantities as Figure 3-13, but is based on the measured quantities. It exhibits all the information necessary to conduct the experiments and analyse the data. The critical speeds are computed as:

n	2	3	4	5
$\Omega_{crit,n}$ [rev/min]	2590	1980	1900	1960

Table 7-1: Measured critical speeds of the tuned system

The critical speeds of the waves with 3, 4, and 5 nodal diameters lie within a band some 80 rev/min wide, and their wave velocities within about 4π rad/s. It was anticipated that exciting these travelling-wave speed coincidences separately would be more difficult than exciting the 2ND coincidence and hence the investigation concentrated on the 2ND coincidence.

The displacement sensors do not measure wave velocities directly but frequencies and so, in order to make the interpretation of the following experimental results easier, Figure 7-1 is replotted for the natural frequencies, Figure 7-2.

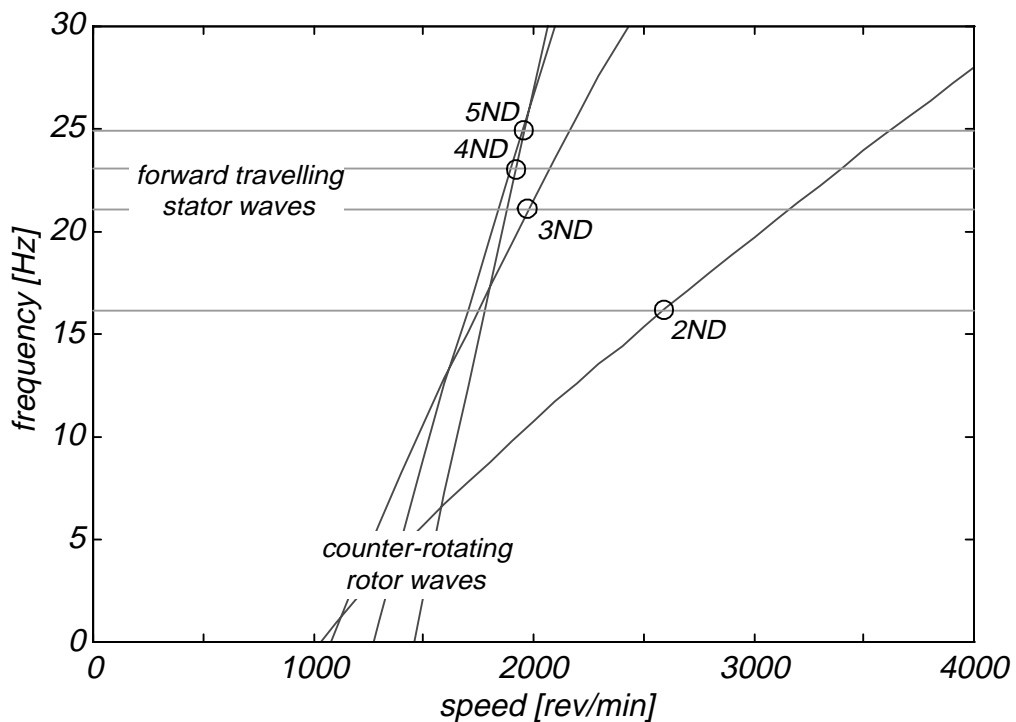


Figure 7-2: Interaction diagram for test rig, natural frequencies, tuned condition

7.3 Interpretation of the Signals from the Displacement Transducers

The displacement transducers used in all experiments were non-contacting eddy-current sensors. Due to their principle of operation, the output voltage of the sensors ranges between 0 V for contact of the sensor with the measured surface and -28 V for the maximum measurable displacement.

7.3.1 AC filtering

In order to record time-varying signals from the test structures, the initial distance between the sensors and the surfaces to be measured was set to half the measurement range, corresponding to an output voltage of -14 V. In order to acquire the dynamic

signals accurately, the resolution of the data-acquisition system would need to be excessively high. This difficulty was circumvented by high-pass filtering the signal to reduce its static, DC, component. This operation is commonly called AC coupling. After the high-pass filter, the signal was amplified to use the full range of the data-acquisition system.

7.3.2 Low-pass filtering

In addition to the AC filtering, the measured signals were low-pass filtered to remove high-frequency components prior to sampling, i.e., the analogue-to-digital conversion, in order to avoid aliasing of high-frequency components in the signal. The anti-aliasing filters must be set to at most half the sampling frequency of the data-acquisition system to identify the frequency contents of a signal correctly. Due to the finite drop of the filter frequency response at the high-frequency end of the pass-band, the sampling rate is usually increased from twice the cut-off frequency to 2.5 times or higher.

The combined band-pass filter has the following schematic shape, Figure 7-3.

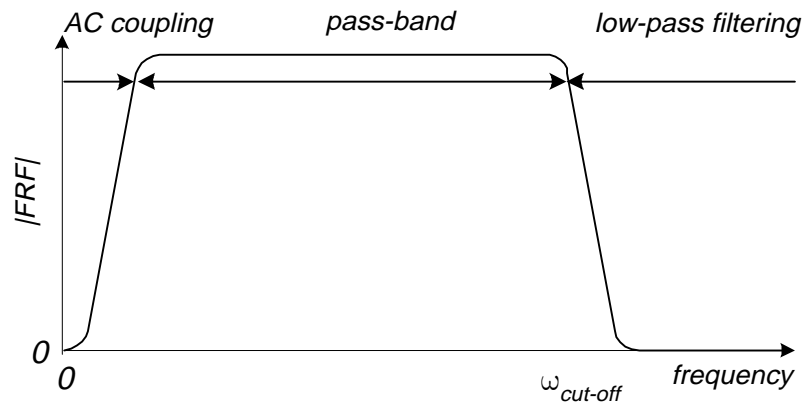


Figure 7-3: Frequency response of the AC-filter and low-pass filter combined

Figure 7-4 and Figure 7-5 show the effect that these two filtering operations have on the signals.

The filtered signals are not proportional to the displacement any more, as the DC- and the high-frequency components are not present. Therefore, the filtered sensor signals cannot be used to identify contact locations easily. However, they can be used to identify the instability or any time-varying signal within the pass band of the filters.

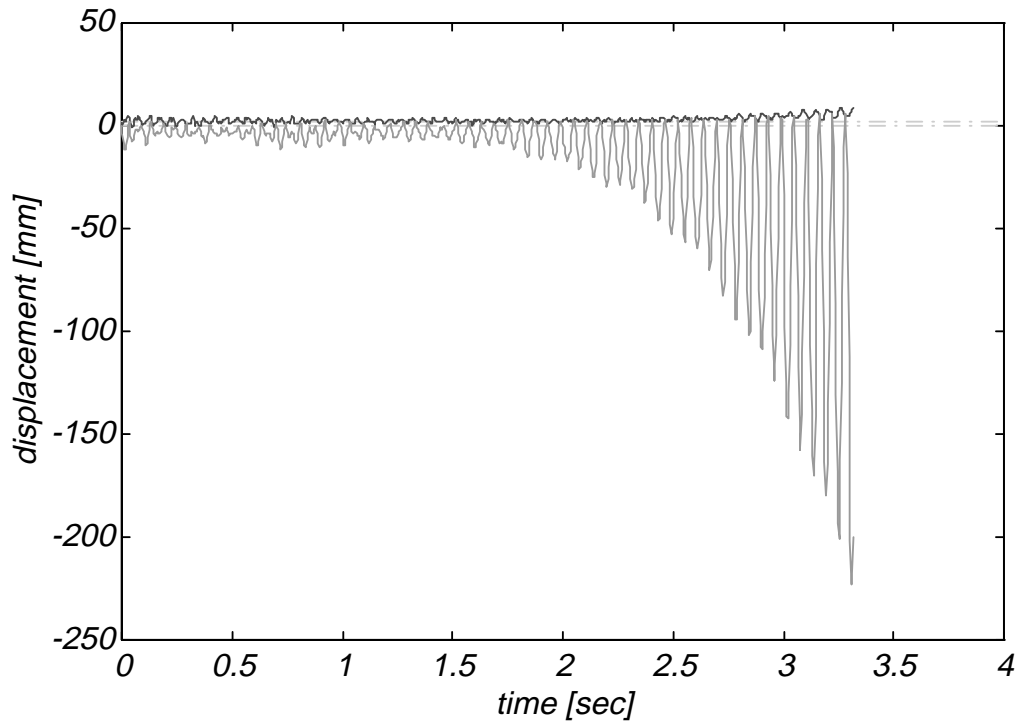


Figure 7-4: Simulated sensor signal, before filtering

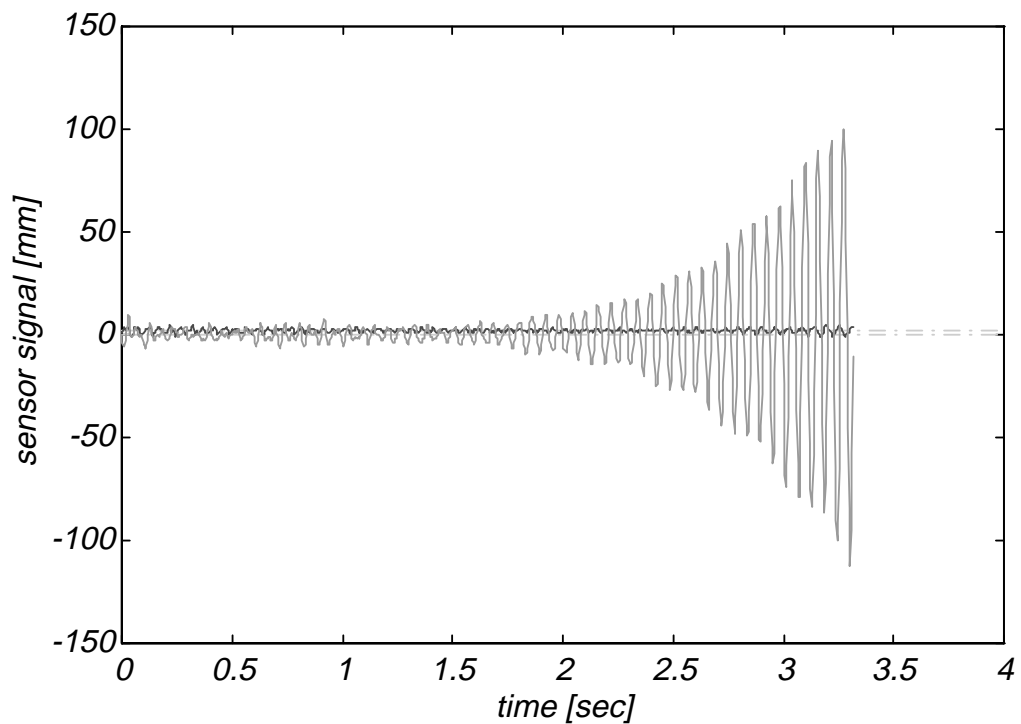


Figure 7-5: Simulated sensor signal, Figure 7-4, after filtering

7.3.3 Spectral analysis

The filtering renders the signal unsuitable for visual interpretation for contact occurrence, but does not change the frequency contents of the signals in the pass-band, Figure 7-3. In that band, the spectral decomposition will look the same, Figure 7-6 and Figure 7-7.

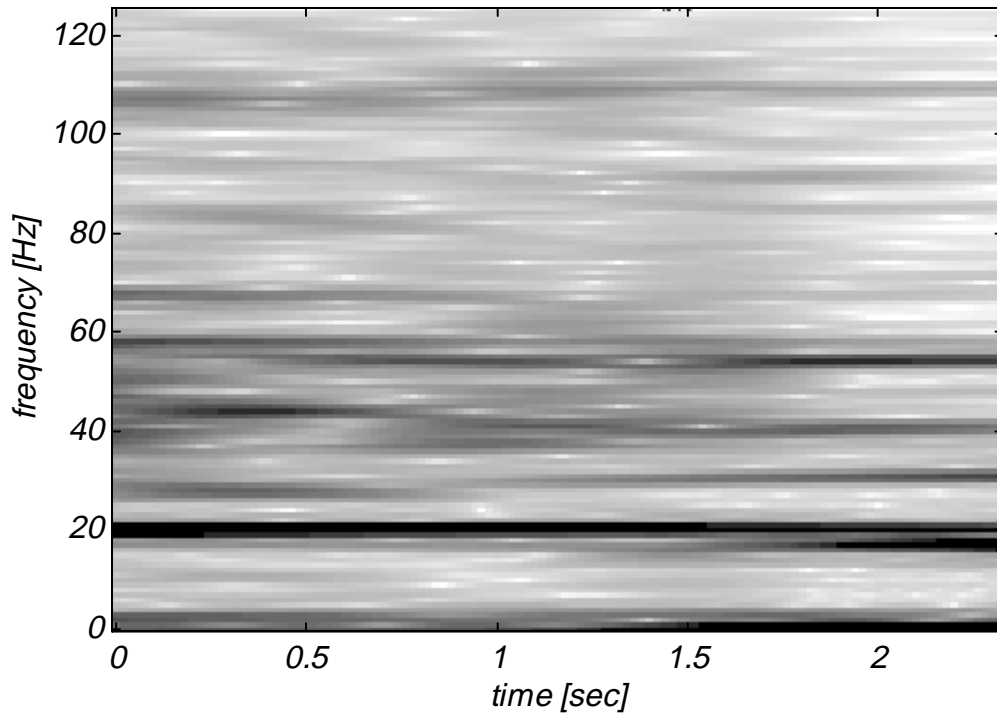


Figure 7-6: Spectrogram of the rotor signal in Figure 7-4

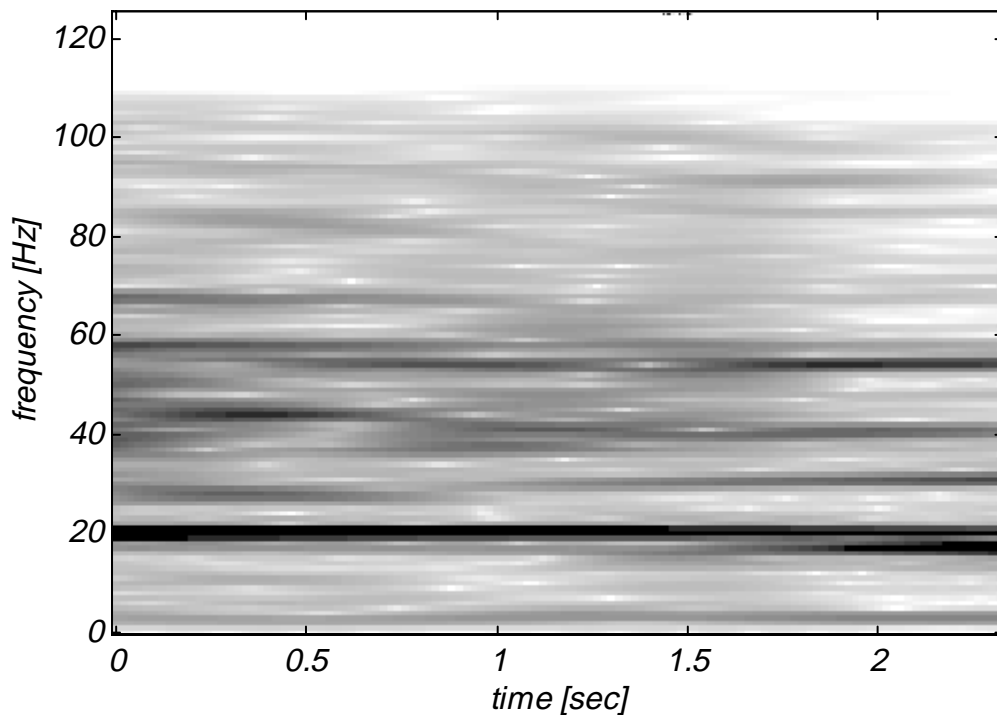


Figure 7-7: Spectrogram of filtered rotor signal of Figure 7-5

The format of the figures will be explained below, but for now it suffices to state that the frequency components at both ends of the spectrum are attenuated by the filtering process, as indicated by the white colour at the low- and high-frequency zones in Figure 7-7. The low-pass filter is set to a cut-off frequency of 100 Hz, and reduces the signal gradually because of the finite slope of the low-pass filter, which can be seen by the decreasing signal strength above the cut-off frequency. An infinitely-steep filter characteristic would attenuate the signal completely beyond the cut-off frequency.

7.4 Test of the 2ND Travelling-Wave-Speed Coincidence

The main focus of the work reported in this thesis lay on the demonstration of the travelling-wave-speed instability. For the reason stated above, the 2ND pattern was chosen as a representative, ND pattern for demonstration of the instability.

7.4.1 Parameters

The main parameters for the following experiments were:

$$\begin{aligned} n &= 2 \\ \omega_{s2} &= 102 \text{ rad/s} = 16.2 \text{ Hz} & \nu_{s2} &= 16.2\pi \text{ rad/s} \\ \Omega_{crit,2} &= 2590 \text{ rev/min} \end{aligned} \quad (7-1)$$

The initial gap for all experiments was set at about 3 mm. It was difficult to measure because of the static deflection of the disc but the analysis indicated that the exact size is not important after initial contact. The sampling frequency was chosen to 250 Hz, 2.5 times the cut-off frequencies of the anti-aliasing filters. The next experiments form the main part of the investigation. They were conducted at different speeds, Figure 7-8.

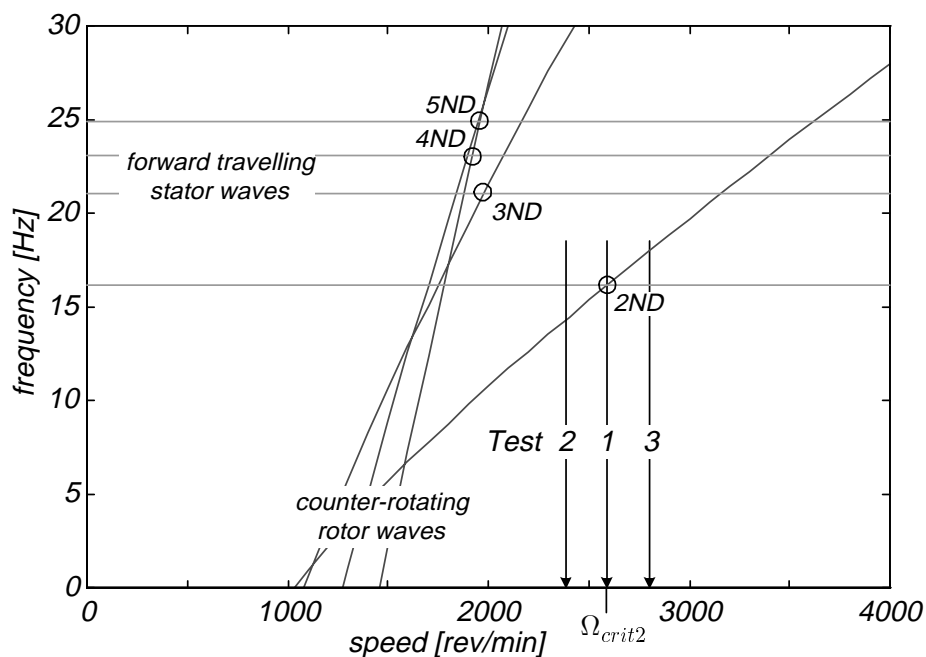


Figure 7-8: Tuned system's interaction diagram, natural frequencies, tested speeds

7.4.2 Test at critical speed of rotation (Test 1)

The rotor speed was set to the critical speed of the two-nodal-diameter mode, $\Omega_{crit2} = 2590$ rev/min, marked Test 1 in Figure 7-8, and the stator was impacted with a plastic hammer close to its outer radius at about 0.5 s.

7.4.2.1 Time histories

Figure 7-9 shows the time histories of the sensor signals: the top signal is that of a displacement probe facing the rotor and the lower one is that of a probe facing the stator. All time histories presented use the same scaling to enable quantitative comparisons.

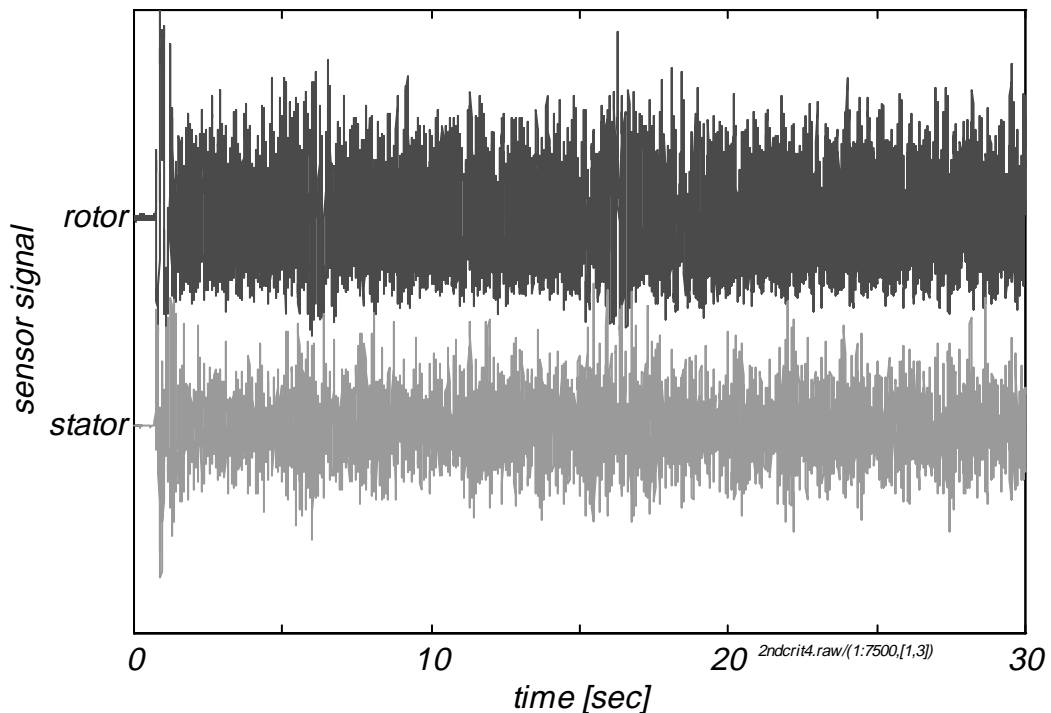


Figure 7-9: Rotor and stator response at 2ND critical speed

The sensor signals as functions of time clearly show the moment of first impact. The rotor starts with a few periods of a low-frequency vibration but changes quickly into vibrations with a higher frequency. The amplitudes of both rotor and stator remain fairly constant after the first impact. Some pulsations are visible in the rotor signal at 6 s and 16 s. Other than that, the interpretation of the sensor signals in the time domain is limited as the absolute magnitudes of the displacement of the structures cannot be recovered from the sensor signals due to the necessary filtering described above.

The filtering and the structural nonlinearities, such as contacting the sensor protection, prevent the recorded signals from showing the growth of the displacements of the structures beyond all limits as predicted for an instability from linear theory. The indications of instability used for the experiments are the maintained high level of vibration and the frequency content of the signals: If the response levels remain constant and the dominant frequency present in the signal is that computed from the travelling-wave-speed

coincidence, then it is assumed that the response would be unstable and would grow exponentially for a truly linear structure.

7.4.2.2 Spectrogram of the rotor signal

For further analysis, the data in Figure 7-9 were transformed into the frequency domain. Figure 7-10 shows the evolution of the spectrum of the signal with time of the rotor and Figure 7-11 that of the stator. Each vertical line in these spectrograms is a short-time, discrete, Fourier transform of part of the signal. The abscissa indicates the starting time of the particular time sample while the record length follows from the frequency resolution. By presenting the transforms in order of increasing starting time of the signal sample, the time variation of the spectra with time is visualised. In order to obtain visually smooth diagrams along the time axis, the analysed time records overlap.

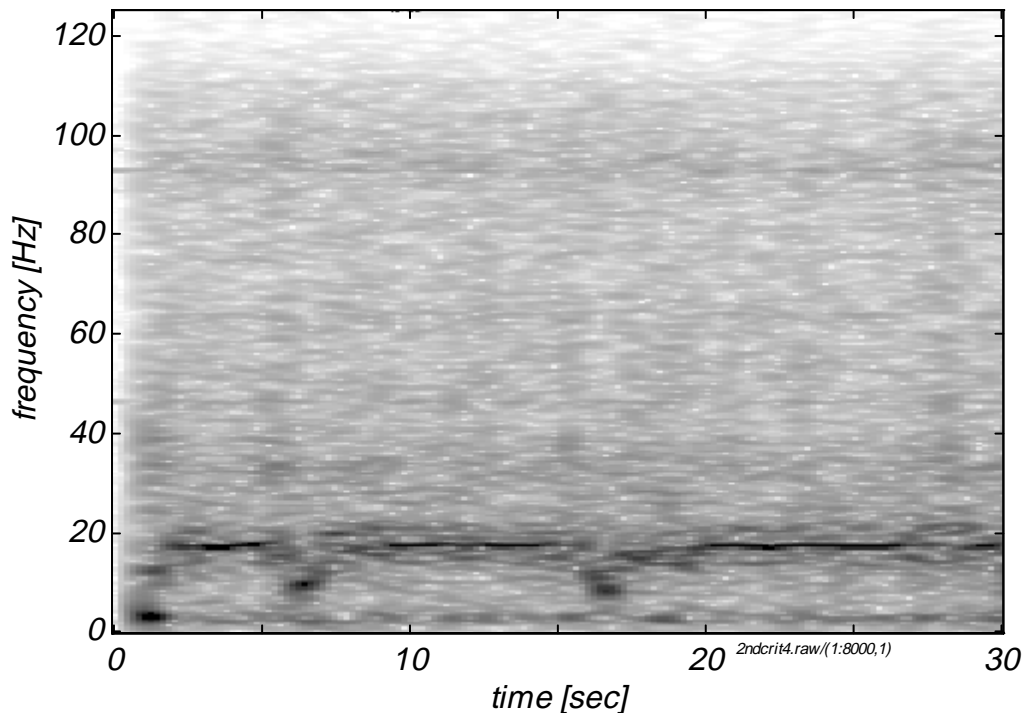


Figure 7-10: Rotor spectrogram at the 2ND critical speed

Dark shades of grey in the spectrograms indicate large amplitudes and light shades small amplitudes in the spectrograms. All spectrograms presented use the same colour scaling from white to dark grey so that results can be compared quantitatively.

It can be seen that before the impact is applied at about 0.5 s, the rotor is vibrating mainly at the engine-order frequencies, Ω_{crit2} , $2\Omega_{crit2}$, corresponding to 43 Hz and 86 Hz respectively. The frequencies are caused by the static deflection of the disc.

Also visible in the time traces, Figure 7-9 is that for about the first second after impact, the rotor vibrates at 3 Hz, which is the natural frequency of the counter-rotating 1ND wave. This is an indication that the initial impact was not symmetric and caused a 1ND response. After the first second, the response is dominated by the 16 Hz frequency

component which corresponds to the natural frequency of the 2ND mode. The speed was set to have the rotor and stator 2ND waves progress at the same velocity, and hence the contact forces were driving the structures in resonance as detailed in Chapter 3.

Clearly visible are the slight pulsations of the 20 Hz line at about 6 s and 16 s in Figure 7-10, that could barely be seen in the time-domain diagram, Figure 7-9. They are most probably caused by a deviation of the speed away from the critical speed.

When interpreting the spectrograms of the rotor, it should be remembered that the signals were recorded in the stationary frame of reference and the rotor frequencies were the apparent natural frequencies modulated by the speed of rotation.

7.4.2.3 Spectrogram of the stator signal

The frequency coincidence becomes clearer when looking at the spectrogram of the stator, Figure 7-11.

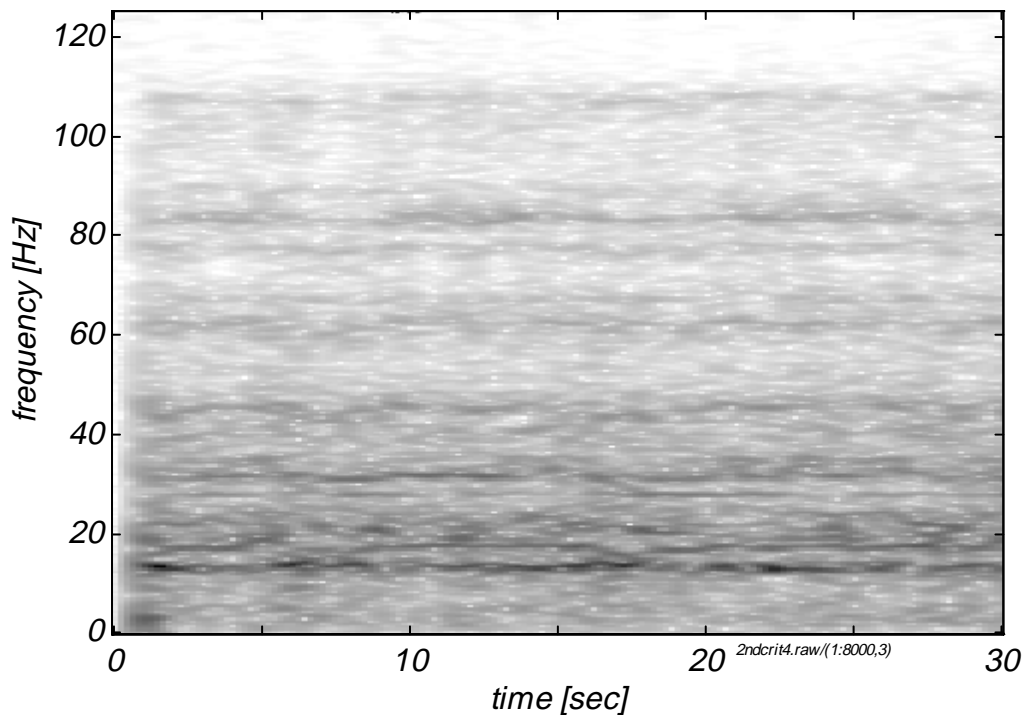


Figure 7-11: Stator spectrogram at the 2ND critical speed

The stator is at rest until the impact starts the interaction at 0.5 s. Immediately after impact, the stator response is dominated by the 16 Hz frequency component, the natural frequency of the 2ND forward wave. The second strongest component is found at the natural frequency of the 2ND mode of the second family, 32 Hz. All other frequencies can be matched to further natural frequencies of the stator, tabulated in the Appendix.

The information extracted from the spectrograms documents the instability at the coincidence of the wave velocities according to the requirements given above: maintained vibration level and dominant frequency of the travelling waves driven in resonance. This experiment demonstrated the travelling-wave-speed instability and proved the theoretical

and numerical results of the preceding chapters. With this experimental proof of the existence of the travelling-wave-speed instability, the main goal of this thesis has been achieved.

Further tests were carried out at the same speed to show the insensitivity of the instability to the initial conditions. The test provided results with little visual difference to the presented test, one further set is presented in the Appendix.

7.4.3 Test at subcritical speed of rotation (Test 2)

The instability is expected only for the coincidence of the travelling-wave velocities according to the theory developed in Chapter 3. Away from the critical speed, both for higher speeds and lower speeds of rotation, the system's behaviour is expected to be stable.

For the subcritical run, the speed was set to 2390 rev/min, 200 rev/min below the critical speed, marked Test 2 in Figure 7-8. The resulting time histories and spectrograms are presented in Figure 7-12 to Figure 7-14:

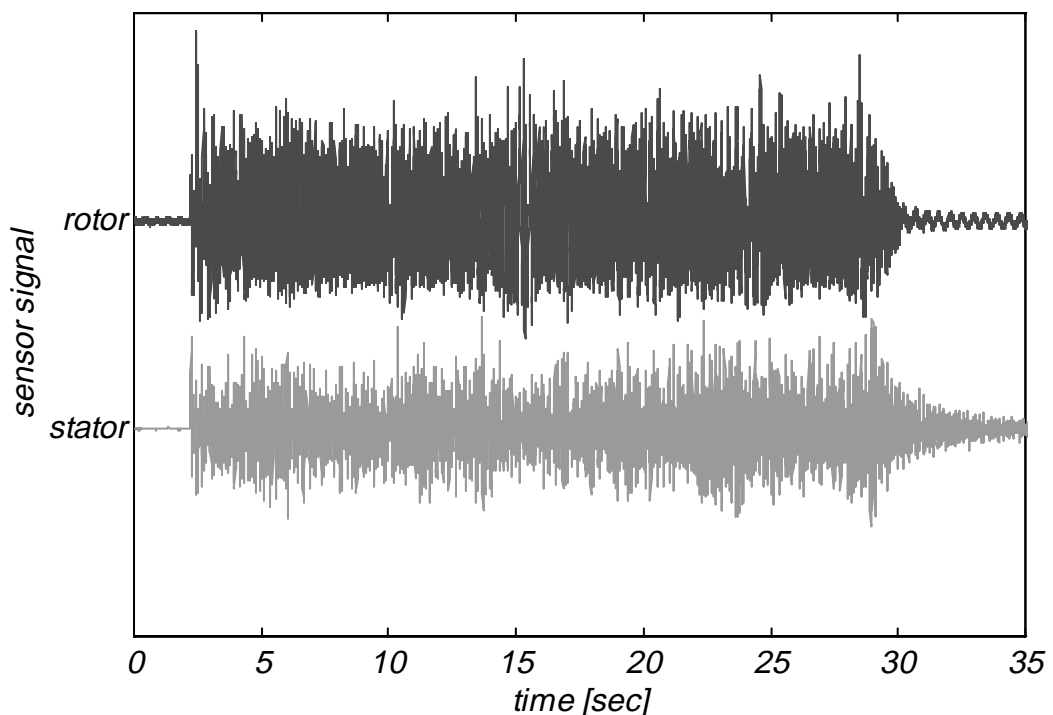


Figure 7-12: Sensor signals at 2ND subcritical speed

The sensor signals are plotted to the same scale as before and it can be seen that they are of equal amplitude compared with those of the critical-speed run, Figure 7-9, but the important feature is that the contact breaks after about 28 s. Also, they are very irregular compared with the compact, dense, signals from the critical-speed run, Figure 7-9.

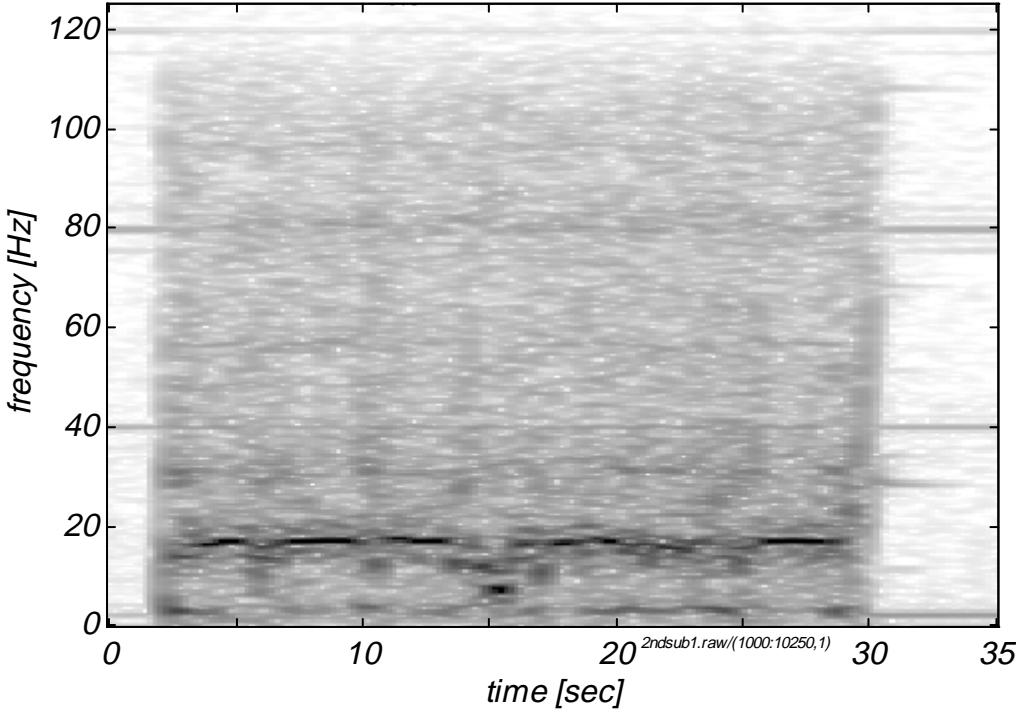


Figure 7-13: Rotor spectrogram at a 2ND subcritical speed

The spectrograms reveal that the 2ND wave component is still the dominant in the signal, as expected, but the average response level is lower than before as the speed of rotation is not the critical speed, and hence the energy input due to the contact is not sufficient to maintain contact between the structures as the blade contacts are not timed correctly.

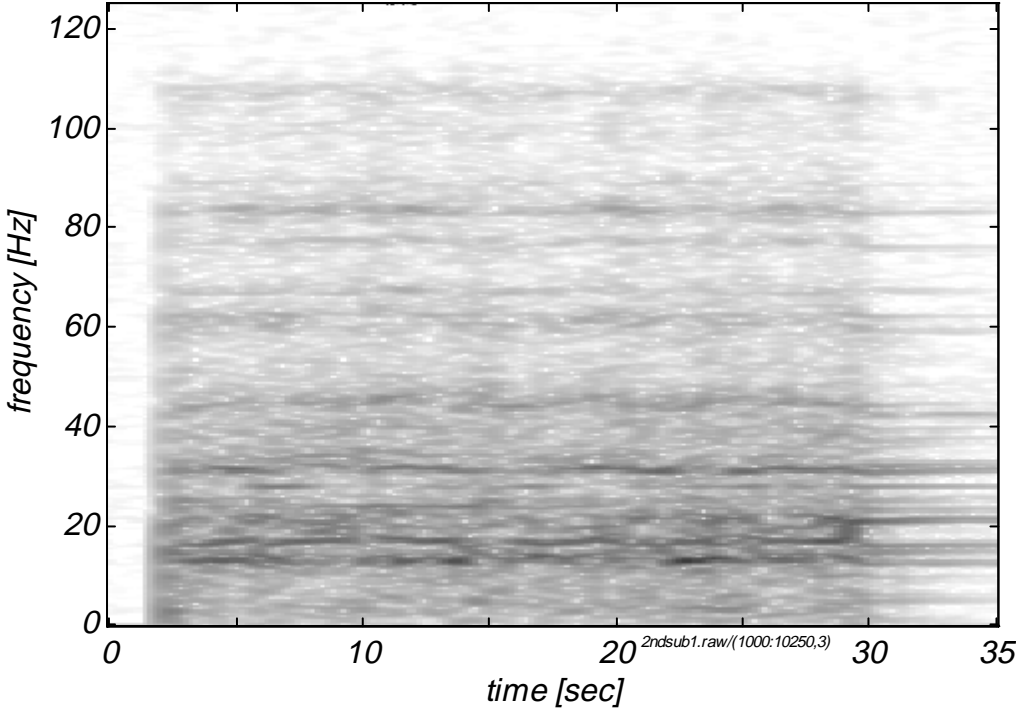


Figure 7-14: Stator spectrogram at a 2ND subcritical speed

The spectrograms show the familiar features and, once the contact has vanished, one can identify the engine-order lines in the rotor spectrogram, Figure 7-13, and the first family modes in the frequency range between 10 and 30 Hz in the stator spectrogram, Figure 7-14.

7.4.4 Test at supercritical speed of rotation (Test 3)

The experiment of the previous paragraphs was repeated for a speed of 2800 rev/min, which is 210 rev/min above the critical speed of the 2ND waves, Test 3 in Figure 7-8.

The data are presented in the same format as before, Figure 7-15 to Figure 7-17, below.

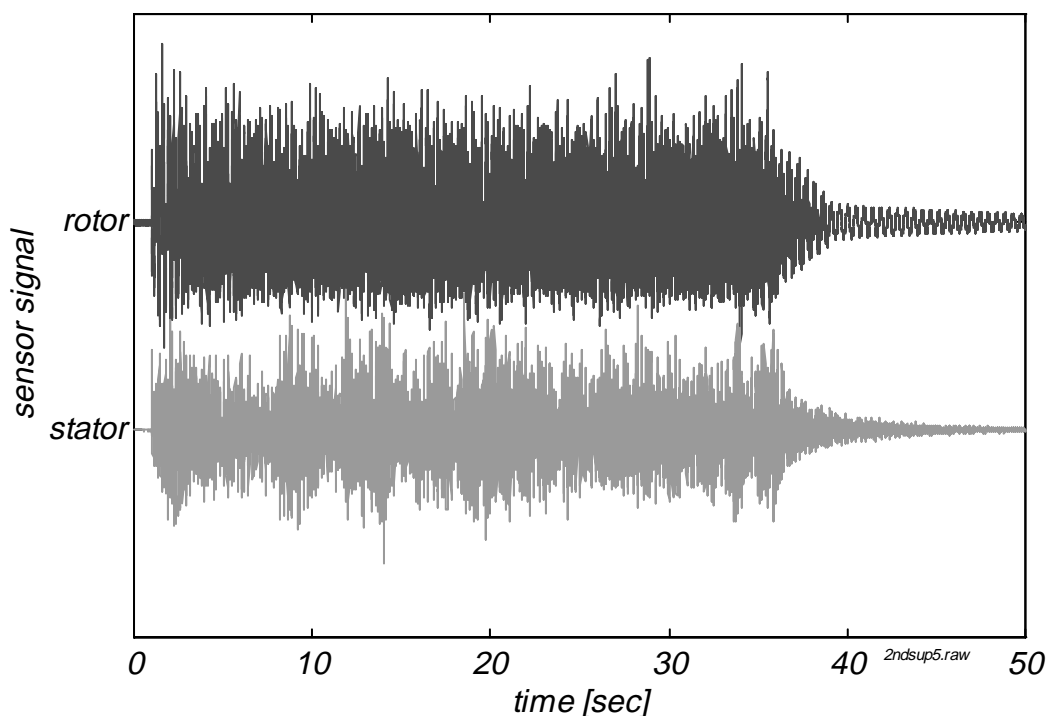


Figure 7-15: Sensor signals at 2ND supercritical speed

Again, as for the subcritical run, the major feature of the time histories is the separation of the two structures, this time approximately 35 s after the initial contact. The time of separation is of the same order as for the subcritical speed. This suggests that the absolute speed of rotation does not enter the energy balance, only the distance from the critical speed is important.

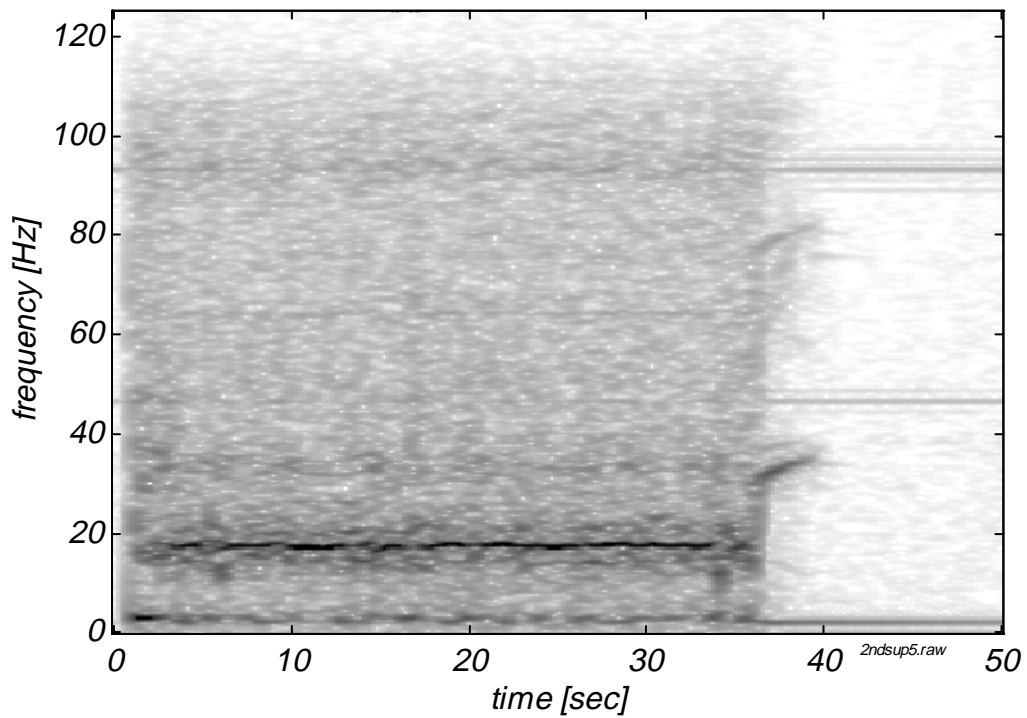


Figure 7-16: Rotor at 2ND supercritical speed

The spectrograms show again how the structures remain in contact for a limited period of time only. The contact is not maintained as the structures' travelling waves are not progressing synchronously.

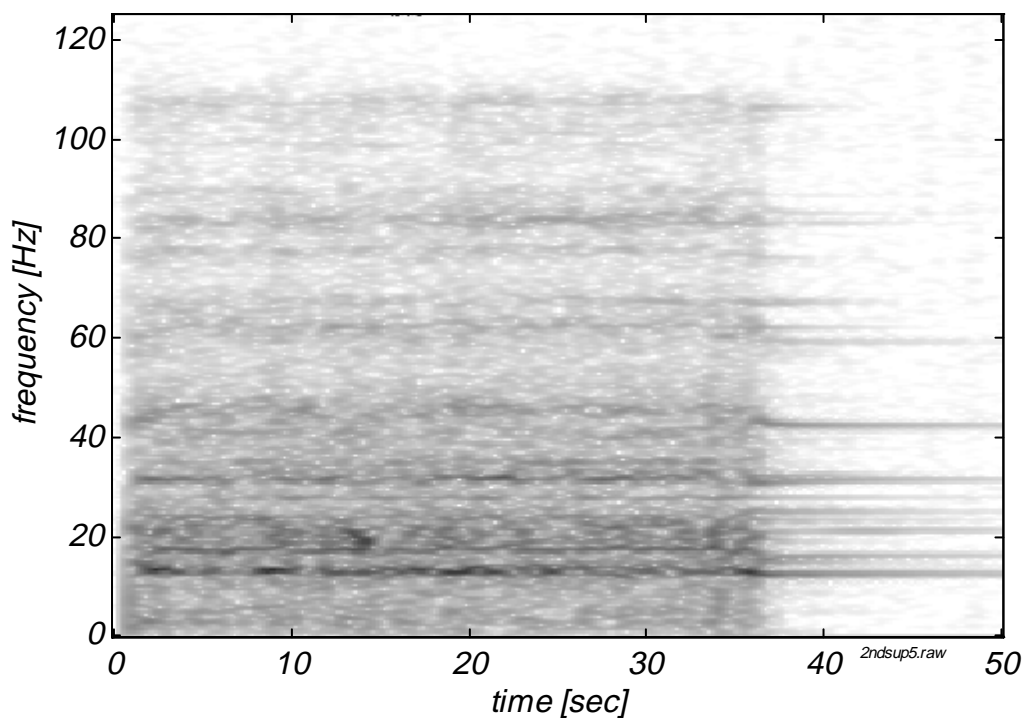


Figure 7-17: Stator at 2ND supercritical speed

After separation, the engine orders and natural frequencies become quickly dominant.

7.4.5 Test of mistuned system at critical speed of rotation (Test 1m to 3m)

The effects of mistuning on the establishment of the travelling-wave-speed instability are discussed in Chapter 3. The simulation results in Chapter 5 suggest that the effect was indeed correctly predicted and that the instability would not occur for a mistuned system.

The experimental set-up was modified to introduce mistuning to the stator by attaching masses to it. Four masses of 65 g were attached at the outer perimeter 90° apart. The masses lower the natural frequencies of all modes that do not have a nodal line at the attachment locations, but split the double modes with an even number of nodal diameters only in accordance with Figure 2-11, Table 7-2.

N	2	3	4	5
$\Omega_{crit,n}$ [rev/min]	2520/2590	1970	1890/1900	1940

Table 7-2: Critical speeds of the mistuned system

The split introduced to the 2ND mode was 0.5% of the frequency of the tuned stator's 2ND double mode. The wave-velocity-speed and frequency-speed diagrams, Figure 7-1 and Figure 7-2 change accordingly, as shown in Figure 7-18 and Figure 7-19.

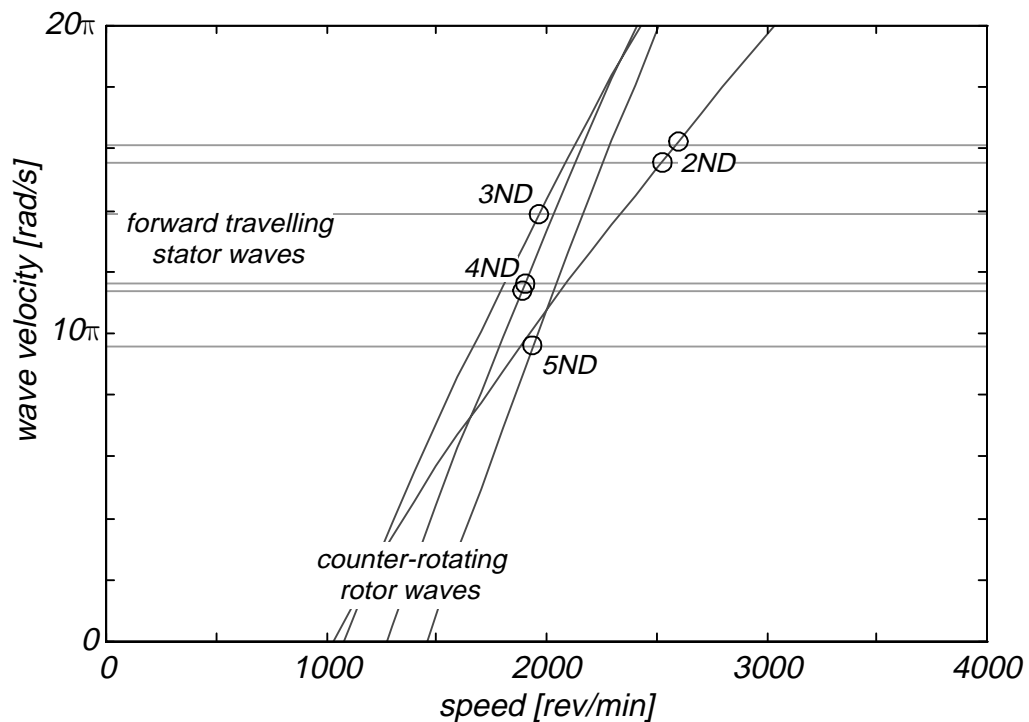


Figure 7-18: Interaction diagram for test rig, mistuned condition

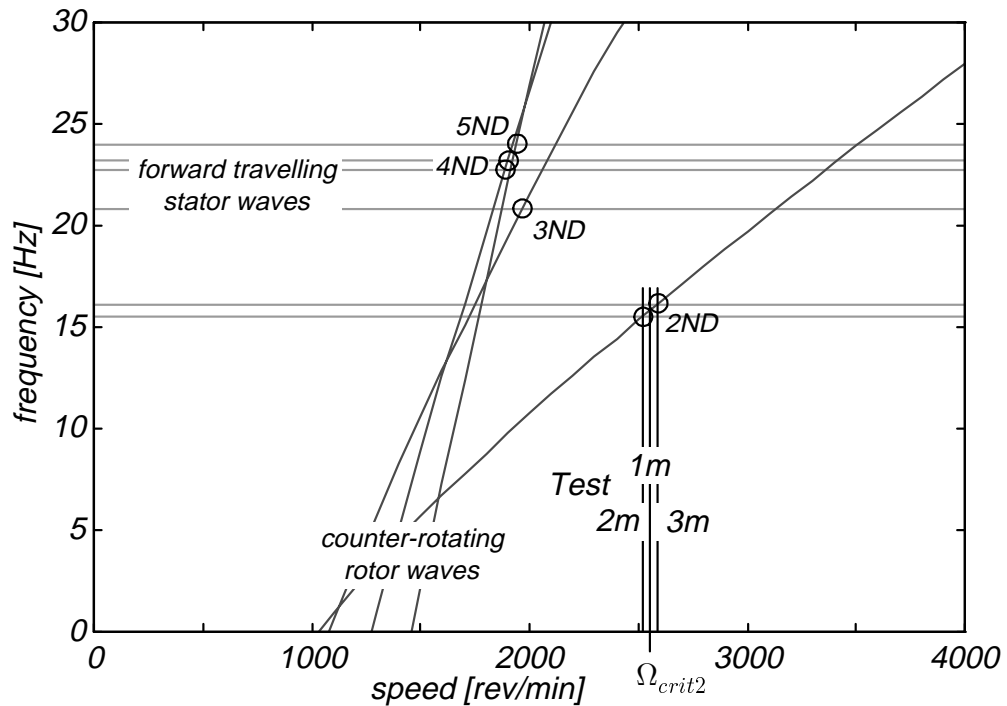


Figure 7-19: Interaction diagram for test rig, frequencies, mistuned condition

The experimental investigation of the mistuning concentrated on the two-nodal-diameter-wave coincidence because of the clustering of the coincidence speeds of the other wave patterns and the small split in critical speeds of the 4ND waves of 10 rev/min only.

The first test of the system with the mistuned stator was conducted at 2555 rev/min, the mean of the critical speeds of the 2ND modes, Table 7-2, Figure 7-19: Test 1m.

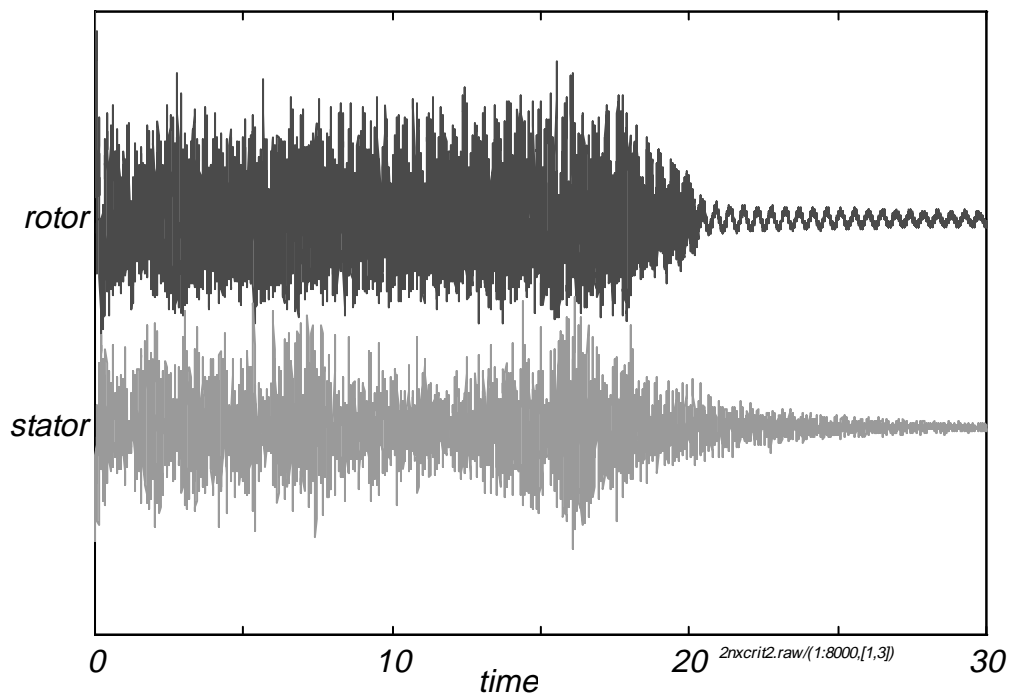


Figure 7-20: Mistuned system, sensor signals at 2ND mean critical speed

The time histories show the separation of the two structures after about 18 s. The envelopes of the signals are again irregular, as it is the case for the tests of the tuned system away from the critical speed. Again, it can be argued that this indicates that the energy input was not sufficient to maintain contact in the presence of energy dissipation.

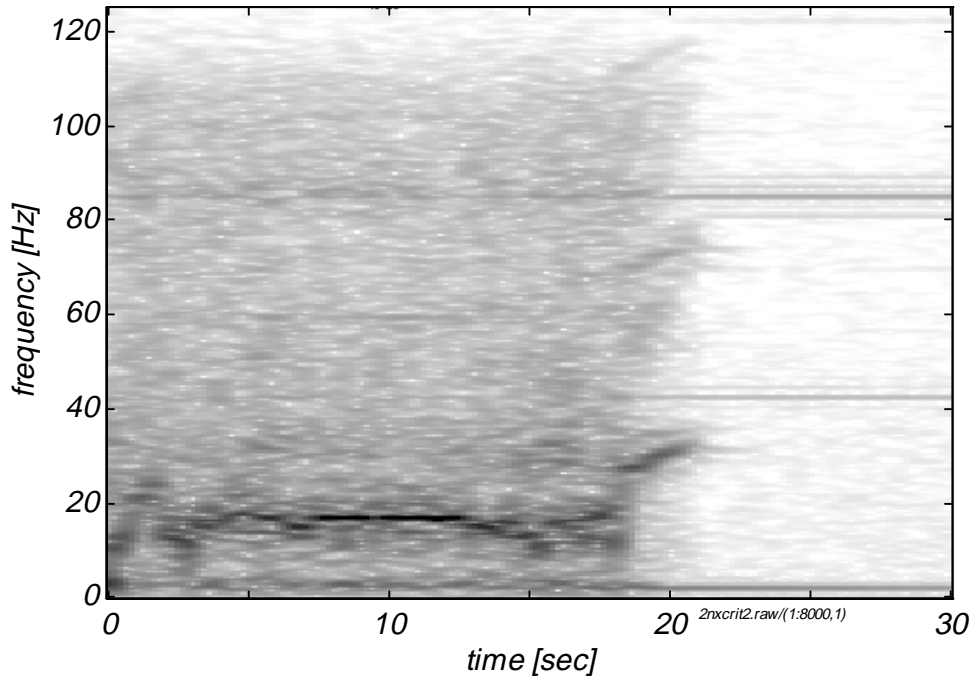


Figure 7-21: Rotor spectrogram, mistuned system, at the 2ND 'mean-critical' speed

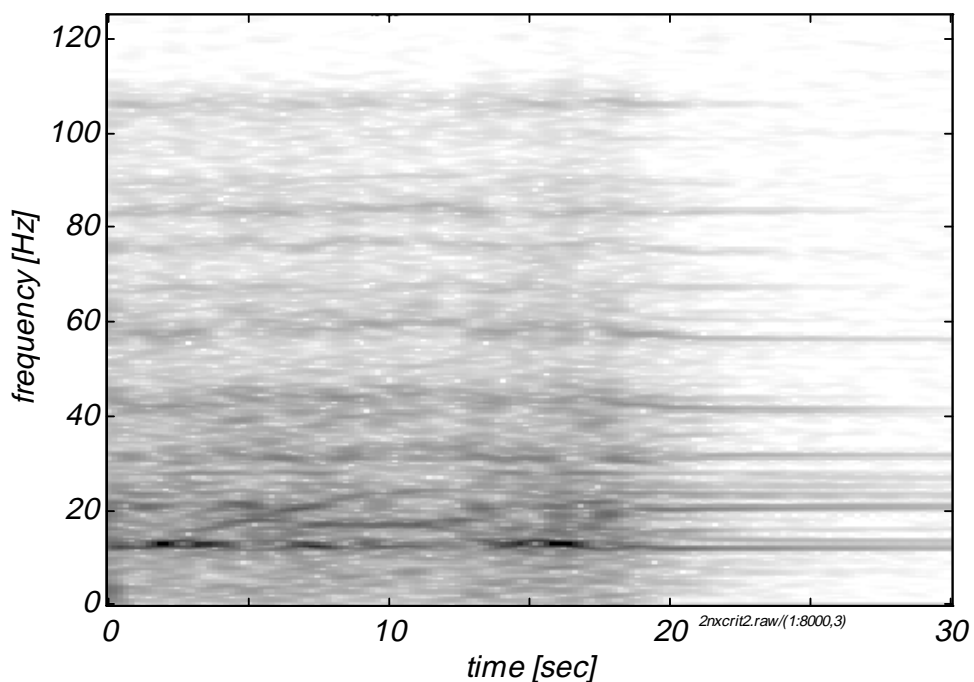


Figure 7-22: Stator spectrogram, mistuned system, at 2ND 'mean-critical' speed

After separation, the first and second engine order frequencies at 35 and 70 Hz become

dominant in the rotor spectrogram, Figure 7-21. The single frequency line of the 2ND modes at about 16 Hz of the tuned system splits into a double line for the mistuned system, Figure 7-22.

For the lower critical speed of the two modes, 2520 rev/min, Figure 7-19: Test 2m, the time traces separate after short 'light' contact, Figure 7-23.

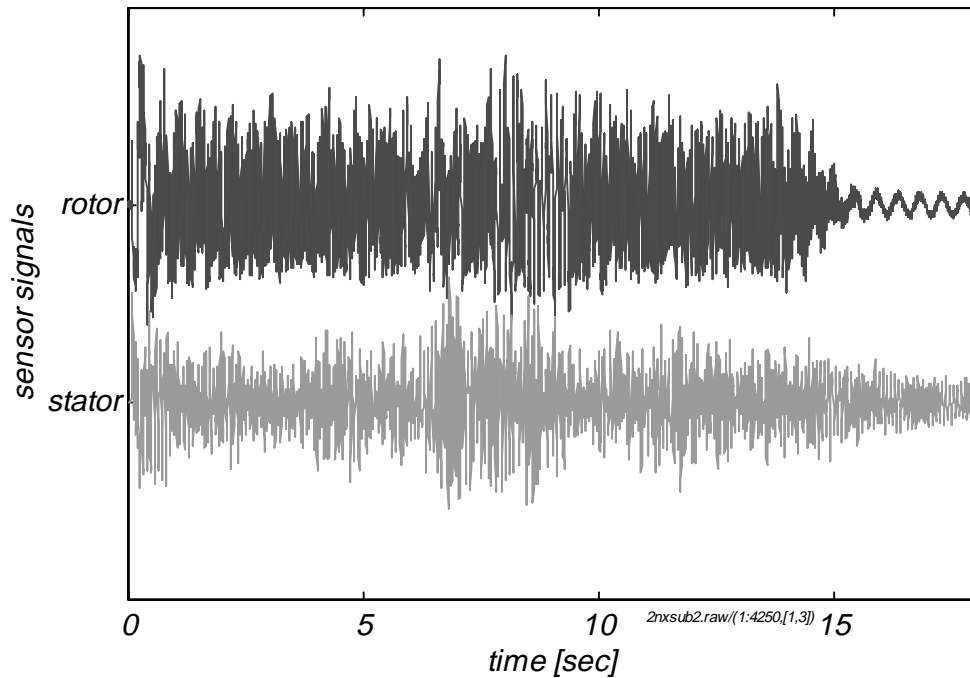


Figure 7-23: Mistuned system, sensor signals, at the lower 2ND critical speed
The same behaviour is observed for the rotor spinning at the critical speed of the higher of the two modes, 2590 rev/min, (Figure 7-19: Test 3), Figure 7-24.

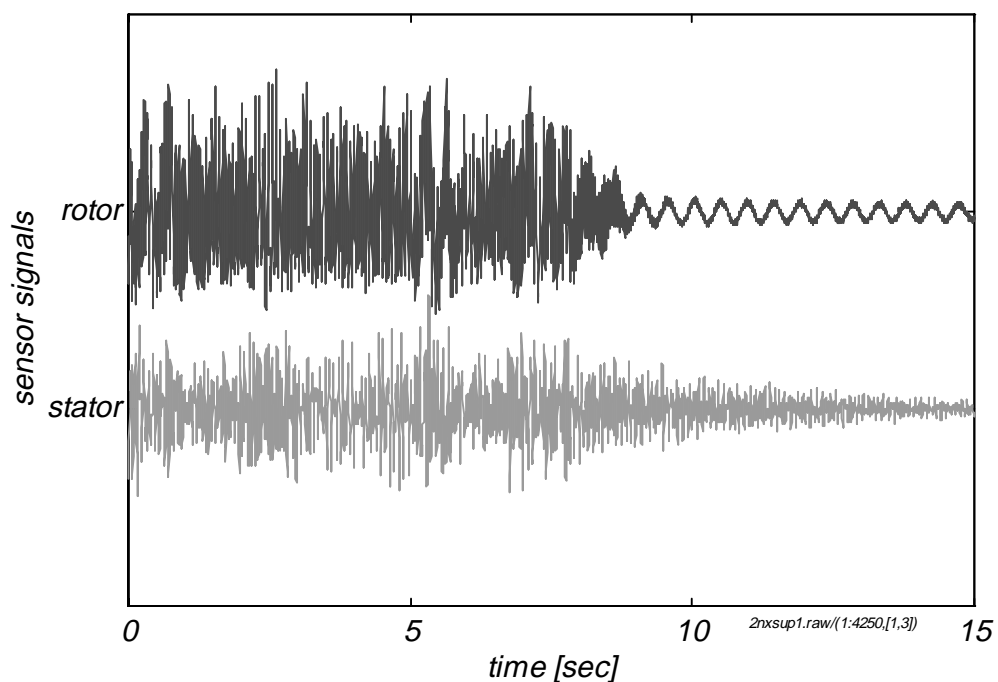


Figure 7-24: Mistuned system, sensor signals, at the higher 2ND critical speed

The system was mistuned by 0.5%, i.e., the frequency split introduced by the masses was 0.5% of the mean of the natural frequencies of the 2ND modes, Equation (3-42):

$$\text{mistuning} = \frac{\omega_2 - \omega_1}{\frac{1}{2}(\omega_2 + \omega_1)} = 0.5\% \quad (2)$$

The results for the three tests of the mistuned system at the ‘mean-critical’ speed of the split 2ND modes and the critical speeds of the two separate modes show that the mistuned system does not become unstable. This puts further weight to the analysis and simulation of the travelling-wave-speed instability, Chapters 3, 4, and 5, which predict analytically and numerically that the mistuned system will not exhibit the travelling-wave-speed instability.

7.5 Test of Higher ND Wave-Speed Coincidences

The speed coincidences of the three, four, and five-nodal-diameter waves almost coincide, Table 7-1, and were analysed together. Due to the strong 2ND component of the initial deflection in the disc, the travelling-wave-speed instability could not be clearly identified. Representative spectrograms for all runs, whether at a critical speed for any of the waves or away from it, are those of the test at 1900 rev/min, the critical speed of the 4ND wave.

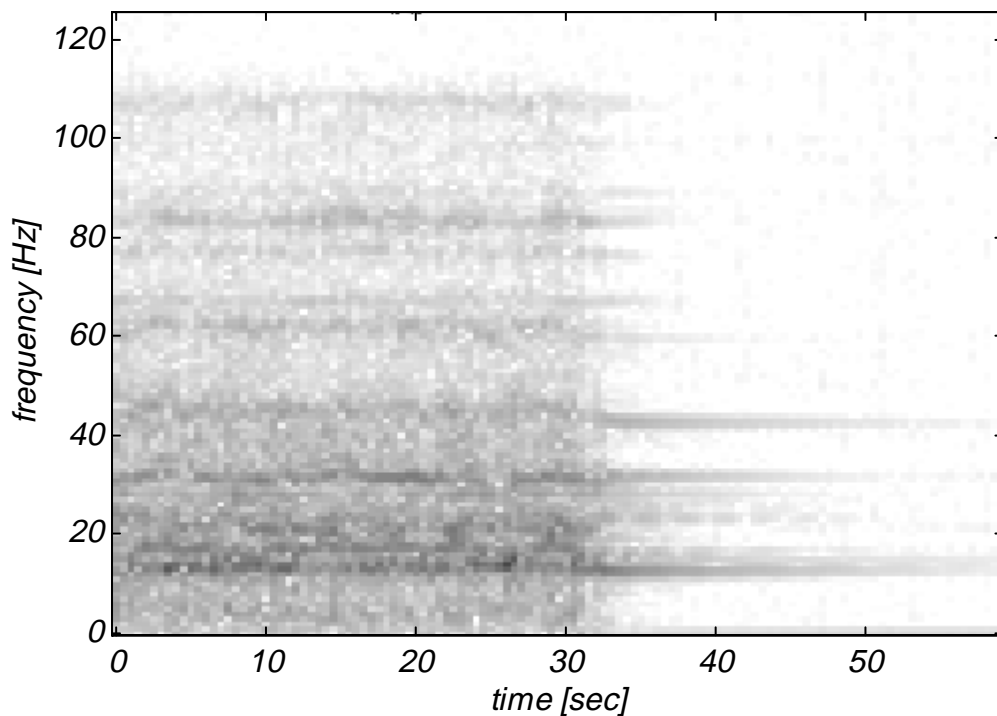


Figure 7-25: Stator at 4ND critical speed

The 2ND frequency line at 16 Hz is still pronounced but the 3ND, 4ND, and 5ND frequency lines at about 21 Hz, 23 Hz, and 25 Hz respectively, now appear much stronger than in the previous runs, as they all are excited close to their resonances.

The experimental data from the travelling-wave-speed coincidences of the higher-nodal-diameter modes remain inconclusive with respect to the establishment of the travelling-wave-speed coincidence because of the practical imperfections of the rotor disc that could not be reduced to the required levels.

7.6 Conclusions

The main objective of this investigation described in this thesis has been achieved by experimental proof of existence of the instability at travelling-wave-speed coincidence.

A detailed test program for the two-nodal-diameter wave was carried out and showed the expected behaviour of the rotor-stator system. As predicted by theory and numerical simulation, the response of the system driven at a speed different from the critical speed remained stable in the experiments, from which it was concluded that the transfer of energy from the rotational kinetic energy of the rotor into vibratory energy of the rotor-stator system was less than the energy dissipation through damping. At or close to a critical speed, the responses of rotor and stator became unstable, but were bounded in the experiment due to structural nonlinearities.

Additional experiments were carried out with deliberate asymmetric mass-distribution or mistuning applied to the stator. This had a stabilising effect on the coupled-system dynamics as predicted by the theoretical development in Chapter 3. The structures were vibrating at their resonance frequencies, but the rotor and stator separated after initial contact. It was argued that mistuning reduced the energy transfer below the level of energy dissipation.

In addition, a test for the 3ND, 4ND, and 5ND modes was carried out, but due to the relatively large static deflection of the disc, the travelling-wave-speed instability did not manifest itself. The spectra of the data from the test run showed pronounced responses at the natural frequencies of the higher-nodal-diameter modes, but the dominance of the 2ND response, caused by the static deflection of the rotor, hindered the establishment of the travelling-wave-speed instability for these modes, which, potentially, are also susceptible to the instability as observed for the 2ND mode.

Chapter 8: Conclusions

In this research we have studied the travelling-wave-speed instability, which can occur between two elastic structures which move relative to each other. The work reported is analytical, numerical, and experimental in nature. The purpose of this chapter is to summarise the achievements and to list the conclusions drawn.

8.1 Achievements

The work reported in this thesis shows that the travelling-wave-speed coincidence can lead to instability. Although postulated, this had not been demonstrated previously. The experimental results are supported by an analytical explanation and numerical simulations.

8.1.1 Theoretical background

A literature survey was carried out and indicated that researchers had previously limited their analyses to one elastic structure in contact with a rigid structure, and had not treated the problem of an elastic rotor in contact with an elastic stator. The need for research into the description of the dynamic behaviour of two elastic structures in contact was established. The following areas were identified to be necessary for further studies: structural dynamics to describe the individual structures and friction contact to characterise the contact between the two structures.

The essential theory of structural dynamics was presented here with details provided particular to rotationally-periodic and axisymmetric structures like the bladed disc representing the stator in this study, or a rotating disc of uniform thickness representing the rotor. From comparison with experimental data, it was found sufficiently accurate to describe the behaviour of the individual structures by their linear dynamics. Different modelling approaches to obtain the eigensolution were presented and the difficulties associated with each were explained. The finite-element method was chosen to obtain the natural frequencies and the modeshapes for its capability of modelling axisymmetric as well as asymmetric, mistuned, structures. The detail of the discretisation was selected to provide accurate data in the frequency range of interest.

The effect of rotation on the dynamics of the rotor was shown and an algorithm presented to compute the speed-dependent natural frequencies for a given geometry. The theoretical predictions and the numerical approximations were validated against published cases and measurements. For the rotor of this study, considering the centrifugal stiffening was important as it changed the natural frequencies of the rotor considerably and thus moved the travelling-wave-speed coincidences towards higher speeds of rotation.

Once the effect of rotation on the natural frequencies of the rotor was determined, it

was possible to draw the wave-velocity-speed diagram and to determine the travelling-wave-speed coincidences. The speeds were called critical speeds for their potential to cause, in malign conjunction with other parameters, the travelling-wave-speed instability.

The necessary conditions for the occurrence of the travelling-wave-speed instability at the critical speeds were derived from the equations of motion and an energy balance. Vibration patterns were identified that fulfil the necessary conditions. The analysis was focused on these vibration patterns, the travelling waves.

The concept of travelling waves, their direction and their spatial interpretation was developed further in this work. In the context of waves, ‘negative frequencies’ can be interpreted as frequencies of backward-travelling or counter-rotating waves, depending on the reference frame. This decomposition is also important if a transformation between frames of reference is to be performed, as the frequencies of waves of different nodal diameters transform differently. The notion of travelling waves made the study of the travelling-wave-speed instability much clearer: the wave notation helped to identify the critical speeds and was an important means to derive a clear understanding of the investigated problem.

8.1.2 Simulation

A mathematical model was developed to simulate numerically the contact between rotor and stator. The rotor and the stator components were each modelled by the finite-element method and the solution of the eigenproblem obtained was used to integrate the nonlinear differential equations describing the rotor and stator dynamics with intermittent contact. The input data to the simulation are the modal data of the individual structures (which for the rotor, are speed-dependent), the damping, and the interface parameters which depend on the contact model chosen. Starting from arbitrary initial conditions, the simulation provided as output sampled time histories of the principal coordinates from which all other responses, such as physical displacements or velocities, were determined.

The results from the simulation demonstrated the analytically-predicted travelling-wave-speed instability numerically and indicated that the instability cannot be controlled by damping in the structures, as was already indicated in the theoretical derivation. This was tested for damping levels realistic for engineering structures.

Mistuning was shown to be a key element in the interaction between the rotor and stator. It was argued that an asymmetric mass distribution reduced the travelling wave component of the response, and, by bringing into existence a standing wave component, made the synchronisation of travelling waves more difficult or even impossible, and hence reduced the energy input into the vibration below a level where damping could control the instability.

It has to be kept in mind that the numerical simulation cannot be used by itself alone to validate the analytical results as the simulation is based on many simplifying assumptions and needs validation from an experiment itself.

8.1.3 Experiment

To support the theory and the simulation of the travelling-wave-speed instability, an experimental test rig was designed and built. Experiments on the rig demonstrated the occurrence of the travelling-wave-speed instability by the conditions forecast by the analysis (and not elsewhere). This proof of existence was a major objective of this research.

Further experimental work carried out confirmed the analytical predictions and showed the validity of the simulation results. Most of the numerically-investigated parameter dependencies could be demonstrated experimentally, such as the effect of different speeds of rotation and the effect of mistuning on the travelling-wave-speed instability, while damping could not be changed in the experimental set up.

In order to take measurements of displacements on the rotor and stator, and of the speed of rotation, a high-speed, multi-channel data-acquisition system controlled from MATLAB running on a PC was developed. Hardware circuits were designed to provide an emergency shut-down capability and to integrate the signal from the incremental encoder to provide the absolute angle from the motor, which is an important item of information in the analysis of rotating structures.

8.1.4 Post-processing

To analyse the data from the simulation and the test rig, special post-processing software was written. For the analysis of rotating machinery, the spatial information can be very important and so tools were devised to extract this information as well as the usual time and frequency data.

The advantage of using a PC with software instead of a dedicated analyser is the significant gain in flexibility of the analysis routines employed. An open software solution can accommodate effects as they occur in the analysis of rotating machines and simplify the development of further algorithms.

8.1.5 Software

Today's computers allow the designer to analyse very complex problems with many thousands of degrees of freedom. The programs developed and used in this study are summarised in the next paragraphs:

8.1.5.1 Analytical solution

For simple shapes such as circular discs of uniform thickness numerical approximations of analytical solutions can be used to compute the modal properties efficiently. The rotation introduces a further term in the energy balance, making the natural frequencies functions of the speed of rotation for which analytical solutions do not exist. A numerical method was implemented in a program, presented in the Appendix.

8.1.5.2 FE program

For reasons of flexibility and convenience, the MATLAB-based code MATFEM was chosen for the FE analysis. The advantage of this program was the full access to the code, including the eigensolver and the post-processor. This way, it was possible to add an efficient subspace eigensolver to the program and to modify the post-processor to display results in the cylindrical coordinate system, natural to the analysis of the bladed disc and other rotationally-periodic structures.

8.1.5.3 Numerical simulation

For the integration of the medium-size set of ordinary differential equations, resulting from the discretisation of the continuous structures, the ODE suite from MATLAB was used for its ease of use and its capabilities.

The simulation used the modal data obtained from the FE program to integrate the equations of motion and returned time histories of the displacements and velocities of the interface points and the contact forces. The computations of the displacements, interferences and contact forces were programmed in a modular fashion and could be changed easily for specific requirements. The main programs are presented in the Appendix.

Current simulation packages allow the engineer to focus on the problem at hand without having to spend time on integration algorithms or graphical display of the data.

8.1.5.4 Modal Analysis

In order to compare the predictions with measured data, modal tests were conducted and the data analysed using the Structural Toolbox of MATLAB. Following the tests, the FE model was modified by adjusting the blade lengths so that predicted and measured natural frequencies matched.

8.1.5.5 Measurement

For the measurements, various programs were written: low-level drivers to access the data-acquisition hardware directly, functions to perform data-acquisition task, and high-level programs to perform operations like conducting a modal test, exciting travelling waves in stationary structures or driving an interaction experiment. The modular design of the measurement software made it possible to accommodate easily for new hardware components or other changing elements in the measurement chain.

8.2 Summary of Conclusions

The main conclusion that can be drawn from the research reported in this thesis is that the travelling-wave-speed instability exists.

The conditions that lead to the travelling-wave-speed instability depend on the structural parameters of the contacting structures, the contact type, and the speed of rotation. In detail, the following list of qualitative parameter dependencies was established.

- A necessary requirement for the occurrence of the travelling-wave-speed instability is that the structures are rotationally periodic or cyclically-symmetric, so that a pair of modes with identical natural frequencies and similar modeshapes exist in each structure that can be cast into pure travelling waves.
- In order for the travelling-wave-speed instability to occur, the vibratory motion of at least one structure must be coupled in at least two spatial dimensions, such as the axial and tangential motions in the case of the stator in this study.
- As the forward-travelling wave of the stator has a positive wave velocity, it can be concluded that the critical speed for the travelling-wave-speed coincidence of the mode with n nodal diameters is always higher than the n^{th} engine-order speed, at which speed the counter-rotating wave of the rotor crosses the 0 Hz line.
- The experiments indicate that only the absolute value of the difference between speed of rotation and critical speed enters the equation of motion.
- Centrifugal stiffening moves the critical speeds towards higher speeds of rotation. For modes where the effect of centrifugal stiffening is dominant at the critical speeds compared with the natural frequency at rest, the absolute difference in wave velocities is a more appropriate measure than the difference in rotation speed.
- Results from numerical simulations show that the lower the levels of damping, the larger the speed range where the instability occurs.
- Any initial contact at the critical speeds will most certainly start an instability of the tuned system. The requirement of having a non-zero spatial component of the initial contact similar to the wave form is generally fulfilled for finite numbers of blades and realistic initial conditions, e. g. stemming from flight manoeuvres or bird strikes, or any impact in both temporal and spatial senses. Spatial components with other numbers of nodal diameters will eventually decrease due to energy dissipation.
- The required amplitude of the initial conditions must be such as to overcome the clearance between rotor and stator.
- From experiments with a mistuned stator, it can be concluded that mistuning impedes the mechanism that leads to the instability, as the existence of stationary waves (fixed in the structure) makes the energy transfer between kinetic rotational energy of the rotor and the vibration of the coupled system inefficient.

8.3 Outlook

Recent reports, (e.g., Aviation Week and Space Technology, 1996), suggest that the interactions between fans and flexible casings are still at the focus of attention of large aircraft-engine manufacturers. Economic considerations require researchers to investigate every possibility to reduce the clearances between rotors and their casings, while the uncertainty in the dynamics and the structural loads demand larger clearances. The work undertaken in this project was aimed at increasing the fundamental understanding of the interaction dynamics. Further studies beyond the presented research could deepen the understanding and yield further insight into the problem that would allow for a reduction of the clearance.

In the thesis, a mathematical model is presented that can predict the dynamics of the rotor-stator system, within the limits and uncertainties of the algorithm and the input data. The uncertainties in the contact friction model, probably the least certain of the many design factors, suffice to explain the quantitative difference between simulated and experimental data. A better understanding of the local, contact friction dynamics would make the overall model more reliable in predicting the behaviour of engineering structures. Reliable data has to accompany any more sophisticated friction models, as otherwise the overall uncertainty of the models remains and the increased modelling effort was spent in vain.

The parameter set can be further extended to include parameters like wear at the interface or temperature dependencies of the contact. Of interest is also, whether, by a change of speed of rotation, stable conditions can be reached once the instability has started.

The mathematical model could be extended further to include the dynamics of the shaft, so that rotor and stator have non-zero boundary conditions at the clamped shaft interface. In addition to the generally more accurate description of the boundary conditions, this would lead naturally to an investigation of the problem of 'windmilling', where the dynamics of an aircraft engine after a blade-off event are investigated: the large unbalance created by the loss of a blade causes large synchronous forces. Together with the likely damage to the bearings and their support, e. g. by fusing, off-centre contact between rotor and stator is highly possible.

In all analyses, the investigations of fundamental aspects with their far-reaching advantages and long-term benefits should be given priority over specialised solutions for particular configurations with possibly immediate, but only short-term, benefits.

Chapter 9: References

- Argyris, J., Mlejnek, H.-P. Dynamics of Structures - Texts on computational Mechanics (V), North-Holland, Amsterdam, 1991.
- Aviation Week and Space Technology, DC-10 CF6 Engine Investigation pressed, *AW&ST*, **November 12**, 28-29, 1972.
- Aviation Week and Space Technology, Airline Outlook: GE90 increased Clearances, *AW&ST*, **January 1**, 15, 1996.
- Balmès, E. **User's Guide to experimental and analytical Structural Dynamics Toolbox**, 2nd ed., Scientific Software Group, Sèvres, 1995.
- Basu, P., Griffin, J.H. The Effect of limiting aerodynamic and structural Coupling in Models of mistuned bladed Disc Vibration, *Proc Conf Noise Vib, Cincinnati*, 1985.
- Bathe, K.-J. **Finite Element Procedures in Engineering Analysis**, Prentice-Hall, Englewood Cliffs, NJ, 1982.
- Bauer, H.F. Vibration of a rotating uniform Beam - Part I: Orientation in the Axis of Rotation, *J Sound Vib*, **72** (2), 177-189, 1980.
- Biezeno, C.B., Grammel, R. **Technische Dynamik I**, 2nd ed., Springer, Berlin, 1953.
- Biezeno, C.B., Grammel, R. **Technische Dynamik II**, 2nd ed., Springer, Berlin, 1953.
- Blevins, R.D. **Formula for Natural Frequency and Mode Shape**, van Nostrand Reinhold, New York, 1984.
- Braddick, H.J.J. **Mechanical Design of Laboratory Apparatus**, Chapman and Hall, London, 1960.
- Bronstein, I.N., Semendjajew, K.A. **Taschenbuch der Mathematik**, 21th ed., Harry Deutsch, Thun und Frankfurt/Main, 1981.
- Chen, L.-W., Chern, H.-K. The Vibrations of pre-twisted rotating Beams of general Orthotropy, *J Sound Vib*, **167**, (3), 529-539, 1993.
- Choy, F.K., Padovan, J. Non-linear transient Analysis of Rotor-Casing Rub Events, *J Sound Vib*, **113**, (3), 529-545, 1987.
- Cornwell, P.J., Bendiksen, O.O. Numerical Study of Vibration Localisation in disordered cyclic Structures, *J AIAA*, **30**, 2, 473-481, 1992.
- Cottney, D.J., Ewins, D.J. Towards the efficient Analysis of shrouded bladed Disc Assemblies, *J Eng Ind*, 1054-1059, 1974.
- Crawley, E.F. Aeroelastic Formulation for tuned and mistuned Rotors, Agardograph No. 298: Aeroelasticity in Axial-Flow Turbomachinery - Structural Dynamics and Aeroelasticity, **2**, (19), NATO, Brussels, 1988.
- Darlow, M. **High Speed Balancing**, Springer, Berlin, 1992.
- Ehrich, F.F. **Handbook of Rotordynamics**, McGraw-Hill, New York, 1992.
- Ehrich, F.F. The Dynamic Stability of Rotor/Stator radial Rubs in rotating Machinery, *J Eng Ind*, November, 1025-1028, 1969.

- Elchuri, V., Smith, G.C.C., Gallo, A.M. NASTRAN forced Vibration Analysis of rotating cyclic Structures, *J Vib Acoust Stress Rel Design*, **106**, April, 224-234, 1984.
- European Union, *Modelling of Rotor/Stator Interaction Dynamics - Work programme*, Brite-Euram Proposal BE5463: Rostadyn, Department General XII, Brussels, 1992.
- Evans, C. **Precision Engineering: an evolutionary View**, Kluwer, Dordrecht, 1989.
- Eversman, W., Dodson Jr., R.O. Free Vibration of a centrally clamped spinning circular Disk, *J AIAA*, **7**, (10), 2010-2012, 1969.
- Ewins, D.J. An experimental Investigation of the forced Vibration of bladed Discs due to aerodynamic Excitation, *ASME Publication on Structural Dynamical Aspects of bladed-disc Assemblies*, 15-27, 1976.
- Ewins, D.J. Basic Structural Dynamics, Agardograph No. 298: Aeroelasticity in Axial-Flow Turbomachinery - Structural Dynamics and Aeroelasticity, **2**, (13), NATO, Brussels, 1988.
- Ewins, D.J. Bladed Disc Vibration - A Review of Techniques and Characteristics, *Proc Int Conf Recent Adv Struc Dyn, Southampton*, 1980.
- Ewins, D.J. **Modal Testing: Theory and Practise**, Research Studies Press, Taunton, Somerset, UK, 1984.
- Ewins, D.J. The Effects of Blade Mistuning on the Vibration Response - a survey, *Proc IFToMM, Prague*, 1991.
- Ewins, D.J. Structural Dynamic Characterietiscs of bladed Assemblies, Agardograph No. 298: Aeroelasticity in Axial-Flow Turbomachinery - Structural Dynamics and Aeroelasticity, **2**, (15), NATO, Brussels, 1988.
- Ewins, D.J. Vibration Characteristics of Bladed Disc Assemblies, *J Mech Eng Science*, **15**, (3), 1973.
- Ewins, D.J. Vibration Modes of mistuned bladed Disks, *J Eng Power*, **75-GT-114**, 1975.
- Ewins, D.J., Han, Z.S. Resonant Vibration Levels of a Mistuned bladed Disk, *J Vib Acoust Stress Reliability Design*, **106**, 211-217, 1984.
- Ewins, D.J., Henry, R. Structural Dynamic Characterietiscs of individual Blades, *Agardograph No. 298: Aeroelasticity in Axial-Flow Turbomachinery - Structural Dynamics and Aeroelasticity*, **2**, (14), NATO, Brussels, 1988.
- Ewins, D.J., Imregun, M. Vibration Modes of packeted bladed Disks, *J Vib Acoust Stress Reliability Design*, **106**, 175-180, 1984.
- Filippov, A.P. **Vibrations of Mechanical Systems**, Kluwer Academic, Dordrecht, 1971.
- Flowers, G.T., Ryan, S.G. Development of a Set of Equations for incorporating Disk Flexibility Effects in rotordynamical Analyses, *J Gas Turbine*, **91-GT-75**, 1991.
- Föppl, A. Das Problem der Laval'schen Turbinenwelle, *Civilingenieur*, **41**, 248-250, 1895.
- Fumigalli, M.A., Schweitzer, G. *Analysis of the Measurements of Rotor/Stator Contact Interactions*, Technical Report, Rostadyn Project BE5463, Zürich, 1995.

- Garvey, S.D., Penny, J.E. Representing periodic Structures efficiently as Substructures, *J Sound Vib*, **178**, (1), 79-94, 1994.
- Gasch, R., and Knothe, K. **Strukturdynamik I**, Springer, Berlin, 1987.
- Gasch, R., and Knothe, K. **Strukturdynamik II**, Springer, Berlin, 1989.
- Gasch, R., Pfützner, H. **Rotordynamik - Eine Einführung**, Springer, Berlin, 1975.
- Géradin, M., Rixen, D. **Mechanical Vibrations - Theory and Applications to Structural Dynamics**, Wiley, New York, 1994.
- Glocker, Ch., Pfeiffer, F. Stick-Slip Phenomena and Applications in **Nonlinearity and Chaos in Engineering Dynamics**, 103-113, Wiley, New York, 1994.
- Goldman, P., Muszynska, A. Chaotic Behavior of Rotor/Stator Systems with Rub, *Proc Gas Turbine, Cincinnati*, **93-GT-387**, 1993.
- Golub, G.H., van Loan, C.F. **Matrix Computations**, John Hopkins University Press, Baltimore, 1983.
- Gorman, D.G. Initiation of transverse Vibration in rotating Discs, *J Sound Vib*, **62**, (2), 467-470, 1979.
- Hagedorn, P., Wallaschek, J. Travelling Wave Ultrasonic Motors I: Working Principle and mathematical Modelling of the Stator, *J Sound Vib*, **155**, (1), 31-46, 1992.
- Hagedorn, P., Wallaschek, J., Konrad, W. Travelling Wave Ultrasonic Motors II: A numerical Method for the flexural Vibrations of the Stator, *J Sound Vib*, **168**, (1), 115-122, 1993.
- Hardy, M.S.A. The Generation of Waves in infinite Structures by moving harmonic Loads, *J Sound Vib*, **180**, (4), 637-644, 1995.
- Harris, G.Z. The normal Modes of a circular Plate of variable Thickness, *Royal Aircraft Establishment*, 1967.
- Hatman, V.G., Haque, I., Bagchi, A. Dynamics of a flexible rotating Beam interacting with a flat rigid Surface: Model Development, Numerical Solution, *J Sound Vib*, **194**, (5), 653-670, 671-683, 1996.
- Heath, S., Imregun, M. Determination of rotating Assembly synchronous Response Characteristics using Blade Tip-timing Techniques, *Proc 15th ASME Biennial Conf Mech Vib Noise, Boston*, **84-2**, 1343-1351, 1995.
- Honda, Y., Matsuhisa, H., Sato, S. Modal Response of a Disk to a moving concentrated harmonic Force, *J Sound Vib*, **102**, (4), 457-572, 1985.
- Hughes, T.J.R. **The Finite Element Method**, Prentice-Hall, Englewood Cliffs, NJ, 1987.
- Hunt, K.H., Crossley, F.R.E. Coefficient of Restitution interpreted as Damping in Vibro-impact, *J Appl Mech*, June, 440-445, 1975.
- Imregun, M. *User's Guide Blipa*, Report 8801, Modal Testing Unit, Imperial College, London, 1988.
- IMSL, **IMSL Library Reference Manual**, 8th ed., IMSL, Houston, TX, 1980.
- Irretier, H. Coupled Vibrations of Blades in Bending-Bending-Torsion and Disks in out-of-plane and in-plane Motion, *J Eng Ind*, **79-DET-90**, 1979.

- Irretier, H. Spectral Analysis of mistuned bladed Disk Assemblies by Component Mode Synthesis, *Proc 9th Conf Mech Vib Noise, Dearborn, MI*, 115-125, 1983.
- Irretier, H., Mahrenholtz, O. Eigenfrequencies and Modeshapes of a free-standing, twisted, tapered and rotating Blade with respect to an elastically supported Root, *Proc Design Eng*, **81-DET-125**, 1-9, 1981.
- Irretier, H., Reuter, F. Experimental Modal Analyse of rotating Disk Systems, *Proc 15th ASME Biennial Conf Mech Vib Noise, Boston*, 1201-1206, 1995.
- Irretier, H., Reuter, F. *Experimentelle Modalanalyse in rotierenden Maschinen*, Abschlußbericht DFG, Universität/Gesamthochschule Kassel, 1994.
- Irretier, H., Schmidt, K.-J. Mistuned bladed Discs - dynamical Behaviour and Computation, *Proc IFToMM Rotordynamic Probs Power Plants, Rome*, 215-226, 1982.
- Jarvis, R.P., Mills, B. Vibrations induced by Dry Friction, *Proc IMechE*, **178**, (32.1), 847-866, 1964.
- Jeffcott, H.H. The lateral Vibration of loaded Shafts in the Neighbourhood of a whirling Speed, *Philosophical Magazine*, **6:37**, 304-314, 1919.
- Jen, C.W., Johnson, D.A. Formulation of centrifugal Stiffening Effect on flexible Multibody Systems via Rayleigh-Ritz based structural Synthesis, *Proc 15th IMAC*, 362-369, 1995.
- Jones, M.G., Barton, M.T., O'Brien, W.F. The Use of circumferentially nonuniform Stators to attenuate LP Compressor Rotor-Stator-Strut aerodynamic and mechanical Interactions, *Proc Conf Gas Turbine, Birmingham*, **96-GT-154**, 1996.
- Jordan, D.W., Smith, P. *Nonlinear ordinary differential Equations*, 2nd ed., Clarendon Press, Oxford, 1992.
- Kaiser, T., Hansen, R.S. Experimental/analytical Approach to understanding Mistuning in a transsonic Wind Tunnel Compressor, *Proc 5th Intl Conf Recent Adv Struc Dyn, Southampton*, 515-528, 1994.
- Kane, T.R., Levinson, D.A. **Dynamics: Theory and Applications**, McGraw-Hill, New York, 1985.
- Kaneko, Y., Mase, M., Fujita, K., Nagashima, T. Vibrational Response Analysis of mistuned bladed Disk, *Int J JSME*, **37**, C1, 33-40, 1994.
- Karnopp, D., Rosenberg, R.C. **Analysis and Simulation of Multiport Systems**, MIT Press, Cambridge, MA, 1968.
- Kaza, K.R.V., Kielb, R.E. Vibration and Flutter of Mistuned Bladed-disk Assemblies, *J Propulsion*, **1**, (5), 336-344, 1985.
- Khader, N., Loewy, R.G. Structural Dynamics of rotating Bladed-Disk Assemblies coupled with flexible Shaft Motions, *J Sound Vib*, 1990.
- Klompas, N. A frictionally Induced Disk/Shaft Instability: Physical Explanation of an experimental Fan Failure, *J Gas Turbines*, **86-GT-131**, 1986.
- Krämer, E. **Dynamics of Rotors and Foundations**, Springer, Berlin, 1993.

- Krautkrämer, J. and H.: **Ultrasonic Testing of Materials**, 3ed., 580-582, Springer, Berlin, 1983.
- Lamb, H., Southwell, R.V. The Vibrations of a spinning Disc, *Proc Royal Soc London A*, **99**, 272-280, 1921.
- Lee, C.-W. **Vibration Analysis of Rotor**, Kluwer, Dordrecht, 1993.
- Lee, C.-W., Kim, M.-E. Identification of travelling Wave Modes in rotating Disks using Wave dFRFs, *Proc 14th IMAC*, 1403-1408, 1996.
- Lee, C.-W., Kim, M.-E. Use of dFRFs for the Separation and Identification of travelling Wave Modes in rotating Disks, *Proc 13th IMAC*, 1368-1372, 1995.
- Leissa, A.W., Lee, J.K., Wang, A.J. Vibrations of twisted rotating Blades, *J Vib Acoust Stress Rel Design*, **106**, April, 251-257, 1984.
- Lesser, M. **The Analysis of complex nonlinear mechanical Systems**, World Scientific, Singapore, 1995.
- Link, M. **MATFEM User Guide**, Gesamthochschule, Kassel, 1994.
- Li-Tang, Y., Qi-Han, L. Investigation on travelling Wave Vibration for bladed Disks in Turbomachinery, *Rotor Dynamics Conference, Lyon*, 133-135, 1992.
- Loewy, R.G., Khader, N. Structural Dynamics of Rotating Bladed-Disk Assemblies coupled with flexible Shaft Motions, *J AIAA*, **22**, (9), 1319-1327, 1984.
- MacBain, J.C., Whaley, P.W. Maximum resonant Response of mistuned bladed Disks, *Proc 9th Biennial Conf Mech Vib Noise Design Production Eng, Dearborn*, 1993.
- Maciejowski, J.M. **Multivariable Feedback Design**, Addison-Wesley, Wokingham, UK, 1989.
- Macke, H.J. Traveling-Wave Vibrations of Gas-Turbine Engine Shells, *J Eng Power*, April, 179, 1966.
- Magnus, K. **Schwingungen**, 3rd ed., B. G. Teubner, Stuttgart, 1976.
- Mansfield, E.H. On the Analysis of elastic Plates of variable Thickness, *Royal Aircraft Establishment, Farnborough*, 1961.
- Mehdigholi, H., Robb, D.A., Ewins, D.J. Simulation of Vibration in a Disc rotating past a static Force, *Proc 10th IMAC*, 1992.
- Meirovitch, L. **Analytical Methods in Vibrations**, Macmillan, New York, 1967.
- Meirovitch, L. **Computational Methods in Structural Dynamics**, Sijthoff & Noordhoff, Alphen aan den Rijn, NL, 1980.
- Meirovitch, L. **Elements of Vibration Analysis**, 2nd ed., McGraw-Hill, New York, 1986.
- Meirovitch, L. **Methods of analytical Dynamics**, McGraw-Hill, New York, 1970.
- Mézière, L. *Vibrations de Structures a Symetrie cyclique: Application au cas des Turbomachines (in French)*, TurboMeca Report, Pau, 1993.
- Mignolet, M.P., Eick, C.D., Harish, M.V. Free Vibrations of flexible rotating Disks, *J Sound Vib*, **196**, (5), 537-577, 1996.

- Mikolajzak, A.A., Arnoldi, R.A., Snyder, L.E., Stargardter, H. Advances in Fan and Compressor Blade Flutter Analysis and Predictions, *J Aircraft*, **12**, (4), 325-332, 1975.
- Minas, C., Kodiyalam, S. Vibration Analysis of bladed Disc Assemblies, *Proc 13th IMAC*, 1331-1337, 1995.
- Mindlin, R.D. Influence of Rotary Inertia and Shear on flexural Motion of isotropic elastic Plates, *J Appl Mech*, **18**, 31-38, 1951.
- National Transportation Safety Board, *National Airlines Inc. DC-10-10, N60NA, near Albuquerque, NM, November 3, 1973*, Aircraft Accident Report PB-239 889, National Technical Information Service, DoC, Washington, DC, 1975.
- Nava, P., Paone, N., Rossi, G.L., Tomasini, E.P. Design and experimental Characterization of a nonintrusive Measurement System of rotating Blade Vibration, *J Eng Gas Turbine Power*, **116**, 657-661, 1994.
- Nelson, H.D. Modeling, Analysis and Computation in Rotordynamics - a historical Perspective, *Proc IFToMM*, 171-177, 1994.
- Okubo, M., Evensen, H.A., van Karsen, C.D. The Influence of Motion to Mode Shape in rotating Disc (Decomposition of standing waves by virtual traverse Method), *Proc 13th IMAC*, 782-790, 1995.
- Ostermeyer, G.-P. Zur numerischen Behandlung von elastischen Stößen in Mehrkörpersystemen, *Ingenieur Archiv*, **58**, 67-79, 1988.
- Owczarek, J.A. Analysis of an axial Compressor Blade Vibration based on Wave Reflection Theory, *J Eng Power*, **83-GT-151**, 1983.
- Padovan, J., Choy, F.K. Nonlinear Dynamics of Rotor/Blade/Stator Rub Interactions, *J Turbo*, **109**, 527-534, 1987.
- Parker, R. Pressure Fluctuations due to Interaction between Blade Rows in Axial Flow Compressors, *Proc IMechE*, **183**, (1), 1968.
- Pfeiffer, F., Glocker, C. Impacts with Friction, *Proc 15th ASME Biennial Conf Mech Vib Noise, Boston*, **84-1**, 171-180, 1995.
- Press, W.H., Flannery, B.P., Teukolsky, S.A., Vetterling, W.T. **Numerical Recipes - The Art of scientific Computing (FORTRAN Version)**, Cambridge University Press, Cambridge, 1989.
- Rao, J.S. **Rotor dynamics**, 2nd ed., Wiley, New York, 1991.
- Renshaw, A.A., D'Angelo III, C., Mote Jr., C.D. Aerodynamically excited Vibration of a rotating Disc, *J Sound Vib*, **177**, (5), 577-590, 1994.
- Rothe, R. **Höhere Mathematik**, 5th ed., B. G. Teubner, Leipzig, 1952.
- Samar, R., Postlethwaite, I., Gu, D.-W. Model Reduction with Balanced Realizations, *Intl J Control*, **62**, (1), 33-64, 1995.
- Sanliturk, K.Y., Imregun, M., Ewins, D.J. An analytical Solution for the forced Vibration Response of tuned bladed Disc Assemblies, *Rotor Dynamics Conference, Lyon*, 523-528, 1992.

- Schlack Jr., A.L., Kessel, P.G. Gyroscopically Induced Vibrations of Circular Plates, *J AIAA*, **7**, (10), 1932-1937, 1969.
- Schmiechen, P. *Demonstration of the Rotor-Stator Interaction*, Technical Report, Rostadyn Project BE5463, London, 1996.
- Schmiechen, P. and Slocum, A.H. Design of Kinematic Systems: A generalised Approach, *Prec Eng*, **18**, (1), 1996.
- Schmiechen, P. *Design Report on the Task 5 Rig*, Technical Report, Rostadyn Project BE5463, London, 1995.
- Schmiechen, P. *Industrial Review of the travelling Wave Speed Coincidence*, Technical Report, Rostadyn Project BE5463, London, 1994.
- Schmiechen, P., Ewins, D.J., Bucher, I. Excitation of arbitrary Displacement/Velocity Conditions in rotationally periodic Structures, *Proc 15th ASME Biennial Conf Mech Vib Noise, Boston*, **84-2**, 1353-1360, 1995.
- Schweitzer, G., Fumigalli, M.A. Measurements on a Rotor contacting its Housing in **Proc IMechE Vib Rot Machinery VI**, 779-788, Oxford, 1996.
- Shampine, L.F., Reichelt, M.W. The MATLAB ODE Suite, The Mathworks Inc, Natick, MA, 1995.
- Slocum, A.H. **Precision Machine Design**, Prentice Hall, Englewood Cliffs, NJ, 1992.
- Smailes, G.T. *Wave Speed Coincidence*, Private Communications, Rolls-Royce, 1993.
- Srinivasan, A.V., Lauterbach, G.F. Traveling Waves in rotating cylindrical Structures, *J Eng Ind*, 1229-1232, 1971.
- Stange, W.A., MacBain, J.C. An Investigation of Dual Mode Phenomena in a mistuned bladed Disk, *J Vib Acoust Stress Reliability Design*, **105**, 402-407, 1983.
- Stelter, P. Reibungserregte Torsionsschwingungen in Schneckenzenrifugen in Proc SIRM III Kaiserslautern, 268-277, Vieweg Verlagsgesellschaft, Braunschweig, 1995.
- Stodola, A. **Dampf- und Gasturbinen**, 4th ed., Springer, Berlin, 1910.
- Swaminadham, M. Large-Amplitude Oscillations of a spinning Disk - Experimental Investigation, *Proc 8th IMAC*, 1990.
- Szabó, I. **Einführung in die Technische Mechanik**, 8th ed., Springer, Berlin, 1984.
- Szabó, I. **Höhere Technische Mechanik**, Springer, Berlin, 1956.
- The Mathworks **Matlab 4.2c - User Guide**, The Mathworks, Natick, MA, 1994.
- Thomas, D.L. Dynamics of rotationally periodic Structures, *Intl J Num Meth Eng*, **14**, 81-102, 1979.
- Timoshenko, S. **Vibration Problems in Engineering**, van Nostrand, Princeton, 1955.
- Tobias, S.A. Free undamped non-linear Vibrations of imperfect circular Disks, *Proc IMechE*, **171**, 1957.
- Tobias, S.A., Arnold, R.N. The Influence of dynamical Imperfection on the Vibration of rotating Disks, *Proc IMechE*, **171**, 1957.

- Tomioka, T., Kobayashi, Y., Yamada, G. Analysis of free Vibration of rotating Disk-Blade coupled Systems by using artificial Springs and orthogonal Polynomials, *J Sound Vib*, **191**, (1) 53-73, 1996.
- Vance, J.M. **Rotordynamics of Turbomachinery**, Wiley, New York, 1988.
- Wagner, L.F., Griffin, J.H. A continuous analog Model for grouped-blade Vibration, *J Sound Vib*, **153**, (5) 110-118, 1992.
- Wang, W. *Dynamic Analysis of flexible bladed Disc-Shaft Rotor Systems*, PhD Thesis, Carleton University, Ottawa, 1992.
- Wang, W., Kirkhope, J. New Eigensolutions and Modal Analysis for gyroscopic/rotor Systems, *J Sound Vib*, **175**, (2), 159-170, 171-183, 1994.
- Weaver, M.M., Fleeter, S. Turbine Rotor generated Forcing Functions for Flow induced Vibrations, *J Gas Turbine*, **94-GT-328**, 1994.
- Weber, J.M. Computational and experimental Investigation of the centrifugal Stiffening of bending Vibrations of axisymmetric Discs, *MSc Thesis, Imperial College, London*, 1996.
- Williams, H.E. On the Boundary Conditions for the Membrane Equations of thin, cylindrical Shells and resulting Natural Frequencies, *J Sound Vib*, **155**, (1), 133-151, 1992.
- Xie, Y.M. An Assessment of Time Integration Schemes for non-linear Dynamic Equations, *J Sound Vib*, **192**, (1), 321-331, 1996.
- Yae, K.H., Inman, D.J. Model Reduction in a Subset of the Original States, *J Sound Vib*, **155**, (1), 165-176, 1992.
- Yang, S.-M. Vibration of a spinning annular Disk with coupled rigid-body Motion, *J Vib Acoust*, **115**, 159-164, 1993.
- Yiu, H. *Forced Vibration Characteristics of mistuned bladed-disc Assemblies*, PhD Thesis, Imperial College, London, 1995.
- Yoram, H. An efficient approximated Algorithm for Balancing and Order Reduction of lightly damped Systems, *Proc 50th Winter Annual Meeting ASME Vibration Conference, Boston*, 1995.
- Zienkiewicz, O.C. **The Finite Element Method**, 3rd ed., McGraw-Hill, New York, 1983.

Appendices

The appendices provide information and data supplementary to the main text. The data are not critical for the main work.

Appendix 1: Eigenanalysis

A.1.1 Eigenproblem derivation

The traditional form of the eigenproblem results from the solution of the homogeneous equation of motion for a discretised structure:

$$[M]\{\ddot{u}\} + [K]\{u\} = \{0\} \quad (\text{A-1})$$

Making an assumption for the solution, the classical harmonic trial solution, a special Bernoulli separation with possibly complex amplitude, $\{\hat{u}\}_r$, and frequency, ω_r :

$$\{u\} = \{\hat{u}\}_r e^{i\omega_r t} \quad (\text{A-2})$$

and substituting $\{u\}$ into the equation of motion, Equation (A-1) yields the standard eigenproblem:

$$(-\omega_r^2[M] + [K])\{\hat{u}\}_r = \{0\} \quad (\text{A-3})$$

For the non-trivial solution, $\{\hat{u}\}_r \neq \{0\}$, and so the determinant of the matrix expression must vanish. The resulting equation is called the characteristic equation and its roots are the natural frequencies, ω_r . The amplitude vector follows from solving the now singular vector equation, Equation (A-3). The solution is the eigenvector associated with that particular eigenvalue: $\{\hat{u}\}_r = \{\psi\}_r$. The matrix is rank deficient and the eigenvector can be scaled by an arbitrary constant. Further details on the numerical and computational aspects are given above in the main text.

A.1.2 Lagrange's method of obtaining the equations of motion

According to, e.g., Meirovitch, (1980), the kinetic energy of a system can be written in the form:

$$T = T_0 + T_1 + T_2 \quad (\text{A-4})$$

The first term usually stems from centrifugal forces, the second one from Coriolis forces and the last one typically from inertia forces:

$$T_2 = \frac{1}{2} \sum_r \sum_s m_{rs} \dot{u}_s \dot{u}_r \quad (\text{A-5})$$

$$T_1 = \sum_r f_r \dot{u}_r \quad (\text{A-6})$$

T_0 does not depend on the generalised velocities but only on the generalised displacements and will vanish in the subsequent analysis.

The potential energy can be expressed as:

$$U = \frac{1}{2} \sum_r \sum_s k_{rs} u_s u_r \quad (\text{A-7})$$

From the kinetic and potential energies, the Lagrangian of the system can be formed:

$$L = T - U \quad (\text{A-8})$$

In order to treat non-conservative systems within this framework, Rayleigh's dissipation function is introduced:

$$D = \frac{1}{2} \sum_r \sum_s c_{rs} \dot{u}_s \dot{u}_r \quad (\text{A-9})$$

If external forces act upon the system, generalised forces can be derived from the projection of the forces onto the generalised coordinates. The equations of motion can be computed from

$$\frac{d}{dt} \left(\frac{\partial L}{\partial \dot{u}_r} \right) - \frac{\partial L}{\partial u_r} + \frac{\partial D}{\partial \dot{u}_r} = Q_r \quad (\text{A-10})$$

For a simple one-dimensional mass-spring-damper system, the kinetic and potential energies around the static equilibrium position and the dissipation function can be expressed as:

$$T = \frac{1}{2} m \dot{u}^2 \quad U = \frac{1}{2} k u^2 \quad D = \frac{1}{2} c \dot{u}^2 \quad (\text{A-11})$$

u is in this one-degree-of-freedom case a principal coordinate and so the Lagrangian is given by:

$$L = T - U = \frac{1}{2} m \dot{u}^2 - \frac{1}{2} k u^2 \quad (\text{A-12})$$

Applying Lagrange's principle, Equation (A-10), results in the equation of motion of the mass:

$$m \ddot{u} + c \dot{u} + k u = 0 \quad (\text{A-13})$$

A.1.3 Example A.1-1: Modal solution of a discrete system

Consider the one-dimensional two-degree-of-freedom system of two bodies each of mass m connected by a spring k .

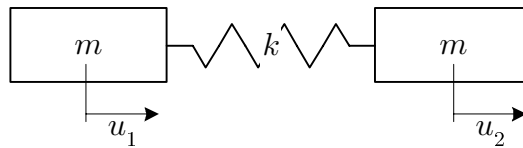


Figure A-1: Two-mass-spring system

The equations of motion for this system can be derived from its kinetic and potential energies, T and U respectively, following Section A.1.2, given by:

$$T = \frac{1}{2}m(\dot{u}_1^2 + \dot{u}_2^2) \quad U = \frac{1}{2}k(u_1^2 + u_2^2) \quad (\text{A-14})$$

from which, by application of Lagrange's principle, EOM(u) follows:

$$\begin{aligned} m\ddot{u}_1 + k(u_1 - u_2) &= 0 \\ m\ddot{u}_2 - k(u_1 - u_2) &= 0 \end{aligned} \quad (\text{A-15})$$

or as a vector equation:

$$\begin{aligned} \begin{bmatrix} m & 0 \\ 0 & m \end{bmatrix} \begin{Bmatrix} \ddot{u}_1 \\ \ddot{u}_2 \end{Bmatrix} + \begin{bmatrix} k & -k \\ -k & k \end{bmatrix} \begin{Bmatrix} u_1 \\ u_2 \end{Bmatrix} &= \begin{Bmatrix} 0 \\ 0 \end{Bmatrix} \\ [M]\{\ddot{u}\} + [K]\{u\} &= \{0\} \end{aligned} \quad (\text{A-16})$$

The equations are coupled through the off-diagonal terms of the stiffness matrix, $[K]$. The eigensolution of this problem can be computed to:

$$[\lambda_r] = \begin{bmatrix} \omega_1^2 & \\ & \omega_2^2 \end{bmatrix} = \begin{bmatrix} 0 & \\ & 2k/m \end{bmatrix} \quad [\Psi] = [\{\psi\}_1 \quad \{\psi\}_2] = \begin{bmatrix} \begin{Bmatrix} 1 \\ 1 \end{Bmatrix} & \begin{Bmatrix} 1 \\ -1 \end{Bmatrix} \end{bmatrix} \quad (\text{A-17})$$

The first mode, which has a natural frequency of 0 Hz, is the rigid-body mode of the system. In this one dimensional example there is only one such rigid body mode, but generally there are as many rigid-body modes as there are coordinate directions (in two dimensions there are three rigid-body modes – two translations and one rotation, in three dimensions there exist six possible rigid body modes) minus the number of constraints constraining the body in the reference frame.

The orthogonality conditions for the mass and stiffness matrices hold:

$$[\Psi]^T[M][\Psi] = \begin{bmatrix} 2m & \\ & 2m \end{bmatrix}, \quad [\Psi]^T[K][\Psi] = \begin{bmatrix} 0 & \\ & 4k \end{bmatrix} \quad (\text{A-18})$$

decoupling the equations of motion by using coordinates p instead of u , yields EOM(p):

$$\begin{bmatrix} 2m & \\ & 2m \end{bmatrix} \begin{Bmatrix} \ddot{p}_1 \\ \ddot{p}_2 \end{Bmatrix} + \begin{bmatrix} 0 & \\ & 4k \end{bmatrix} \begin{Bmatrix} p_1 \\ p_2 \end{Bmatrix} = \{0\} \quad (\text{A-19})$$

Mass-normalisation leads to, after simplification:

$$\begin{Bmatrix} \ddot{p}_1 \\ \ddot{p}_2 \end{Bmatrix} + \begin{bmatrix} 0 & \\ & 2k/m \end{bmatrix} \begin{Bmatrix} p_1 \\ p_2 \end{Bmatrix} = \{0\} \quad (\text{A-20})$$

A.1.4 Example A.1-2: Modal solution of a discretised system: FE analysis

As an example of an FE analysis, the analysis of a beam is presented. For simplicity of the example and comparison of methods, a shape is chosen that could be solved analytically. The element matrices can be derived from variational principles using shape

functions, (Gasch and Knothe, 1989). These ‘element modeshapes’ are linear or quadratic functions in the dimensions describing the assumed distributions of quantities like displacement or stresses. For the simple Euler-Bernoulli beam, which neglects rotary inertia, the degrees of freedom are the deflection and slope at each end. The mass and stiffness matrices are given by

$$[M_{beam}] = \frac{\rho A l}{420} \begin{bmatrix} 156 & -22l & 54 & 13l \\ -22l & 4l^2 & -13l & -3l^2 \\ 54 & -13l & 156 & 22l \\ 13l & -3l^2 & 22l & 4l^2 \end{bmatrix} \quad [K_{beam}] = \frac{2EI}{l^3} \begin{bmatrix} 6 & -3l & -6 & -3l \\ -3l & 2l^2 & 3l & l^2 \\ -6 & 3l & 6 & 3l \\ -3l & l^2 & 3l & 2l^2 \end{bmatrix} \quad (A-21)$$

where E , I , ρ , A , and l have their usually meaning. Assuming a clamped end, the matrices can be reduced to the degrees of freedom at the free end:

$$[M_{beam}]_1 = \frac{\rho A l}{420} \begin{bmatrix} 156 & 22l \\ 22l & 4l^2 \end{bmatrix} \quad [K_{beam}]_1 = \frac{2EI}{l^3} \begin{bmatrix} 6 & 3l \\ 3l & 2l^2 \end{bmatrix} \quad (A-22)$$

Solving the eigenproblem gives the spatial eigenvalues which are compared to the exact values from an analytic solution, (Gasch and Knothe, 1989):

FE ₁ :	1.88	5.90
analytic:	1.875	4.69

Table A-1: FE prediction with 1 element and analytical results

The lower mode is already well approximated, but the difference in the higher mode is 26% over-estimated.

In order to increase the accuracy, two elements of half length can be coupled. Each element has four degrees of freedom, two of which coincide at the connection point between the elements and two are deleted due to the boundary condition, so that the resulting eigenproblem is of order four:

$$[M_{beam}]_2 = \frac{\rho A}{3360l} \begin{bmatrix} 1248 & 0 & 216 & 26l \\ 0 & 8l^2 & -26l & -3l^2 \\ 216 & -26l & 624 & 44l \\ 26l & -3l^2 & 44l & 4l^2 \end{bmatrix} \quad [K_{beam}]_2 = \frac{B}{l^3} \begin{bmatrix} 48 & 0 & -24 & -6l \\ 0 & 4l^2 & 6l & l^2 \\ -24 & 6l & 24 & 6l \\ -6l & l^2 & 6l & 2l^2 \end{bmatrix} \quad (A-23)$$

The spatial eigenvalues follow to

FE ₂	1.875	4.71	8.67	14.8
analytic	1.875	4.69	7.85	11.0

Table A-2: FE prediction with 2 elements and analytical results

Now the second mode is well approximated to within 0.5%, while the next higher mode, that can not be predicted by the single-element model at all, has an error of 12%, and the

highest mode has an even larger error. In accordance with a rule of thumb, about 50% to 70% of the eigenvalues are predicted accurately by the FE solution.

A.1.5 Example A.1-3: Modal solution of a continuous system

As an example of a continuous system consider the bending vibration of a free-free Euler-Bernoulli beam with constant properties along the axis for which the EOM(u) can be written as, (Gasch and Knothe, 1989):

$$EI \frac{\partial^4 u(x,t)}{\partial x^4} + \rho A \frac{\partial^2 u(x,t)}{\partial t^2} = 0 \quad (\text{A-24})$$

subject to four boundary conditions. Using a Bernoulli-separation:

$$u(x,t) = \psi(x)p(t) \quad (\text{A-25})$$

this equation simplifies to two ordinary differential equations:

$$\begin{aligned} \frac{d^4 \psi}{dx^4} + \beta^4 \psi &= 0 \\ \frac{d^2 p}{dt^2} + \omega^2 p &= 0, \quad \beta^4 = \frac{\rho A}{EI} \omega^2 \end{aligned} \quad (\text{A-26})$$

with four spatial eigenvalues and two temporal natural frequencies. The general solution for the spatial, fourth-order ordinary differential equation can be written as:

$$\psi(x) = A_1 \cosh(\beta x) + A_2 \cos(\beta x) + A_3 \sinh(\beta x) + A_4 \sin(\beta x) \quad (\text{A-27})$$

where the four coefficients A_i are determined by the four spatial boundary conditions. The determinant of the coefficient matrix must be zero, which leads to a transcendental equation with an infinite number of solutions for the spatial eigenvalue. The temporal eigenvalue is then computed from Equation (A-26).

A.1.6 Orthogonality condition for eigenfunctions of continuous structures

Continuous systems, where the dynamics are described by partial differential equations, have an infinite number of modes and the modeshapes are continuous functions over the whole structure, called eigenfunctions. The orthogonality condition holds for the eigenfunctions of continuous systems, $\{\psi\}$ where it can be stated as, (Szabó, 1956):

$$\int_{body} \rho \{\psi\}_r \{\psi\}_s^* = \begin{cases} 0 & r \neq s \\ \int_{body} \rho \{\psi\}_r \{\psi\}_r^* & r = s \end{cases} \quad (\text{A-28})$$

The integral has to be taken over the whole body and the star denotes the complex conjugate. ρ denotes the, possibly spatially-varying, mass density. Complex modes occur commonly in rotating machinery but also in systems with non-proportional damping, (Ewins, 1984). Mass-normalisation changes Equation (A-28) accordingly to:

$$\int_{body} \rho \{\phi\}_r \{\phi\}_s^* = \delta_{rs} = \begin{cases} 0 & r \neq s \\ 1 & r = s \end{cases} \quad (\text{A-29})$$

where δ is the Kronecker Delta.

Appendix 2: Physical Data of Rotor and Stator

A.2.1 Material properties

Schmiechen, (1996), attempted to obtain material properties from measured wave velocities, but due to the unfavourable geometry, (Krautkrämer, 1983), the ultrasonic measurements were only accurate to within standard textbook values, (Beitz and Küttner, 1985). The values used in all calculations are:

$$\begin{aligned} E &= 211 \cdot 10^9 \text{ Nm}^{-2} \\ \rho &= 7850 \text{ kg m}^{-3} \\ \nu &= 0.29 \end{aligned} \quad (\text{A-30})$$

A.2.2 Geometry of the structures

A.2.2.1 Rotor

The rotor is a disc made from sheet metal with the following dimensions and boundary conditions:

$$\begin{aligned} r_i &= 20 \text{ mm} && \textit{clamped} \\ r_o &= 250 \text{ mm} && \textit{free} \\ h &= 0.8 \text{ mm} \end{aligned} \quad (\text{A-31})$$

Due to the slenderness of the disc and the necessary machining, there is always a bend in the rotor. The centrifugal force reduces it, but it never vanishes and makes itself visible as strong engine-order lines in the experimental data.

A.2.2.2 Stator

The stator is build from a metal disc with the following geometry

$$\begin{aligned} r_i &= 20 \text{ mm} && \textit{clamped} \\ r_o &= 250 \text{ mm} && \textit{free} \\ h &= 1 \text{ mm} \end{aligned} \quad (\text{A-32})$$

to which $N_{blades} = 20$ blades with the following geometric data:

$$\begin{aligned} l &= 175 \text{ mm} && 10 \text{ mm radius at free end} \\ w &= 20 \text{ mm} \\ h &= 1 \text{ mm} \end{aligned} \quad (\text{A-33})$$

are attached by means of clamps or roots:

$$\begin{aligned}
 l &= 25.4 \text{ mm} \\
 w &= 20 \text{ mm} \\
 h &= 9.5 \text{ mm}
 \end{aligned}
 \tag{A-34}$$

Appendix 3: Modal tests

A.3.1 Tuned stator

An example of an estimated frequency response function from a modal test of the bladed disc and the corresponding fitted, identified, FRF is shown in Figure A-2.

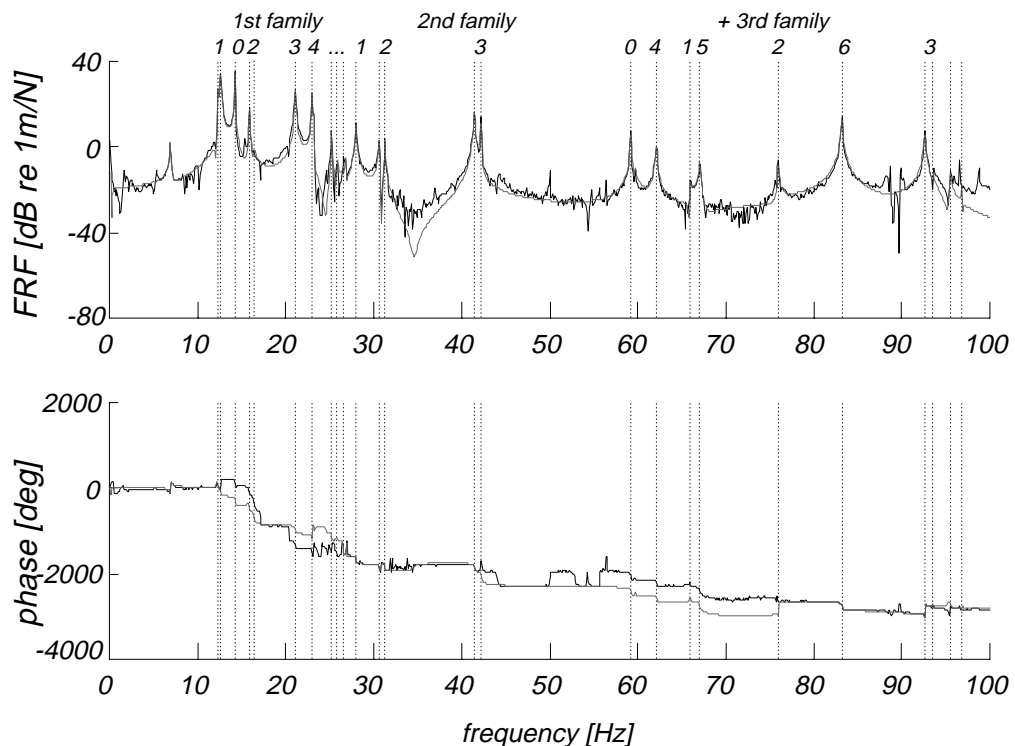


Figure A-2: Estimated and identified FRF

The difficulties of analysing a rotationally periodic structure like the bladed disc lie in the existence of double modes and the high modal density in the vicinity of the blade cantilever frequency, in Figure A-2 around 27 Hz. The identified model shows some deviation, especially in the phase, as some mode are not identified, for example in the region between 50 and 60 Hz. The modes may be spurious modes, most certainly the one at exactly 50 Hz.

Assumed that more than one measurements are made, the analysis is simplified if the spatial information is taken into account by analysing all measurements simultaneously. The identified modeshapes can then be matched reliably to the predictions by the number of nodal diameters, indicated by the numbers and the family number in Figure A-2.

frequency [Hz]	ND	family
12.3/12.6	1	1
14.2	0	1
16.1/16.3	2	1
21.1	3	1
23.0	4	1
24.9	5	1
25.1	6	1
26.6	10	1
28.0	1	2
30.6	2	2
31.4	2	2
42.3	3	2
59.3	0	3
62.2	4	2
67.0	1	3
76.0	5	2
83.3	2	3
92.6	6	2

Table A-3: Identified natural frequencies and nodal patterns

A.3.2 Mistuned stator

The system is mistuned for some of the tests by attaching four masses of 65 g each at the perimeter of the stator disc, 90° apart.

The natural frequencies of the first family are given in Table A-4.

frequency [Hz]	ND	family
11.7/12.0	1	1
13.3	0	1
15.4/16.1	2	1
20.8	3	1
22.8/23.3	4	1
24.0	5	1

Table A-4: Natural frequencies and nodal patterns, mistuned stator

Clearly visible are the splits of the 2ND and 4ND modes, while the natural frequencies of all modes are lowered.

A.3.3 Rotor

The modal test of the rotor reveals that the natural frequencies of the zero-nodal-circle mode family is predicted accurately. Larger errors exist in the predictions of the one-nodal-circle family which is over-estimated by about 15%.

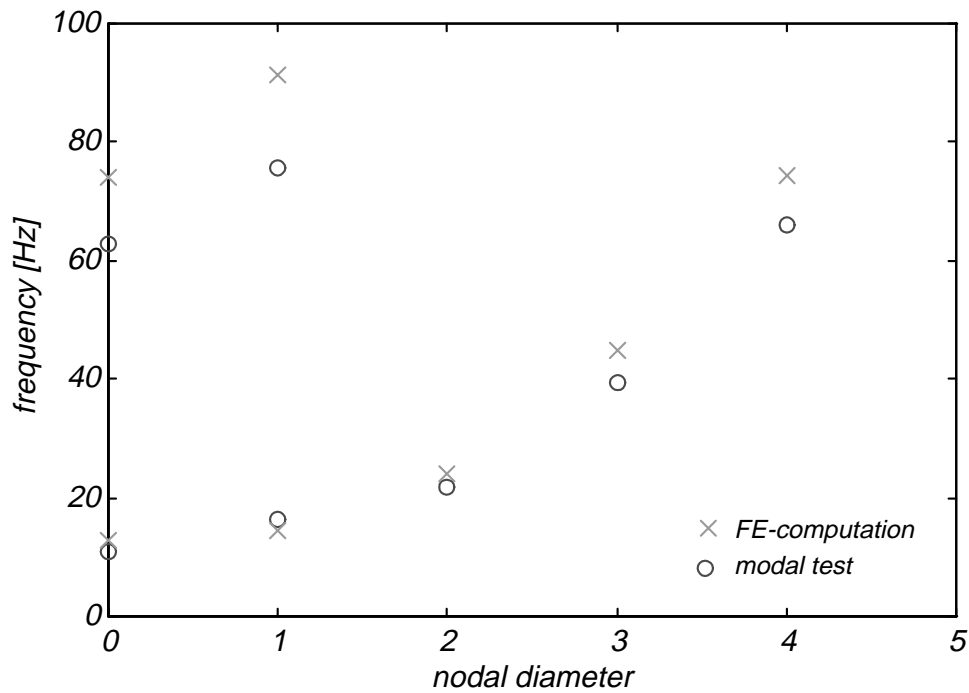


Figure A-3: Rotor natural frequencies: measured and predicted

Appendix 4: Natural Frequencies of a Rotating Disc

The expressions J_b/J_k and J_Ω/J_k are computed using the method presented in the main text by limit computations of the variational parameter ϵ . The geometric data are adjusted to produce the experimentally obtained frequencies, (Weber, 1996).

n	0	1	2	3	4	5	6	7	8	9	10
J_b/J_k	1.78	1.28	2.92	14.4	44.9	105	211	389	665	1069	1635
J_Ω/J_k	0.65	1.00	2.39	4.14	6.31	9.08	12.5	16.5	21.1	26.3	32.2

Table A-5: Eigenvalue coefficients

These values are in good agreement with the analytical predictions from Lamb and Southwell, (1921), and Tobias (1957), Table A-6.

n	0	1	2	3	4	5	6	7	8	9	10
β_b	–	–	2.67	14.5	45.2	108	218	394	661	1042	1566
β_Ω	–	–	2.36	4.06	6.13	8.55	11.3	14.5	17.9	21.8	26.0

Table A-6: Eigenvalue coefficients from literature

The differences can be explained by the fact that the previous researchers considered a circular disc, whereas in this study the coefficients for an annular disc are computed.

Appendix 5: Data of the Test Rig

A.5.1 Motor and controller

The motor is a 2 kW brushless DC motor which is an AC motor with a controller making the interface identical to that of an DC motor.

Due to the high power rating it is sufficient to assume constant speed during the analysis and simulation and neglect the torsional dynamics of the system. If the motor does not provide an 'infinite' torque so that the moments caused by the tangential forces are large enough to change the speed of rotation, then the model would need to be extended to include this torsional dynamics. In most cases this would cause a much more intricate situation as the wave velocity of the rotor observed in the stationary frame of reference would not remain constant any more, and the equality of the wave velocities would only hold for the average velocities, possibly invalidating the further analysis.

A.5.2 Controller

The experiment is controlled from a standard PC running MATLAB version 4.2b. From within this environment the whole rig can be operated: the motor, the data-acquisition system, and the filter. From a user point of view, the system is a MATLAB environment with added procedures to add the functionality required to conduct vibration tests. Low-level driver routines are written in a procedural language for which the software interface is provided by the hardware manufacturers.

A.5.3 Anti-aliasing filters

Anti-aliasing filters are used for all response measurements. The signals are AC coupled to filter out the static, DC, component and to increase the resolution of the dynamic signal component. The filter used are 8-pole elliptic filters with two settings for highest attenuation or best phase linearity.

A.5.4 Data acquisition system

The data-acquisition system uses a 16 bit-resolution-16 channel interface card. The combined maximum sampling rate of 72 kHz can be maintained over minutes by streaming the data to the harddisc. The measurements can be synchronised with the shaft rotation by an incremental shaft encoder or the measurements can be triggered by an event, such as a once-per-revolution signal.

A.5.5 Displacement sensors

The proximity probes used are Bently Nevada 25 mm, 11 mm and 8 mm probes with linear measurement ranges 12.7 mm, 10 mm, and 4 mm respectively. The quoted measurement resolution of 789 mV/mm (20 V/inch) has been confirmed in a test.

A.5.6 Design sketch

This sketch shows the main elements of the test rig:

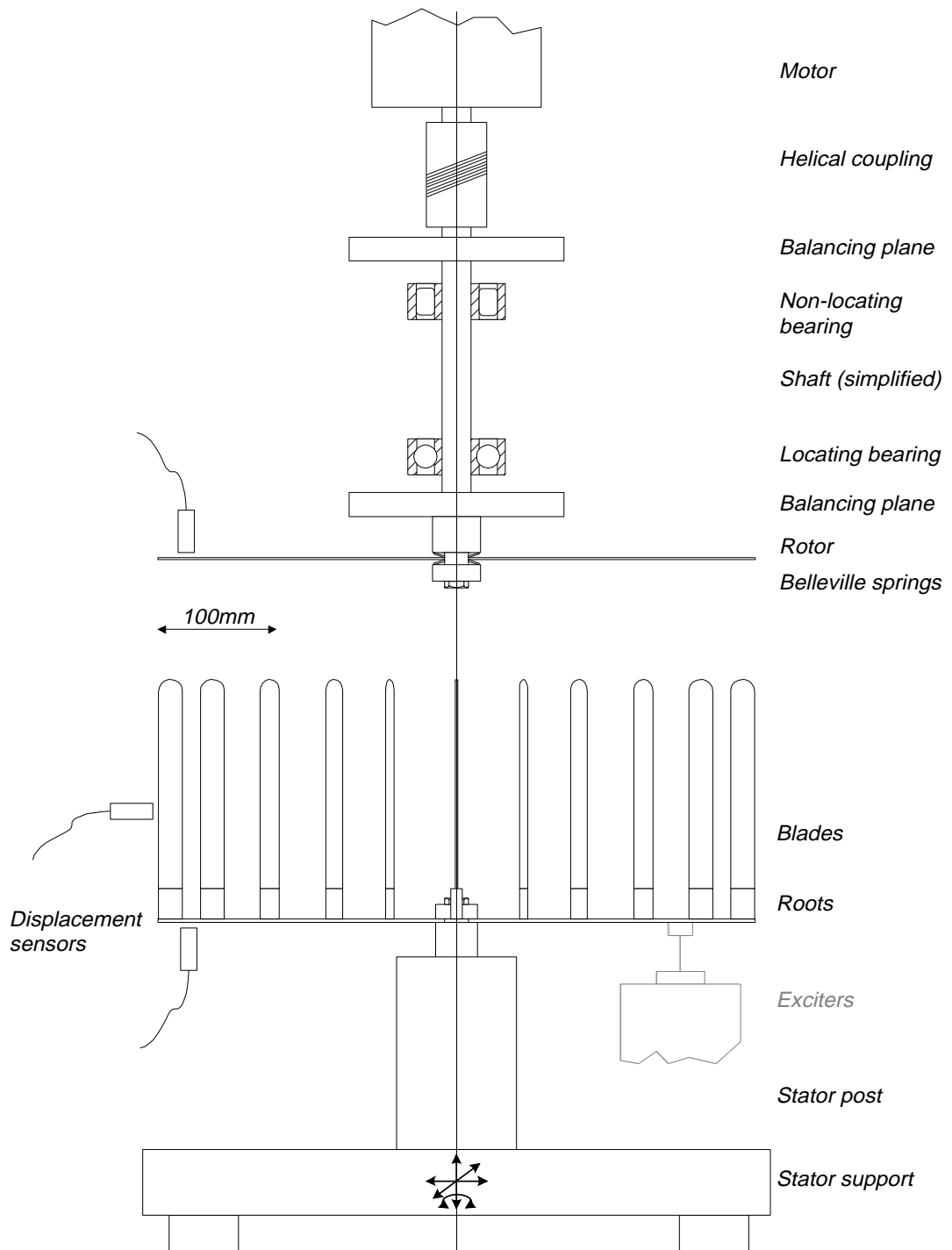


Figure A-4: Schematic of the test rig

Appendix 6: Interaction Experiments

The following figures show a second set of spectrograms of rotor and stator at the critical speed. The similarity of the figures to Figures 7-10 and 7-11 shows that the response is indifferent to the initial conditions, as the impact is not controlled.

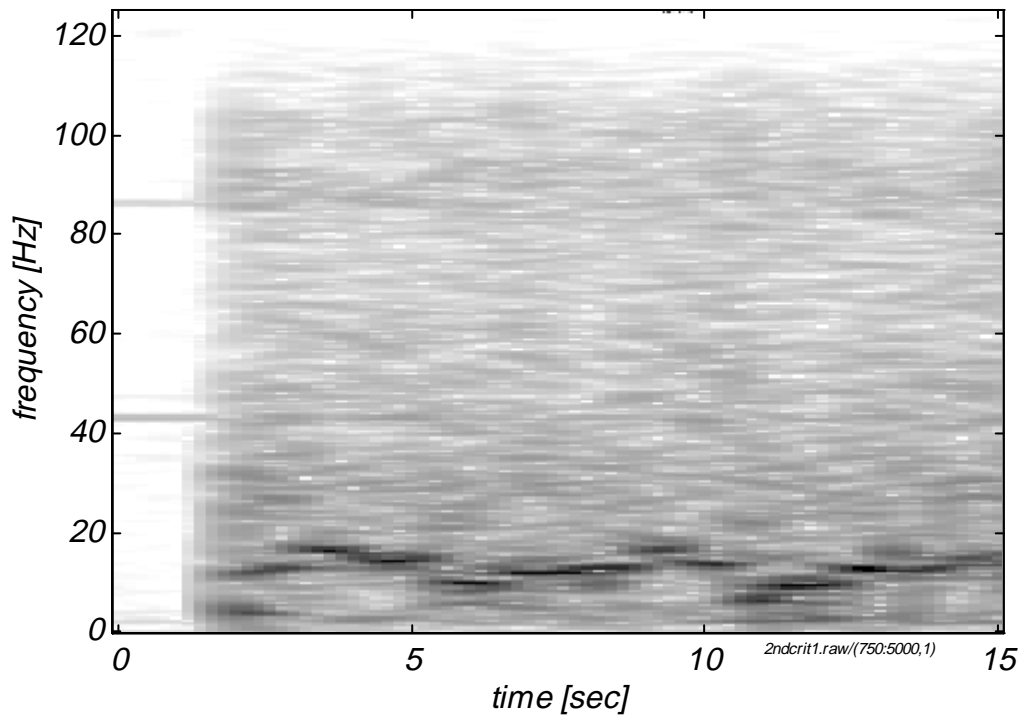


Figure A-5: Rotor response at critical speed

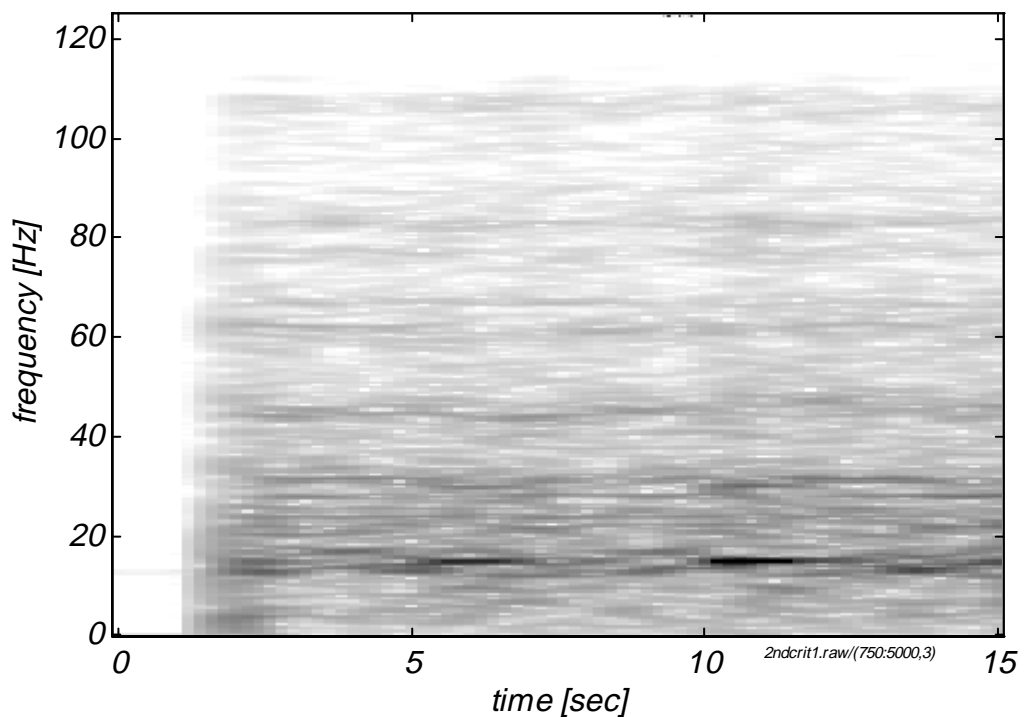


Figure A-6: Stator response at critical speed

Appendix 7: Programs

This appendix presents the program to compute the natural frequencies of the rotor as function of the speed of rotation and the main programs of the simulation package with the main functional dependencies highlighted.

A.7.1 Natural frequencies of the rotor as function of the speed of rotation

Natural Frequencies of a Spinning Disc with Centrifugal Forces

Mass of blades on rim can be considered.

Equation numbers Biezeno/Grammel II.

Varying thickness prepared, but not used, watch for modeshape approximations!

Dimensional equations, integrals run from r_i to r_o .

Material Properties:

$$\rho := 7850 \cdot \text{kg} \cdot \text{m}^{-3} \quad E := 205 \cdot 10^3 \cdot \text{N} \cdot \text{mm}^{-2} \quad \nu := 0.29 \quad W := 6000 \cdot \text{rpm}$$

Geometry of the disc:

$$r_i := 20 \cdot \text{mm} \quad r_o := 250 \cdot \text{mm} \quad dr := r_o - r_i \quad i := 0.. \frac{dr}{\text{mm}} \quad r_i := r_i + i \cdot \text{mm} \quad h_i := 0.75 \cdot \text{mm}$$

Geometry of added masses (assumed in the middle of the disc), currently not used

$$h_c := 0 \cdot \text{mm} \quad r_c := r_o + 0 \cdot \text{mm} \quad h_I := h_c \quad (\text{equivalent height})$$

$$m_w := 24 \cdot 20 \cdot \text{mm}^2 \cdot h_c \cdot \rho \quad \alpha := 15 \cdot \text{deg} \quad h(r) := \text{if}(r \leq r_o, h_i, h_c)$$

Stresses

Equivalent centrifugal stress on the outer rim of the disc

$$\sigma_w(W) := \frac{m_w \cdot r_o \cdot W^2}{r_o \cdot \alpha \cdot h_i} \quad \sigma_w(W) = 0 \cdot \text{N} \cdot \text{mm}^{-2}$$

Stresses in the disc at running speed

Eq. 5.6

$$\text{Auxiliary quantities:} \quad a_1 := \frac{3 + \nu}{8} \quad a_2 := \frac{1 + 3 \cdot \nu}{8}$$

$$A_1(W) := \sigma_w(W) \cdot \frac{r_o^2}{r_o^2 - r_i^2} + a_1 \cdot \rho \cdot W^2 \cdot (r_o^2 + r_i^2) \quad A_2(W) := -\sigma_w(W) \cdot \frac{r_o^2 \cdot r_i^2}{r_o^2 - r_i^2} - a_1 \cdot \rho \cdot W^2 \cdot r_o^2 \cdot r_i^2$$

The stress distribution over the disc

Eq. 23.2a

$$\sigma_{r_o}(r, W) := A_1(W) + \frac{A_2(W)}{r^2} - a_1 \cdot \rho \cdot W^2 \cdot r^2 \quad \sigma_{\phi_o}(r, W) := A_1(W) - \frac{A_2(W)}{r^2} - a_2 \cdot \rho \cdot W^2 \cdot r^2$$

The stress distribution over the disc and the rim (blades)

$$\sigma_r(r, W) := \text{if}\left(r \leq r_o, \sigma_{r_o}(r, W), \sigma_{r_o}(r_o, W) \cdot \frac{r_c - r}{r_c - r_o}\right) \quad \sigma_{\phi}(r, W) := \text{if}\left(r \leq r_o, \sigma_{\phi_o}(r, W), 0 \cdot \text{N} \cdot \text{mm}^{-2}\right)$$

Eigenfrequencies

Rayleigh quotient:
$$\lambda_{\max}(k, \text{eps}) < \frac{J_b(k, \text{eps}) \cdot \beta^2 + J_w(k, \text{eps}, W) \cdot W^2}{J_k(\text{eps})}$$

The eigenvalue of the spinning disc is smaller than the sum of the eigenvalue of a disc at rest and that of a spinning membrane.

Assumed mode-shape (only zero nodal diameter modes are of interest)

$$Z(r, e) := \frac{(r - r_i)^2}{r_o} \cdot \left(1 + e \cdot \frac{r - r_i}{r_o} \right) \tag{Eq. 29.30}$$

Support computation by calculating the derivates beforehand (not strictly necessary):

$$Zr(r, e) := (r - r_i) \cdot \frac{(2 \cdot r_o + 3 \cdot e \cdot r - 3 \cdot e \cdot r_i)}{r_o^2} \qquad Zrr(r, e) := 2 \cdot \frac{(r_o + 3 \cdot e \cdot r - 3 \cdot e \cdot r_i)}{r_o^2}$$

The integral expressions

$$J_k(e) := \int_{r_i}^{r_c} h(r) \cdot Z(r, e)^2 \cdot r \, dr \tag{"kinetic integral"}$$

$$J_b(k, e) := \frac{1}{12 \cdot (1 - \nu^2)} \cdot \int_{r_i}^{r_o} h(r)^3 \cdot \left(Zrr(r, e) + \frac{1}{r} \cdot Zr(r, e) - k^2 \cdot \frac{Z(r, e)}{r^2} \right)^2 \cdot r \, dr \dots$$

$$+ \left[\frac{2 \cdot (1 - \nu)}{12 \cdot (1 - \nu^2)} \cdot \int_{r_i}^{r_o} h(r)^3 \cdot \left[\frac{1}{r} \cdot Zrr(r, e) \cdot \left(Zr(r, e) - k^2 \cdot \frac{Z(r, e)}{r} \right) - \frac{k^2}{r^2} \cdot \left(Zr(r, e) - \frac{Z(r, e)}{r} \right)^2 \right] \cdot r \, dr \right]$$

$$+ \frac{h_I^3}{12} \cdot \int_{r_o}^{r_c} Zrr(r, e)^2 \cdot r \, dr$$

$$J_w(k, e, W) := \int_{r_i}^{r_c} h(r) \cdot \frac{\sigma_r(r, W)}{\rho \cdot W^2} \cdot Zr(r, e)^2 \cdot r \, dr + k^2 \cdot \int_{r_i}^{r_o} h(r) \cdot \frac{\sigma_\varphi(r, W)}{\rho \cdot W^2} \cdot \frac{Z(r, e)^2}{r} \, dr \tag{"elastic integral"}$$

"centrifugal integral"

$$\beta := \sqrt{\frac{E}{\rho}} \qquad \beta^2 = 2.611 \cdot 10^7 \frac{\text{m}^2}{\text{s}^2} \qquad \text{Speed of transversal waves Eq. 36.5}$$

β different from 36.5 because h and r are left in the integrals

Rayleigh-Ritz quotient to be minimised by eps

$$\lambda(k, \text{eps}, W) := \frac{J_b(k, \text{eps}) \cdot \beta^2 + J_w(k, \text{eps}, W) \cdot W^2}{J_k(\text{eps})} \quad \text{Eq. 35.9}$$

Given

$$\lambda(k, \text{eps}, W) = 0 \cdot s^{-2}$$

$$\text{eps}_{\min}(k, W) := \text{MinErr}(\text{eps})$$

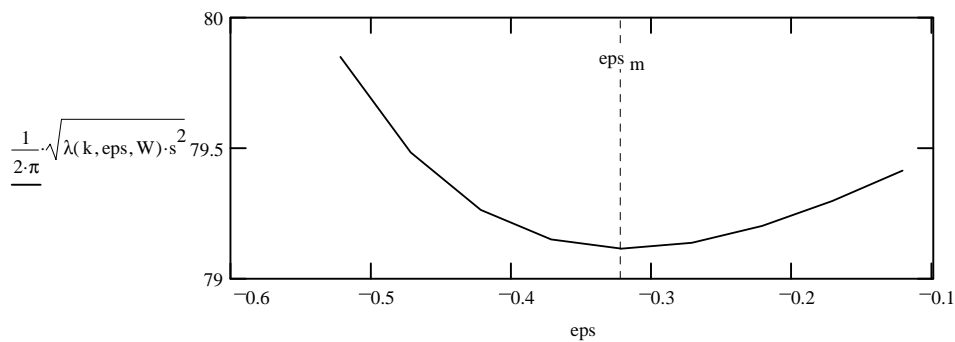
Solve: $k := 2$ $W := 3000\text{-rpm}$ $\text{eps}_m := \text{eps}_{\min}(k, W)$

$$f_{kW} := \frac{1}{2 \cdot \pi} \cdot \sqrt{\lambda(k, \text{eps}_m, W) \cdot s^2} \quad f_{kW} = 79.115$$

Plot the result to check local minimum

$$\text{eps}_m = -0.322$$

$$\text{eps} := \text{eps}_m - 0.2, \text{eps}_m - 0.15 \dots \text{eps}_m + 0.2$$



A.7.2 Driver program of the simulation

```
%STARTINT - Global settings for the integration
%
%REVISION PS9606251700: general layout fixed
%REVISION PS9610201700: more variable control
%
%COPYRIGHT 1996 P. Schmiechen

%GLOBAL VARIABLES
% DEBUG governs amount of output:
global DEBUG
DEBUG= 1;

% Highest natural frequency considered in Hz:
global WMAX
WMAX= 2*pi*50;

% Minimum sampling frequency
global FSMIN      % computed from highest natural frequency
```

```

% Contact parameter
global RCONTACT % radius computed from modal data in modparms
global RSK RSGAP RSMUE RSD
global d
RSK = 1e8; % infinite stiffness
RSGAP= 2e-3; % gap in meters
RSMUE= 0.2; % coefficient of friction (Coulomb), Szabo I,284
RSD = 0.001; % impact damping -> loss (0.0001 works), Rabinowicz

% Investigated nodal diameter and distance to critical speed in Hz
d = 0.01; % modal damping for all modes
theND= 2; % investigated nodal diameter
faway= 3; % running speed away from critical
fsplit=0.00; % frequency split for detuning

% No more user input necessary No more user input necessary %%%%%%%%%%

% Modal parameters at 0 rpm from MATFEM
modaldir='modaldat/200';
modelr='disc'; models='bladdisc';
[Phir,Wr,Muer,NDr,Phis,Ws,Mues,NDS]=modparms(modelr,models,modaldir);

% Select Speed
moder= min(find(NDr==theND));
modes= min(find(NDS==theND));
Omega= omegacrt(Wr(moder),Ws(modes)+faway*2*pi,theND); % TW coincidence

WrOmega= cfomega(Omega,Wr,NDr)'; % correct natural frequencies

% Introduce frequency split in rotor
WrOmega(moder) = (1-0.5*fsplit)*WrOmega(moder);
WrOmega(moder+1)= (1+0.5*fsplit)*WrOmega(moder+1);

% Reduce rotor data
% Find frequencies below wmax
fir= find(WrOmega+NDr*Omega<=WMAX | abs(WrOmega-NDr*Omega)<=WMAX);
% fix modes according to participation
fir= [1,2:7,9:10, 13:14]';
wr= WrOmega(fir); phir= Phir(:,fir); muer= Muer(fir); ndr=NDr(fir);
wrmax= max(abs(wr+ndr*Omega));

% Reduce stator data
% determining frequency is the highest rotor frequency needed:
fis= find(Ws<=wrmax);
% select modes according to participation
fis= [1:2,3,4:20,21]'; % include torsional mode, may help
ws= Ws(fis); phis= Phis(:,fis); mues= Mues(fis); nds=NDS(fis);

% Determine sampling rate from highest natural frequency
FSMIN= 1.2*wrmax/2/pi*2; % 20% oversampling

inis= iniconds('rand',[0.001 0 0 0])+ ...
      iniconds('wave',[-theND,0.0015,10*pi/180]);

% integration options
op= odeset('outfun','rsodeplt','rtol',1e-4,'atol',1e-4,'minstep',1e-12);
tic; [t,y]= ode45('deriv',[0:1/FSSIM:4],inis,op); TOC=toc;
disp(['Total integration time: ',num2str(TOC/60),' min.']);

eval(['save ' fname ' y t Omega d RSD RSK RSMUE theND faway fsplit']);

```

A.7.3 Critical speed and engine-order speed

```
function Omega=omegacrt(wr,ws,ND);
%OMEGACRT - critical speed for a given nodal diameter pattern
%
%INPUT:
% wr,ws      natural frequencies of rotor and stator mode at 0 rpm
% ND        the nodal diameter pattern of the rotor
%
%OUTPUT:
% Omega     critical speed
%
%EXAMPLE:
% Omega= omegacrt(Wr(4),Ws(4),2);

%COPYRIGHT (c) 1996, P. Schmiechen, PS9606261300

a2= jwjk(ND);

Omega= 1./(ND.^2-a2).*(ND.*ws+sqrt(a2.*ws.^2+(ND.^2-a2).*wr.^2));

ze= find(ND==0 | ND==1);
if ~isempty(ze),
    Omega(ze)= inf*ones(size(ze)); % No critical speeds for 0ND and 1ND
end;
```

A.7.4 Speed adjustment of modal data

```
function wr= cfomega(Omega,Wr,NDr);
%CFOMEGA - rotor natural frequencies for a given speed
% wr= cfomega(Omega,Wr,NDr);
%
%INPUT:
% Omega:    speed of rotation in rad/s = 2*pi*rpm/60 = 2*pi*Hz
% Wr:      if specified: the natural frequencies at 0 rpm
% NDr:     the nodal diameter pattern of the rotor
%
%OUTPUT:
% wr:      corrected natural frequencies
%
%NOTE:
% Wr can be left unspecified
% If Wr and Omega are vectors then a matrix
% is returned with length(wr) columns

%COPYRIGHT (c) 1996, P. Schmiechen, PS9606261300

% Material constants, if w0 not supplied
E= 211e9; rho= 7850; h= 0.75e-3; ro= 0.250; % strictly metric
beta2= E/rho;

if Wr==[],% use formula
    wr=sqrt(ones(size(Omega))*beta2*jbjk(NDr)'*(h/ro^2)^2+...
            Omega.^2*jwjk(NDr)');
else % use w0 from experiment or FEM
    wr=sqrt(ones(size(Omega))*Wr'.^2+Omega.^2*jwjk(NDr)');
end;
```

A.7.5 Dynamics of the state vector

```

function yt= deriv(t,y)
%DERIV - returns the derivative of the state vector y
% yt=deriv(t,y)

%COPYRIGHT (c) 1996 P. Schmiechen, PS9606201800

% stator
xsS= phis*y(psi);
xstS= phis*y(psti);
% theta at blade tips: geometric position + deflection from thetadof
thetasS= (allblades-1)/NBLADES*2*pi+ ...
          atan(xsS(thetadof+onedofs)/RCONTACT);

% rotor
xrR= phir*y(pri); % rotor deflections in rotating reference frame
xrtR= phir*y(prti); % velocities
% theta of nodes: geometric position + rigid body phase
thetarS= (allnodes-1)/NNODES*2*pi+Omega*t;

%xrS and xrtS only at the NBLADES positions of the blade tips
[xrS,xrtS,cnodes,fweights]=deflcont(thetasS,thetarS,xrR,xrtR);
[dxz, dxtSn]=interfer(xrS,xrtS,xsS,xstS);
dxz= (dxz>0).*dxz;
[FcrR,FcsS]= forcec(dxz,dxtSn,xrS,cnodes,fweights);

PrR= phir'*FcrR;
PsS= phis'*FcsS;

yt= [
      y(prti)
      y(psti)
      (-wr.*wr.*y(pri)-d.*wr.*y(prti)+PrR)
      (-ws.*ws.*y(psi)-d.*ws.*y(psti)+PsS)];

```

A.7.6 Displacement at possible contact points

```

function [xrS,xrtS,cnodes,fweights]=deflcont(thetasS,thetarS,xrR,xrtR);
%DEFLCONT - deflections and angles of the rotor at thetasS
% [xrS,xrtS,cnodes,fweights]=deflcont(thetasS,thetarS,xrR,xrtR);
%
%INPUT:
% thetasS, thetarS: stator and rotor angles in stat. frame
% xrR: rotor displacement in rot. frame
% xrtR: rotor velocity in rot. frame
%
%OUTPUT:
% xrS deflection of rotor at blade positions (ndof*NBLADES,1)
% xrtS velocity of rotor at blade positions (ndof*NBLADES,1)
% cnodes adjacent nodes of contact (NBLADES,2)
% fweights force-weightings (NBLADES,2)
%
%ASSUMPTION:
% Angle thetarS positive and monotonuously increasing!
% thetasS as computed by thetaBlades+angdeflect (tang. deflection)
% thetarR = node location (assuming small xrRzz)

```

```

NBLADES=length(thetasS);
NNODES=length(thetarS);
dthetar=2*pi/NNODES; % angle between nodes

% Map to [-pi,3*pi+]
if thetarS(NNODES)>1.5*(2*pi),
    thetarS=thetarS-round(thetarS(1)/2/pi)*2*pi;
end;
% Expand span to make life easier
thetarS=[thetarS-2*pi; thetarS; thetarS+2*pi];
if thetarS(1)>thetasS(1) | thetarS(length(thetarS))<thetasS(NBLADES),
    error('thetarS does not cover the range of thetasS completely!');
end;

cnodes=zeros(NBLADES,2);
fweights=zeros(NBLADES,2);

xrS=zeros(ndof*NBLADES,1); % all displacements
xrtS=zeros(ndof*NBLADES,1); % all velocities

for blade=1:NBLADES,
    leftnode=max(find(thetarS<=thetasS(blade))); % do not wrap here
    if DEBUG>3,
        [leftnode, min(thetarS), max(thetarS), thetasS(blade)]
    end;

    leftlever= (thetasS(blade)-thetarS(leftnode));
    rightlever= dthetar-leftlever;
    fweight= 1-[leftlever rightlever]/dthetar;
    fweights(blade,:)= fweight;

    leftnode= rem(leftnode-1,NNODES)+1;
    rightnode= rem(leftnode,NNODES)+1;

    nodes= [leftnode, rightnode];
    cnodes(blade,:)= nodes; % left and right node on rotor

    % thetadof: only for velocities
    xrtS(ndof*(blade-1)+thetadof)=xrtS(ndof*(blade-1)+thetadof)+...
        fweight*xrtR(ndof*(nodes-1)+thetadof);

    % rrdof: only rotation
    xrS(ndof*(blade-1)+rrdof)=xrS(ndof*(blade-1)+rrdof)+...
        fweight*xrR(ndof*(nodes-1)+rrdof);

    % zdof: interpolate parabolically, NEEDS rrdof!
    % mean slope between left node and tip position
    meanslope= (xrR(ndof*(leftnode-1)+rrdof)+xrS(ndof*(blade-1)+rrdof))/2;
    xrS(ndof*(blade-1)+zdof)=xrS(ndof*(blade-1)+zdof)+...
        xrR(ndof*(leftnode-1)+zdof)+meanslope*leftlever;
    xrtS(ndof*(blade-1)+zdof)=xrtS(ndof*(blade-1)+zdof)+...
        xrtR(ndof*(leftnode-1)+zdof)+meanslope*leftlever;
end;

```

A.7.7 Interference

```

function [dxz,dxtSn]=interfer(xrS,xrtS,xsS,xstS);
%INTERFER - computes interferences at blade tips and time derivatives
% [dxz,dxtSn]=interfer(xrS,xrtS,xsS,xstS);
%
% Distance at blade tips and normal velocity (for impact)
%
%INPUT:
% input      from deflcont
%
%OUTPUT:
% dxSz      distance at locations of blade tips (interference positive)
% dxtSn     normal component of relative velocity (to rotor surface)

% distance in z-direction, positive is interference
dxz=(xsS(zdof+onedofs)-RSGAP)-xrS(zdof+onedofs);

% the angle
xrSrr= xrS(rrdof+onedofs); % NBLADES positions
if any(abs(xrSrr)>0.9*pi/2),
    disp(xrSrr')
    error('xrSrr > 0.9*pi/2 unrealistically large.');
```

```

end;

% Impact loss: velocity in normal direction for impact
% [n] = [ cos -sin]*[z      ]
% [t] = [ sin  cos] [R*theta]
xrtSn= cos(xrSrr).*xrtS(zdof+onedofs)-
sin(xrSrr).*xrtS(thetadof+onedofs);
xrtSt= sin(xrSrr).*xrtS(zdof+onedofs)+cos(xrSrr).*...

(xrtS(thetadof+onedofs)+RCONTACT*Omega*ones(NBLADES,1));
xstSn= cos(xrSrr).*xstS(zdof+onedofs)-
sin(xrSrr).*xstS(thetadof+onedofs);
xstSt=
sin(xrSrr).*xstS(zdof+onedofs)+cos(xrSrr).*xstS(thetadof+onedofs);

% relative velocities:
dxtSn= xrtSn-xstSn;
dxtSt= xrtSt-xstSt;
if any(dxtSt<0),
    error('contact velocity changed direction! dx/dt>RCONTACT*Omega');
```

```

end;

```

A.7.8 Contact forces

```

function [FcrR,FcsS]=forcec(dxz,dxtSn,xrS,cnodes,fweights);
%FORCEC - contact forces
% [FcrR,FcsS]=forcec(dxz,dxtSn,xrS,cnodes,fweights);
%
%INPUT:
% input from deflcont and interfer
%
%OUTPUT:
% FcrR      contact forces acting on the rotor in rotating coordinates
% FcsS      contact force acting on the stator in stationary coordinates

```

```

%
%NOTE:
% The axial force is computed from an assumed interface stiffness RSK
% and the tangential force is computed from Coulomb's law with RSMUE
% Some loss is introduced, see rsk.m

% Interference
dxz= (dxz>0).*dxz; % penetration

if any(dxz), % for speed
    % Magnitude of axial force
    Fz= -rsf(RSK,dxz,RSD,dxtSn,1e-4); % -k*dx-d*dxt

    % Magnitude of azimuthal force
    % Ftheta = -mue*Fn*sign(vt)
    %
    % Fz      = const [ cos  sin] Fn
    % Ftheta =      [-sin  cos] Ft
    %
    % Ft=RSMUE*Fn

    if RSMUE~=0,
        % the angle
        xrSrr= xrS(rrdof+onedofs); % at NBLADES blade tips
        Ftheta= -Fz.*abs((RSMUE-tan(xrSrr))./(1+RSMUE*tan(xrSrr)));
    else
        Ftheta= 0.0*ones(NBLADES,1);
    end;

    %Stator force acts on blade-tips
    FcsS= kron(Fz,[0 0 1 0 0 0]') + kron(Ftheta,[0 1 0 0 0 0]');
    % alternatively: FcsS=zeros(ndof*NBLADES,1); FcsS(zdof+onedof)=Fz;...
    if any(Fz>0) | any(Ftheta<0) | DEBUG>2,
        disp('FORCEC: [Fz?<0 Ftheta?>0]'' [kN]:');
        disp([Fz Ftheta]'/1000);
    end;

    %Rotor force needs some sorting to the nodes
    % cnodes includes the coordinate back-transformation
    Qrz= zeros(NNODES,1);
    Qrtheta= zeros(NNODES,1);
    for i= 1:NBLADES, %that many contact points, exactly!
        Qrz(cnodes(i,:))= Qrz(cnodes(i,:)) -Fz(i) *fweights(i,:);
        Qrtheta(cnodes(i,:))= Qrtheta(cnodes(i,:))-Ftheta(i)*fweights(i,:);
    end;
    if any(Qrz<0) | any(Qrtheta>0) | DEBUG>2,
        disp('FORCCONT: [Qrz?>0 Qrtheta?<0]'' [kN]:');
        disp([Qrz Qrtheta]'/1000);
    end;
    FcrR= kron(Qrz,[0 0 1 0 0 0]') + kron(Qrtheta,[0 1 0 0 0 0]');
else
    FcsS= zeros(NBLADES*ndof,1);
    FcrR= zeros(NNODES*ndof,1);
end;
end;

```

A.7.9 Normal Force

```

function f=rsf(k,x,d,xt,x0);
%RSF      - interface force f=f(x,dx/dt)
% f= rsf(k,x,xt,x0);
%
% The interface force with a continuous slope at d=0
% and velocity hysteresis
%
%INPUT:
% k        linear stiffness
% x        interference (positive)
% d        damping of impact, relates to loss
% xt       relative velocity
% [x0]     changeover to linear regime [10e-6]
%
%OUTPUT:
% f        interface force

%COPYRIGHT 1996 P. Schmiechen

if nargin<5,
    x0= 10e-6;
elseif x0<=0.0,
    error('If you want a linear spring, set x0=1e-9 but not 0!')
end;
if size(x)~=size(xt),
    error('Vectors x and xt must be the same size.')
end;

xg= x0/2; % change-over point
k2= k/2/x0; % "stiffness" in square regime

f= zeros(size(x));
fi= find(x<=x0); % points in square regime
f(fi)= k2*x(fi).^2;
gi= find(x>x0); % points in linear regime
f(gi)= k*(x(gi)-xg);

f= f.*exp(-1000*d*xt);

%EXPLANATION:
% f(x0)=g(x0) : k2*x0^2=k*(x0-xg)
% df/dx=dg/dx (x=x0) : 2*k2*x0=k

%LOCAL STIFFNESS:
% square regime: ksquare= 2*k2*x = k/x0*x
% linear regime: klinear= k

```

Appendix 8: Terminology

Because of the complexity of the dynamics of rotating machinery, a clear definition and description of the quantities used is essential. Some of the following discussion on terminology applies to non-rotating structures as well, but most of the comments will be of concern to engineers analysing rotating machinery.

All terms are introduced in the main body of the thesis, but this glossary is intended to provide the reader with a concise description of each concept or term.

A.8.1 Description

Seeking to describe a matter or situation makes it necessary to express it in a logical way by words and sentences or mathematical symbols and equations. The expressions and descriptions are non-unique but depend on the context while the described matter, for example the dynamics of an elastic body, is governed by underlying principles, the laws of physics in our case.

A.8.2 Frame of reference

A frame of reference is an aid to describing the position of objects in a space of arbitrary dimensions. Each frame of reference is related to other reference frames by a time-varying transformation. If the transformation between the frames of reference is not time-varying, it means that one frame of reference is sufficient to describe the position of any object and the further frames of reference are introduced either because of lack of knowledge of the system or because of convenience. According to Kane and Levinson, (1985), frames of reference are equivalent to rigid bodies.

So, for a system consisting of two structures able to move with respect to each other, like the rotor and the stator in this study, two reference frames must be introduced. If, in addition, the two bodies move with respect to a fixed reference, a further reference frame must be used to define the dynamics of the two structures.

A.8.3 Coordinate systems

Many frames of reference can be attached to a rigid body as mentioned above. As they are all attached to the same rigid body, the position of any point on the body can be expressed in any frame. They are introduced for convenience of description solely, and are related to each other by a time-invariant transformation, making them coordinate systems.

The global coordinate systems used in the analysis of the rotor-stator system are the Cartesian coordinates (x, y, z) , used in FE programs, and the cylindrical coordinates (r, θ, z) , used throughout the rest of the analysis, Figure A-7, where only the distinct coordinates are given different symbols.

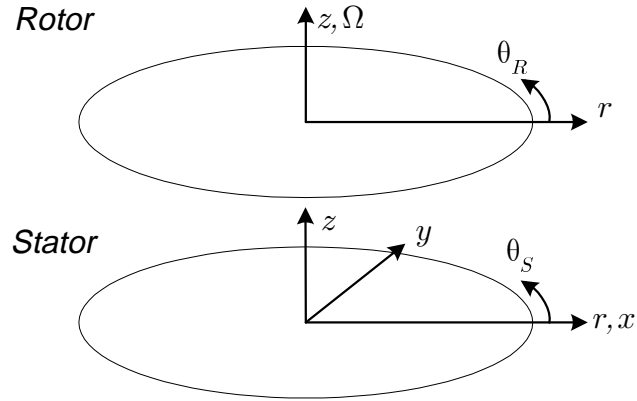


Figure A-7: Global coordinate systems

Local Cartesian coordinate systems, normal and tangential (and bi-tangential) direction, attached to each of the contact points, $(n, t, b)_i$, are used in the computation of the contact forces.

All coordinate systems presented, Cartesian and cylindrical, are defined as right-handed, orthogonal coordinate systems. For the unit vectors $\{e\}$, the following right-hand rule for the cross-product holds:

$$\{e\}_1 \times \{e\}_2 = \{e\}_3 \quad (\text{A-35})$$

and all permutations thereof.

A.8.4 Axis of rotation

The z -axis of both rotating and stationary reference frame are supposed to coincide and, for constant speed of rotation around this axis, the tangential coordinates in the rotating and stationary frame of reference are related by:

$$\theta_R = \theta_S - \Omega t \quad (\text{A-36})$$

In the present analysis, the axis of rotation is assumed to be the z -axis of the global coordinate system, Figure A-7. In rotordynamics, as opposed to bladed disc analysis, the axis of rotation is often assigned the x -axis.

A.8.5 Direction

Directions are defined in terms of the coordinates. A positive rotation causes an increase in the tangential direction. This can be determined conveniently by the cross-product of the vectors, Equation (A-35):

$$\{e\}_2 \times \{e\}_3 = \{e\}_1 \quad \text{i.e.,} \quad \begin{Bmatrix} 0 \\ 0 \\ \Omega \end{Bmatrix} \times \begin{Bmatrix} r \\ 0 \\ 0 \end{Bmatrix} = + \begin{Bmatrix} 0 \\ r\Omega \\ 0 \end{Bmatrix} \quad (\text{A-37})$$

When an elastic wave propagates through a body, its direction of travel is an important attribute in the description of the motion. In rotationally-periodic structures the terms

‘forward’ and ‘backward’ are common but other combinations are used too, like ‘progressive’ and ‘retrogressive’ by Loewy and Khader, (1984). In this thesis, the terms ‘forward’ and ‘backward’ are used in the stationary reference frame, in the rotating frame of reference, the terms ‘co-rotating’ and ‘counter-rotating’ are used. The direction and velocity of the waves determines the sign and the magnitude of the frequency for any reference frame. Positive frequencies indicate positive wave velocities and negative frequencies indicate negative wave velocities, Figure A-8:

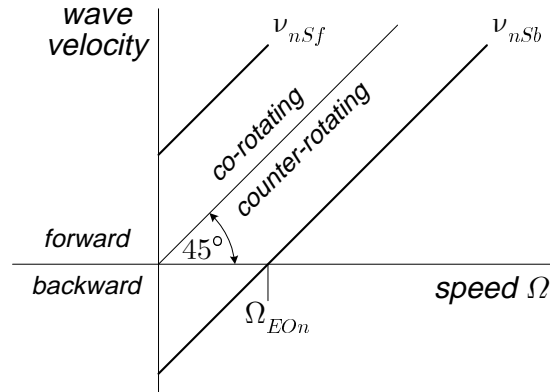


Figure A-8: Wave velocity over speed explaining directional terms

In the context of travelling waves and rotating machinery, the notion of negative frequencies is very useful and so the conventional simplification of neglecting the negative roots of the eigenvalues and taking the positive roots only as the natural frequencies, is actually not simplifying the description, but makes it, at times, more difficult.

A.8.6 Modes - waves

Waves are phenomena of energy transport. After a wave passes through a structure, the material points of the structure return to their original position: no transport of material occurred, but energy was transmitted.

For some special classes of structures, e.g., rotationally-periodic and axisymmetric structures, waves are a convenient way of describing the vibration: instead of describing the vibrations in terms of modes, one can use wave notation. A mode pair of cosine and sine modes transforms into a wave pair of forward and backward waves when combined in a particular way:

$$\begin{aligned} \cos(n\theta) + i \sin(n\theta) &= e^{in\theta} \\ \cos(n\theta) - i \sin(n\theta) &= e^{-in\theta} \end{aligned} \tag{A-38}$$

A scaled, linear, combination of modes still solves the eigenproblem, and thus waves are eigensolutions. As they are just a different description of the same physical quantities, they can be used interchangeably and the orthogonality conditions holds for modes and waves:

$$\begin{aligned}
\int_0^{2\pi/n} \cos(n\theta) \cos(n\theta) d\theta &= \pi & \int_0^{2\pi/n} e^{in\theta} (e^{in\theta})^* d\theta &= \pi \\
\int_0^{2\pi/n} \cos(n\theta) \sin(n\theta) d\theta &= 0 & \int_0^{2\pi/n} e^{in\theta} (e^{-in\theta})^* d\theta &= 0
\end{aligned} \tag{A-39}$$

The free response is composed of the sum of generalised coordinates, in complex wave notation:

$$u_R = \sum_{r=-\infty}^{\infty} e^{ir\theta_R} e^{i\omega_r t} = \sum_r e^{i(r\theta_R + \omega_r t)} \tag{A-40}$$

Here r runs from minus infinity to plus infinity for the backward and forward waves. In Equation (A-40), it is understood that only the real part constitutes the response.

A.8.7 Frequency - speed - velocity

In this work, frequency is associated with vibration while speed will be used for rotation and velocity will be used for wave motion. All three quantities have the unit $[1/time]$ but are very different in all other aspects. Frequency, measured in Hz is often used in the context of angular velocity, measured exclusively in rad/s, and both quantities are related by $2\pi f = \omega$. This notion of angular velocity was devised from a different concept of continuous repetitive motion and is different to the speed of rotation, Ω , measured in rev/min. In order to distinguish wave motion from the other two, the term wave velocity or just velocity will be used. Its units within this thesis are rad/s. Strictly, the different units can be interchanged arbitrarily, as they serve only to describe a physical quantity, but in the thesis for reasons of clarity, frequency, speed, and velocity have been kept as separate as possible.